ARCHIVES OF ACOUSTICS
22, 3, 219–244 (1997)

ARTICULATION-RELATED FEATURES IN THE PIPE ORGAN SOUND

B. KOSTEK

Sound Engineering Department
Faculty of Electronics, Telecommunications and Informatics,
Gdańsk University of Technology
(80-952 Gdańsk, ul. Narutowicza 11/12)

Investigations in the domain of sound growth in organ pipes resulted in describing some of the articulation-related features. An equivalent electrical circuit of an organ action was created basing on computer modeling techniques. The response characteristics of the circuit were obtained numerically and are discussed. The concept of an organ action governing a digitally controlled valve is proposed and examined. A comparison between the response characteristics of the equivalent electrical circuit, the tonal characteristics of an exemplary pipe and characteristics obtained through the analytic modeling of pipes is presented and discussed. Numerical simulations are found to be in good conformity with experimental results. Among the latest electronic hardware achievements, the fuzzy logic-based knowledge acquisition and control system seems to be a capable tool for solving the problem of control of the electromagnetic valve of the organ pipe. A model of a pipe organ with a fuzzy logic-based control system was designed, constructed and investigated. Results of studies and experiments in the domain of pipe organ valve control are presented in the paper.

1. Introduction

Computerizing classical pipe organs opens a new domain of interests, in which modern technology meets the traditional way of playing such instruments. The application of a microprocessor system to an organ may significantly improve many of the control and display functions of the console. Computer control of the pipe organ also enables a new approach to the problem of existing musical articulation limitations in a pipe instrument with an electromagnetic action. This kind of pipe organ control is characterized by the promptness in the pipe response, as the air flow cannot be controlled otherwise than by the rapid opening and equally fast closing of the valve. In the opinion of organists, this deprives them of the possibility to interpret music according to their wishes.

The differences between particular organ instruments in terms of control system design directly affect their performance evaluation as expressed by musicians and listeners. This type of research was carried out during the 1950's and 1960's. However, the research methods applied then were scarcely precise. New interest in the analysis of pipe organ sound derives from the fact that many physical features formed during instrument

production are not sufficiently recognized to form a basis for the design of contemporary pipe organ instruments. The theoretical studies of organ pipes, both the classical ones of Lord Rayleigh and Brown and later those of POWELL [23], BENADE [1] and COLTMAN [5], do not present a uniform opinion on the dynamic behavior of wind instruments. That is why a fully adequate pipe simulation model was not as yet elaborated. Various techniques have been applied in order to extract parameters relevant to the physics of an organ pipe. Some of these date from at least the early 1950's, with papers by RICHARDSON [26] and RAKOWSKI and RICHARDSON [25] being among the earliest references. Another approach based on the work of CADDY and POLLARD [3] considers only time domain analysis of attack transients for a tested pipe organ. Early work of FLETCHER [9] was based on calculations of both steady state oscillations of the organ pipe and overblown regimes in nonlinear interaction with excitation. As pointed out by KEELER [12], the evidence of overblown regimes in initial transients cannot be neglected. During the build-up of the sound, the sound pressure is changing significantly. An efficient method of modeling the pipe sound, both analytically and numerically, was originally described by FLETCHER [10] and has been used for this purpose by SCHUMACHER [27], NOLLE and FINCH [20] and re-examined by KOSTEK and CZYŻEWSKI [14]. Schumacher based his study on Fletcher's model in terms of a nonlinear equation of the Hammerstein type and obtained the oscillating waveform to an arbitrary harmonic number. Nolle and Finch described both experimental study and numerical simulations of flue pipe starting transients, based on the elaborated model. They reported the relation between the speed of pressing the key and the overshoot which appears in the sound attack in organs having mechanical tracker action. They observed the percussive character of an attack in two cases, namely when the burst occurs (a second or third harmonic dominates the starting transient) or when the energy of higher harmonics is bigger than that of the fundamental. Nolle and Finch observed these phenomena in their experimental tests. They also apply test results to the numerical simulations, and as a result some initial parameters were based on observations made during their experiments [20]. Rakowski and Richardson and also Lottermoser mentioned another effect, which may be referred to as the precursor, preceding the attack itself. However, this happens when the air is just starting to be admitted into the pipe, thus from the musical viewpoint the resulted sound does not last long enough to have discernible pitch [18, 25].

Reviewing the most common organ action types, one can find significant mechanism features which cause differences in the sound produced. Among the organ actions, mechanical, pneumatic, electrical and mixed ones may be identified [29]. The first type provides the sound most preferred both by organists and by listeners. The pneumatic or electropneumatic control of the organ are only found in organs built previously. On the other hand, the electrical action is usually chosen by modern organ builders because of the possibility of separating the control system from the rank of pipes. Time delay caused by the operation of the organ mechanism might be one of the criteria of the quality of an organ action [15, 22] and the resulting sound. Up to some value, time delays in the operation of an instrument may be tolerable, though a synchronous response to the performance of the organist is desirable. In the case of a mechanical action, delays caused by this system are mainly that of opening the pallet in order to build up the

pressure in a key chamber. The direct electrical control due to the lack of intermediate air or wood passages does not affect the time of opening the pallet. Nevertheless, the initial time delay is only one of the factors characteristic of the differences in a pipe sound response. It is possible to determine another factor associated with the articulation features having an influence on the quality of the pipe sound, namely the way in which the transient attack is building up [12, 14]. The measurement procedures which allow the extraction of parameters for the above mentioned investigations will be reviewed in the next paragraph.

The aim of the presented research is three-fold. First of all, the aim is to examine the operation mechanisms in order to build up an equivalent electrical circuit of a mechanical organ action. The proposed and examined model is later modified using a multi-step source in order to discuss the concept of a digitally controlled organ action. Secondly, a comparison is presented between the response characteristics of the pipe-equivalent electrical networks, the data taken from the experimental investigations, and characteristics obtained from the analytic model of the pipe based on Fletcher's analytic model [10]. The third aim of the present investigations concerns the possibility of equipping an organ tracker action with a fuzzy-logic-based control system. A model of a pipe organ using a fuzzy-logic-based control system was designed, constructed, and investigated. These investigations were mainly confined to the sound features of the starting transient in order to meet quality requirements for the pipe organ sound in the domain of musical articulation.

2. Experimental background of the organ pipe sound articulation

2.1. Time delays

For the purpose of investigating and comparing various tone qualities of the organ sound, a measurement program was established. It should be remembered that the change of velocity of opening the mechanical pallet is the result of the force impressed upon the key. Consequently, the velocity of the key motion has been selected as a relevant parameter associated with the articulation features in organ music. That choice was also confirmed in previous tests [16]. Subsequently, it was noticed that the velocity of the key motion can be replaced by a quantity being more convenient to measure, namely by the time of key depression from its upper to its lower position, the latter being the state of full depression.

Resulting from the above assumptions, the data for analyses was acquired through the simultaneous recording of the time of key depression and the resulting sound produced by the pipe. The lay-out of such a measurement method is presented in Fig. 1. Sounds were recorded in the St. Nicholas Basilica in Gdańsk, having a mechanically controlled organ, and in the Oliva Cathedral, where the organ is controlled with both electropneumatic and direct electrical pallet control. A microphone was placed close to the selected pipe, in the direct field, in order to limit the influence of church acoustics. The position of the key motion was registered through a pair of piezoelectric film sensors installed at

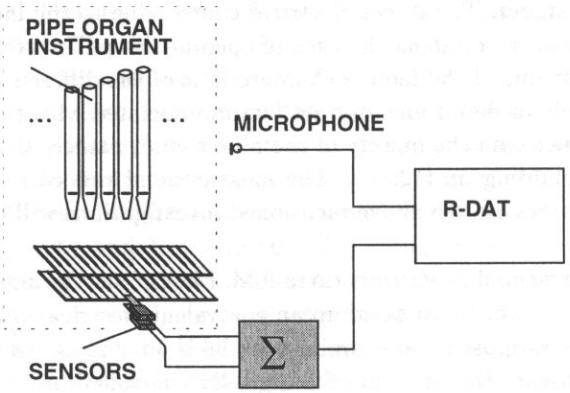

Fig. 1. Lay-out of the signal recording system.

the depressed key (Fig. 2 a, b) which corresponded to the pipe being recorded. Special construction of the sensors allows for their activation only when the plate is moving in one direction, which in this case is from the upper position to the lower one. Therefore, the sensor placed above the key (Fig. 2 a) generates an impulse in the initial phase of pressing the key, whereas the sensor placed under the key (Fig. 2 b) does it in the final phase. The time between the activated impulses can be taken as approximately the time of pressing the key. The sensors are constructed with the use of piezoelectric foils adhered with thin band layers [21]. Electrodes are applied to the polarized film. The sensors have a built in electronic commutator which enables impulse generation at the moment of pressing the piezoelectric film. The structure of electrical connections in this commutator is shown in Fig. 2 c. The assigned letters, namely: A, B, C, D, E in the schema, correspond to points where electric current was measured. Exemplary current characteristics are shown in Fig. 2 d. During the recording, impulses from the sensors were recorded on one of the tape recorder channels which later allowed for identifying the time of pressing the key.

Organs were tested in two different ways, with fast and slow depression of the key according to the demands of musical articulation. The recorded material was subjected to a detailed analysis in order to study the relation between the velocity of the key motion and the resulting articulation features. This made it possible to find the values of the time interval corresponding to the duration of the key motion. This kind of analysis is shown in Fig. 3. Values of Δt in Fig. 3 correspond to key depression times. Additionally, the results of the analyses of key motion are shown in Table 1. The values of time intervals for different key velocities in Tab. 1 are divided into three ranges in the case of the mechanical action. Consequently, as is seen from Tab. 1, the initial delay corresponds very closely to the values quoted in the literature [15, 22] and the mechanism operation of the wood tracker connections may be neglected, both for a slow and fast depressing of the key. On the other hand, there is practically no correlation between the corresponding values of the way a key is depressed when performing on an organ using either an electropneumatic or an electrical action. In the case of the electropneumatic

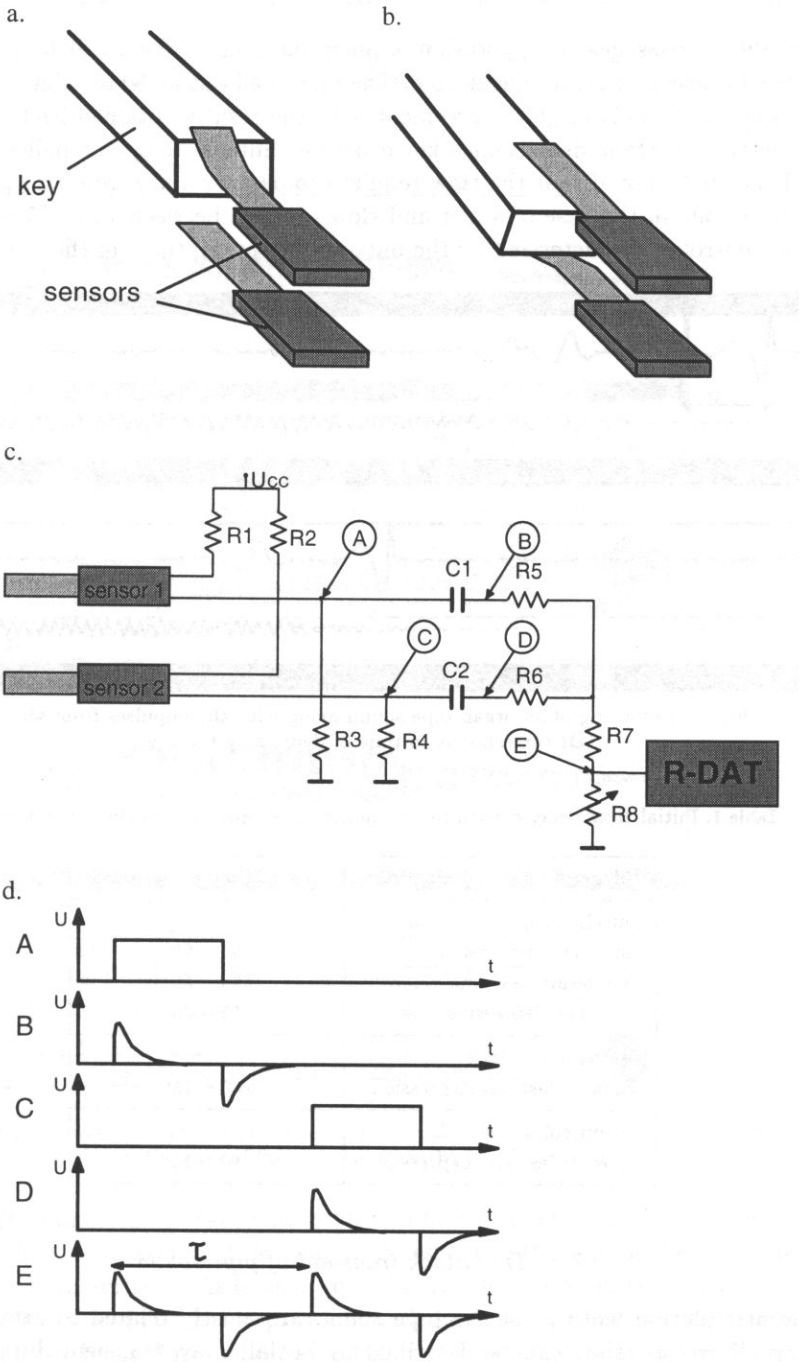

Fig. 2. Registering the time of pressing the key with the use of piezoelectric sensors, a) the key in the resting position, b) the key pressed, c) block diagram of the electronic commutator, d) exemplary current characteristics measured in the assigned measurement points (see Fig. 2 c).

system, the air passages and operation of pneumatic motors cause such delays that the time of key movement may be neglected. The increased initial delay value in comparison to the other systems is in good agreement with the results obtained by POLLARD [22]. In the electrical system, depressing a key evokes an impulse to open a pallet without any delay. It has been noted that the time required to depress a key from its upper position to the lower one in the case of a fast and slow touch is between 10 to 15 ms. This type of organ control is characterized by the outstanding promptness in the pipe response.

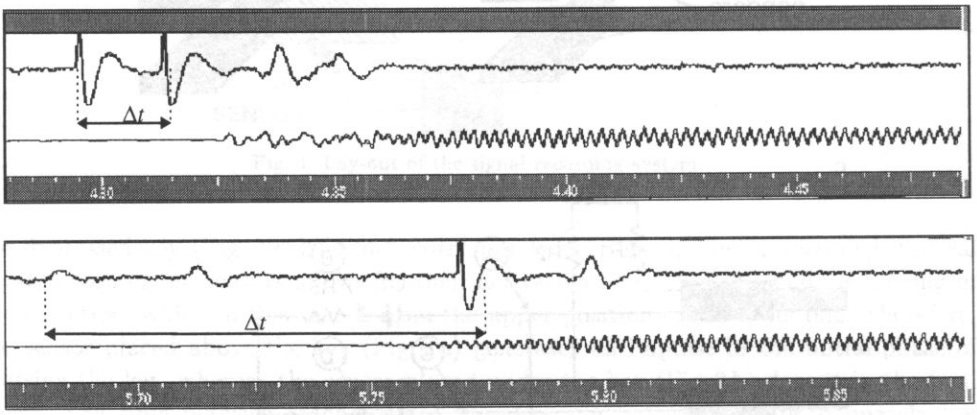

Fig. 3. Recording of an organ pipe sound along with the impulses from sensors (Δt corresponds to time of depressing the key).

Table 1. Initial time delay caused by key motion and operation of the control system.

Type of pipe organ action	Initial time delay [ms]
mechanical:	
slow key depression	50 – 90
moderate key depression	30 – 50
fast key depression	15 – 30
electropneumatic:	
slow & fast key depression	100 – 150
electrical:	
slow & fast key depression	10 – 15

2.2. The attack transient of pipe sound

The articulation features of the pipe sound are mostly related to attack transient building. Therefore, they can be described by initial delay, transient duration and by growth of subsequent harmonics. Figure 4 illustrates the signal envelopes of the note a (110 Hz) of the Principal 8′ in the cases of quickly and slowly depressing the key. Comparison of the two characteristics clearly shows the differences occurring during the stage of growth of the sound. Thus, it is expected that the differences in musical

articulation are determined by the attack transient. Subsequent listening to the extracted transients shows that the pitch of the initial transient is an octave above the pitch of the fundamental.

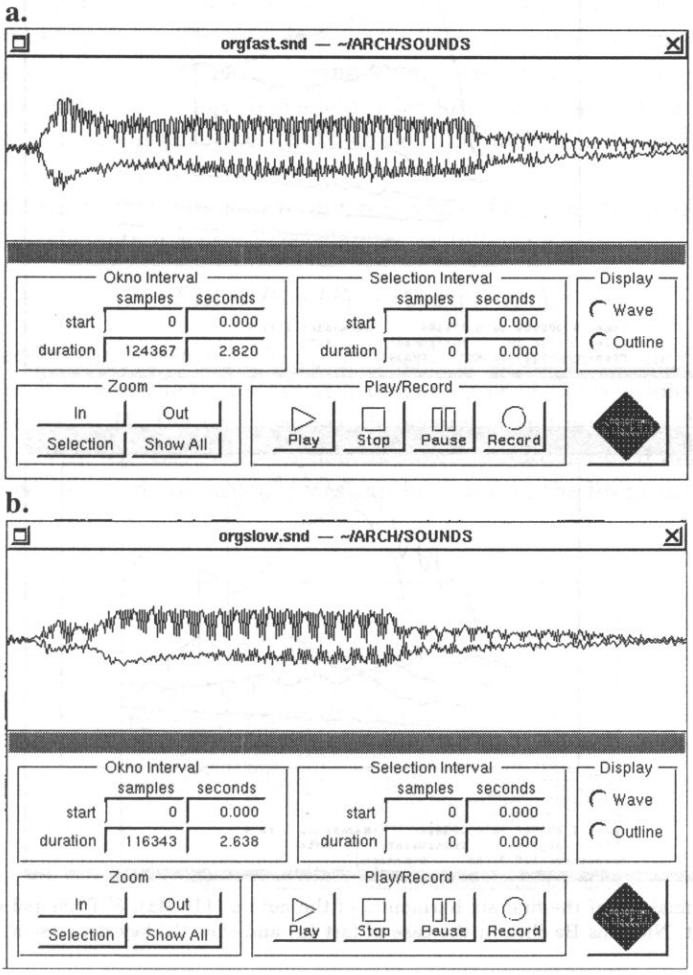

Fig. 4. Signal envelopes, note *a* (110 Hz), 8′ Principal of the organ of St. Nicholas Basilica in the case of fast (a) and slow (b) key depression.

The spectral analysis of transients is plotted in Fig. 5. The attack transient is dominated by the first two harmonics. A delay with respect to the way the key is depressed is visible in the characteristics. As is seen from Fig. 5 a, there is an initial rise in the second harmonic in the case of fast key depression, and the delay of the signal transient differs in character, being longer for the fundamental. It was noted that during the period of the overblown regime, the produced sound is an octave higher than the normal pitch. In the case of a slow attack (Fig. 5 b), the rise of the transient is also slow and the fundamental builds up very smoothly, rising more quickly and at the same time more strongly than the other components.

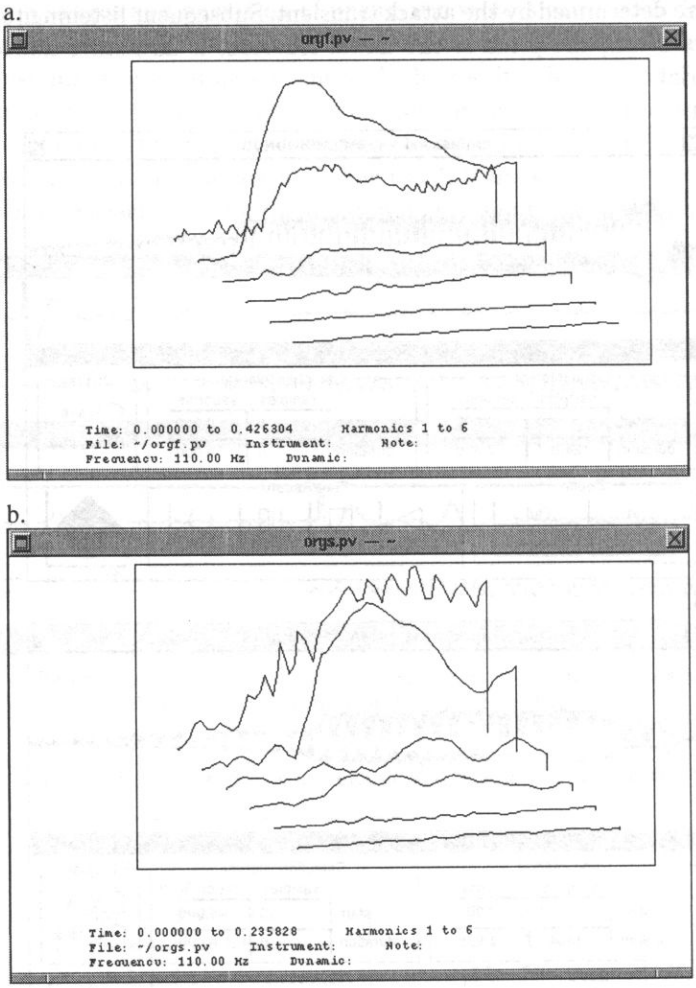

Fig. 5. Spectral analysis of the first six harmonics of the note a (110 Hz), 8′ Principal of the organ of St. Nicholas Basilica in the case of fast (a) and slow (b) key depression.

To verify the above stated observations, sound simulations were performed based on the physical model of pipe organs. One of the methods belonging to the category of physical modeling is "digital waveguide" synthesis [6, 7, 28, 30, 31]. In this method, the wave equation is first solved in a general way to obtain the traveling waves in the instrument body that are then simulated in the waveguide model [6, 7, 28]. What is important, the initial stage of sound rise, critical to the subjective assessment of the naturalness of the organ sound produced by pipes, was modeled with results showing that sounds produced in models in which the air flow conditions were differentiated better resemble the natural sound [7].

Another approach to physical modeling is focused on the mathematical model of the behavior of the pipe when treated as a system. A detailed analytic description and

modeling of transients in the speech of organ flue pipes has been treated by FLETCHER [10] and reviewed intensively in the literature [7, 11, 14, 20]. Several models of organ flue pipe have been developed during recent years (e.g. [4, 5, 8, 19, 32, 33]). However, the existing general concept of the pipe system assumes at least two sub-systems and the interaction between them. The first is a nearly linear resonant system of the pipe and the second is a nonlinear system of blowing wind, with the assumption of its interaction with the pipe. Also, a frequency-dependent delay element, representing the time for jet deflection waves to transverse the height of the pipe mouth, is to be included in this model.

By relating the air pressure flow to different ways of opening the pallet, it is possible to express the articulation aspect according to the following equation:

$$P(t) = P_0 + (P_1 - P_0)\exp(-t/\tau), \tag{2.1}$$

where P_1 specifies the pressure peak, P_0 the steady pressure and τ the decay time from the peak level. It is possible to discuss at least two cases of the relationship between P_1 and P_0. When $P_1 \gg P_0$, the pressure peak is occurring and may be referred to as fast attack. When $P_1 \ll P_0$, then the transient is slow. A more detailed description of the features related to sound rise in flue pipes can be found in the literature [7, 10, 16].

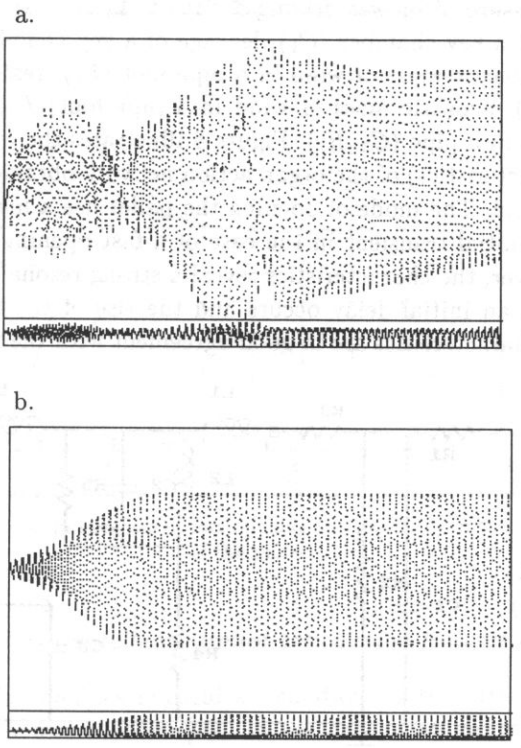

Fig. 6. Graphical presentations of pipe sound simulations, a) in the case of fast attack, b) in the case of slow attack.

The numerical model implemented on the UNIX workstation using the *Mathematica* system was verified by multiple listening examinations of the model output sounds obtained from real-time simulation of the pipe speech response (see Fig. 6). Listening to the signal patterns from the computer simulations makes it possible to state that if the air pressure is activated slowly, the resulting sound is in agreement with the fundamental pitch. If the air flow is fast, then the pitch of the initial transient seems to be one octave higher than that of the steady sound, confirming previously obtained results. Moreover, the impression of the pitch being of the proper tune occurs only after the delay of about 100 ms.

3. Pipe organ action modeling

3.1. Equivalent electrical circuit of an organ action

A general approach to the design of an equivalent electrical circuit of an organ action was made by CADDY and POLLARD [3]. However, the description of the resulting circuit was very simplified, thus requiring completion and then verification. Therefore, a revised and completed equivalent electrical circuit was built up in order to model the operation of the organ action. In Fig. 7, the organ action is represented by the following parameters: pressure of blower driving a circuit (V_1), internal resistance of blower (R_1), capacitance of a key chamber (C_1), leakage of a key chamber (R_2), resistance of a pipe foot (R_3), acoustic mass of wind in a pipe foot (L_1), resonant system of a pipe foot (L_2, C_2, R_5, R_4), acoustic mass of wind in a pipe foot (L_3, R_6), and capacitance and leakage of wind in a pipe (C_3, R_7). Figure 8 illustrates the response characteristics (the indicated characteristics) of the organ action network obtained using the computer modeling analysis tool. The mode of opening the pallet has a marked effect on the initial transient. The initial transient in the case of a fast opening of the pallet is sharp and smooth. Moreover, the characteristics reveal a strong resonance effect. For slow depression of the key, an initial delay occurs and the rise of the transient is slow. It is notable that both characteristics are in good agreement with the results obtained in the

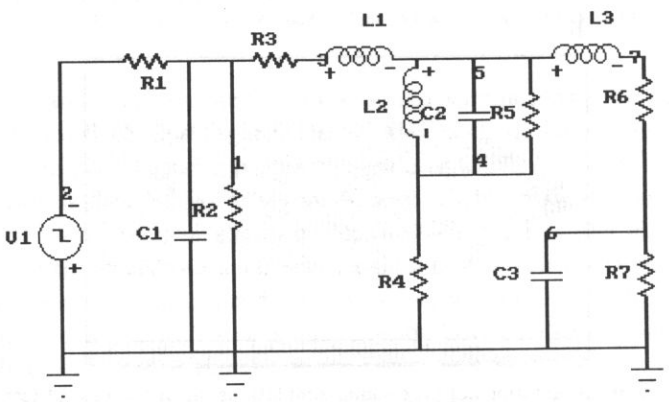

Fig. 7. Equivalent electric network of an organ action.

experimental procedure described previously. In order to examine the influence of the parameters on the response characteristics, the value of the capacitor C_1 was changed. An increase in the value of the capacitor C_1, representing the volume of the key chamber, eliminates the resonance effect and the response curve becomes flat. This relation between the volume of the key chamber and the resulting pipe response is confirmed both by theory [18] and in practice.

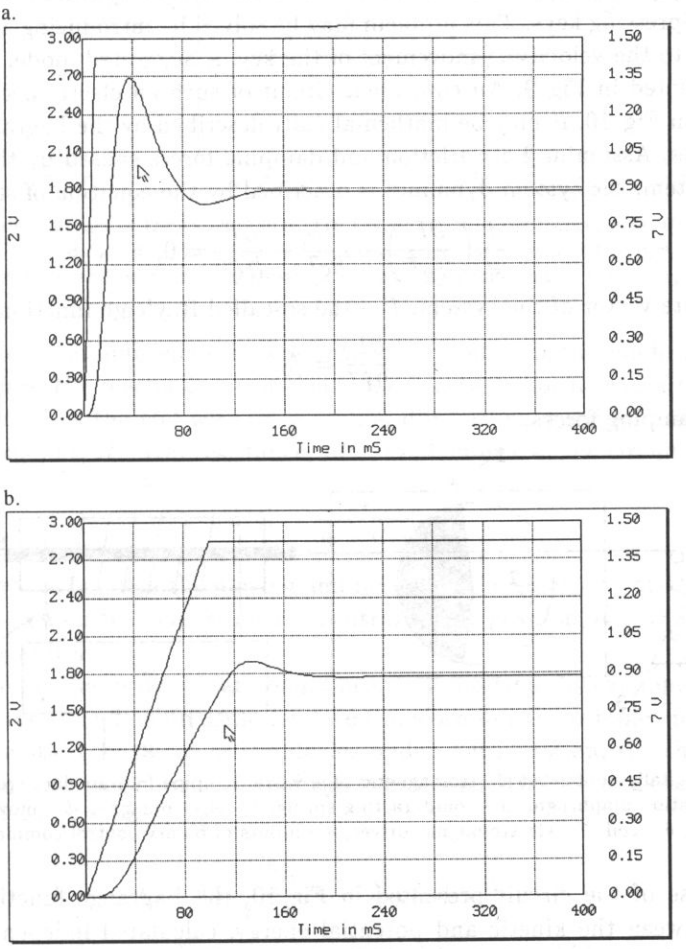

Fig. 8. Initial transient, a) in the case of fast opening the pallet, b) in the case of slow opening of the pallet.

3.2. Digitally controlled articulation features

A mechanical action enables musical articulation by the direct wood tracker connections between a key and a pallet [29]. In the case of an electrical organ action, in whatever way a key is depressed, the electromagnet reacts equally quickly. Digital control of an organ makes possible a system which consists of an electronically controlled

articulation action but which still ensures the quality of sound similar to that obtained from organs having mechanical actions. Such digital control of an organ imposes quantization of the key velocity or another related parameter easier to measure, namely that of key depression time from its upper to its depressed position.

3.2.1. General characteristics of a valve model. In order to control the articulation features in a pipe organ, it is necessary to relate the way of opening the pipe valves to the way of depressing keys. This problem may be solved by introducing a stepping valve which reacts to the velocity of movement of the key. A suggested model of that kind of valve is presented in Fig. 9. An equivalent circuit of such an electromechanical system is presented in Fig. 10. It may be mathematically described by the Lagrange function of state variables. Assuming both friction and damping forces caused by the operation of the given system, the system dynamics is described by the equation of state [24]:

$$\frac{d}{dt}\left(\frac{\partial L}{\partial \dot{q}^T}\right) - \frac{\partial L}{\partial q^T} - \frac{\partial F}{\partial \dot{q}^T} = 0, \tag{3.1}$$

where q – state vector of the system, F – the so-called Rayleigh function defined as:

$$\frac{\partial F}{\partial \dot{q}^T} = f_0, \tag{3.2}$$

where f_0 – damping forces.

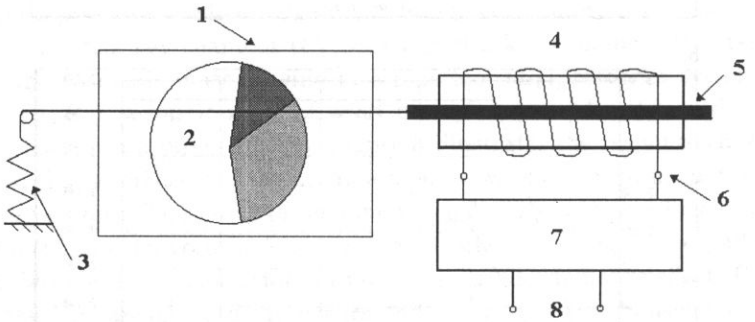

Fig. 9. Digitally controlled electromagnetic pipe valve: *1* – pipe foot air duct cross-section, *2* – attenuation diaphragm, *3* – counteracting spring, *4* – electromagnet, *5* – moving magnet coil, *6* – coil, *7* – electromagnet driver, *8* – inputs of binary control commands.

In the case of the circuit presented in Fig. 10, the Lagrange function equals the difference between the kinetic and potential energy, calculated independently for the mechanical and electrical subsystems [24]. The above assumptions and the condition that potential energy U_0 equals 0 for the electrical subsystem result in a set of differential equations describing the dynamic performance of the system. The first equation (3.3) describes the motion of the moving core, and the second (3.4) is related to the current induced in the windings:

$$M\ddot{l}(t) + B\dot{l}(t) + K[l(t) - l_0] + \frac{A}{2[d_0 + l(t)]^2} i^2(t) = 0, \tag{3.3}$$

$$\frac{A}{d_0 + l(t)}\dot{i}(t) + Ri(T) - \frac{A}{[d_0 + l(t)]^2} i(t)\dot{l}(t) = u(t), \tag{3.4}$$

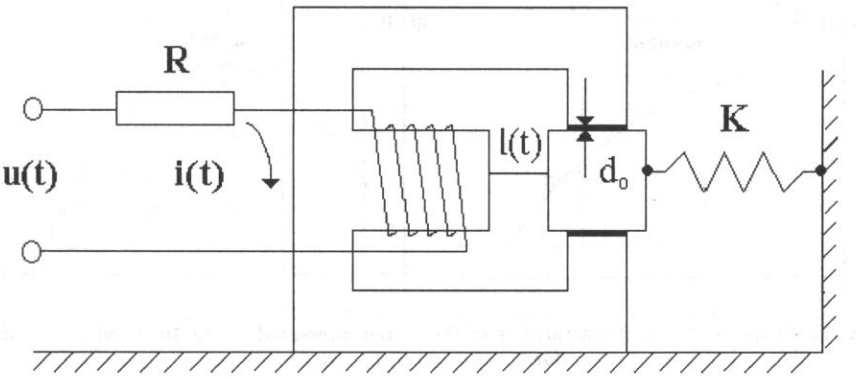

Fig. 10. Equivalent model of the system shown in Fig. 9: R – coil resistance, $u(t)$, $i(t)$ – voltage and current in the windings, d_0 – thickness of the antimagnetic separator, $l(t)$ – distance between the moving and permanent magnet, K – elasticity coefficient of the spring.

where $i(t)\,\dot{q}(t)$ – current induced in the windings, $u(t)$ – voltage in the windings, M – mass of the moving core, B – mechanical resistance, K – elasticity coefficient of the spring, A – coefficient related to the coil wire cross-section dimensions, number of windings and the magnetic constant, R – coil resistance, $L(t)$ – inductance of the circuit:

$$L(t) = \frac{A}{d_0 + l(t)}\,, \tag{3.5}$$

where $l(t)$ – distance between the moving and permanent magnet, l_0 – distance between the moving and permanent magnet for the neutral spring position, d_0 – thickness of the antimagnetic separator.

On the basis of the system state equations, it is possible to examine the system performance in the time domain using Laplace transforms or the complex plane. Taking into account the static behavior of the device under consideration, the characteristics $U = f(L)$, relating a given value of the voltage U in the steady-state to a certain position of the movable core (L), becomes:

$$U = \pm R\sqrt{\frac{2K}{A}(l_0 - L)(d_0 + L)^2}\,. \tag{3.6}$$

Assuming $l_0 < d_0/2$ for $0 < L < l_0$ the characteristic $U = f(L)$ may have the form shown in Fig. 11 a. On the other hand, when $l_0 > d_0/2$, then the expression $U = f(L)$ has its maximum, therefore the characteristics is indeterminate (Fig. 11 b).

The mathematical description of physical artefacts occurring in the presented model result in a fairly complicated form. Although it is possible to devise the control structure of such a model, it is not enough to operate the system based on the adopted formula. However, taking into consideration a simplified description of the system it is possible to derive some practical rules governing the relationship between the speed of diaphragm motion and the supplying current. These principles may be intuitively explained on the basis of Fig. 9. Analysis of Fig. 9 shows that the electromagnet opening the attenuation

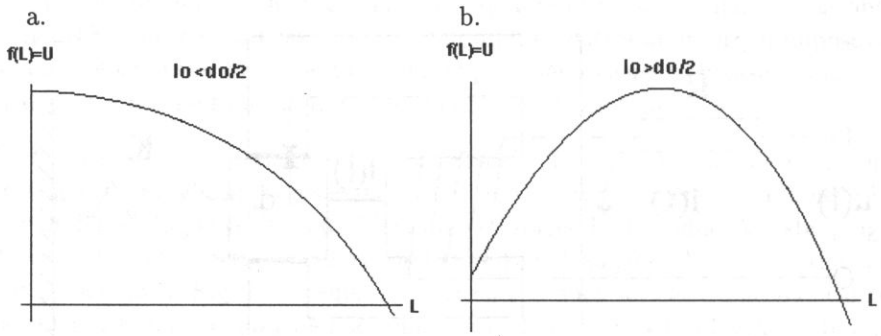

Fig. 11. Shapes of static characteristics of the system presented in Fig. 10, a) when $l_0 < d_0/2$ for $0 < L < l_0$, b) $l_0 > d_0/2$.

diaphragm must overcome the resistance of the counteracting spring. This may occur, provided the electromagnet coil is fed with sufficient electrical power. Providing that the power is limited, the valve remains in a partially-opened position. Consequently, the value of the current in the coil circuit is decisive to the position of the air flow diaphragm. Thus, the dynamic which governs the regulation of the coil current may allow for the control of valve diaphragm motion according to the way of the key is depressed.

Obviously, digital control of an organ imposes the discretization of the key velocity parameter and, consequently, the coil current value. The system should generate signals that for a given control structure, will set the system into the desired state within a minimum time and with minimum energy consumption. That problem is directly related to the organization of data transmission from the console to the organ wind chests. Nevertheless, using a fiber-optic link for fast data transmission, that matter becomes of secondary importance. On the contrary, the influence of the number of discretization levels on the cost of the electromagnetic valve should not be neglected. Since several hundreds of pipe electromagnets are used in typical organs, the application of digital-to-analog converters in the coil drivers cannot be considered because this kind of electrical drive would be impractical and costly. Hence, the coil current might be switched on in four steps, namely 0, 1/2, 2/3, 1/1 of its full value. However, as it will be shown in Sec. 4, by using fuzzy control technology this problem can be solved differently and in a less expensive way.

3.2.2. Validation of the model. In the preceding paragraph, a simple organ action system was considered (see Fig. 7). It is also possible to create an equivalent electrical circuit analogous to the mechanical organ action network with regard to articulation features. The model consists of a modified source of blowing wind, namely a multi-step source reacting to the way of depressing a key. The model is shown in Fig. 12. All the symbols are the same as described in Sec. 3.1. The only modification made was to replace V_1 and R_1 by the consecutive parameters V_{11}, V_{22}, V_{33} and R_{11}, R_{12}, R_{13}, representing the multi-source and their internal resistances. The four-step source simulates the consecutive phases of opening the pallet, namely closed, opened slightly, opened to 2/3 of the full flow of wind, opened to the full flow of wind.

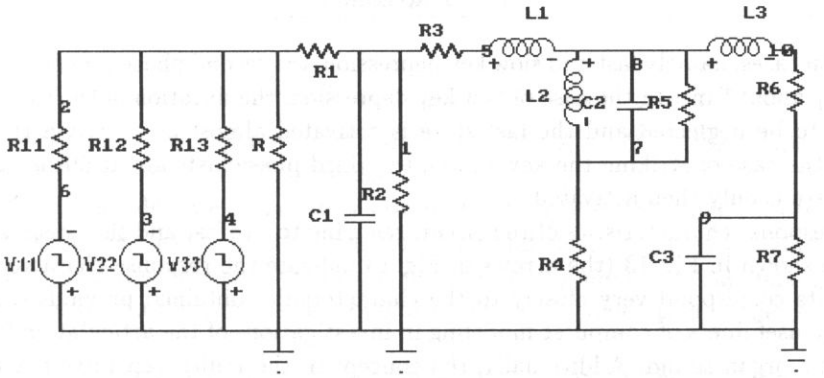

Fig. 12. Equivalent electric network of an organ action with a modified source.

a.

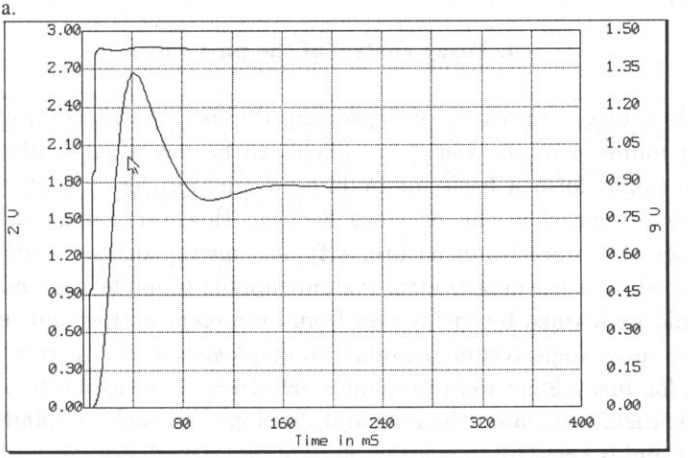

b.

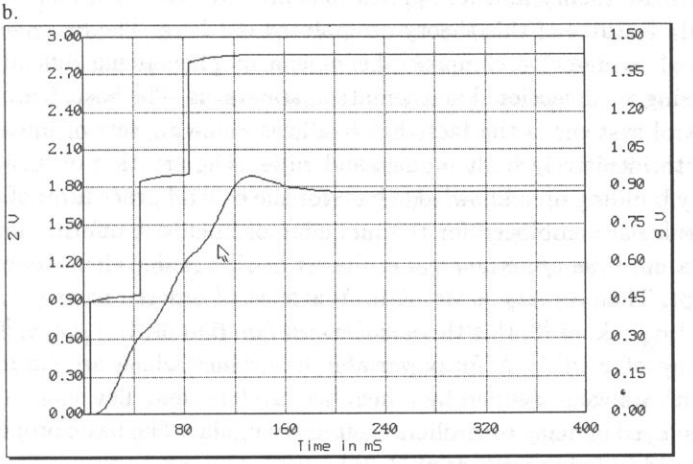

Fig. 13. Initial transient: a) in the case of fast opening of the pallet (four-step source), b) in the case of slow opening of the pallet (four-step source).

In both cases, namely fast and slow key depression, the second phase (opened slightly) takes only about 5 ms. In the case of fast key depression, the duration of the third phase is nearly to be neglected and the last state is activated almost at once. On the other hand, in the case of striking the key slowly, the third phase lasts about 50 ms, and the fourth state is only then activated.

The response characteristics of the circuit referring to the fast and slow depression of a key are shown in Fig. 13 (the arrows in Fig. 13 indicate the response characteristics). The results correspond very closely to the characteristics obtained previously, so this proves the usefulness of computer modeling in investigations of the articulation features in the pipe organ sound. Additionally, the concept of the multi-step valve reacting to the way a key is depressed has been verified using this technique.

4. Fuzzy control of the pipe valve

The whole process consisting of depressing the key, the reaction of the valve and the resulting build-up of the sound is difficult to be described mathematically. Such a description might form a basis for building a microprocessor control system of the organ, as was presented in the previous Section. However, taking into account that these processes are imprecise in nature, a typical microprocessor system for an organ may be replaced by a learning control system capable of modeling nonlinearities. Such modeling could be learned by the system from exemplary entries and related decisions. Consequently, fuzzy logic techniques may be employed in such a control system. The assumptions for fuzzy logic were originally defined in 1965 by Lofti A. Zadeh. Later, numerous scientists worked on the idea and developed it, such as Kandel, Lee, Sugeno, Kosko, Yager and others [13].

As fuzzy logic theory and its applications are covered extensively in the literature, only the main features of this theory are pointed out here. The fuzzy set theory results from the need to describe complex phenomena or phenomena difficult to define and determine using a conventional mathematical apparatus. The basic feature of fuzzy logic used in control systems is the fact that it allows following sets of linear and nonlinear functions with intuitively built models and rules. The creation of fuzzy rules must be proceeded by building up a knowledge base for the control procedures of a system. Fuzzy *IF–THEN* rules are employed for the modeling of linguistic information. Suppose that $X = \{x\}$ is a *universe of discourse*, i.e. the set of all possible elements with respect to a fuzzy concept. Then a *fuzzy subset* A in X is a set of ordered pairs $\{(x, \mu_A(x))\}$, where $\{x\} \in X$ and $\mu_A : X \to [0, 1]$ is the *membership function* of A; $\mu_A(x) \in [0, 1]$ is the *grade of membership* of x in A. A fuzzy variable has values which are expressed in natural language, with its value defined by a membership function. The shape of a membership function employed in fuzzy controllers is often triangular. The basic properties of Boolean theory are valid in fuzzy set theory [2, 13].

The design of fuzzy controllers includes the collection of control rules consisting of linguistic statements that link the controller inputs with the appropriate, respective outputs. Assuming a two input-one output system, these rules have the following general

structure:

$$R^{(r)}: \quad \text{if } x \text{ is } A_i^{(r)} \text{ and } y \text{ is } B_i^{(r)} \text{ then } z \text{ is } U_i^{(r)}, \tag{4.1}$$

where $r = 1, 2, 3, ..., n$; x, y, u – fuzzy variables, $A_i^{(r)}$, $B_i^{(r)}$, $U_i^{(r)}$ – fuzzy subsets in the universe of discourses X, Y, Z, respectively.

For the given rule base of a control system, the fuzzy controller determines the rules to be fired for the specific input signal condition and then computes the effective control action. Applying inference operators *sup-min* or *sup-prod* (e.g. *supreme-minimum, supreme-product*) to the composition operation results in generation of the control output [2].

In fuzzy set terminology, another notion is defined, namely the "*fuzzification*" operation. It can be performed by considering the crispy input values as "singletons" (fuzzy sets that have membership value of 1 for a given input value and 0 at other points) and taking the values of the set membership function at the respective data value [2]. Additionally, the "*defuzzification*" operation can be performed by a number of methods of which center-of-gravity (centroid) and height methods are common [2]. The centroid defuzzification method determines the output crisp value U_0 from the center of gravity of the output membership function weighted by its height $\mu(U)$ (*degree of membership*) and may be described by the following expression:

$$U_0 = \frac{\int U \cdot \mu(U)\, dU}{\int \mu(U)\, dU}. \tag{4.2}$$

For the purpose of this research, a physical model of a pipe organ was designed and constructed [17]. It consists of two elements: a model of an organ tracker action and a control system based on fuzzy logic technique (Fig. 14). The model of the organ was made from oak, and consists of: bellows with a volume of $0.06\,\mathrm{m}^3$, covered with leather (the bellows are filled with air through a foot pedal); wind chest sized $0.4\,\mathrm{m} \times 0.3\,\mathrm{m} \times 0.2\,\mathrm{m}$; two organ pipes (Principal 8′ – tin pipe, and Bourdon 8′ – wooden pipe); and a tracker action which enables both mechanical control and electrical activation. Three electromagnets used in this control system are combined electrically to one key. The valve is driven by electromagnets with counteracting spring. Electric activation is obtained through the use of a set of electromagnets controlled by a system constructed on the basis of fuzzy logic. Activating the electromagnets causes the air inflow to a selected pipe. A block diagram of the system which controls the electromagnets of the organ pipe valves is shown in Fig. 15. Additionally, the system configuration is shown in Fig. 16. The following components are included: dynamic keyboard, sensitive to the velocity of key motion, connected through a MIDI interface to the computer; PC computer with software operating the FUZZY microprocessor card; FUZZY microprocessor card and the MIDI interface card installed in a PC computer; specially constructed control display of key number and key velocity; buffer of information exchange between the MIDI and FUZZY cards; and buffer to control the electromagnets via the transistor drivers (Fig. 16). The applied Yamaha PSR-1500 MIDI keyboard is of a *touch-sensitive* type, therefore according to the velocity with which the key was pressed a MIDI code is generated. A sensor under the keyboard picks up the signal correlated to the way of depressing the key and at the same time transforms it into the system input signal.

The information on pressing or releasing the key is transmitted from the keyboard through the MIDI interface in the form of 2 or 3 bytes of data:

— the first command means that data will be transmitted,

— the second byte – information on the key number within the range from 0 to 127,

— the third byte – information on the velocity of pressing the key, in the range from 1 to 127.

The information related to the key number is essential because of the relation between the size of the pipe and the articulation artefacts. In traditional, mechanical organs, articulation features appear mostly in low tones. The sound rise in large pipes may be fast or slow, so it is possible to hear the differences in the articulated sounds. Small pipes, because of their size, are excited by the wind blow very quickly and speak nearly always in the same way.

The above information is decoded by the computer through a MIDI decoding procedure. Obtained values are periodically transmitted to the fuzzy logic control system at the speed of 31.25 kBaud. The total transmission time t (Eq. (4.3)) consists of at least three delays, namely:

— t_1 – connected to the data transmission from the keyboard to the MIDI card:

$$t_1 = \frac{20 \text{ bit}}{31250 \text{ bit/s}} = 640 \,\mu\text{s}\,;$$

— t_2 – corresponds to the data processing in the MIDI card:

$$t_2 \approx 30 \,\mu\text{s}\,;$$

— t_3 – needed for the data processing in the FUZZY microprocessor card: $t_3 \approx 8 \,\mu\text{s}$

$$t \approx t_1 + t_2 + t_3 \approx 640 \,\mu\text{s} + 30 \,\mu\text{s} + 8 \,\mu\text{s} \approx 678 \,\mu\text{s}\,. \tag{4.3}$$

As is shown in Fig. 16, three parallel connected electromagnets are applied to drive the pallet opening the air inflow. The electromagnets are switched on and driven by the current, the value of which is defined by the fuzzy rule system. Thus, any key motion rates will be translated into the way of opening the valve, and in consequence into the building of air pressure in the pipe that is decisive to the character of the rising sound.

Two parameters that are extracted periodically from the MIDI code, namely the key number and the velocity, create two fuzzy inputs, labeled as:

INPUTS: *KEY_NUMBER; VELOCITY,*

and output is associated with the current applied to electromagnet coils and is denoted CURRENT. Corresponding membership functions are labeled as follows:

OUTPUT: *LOW_CURRENT; MEDIUM_CURRENT; HIGH_CURRENT.*

The fuzzifiers were named as follows:

FUZZIFIERS: for *KEY_NUMBER* and *VELOCITY*: – *LOW*,
– *MEDIUM*,
– *HIGH.*

Fig. 14. Fuzzy logic-based control system for a pipe organ.

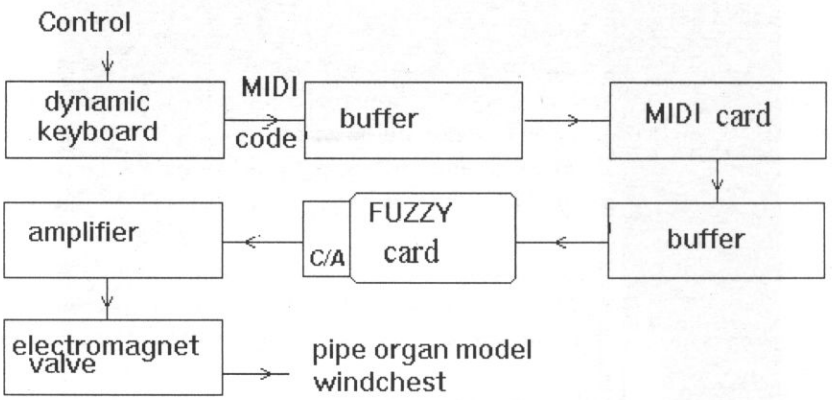

Fig. 15. Block diagram of the control system.

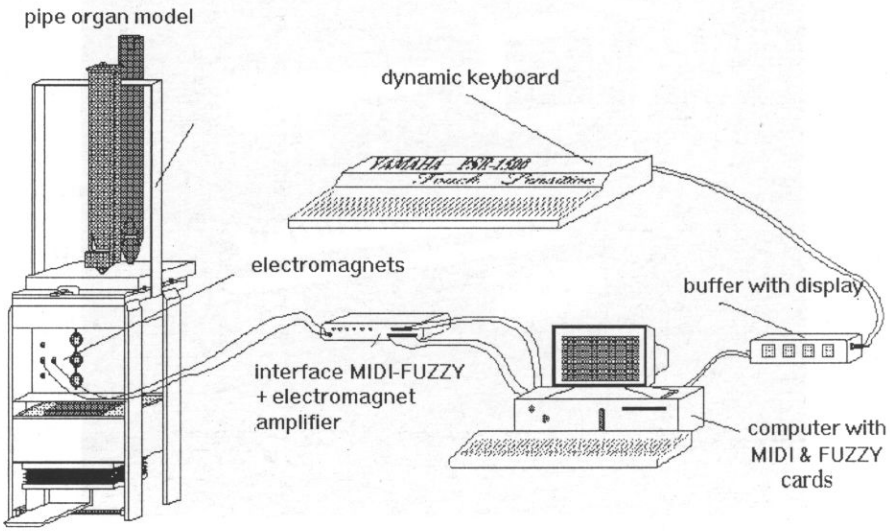

Fig. 16. Lay-out of the fuzzy logic-based control system configuration.

Table 2. Mapping of the keyboard.

KEY_NUMBER	CENTER	WIDTH
LOW	30	29
MEDIUM	70	25
HIGH	100	27

Table 3. Velocity mapping.

VELOCITY	CENTER	WIDTH
LOW	30	29
MEDIUM	70	15
HIGH	101	26

The output of the system is set at the beginning to the value equivalent to 0. The MIDI code assigns the keys with numbers from a range starting from 0 (when no key is pressed) to 127. The mapping of the keyboard was reflected as *KEY_NUMBER*, and is presented in Table 2. The velocity values are represented as in Table 3.

The above listed values (Tab. 2 and 3) were set experimentally. The performed experiments allow one to show the plot of membership functions corresponding to the input *KEY_NUMBER* and *VELOCITY* and *CURRENT* denoted as OUTPUT (Fig. 17). As can be seen from Fig. 17, triangular membership functions are employed in the fuzzy controller.

The inputs and fuzzifiers are producing terms that are used in the following rules:

RULES:

if *KEY_NUMBER* **is** *OFF* **then** 0

if *VELOCITY* **is** *OFF* **then** 0

if *KEY_NUMBER* **is** *LOW* **and** *VELOCITY* **is** *LOW* **then** *LOW_CURRENT*

if *KEY_NUMBER* **is** *MEDIUM* **and** *VELOCITY* **is** *LOW* **then** *LOW_CURRENT*

if *KEY_NUMBER* **is** *HIGH* **and** *VELOCITY* **is** *LOW* **then** *MEDIUM_CURRENT*

if *KEY_NUMBER* **is** *LOW* **and** *VELOCITY* **is** *MEDIUM* **then** *MEDIUM_CURRENT*

if *KEY_NUMBER* **is** *MEDIUM* **and** *VELOCITY* **is** *MEDIUM* **then** *MEDIUM_CURRENT*

if *KEY_NUMBER* **is** *HIGH* **and** *VELOCITY* **is** *MEDIUM* **then** *HIGH_CURRENT*

if *KEY_NUMBER* **is** *LOW* **and** *VELOCITY* **is** *HIGH* **then** *HIGH_CURRENT*

if *KEY_NUMBER* **is** *MEDIUM* **and** *VELOCITY* **is** *HIGH* **then** *HIGH_CURRENT*

if *KEY_NUMBER* **is** *HIGH* **and** *VELOCITY* **is** *HIGH* **then** *HIGH_CURRENT*.

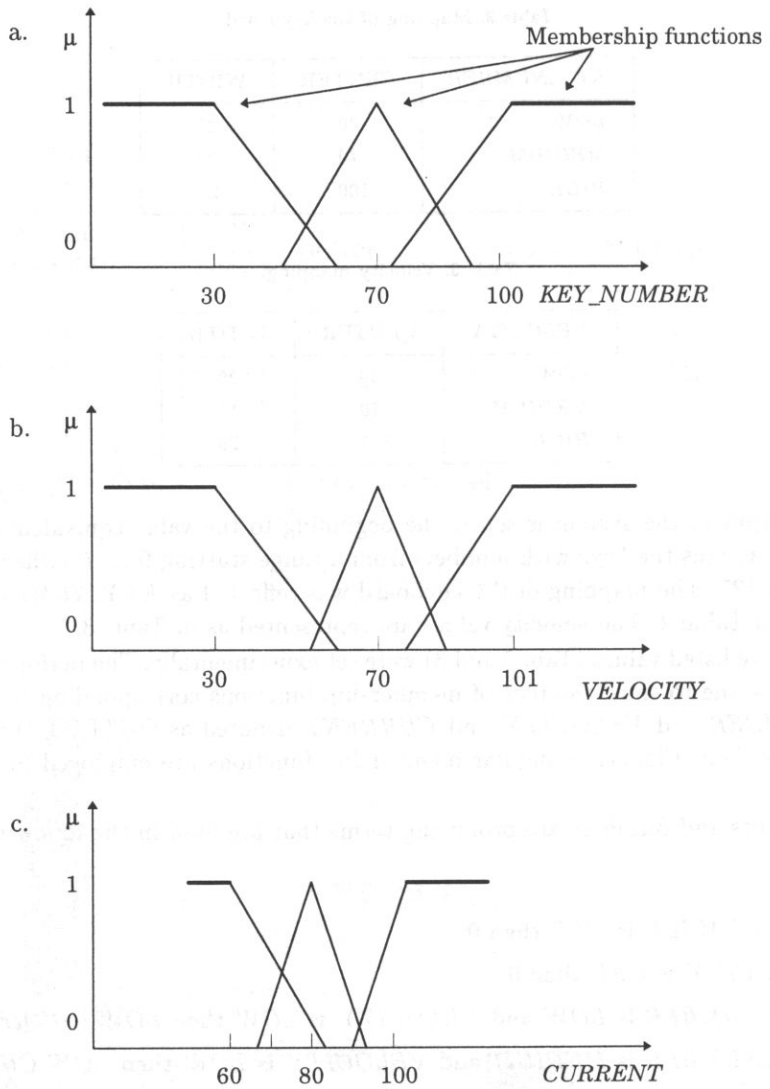

Fig. 17. Membership functions corresponding to the *VELOCITY* (a), *KEY_NUMBER* (b) inputs and CURRENT denoted as output (c), where μ – degree of membership.

Each rule produces a number which is calculated according to fuzzy logic principles from the cross-section of the input values with the membership functions [13] (see Fig. 17). The winning rule is one that has the highest value assigned during the calculations. On the basis of the adopted terms, the numerical values are converted to the respective current which is driving the electromagnets. This means that the lowest output value causes the slowest opening of the valve, while other values appearing on the output, which match other terms, result in a faster opening of the valve.

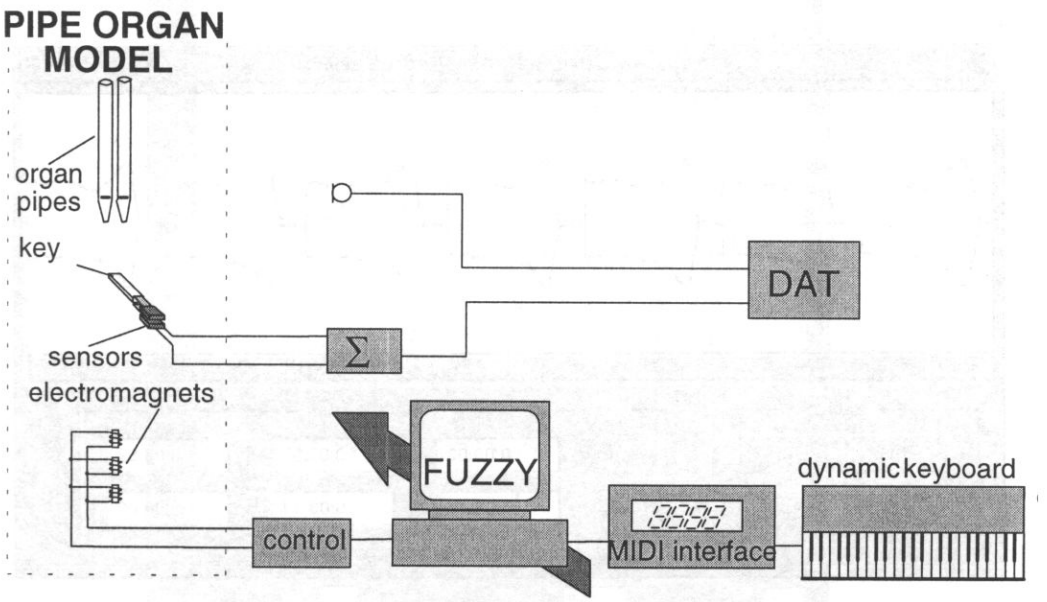

Fig. 18. Block diagram of the recording system of the pipe organ model.

Recordings of the signals generated by the model were made based on the system whose block diagram is presented in Fig. 18. A pair of sensors were attached to the key, and are activated electrically. The input of the system was controlled through a touch-sensitive keyboard. Impulses from sensors responsible for the time of depressing the key in the model were registered. The value of the velocity of depressing the key was read from the MIDI interface display. The output signal from the control system was recorded on the left channel of the tape recorder, while the sound of the pipe was registered on the right channel.

Examples of analyses of the time- and frequency-domain characteristics of the recorded sounds are presented in Fig. 19 and 20. The plots show the differences that are visible in the time representation of the analyzed sounds, as well as in the representation of waterfall plots, respectively for fast (Fig. 19 a and 20 a) and slow (Fig. 19 b and 20 b) opening of the valve. Both spectral characteristics differ mainly in the behavior of the second harmonic which grows very quickly in the case of pressing the key quickly and slowly in the other case. There are also other discrepancies for the sounds presented. It is easy to observe that the fundamental is much weaker when depressing the key quickly. The arrows "A" in Fig. 20 show the starting point of the rising of fundamentals, whereas the arrows "B" show the rising of second harmonics.

These results show a clear similarity between previously obtained analyses. Therefore, it may be said that the constructed fuzzy logic control system for a pipe organ action responds properly depending on differentiated musical articulation.

a.

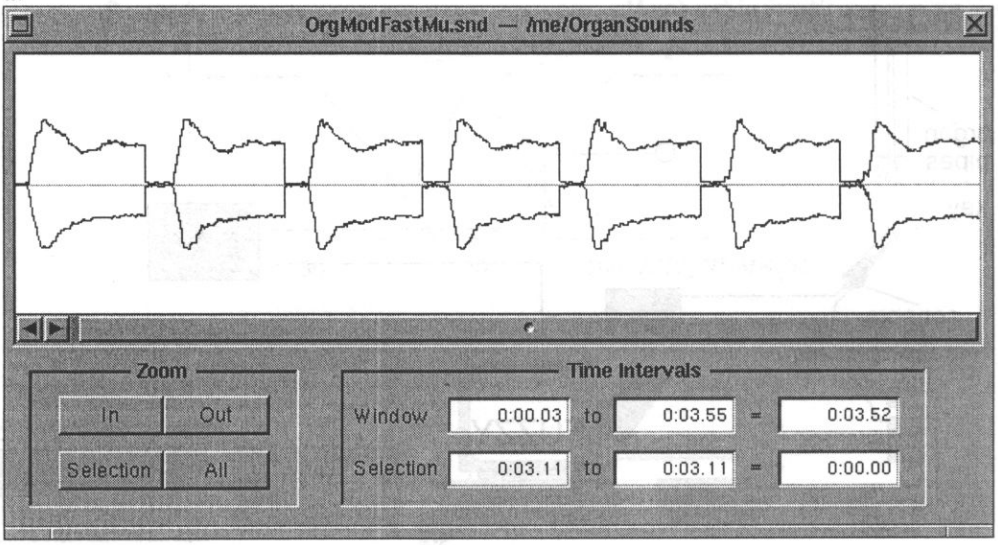

b.

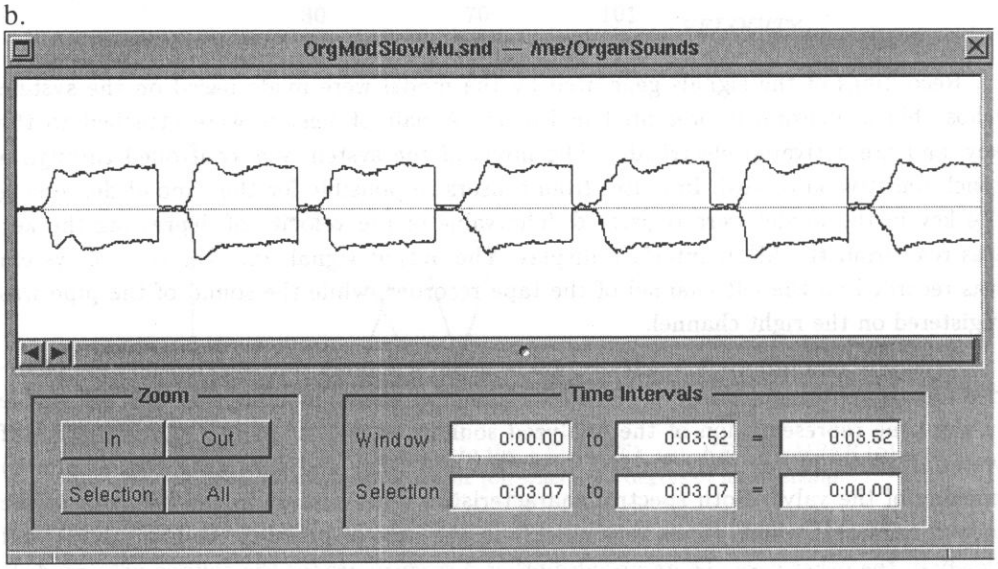

Fig. 19. Analyses of time-domain characteristics of sounds of Principal 8′ in the case of: a) fast opening of the valve, b) slow opening of the valve.

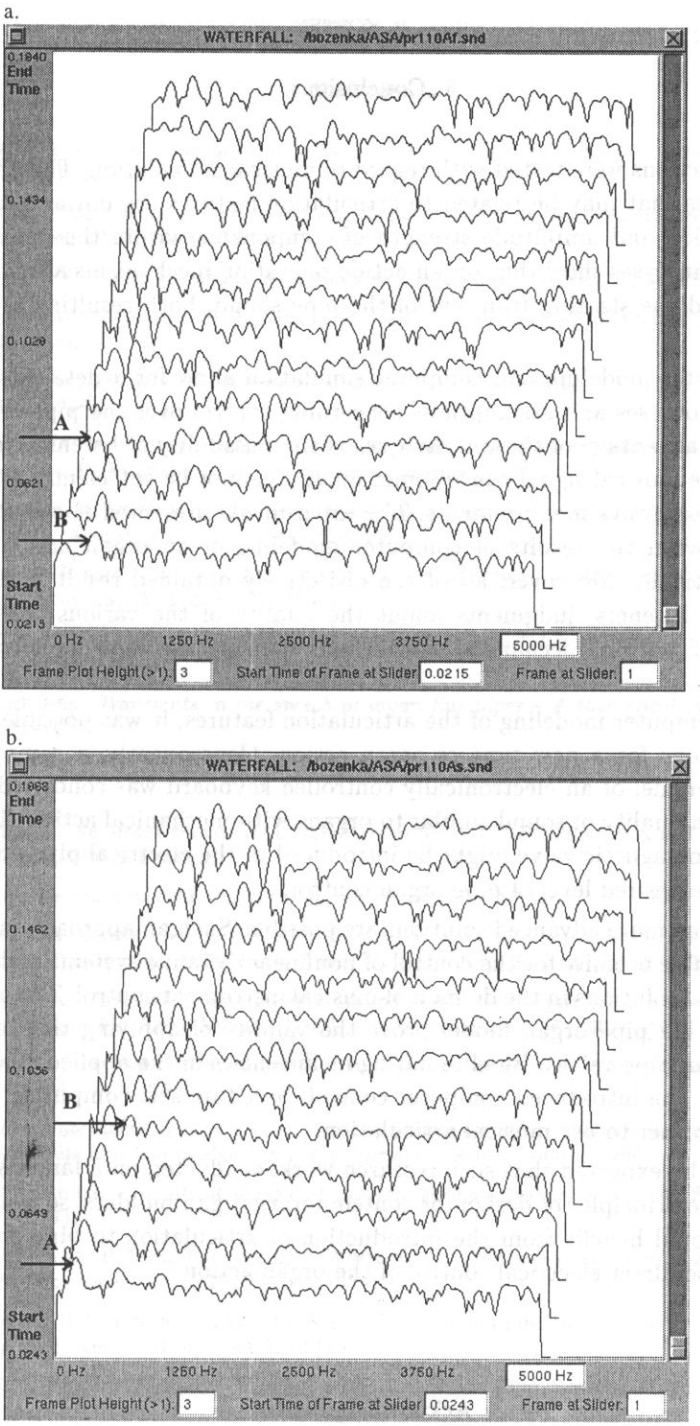

Fig. 20. Analyses of frequency-domain characteristics of sounds of Principal 8′ in the case of: a) fast opening of the valve, b) slow opening of the valve.

5. Conclusions

The organ actions were tested with regard to musical articulation. The physical pipe sound properties that may be related to articulation features are initial delay, starting transient duration and amplitude strength of components within the duration of the transient. The analyses show that organ action operation mechanisms affect mainly the initial delay and the starting transient of the pipe sound, both resulting in a different sound quality.

Both computer modeling and computer simulation allow for a detailed verification of different hypotheses and assumptions concerning control over the pipe organ sound. The additional advantage of these techniques is the possibility of listening to extracted fragments of the musical signal, since sound quality cannot be sufficiently assessed only on the basis of objective measurements. The experiments presented above showed good correlation between the results of computer modeling of an organ action and those obtained analytically. Moreover, all of the objectively obtained results confirmed the musicians' and listeners' judgments about the quality of the various types of organ control systems, with a mechanical tracker action being the most preferred in their opinions.

Based on computer modeling of the articulation features, it was possible to propose technical solutions for a new type of organ action. Consequently, a computer action system with a model of an electronically controlled keyboard was conceived and simulated, showing a quality of sound similar to organs with mechanical action. Therefore, a four-step electromagnetic valve might be introduced in the electrical pipe organ action, approaching the desired level of pipe organ control.

However, even more advanced solutions are possible. Such an approach as fuzzy logic shows considerable promise for the control of nonlinear dynamic systems and may result in some practical solutions in the domain of musical instrument control. The experiments carried out on the pipe organ model prove the validity of applying this technique to controlling organ pipe valves. By eliminating inefficiencies in the applied mechanisms of electric actions, the introduced computer control, based on soft computing techniques, allows the performer to use musical articulation.

It may also be expected that such research work, conducted on a larger scale, might result in reliable principles of design for contemporary organ builders, so that musicians and listeners could benefit from the introduction of articulation to pipe organ instruments which use direct electrical control of the organ action.

Acknowledgments

This research work was partially supported by the Committee for Scientific Research (KBN), Warsaw, Poland, Grant No. 8 T11C 02808.

References

[1] A.H. BENADE, *On the propagation of sound waves in a cylindrical conduit*, J. Acoust. Soc. Amer., **44**, 2, 616–623 (1968).

[2] B.K. BOSE, *Expert system, fuzzy logic, and neural network applications in power electronics and motion control*, IEEE, **82**, 8, 1303–1323 (1994).

[3] S. CADDY, H.F. POLLARD, *Transient sounds in organ pipes*, Acustica, **7**, 227–280 (1957).

[4] J.W. COLTMAN, *Sounding mechanism of the flute and organ pipe*, J. Acoust. Soc. Amer., **44**, 4, 983–992 (1968).

[5] J.W. COLTMAN, *Jet drive mechanisms in edge tones and organ pipes*, J. Acoust. Soc. Amer., **60**, 3, 725–733 (1976).

[6] P.R. COOK, *A Meta-wind-instrument physical model, and meta-controller for real time performance control*, Proc. of the ICMC, San Jose, California (1992).

[7] A. CZYŻEWSKI, B. KOSTEK, S. ZIELIŃSKI, *Synthesis of organ pipe sound based on simplified physical models*, Arch. Acoustics, **21**, 2, 131–147 (1996).

[8] B. FABRE, A. HIRSCHBERG, A.P.J. WIJNANDS, *Vortex shedding in steady oscillation of a flue organ pipe*, Acta Acustica, **82**, 6, 863–877 (1996).

[9] N.H. FLETCHER, *Nonlinear interactions in organ flue pipes*, J. Acoust. Soc. Amer., **56**, 2, 645–652 (1974).

[10] N.H. FLETCHER, *Transients in the speech of organ flue pipes – A theoretical study*, Acustica, **34**, 224–233 (1976).

[11] N.H. FLETCHER, T.D. ROSSING, *The physics of musical instruments*, Springer-Verlag, New York (1991).

[12] J.S. KEELER, *The attack transients of some organ pipes*, IEEE Trans. on Audio and Electroacoustics, **AU-20**, 5, 378–391 (1972).

[13] B. KOSKO, *Neural networks and fuzzy systems*, Prentice-Hall Intern. Ed., New Jersey (1992).

[14] B. KOSTEK, A. CZYŻEWSKI, *Articulation features in the digitally controlled pipe organ*, 90th AES Convention, Preprint No. 3023, Paris (1991), J. Audio Eng. Soc. (A), **39**, 5, 382 (1991).

[15] B. KOSTEK, A. CZYŻEWSKI, *Computer modeling of the pipe organ valve action*, 92nd AES Convention, Preprint No. 3266, Vienna (1992), J. Audio Eng. Soc. (A), **40**, 5, 440 (1992).

[16] B. KOSTEK, A. CZYŻEWSKI, *Investigation of articulation features in organ pipe sound*, Arch. Acoustics, **18**, 2, 3, 417–434 (1993).

[17] B. KOSTEK, *Intelligent control system implementation to the pipe organ instrument*, [in:] Rough Sets, Fuzzy Sets and Knowledge Discovery, Springer-Verlag, London 1994.

[18] W. LOTTERMOSER, *Acoustical design of modern german organs*, J. Acoust. Soc. Amer., **29**, 6, 682–689 (1957).

[19] M.E. MCINTYRE, R.T. SCHUMACHER, J. WOODHOUSE, *On the oscillation of musical instruments*, J. Acoust. Soc. Amer., **74**, 5, 1325–1345 (1983).

[20] A.W. NOLLE, T.L. FINCH, *Starting transients of flue organ pipes in relation to pressure rise time*, J. Acoust. Soc. Amer., **91**, 4, 2190–2202 (1992).

[21] *Piezo Film Sensors Technical Manual*, AMP Inc. Piezo Film Sensors, Basic Design Kit, USA (1993).

[22] H.F. POLLARD, *Time delay effects in the operation of a pipe organ*, Acustica, **20**, 4, 189–199 (1968).

[23] A. POWELL, *On the edgetone*, J. Acoust. Soc. Amer., **33**, 4, 395–409 (1961).

[24] J. PUŁACZEWSKI, K. SZACKA, A. MANITIUS, *Theory of automation* [in Polish], PWN, Warsaw 1974.

[25] A. RAKOWSKI, E.G. RICHARDSON, *Eine Analyse des Intonierungsvorganges bei Orgeln*, Gravesaner Blätter, **15**, 16, 46–58 (1960).

[26] E.G. RICHARDSON, *The transient tones of wind instruments*, J. Acoust. Soc. Amer., **26**, 6, 960–962 (1954).

[27] R.T. SCHUMACHER, *Self-Sustained oscillations of organ flue pipes: An integral equation solution*, Acustica, **39**, 225–238 (1978).

[28] J.O. SMITH III, *Physical modeling using digital waveguides*, Computer Music Journal, special issue on Physical Modeling of Musical Instruments, Part I, **16**, 4, 74–91 (1992).

[29] *The New Grove Dictionary of Music and Musicians*, S. SADIE [Ed.], Macmillan Publishers, London, Washington, Hong Kong 1980, 13, pp. 715.

[30] V. VÄLIMÄKI, M. KARJALAINEN, Z. JANOSY, U.K. LAINE, *A Real-Time DSP Implementation of a Flute Model*, [in:] Proc. Int. Conf. Acoustics, Speech and Signal Processing (ICASSP'92), San Francisco, California, USA (1992).

[31] V. VÄLIMÄKI, J. HUOPANIEMI, M. KARJALAINEN, Z. JANOSY, *Physical modeling of plucked string instruments with application to real-time sound synthesis*, 98th Audio Eng. Soc. Conv., Preprint 3956, Paris (1995), J. Audio Eng. Soc. (Abstr), **41**, 5 (1995).

[32] M.P. VERGE, B. FABRE, W.E.A. MAHU, A. HIRSCHBERG, *Jet formation and jet velocity fluctuations in a flue organ pipe*, J. Acoust. Soc. Amer., **95**, 2, 1119–1132 (1994).

[33] M.P. VERGE, R. CAUSSÉ, B. FABRE, A. HIRSCHBERG, A.P.J. WIJNANDS, A. VAN STEENBERGEN, *Jet oscillations and jet drive in recorder-like instruments*, Acta Acustica, **2**, 5, 403–419 (1994).

ARCHIVES OF ACOUSTICS
22, 3, 245–266 (1997)

DISSONANCES IN CARILLON CHORDS

G. BUDZYŃSKI and M. SANKIEWICZ

Sound Engineering Department
Faculty of Electronics, Telecommunications and Informatics,
Gdańsk University of Technology
(80-952 Gdańsk, ul. Narutowicza 11/12)

The sound quality of the carillons may pose problems, the more so, as carillon music has often a large, sometimes involuntary, audience. Particular carillon chords, although composed from well tuned bells, produce more or less dissonant sounds. A performed computer analysis of such chords, recorded in the St. Catherine Carillon belfry in Gdańsk, shows origins of dissonances and characterizes their properties. Some possible solutions leading to an enhancement of quality of carillon chords are discussed.

1. Introduction

The problem of dissonant vs. consonant sounding of complex sounds is often considered in musical acoustics. Chords consisted of most simple sounds, even those composed of two sounds, each containing only a few harmonic components may present difficulties at subjective assessment of their sound quality. The more so, when both sounds have rich spectra with many harmonic and inharmonic partials as in the case of bell sounds. Usually, the more rough seems the timbre of a chord, the lower is appreciated the quality of such chord, and it is qualified as sensory dissonance [17].

The phenomenon of dissonance plays an important role in the psychology of music and its theoretical aspects were thoroughly examined in the literature [7]. In the following study, however, authors deal with the practical aspect of the problem, which they encountered during investigations on bells, especially on sounds of bell-chords. Such bell-chords were analyzed on examples recorded from the St. Catherine's carillon, in Gdańsk. The recordings were made inside the belfry-tower of the St. Catherine church (see Figs. 1 and 2).

The carillon, made by the renowned Dutch foundry Koninklijke Klokkengieterij Eisbouts in Asten, was mounted in 1989, in the St. Catherine belfry, as a symbol of reconciliation between German and Polish nations, after all the atrocities of the Nazi regime and the Second World War.

The carillon consists of 37 bells. They are tuned according to the chromatic, equally tempered scale, ranging from c' to c'''' (i.e. from C4 to C7) [5]. Earlier investigation

proved the high accuracy of internal and external tuning of the carillon bells [10]. The bells are listed in Appendix A.

The carillon is equipped with a digital steering system which actuates electromagnetically driven hammers (Fig. 3). The four biggest bells besides hammers are equipped with swinging mechanisms and clappers, to produce pealing sounds. The biggest bell also serves as a clock-bell.

The carillon play is executed either automatically, as preprogrammed melodies introduced into the system memory, or manually from a MIDI-keyboard. A traditional keyboard with mechanical system of hammers is to be installed.

Just experimenting with the use of MIDI-keyboard the authors had recently an opportunity to listen to various two-bell chords. Some sounded more-, other less-dissonantly, which became the starting point of an acoustic investigation reported below.

2. Investigation

The continuous progress in understanding the bell properties, in particular those of carillon bells, is due to numerous experimental investigations, the results of which were published in the past [1, 3, 11, 12]. Most of those were obtained in laboratory conditions, i.e. with a bell mounted in a stand, enabling to excite and record bell vibrations in a strictly controlled way. An unusual occasion in such situations was created in Europe after the Second World War, during which forced dismountings of many carillon- and peal-bells were ordered; thereafter some recovered bells were to be checked and measured before their eventual remounting [9].

There is, however, a need for a less precise yet easier and faster investigation of bell instruments, aimed at the general assessment of their sound quality, as well as description of their acoustic properties which have to be introduced into the historical fine-arts documentation of the instrument. Thus, the actual state of knowledge of bell sounds is to be applied to estimate objectively the quality of the bell instruments.

In the particular case of the St. Catherine's carillon, the aim of the investigation, reported here, was to deliver an objective description of the dissonant sounding of particular chords, based mainly on measurements and analyses. Such description may serve as a tool for musicians to prepare scores for carillon music, with frequent use of well sounding chords and omission of dissonant ones.

Measurements, i.e. recordings of carillon sounds were done electroacoustically *in situ* within the belfry. Although a pair of microphones was situated on a gallery at the level of the bells, and sounds were recorded with a two-channel digital recorder, only one channel was used for further processing and analysis.

Recorded sounds were analyzed in the laboratory. Neither direct access to the bells was provided nor any experiments with bell particular excitation or special recording process. This provision is conditioned by the general purpose of the investigation which should be easy to be performed on numerous bells all over the country, with the use of simple technical equipment.

Fig. 1. View of Gdańsk old town with St. Catherine's church belfry-tower in the middle.

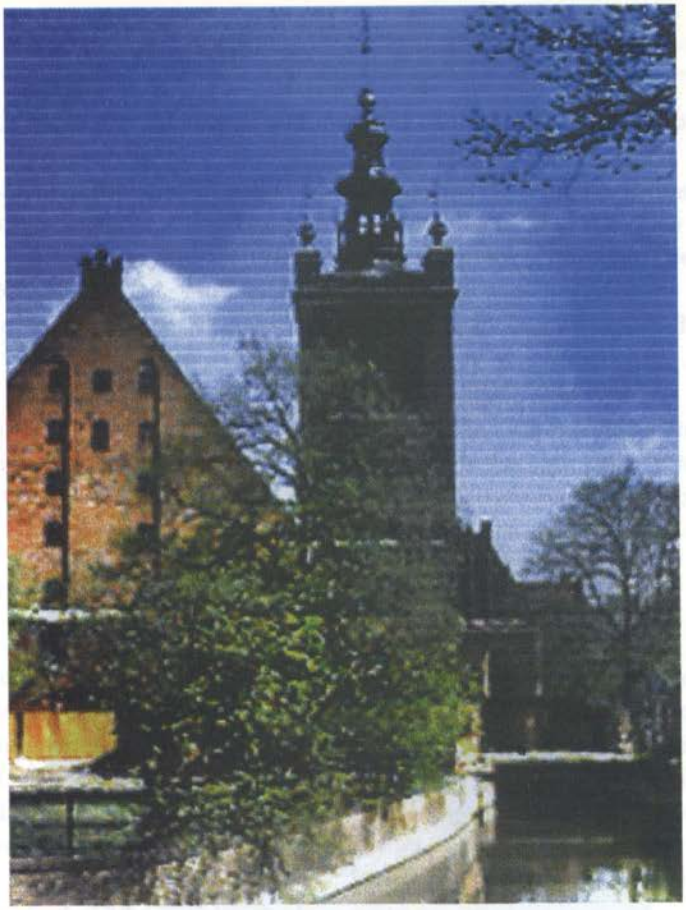

Fig. 2. View of the St. Catherine's tower from the West (the Big Mill and Radunia river on the foreground).

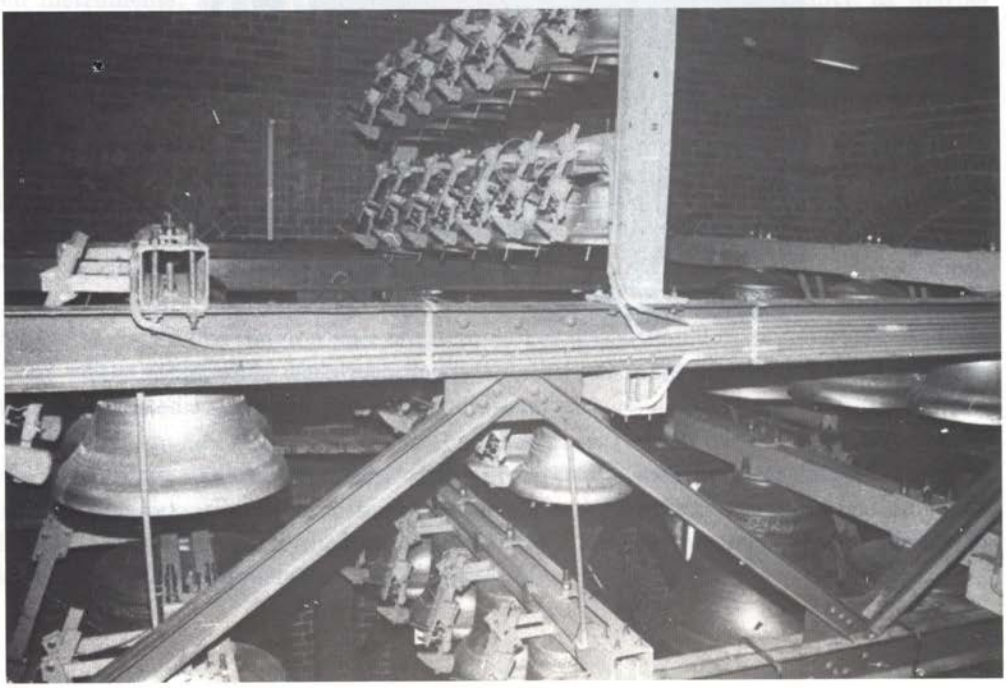

Fig. 3. System of electromagnetic hammers excitating carillon bells.

2.1. Theoretical approach

The general cause of dissonant, i.e. rough or unpleasant sounding of complex sounds, in particular two-bell chords, are, according to Helmholtz's theory [8], fast audible beats, produced by pairs of partials, having comparable levels and differing in frequency by less than three, to three and half semitones. It corresponds, in relation to the middle octave sounds, about 50 to 60 Hz while the lower limit, denoting the beginning of sensation of unpleasantness, may be estimated at about 20 Hz [2]. Further well known physio- and psychological factors influencing the dissonant sounding of musical sounds may be disregarded in this simplified approach.

As compared with other musical instruments, the sound of a bell is extremely rich in well developed partials, especially in its initial period, directly after a clapper- or hammer-stroke. E.g. special laboratory measurements performed on a church bell in 1982 by PERRIN, CHARNLEY and DEPONT showed the existence of 134 distinct, measurable partials [6]. Many of them were so close to each other in frequency that they were producing beats or warble. Yet such beats are mostly inaudible due to their small amplitudes. Some of them can, however, be distinctly heard. On the other hand, measurement of both partial frequencies producing such beats is usually beyond the possibilities of the typical analysis methods due to their limited separating power.

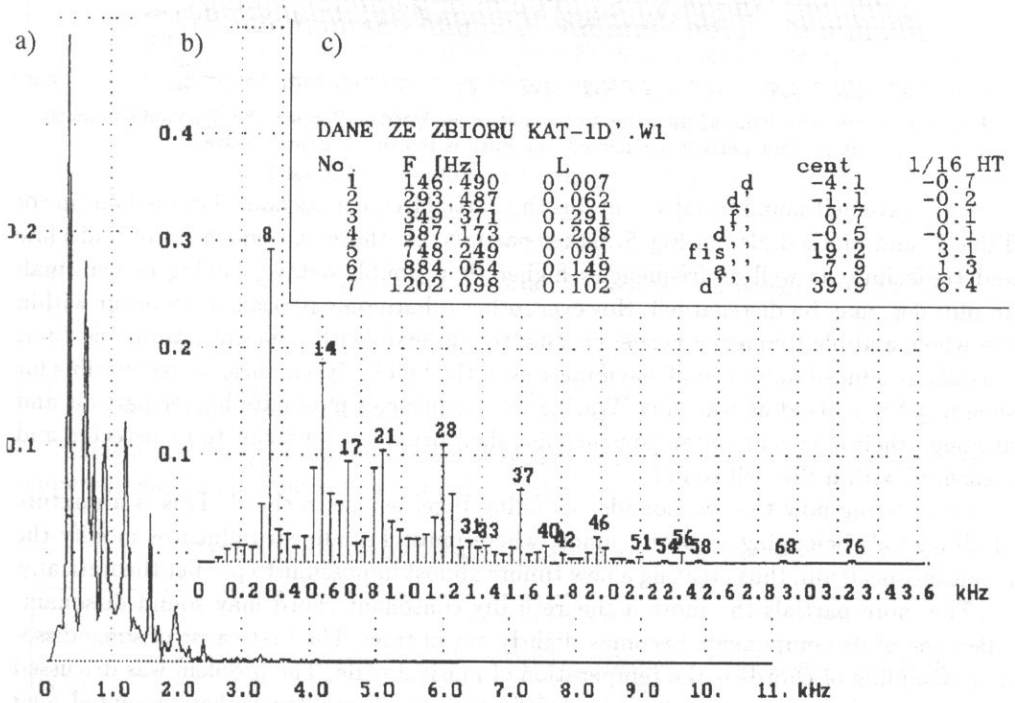

Fig. 4. Momentaneous spectrum of a carillon bell sound (for $t = 600$ ms), a) usual form, b) multi-line form with partials numbered for analysis, c) printed results of the analysis: frequency, level, pitch on musical scale, tuning deviation in cents and in sixteenths of a semitone.

Usual FFT analysis for an octave, good quality carillon bell, measured within this investigation, yields at least 8 distinct partials (see Fig. 4). The evolutive spectrum (Fig. 5) delivers here a better insight into the time-structure of the spectrum and, in particular, shows the amplitude proportions during partial decays.

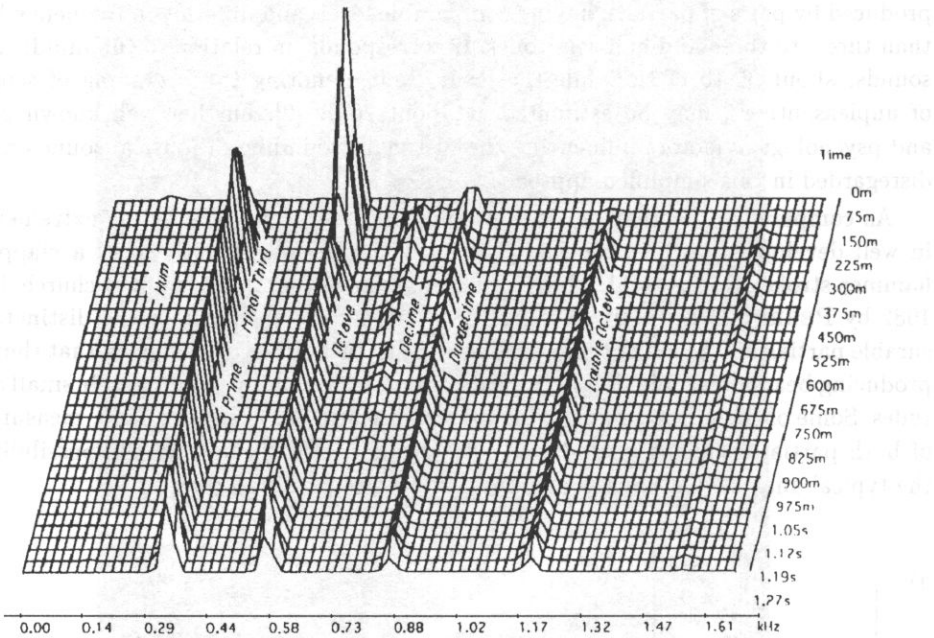

Fig. 5. Evolutive spectrum of the same bell sound as analyzed in Fig. 4 – the d′ sound (its most important partials are named; the Fifth is too small to be perceived).

An octave bell sound usually contains the partial frequencies named in the first line of Table 1, and marked also in Fig. 5. Other partials, i.e. those at frequencies of undecime and tredecime, as well as frequencies higher than double octave, having rather small amplitudes, may be disregarded. However, other inharmonic partials often occur within the whole audible frequency range, causing rough beats with adjacent harmonics. Split partials, produced due to small asymmetries of the bell body, can also be responsible for slow beats perceived as warbling. Warble low frequencies modulate higher partials and although their effects are often conspicuous, their origins are difficult to be detected and measured within the bell sound.

Considering now the two sounds, sounding together, i.e. a chord. This is a mixture of all partials belonging to both sounds, where mutual nonlinear influences modify the resultant spectrum, thus creating a new timbre almost impossible to predict theoretically.

The more partials the more a theoretically consonant chord may sound dissonant, when one of its components becomes slightly out of tune. The first cause of some dissonant sounding of chords is the temperation of musical scale. The problem was discussed thoroughly [3] and seems to be solved definitely, as all carillon makers accepted long ago the equally tempered scale. However a question remains unanswered so far, why the aerophonic instruments which use overblowings (i.e. untempered just intervals) are well

sounding together with other equally tempered instruments of the orchestra, while the carillons, never accompanied by other instruments could not remain tuned according to one of the historical systems of the just intonation or of a meantone-temperament. Then some chords would sound better than equally tempered do, first of all the Minor Third where the difference of 16 cents from consonant sounding is easily noticeable.

Taking e.g. a weakly consonant chord of a Minor Third c′ – es′, in equal temperament, one can calculate the following partials (Table 1):

Table 1. Partials of the equally tempered Minor Third c′ – es′ (C4 – E♭4).

	Frequency in Hz							
	Hum	Prime	Third	Fifth	Octave	Decime	Duodecime	Double Oct.
f/f_H	1	2	2.378	2.997	4	5.04	5.99	8
c′	130.81	261.63	311.13	392.00	523.25	659.26	783.99	1046.50
Δ_{aud}	*24.75*		*22.01*	*57.09*	*37.01*			
es′	155.56	311.13	369.99	466.16	622.25	783.99	932.33	1244.51

Higher partials are not considered, as mentioned before, due to their small amplitudes. Checking the differences Δ_{aud} between consecutive partials one finds the four audible beating frequencies (22.01, 24.75, 37.01, 57.09 Hz), falling into the frequency range of audible rough beats. However, a small detuning of a partial may produce further rough beats, resulting in an increase of roughness of timbre.

Contrary to the example presented the pure Fifth without any temperament is the most consonant chord, besides the perfect intervals of prime, octave, duodecime etc. Here (see Table 2) no roughly beating frequencies are to be found.

Table 2. Partials of the just Fifth c′ – g′ (C4 – G4).

	Frequency in Hz							
	Hum	Prime	Third	Fifth	Octave	Decime	Duodecime	Double Oct.
f/f_H	1	2	2.4	3	4	5	6	8
c′	132.0	264.0	316.8	396.0	528.0	660.0	792.0	1056.0
Δ_{aud}								
g′	198.0	396.0	475.2	594.0	792.0	990.0	1188.0	1584.0

Taking as a further example the same chord, namely the Fifth c′ – g′ however, equally tempered, one obtains the values quoted in Table 3:

Table 3. Partials of the equally tempered Fifth c′ – g′ (C4 – G4).

	Frequency in Hz							
	Hum	Prime	Third	Fifth	Octave	Decime	Duodecime	Double Oct.
f/f_H	1	2	2.378	2.997	4	5.04	5.99	8
c′	130.81	261.63	311.13	392.00	523.25	659.26	783.99	1046.50
Δ_{aud}						↙	*58.73* ↗	
g′	196.00	392.00	466.16	587.33	783.99	987.77	1174.66	1567.98

Although the detuning of the natural harmony, caused by the superimposed equal temperament, is small, one audible beats frequency results. Contrary to this, partials entering into a Fourth chord c′ – f′ (C4–F4) yield the five rough beating frequencies: Δ_{aud} = 23.31; 38.40; 39.20; 42.77; 43.80 Hz. Similar calculations were done for other chords resulting for everyone in several beat frequencies.

A mathematical approach to a part of that problem was recently presented by SLOANE, who in his Correspondences [13, 14, 15, 16] calculated frequencies and amplitudes of beats caused by scale temperament and by small detuning of a partial. He considered not only dyad sounds but also triads, composed of Major and Minor Thirds.

Of course, there are other causes of inharmonicity of carillon bell chords and other beating frequencies. Their occurrence and sources might undergo a broader theoretical investigation. For this study, however, from a practical point of view, their influence may be taken into consideration by analyzing the global dissonance effects occurring at particular chords. Such approach required the sounds of all carillon bells to have been recorded in order to analyze them and subjectively assess in laboratory conditions. For obvious reasons multiple sound experiments *in situ* were impracticable and intolerable for the public in the neighbourhood.

2.2. Sound recording and digital processing

All carillon bells have been recorded by means of a microphone system (Neumann KM83i) and a MiniDisc recorder (Sony MZ1). Microphones were situated inside the belfry, at the height of the bell gallery. Bells were actuated from the MIDI-keyboard, switched into the carillon computer.

Analyses were executed with the aid of a Macintosh Quadra 840 AV computer, equipped with an Audiomedia II Chart. Two software programs were used: the Sound Designer II (DSP/FFT), and the specially designed FFT-anl and FFT-lab programs, which, beside of evaluating sound spectra, permitted to measure the damping rate of a chosen partial in dB/s. This value may be applied as one among several quality criteria for bells.

The investigated chords were synthesized from separate bell sounds by means of the digital processing methods available in the Sound Designer software. Beats were observed using a tunable diapason contained within the same software. Measurements of partial frequencies were executed by means of the flexible and highly accurate FFT-lab program. This program uses a local tracking of phase versus time, to introduce precise frequency corrections to all significant partials within the evaluated sound spectrum. An automated program FFT-anl permitted for quick evaluations and comparisons of the investigated sound spectra.

2.3. Results

The presented results show, first of all, the evolutive spectra of the recorded and analyzed sounds of carillon bells. Among those sounds five examples are selected to illustrate differences between particular spectra, namely c′, cis′, f′, g′, c″ (Figs. 6–10).

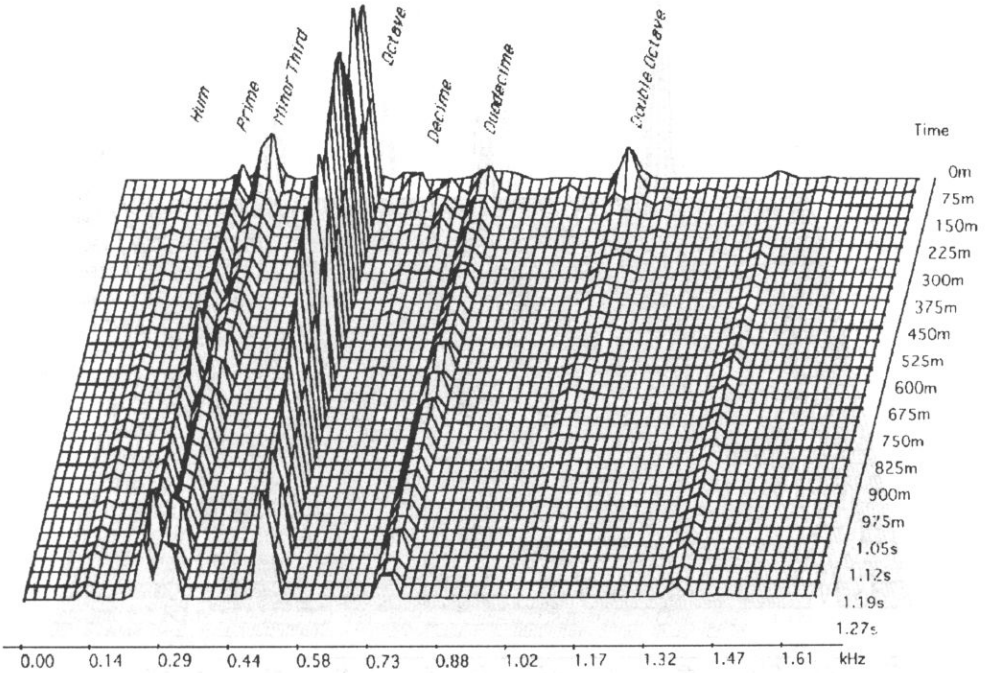

Fig. 6. Evolutive spectrum of the bell sound c′.

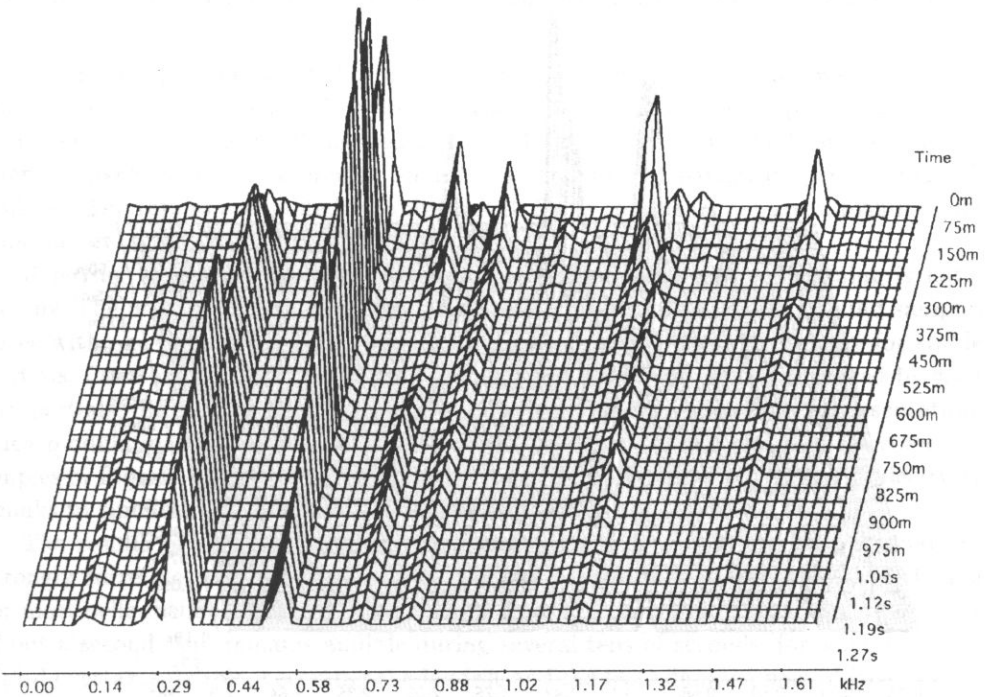

Fig. 7. Evolutive spectrum of the bell sound cis′.

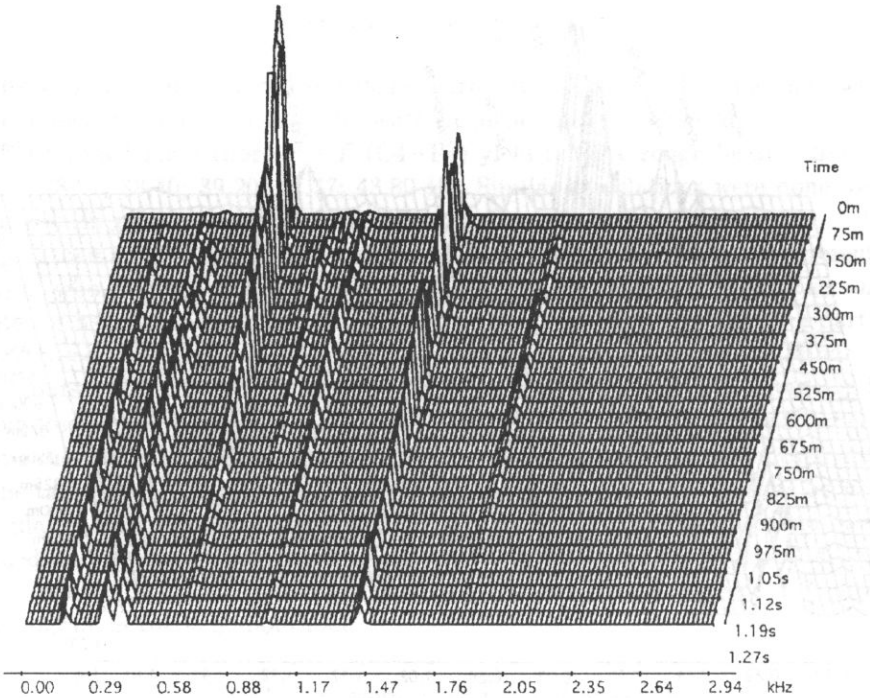

Fig. 8. Evolutive spectrum of the bell sound f′.

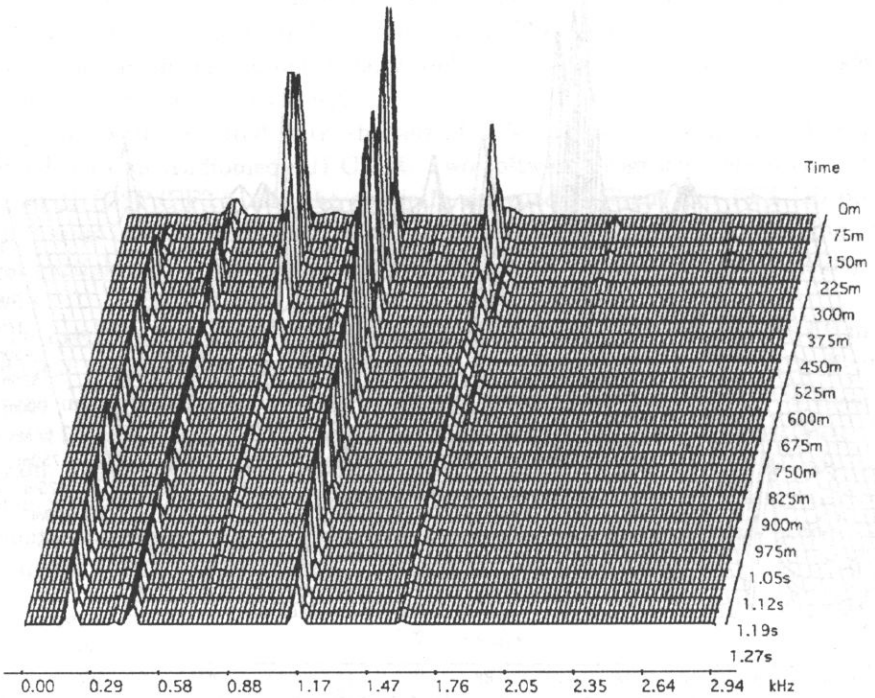

Fig. 9. Evolutive spectrum of the bell sound g′.

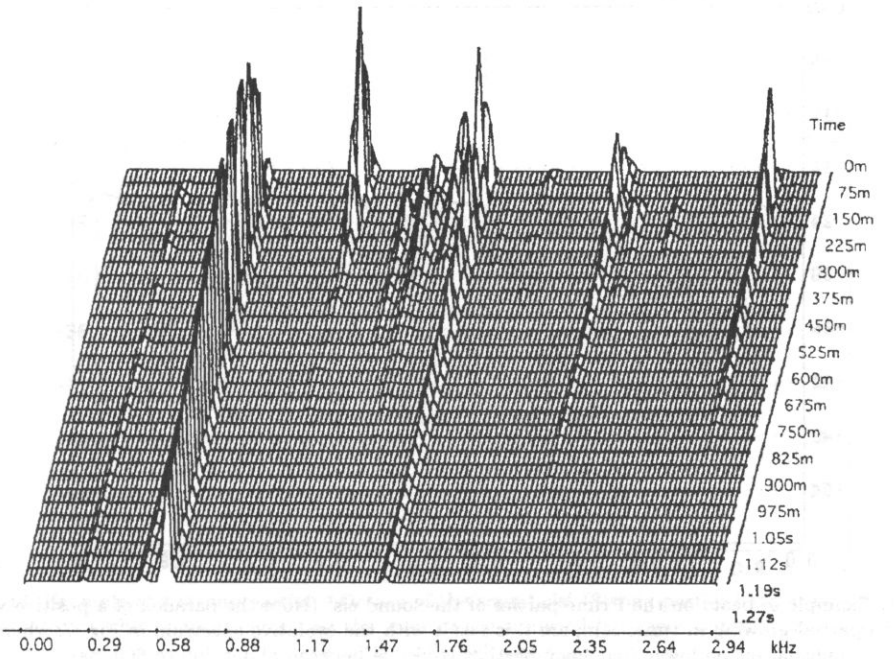

Fig. 10. Evolutive spectrum of the bell sound c''. (Note the prevailing power of the Minor Third).

Moreover, prints of the selected typical examples of computer evaluated wave-forms for the specified partials are joined, in order to visualize their properties, especially the levels and frequencies of the resulting beats (Figs. 11 – 16), as well as amplitude and phase characteristics, serving for precise corrections of measured partial frequency (Figs. 17 and 18). The results are quoted in Appendix B. Some comments are given within figure captions.

Referring to the presented results the precision of frequency determining is noteworthy. The most values obtained from repeated evaluations of recorded sound samples agree with one per mil accuracy (see e.g. Fig. 17). However, this is true only for stable partials. Contrary to these, there are partials modulated with beats, produced by split sub-partials, difficult to be determined within a momentaneous spectral presentation. Such modulations are often conspicuous within evolutive sound spectra (see some examples in Figs. 6 – 10). The above analyzed sound samples may be assessed subjectively thanks to simultaneous multiple sound demonstrations.

The results of spectral amplitude measurements and of damping rate evaluations strongly correlate with the total sound sensations for the investigated bells. Although for most bells the Hum (Lower Octave) prevails over all remaining partials already after about a second, and remains audible during several tens of seconds, for some bells the Third overtakes its role, becoming the loudest and the least damped partial (see e.g. the c'' bell evolutive spectrum shown in Figs. 10 and 14). It proves that amplitude relations participate as much as frequency relations in creating a particular sound sensation of a bell sound.

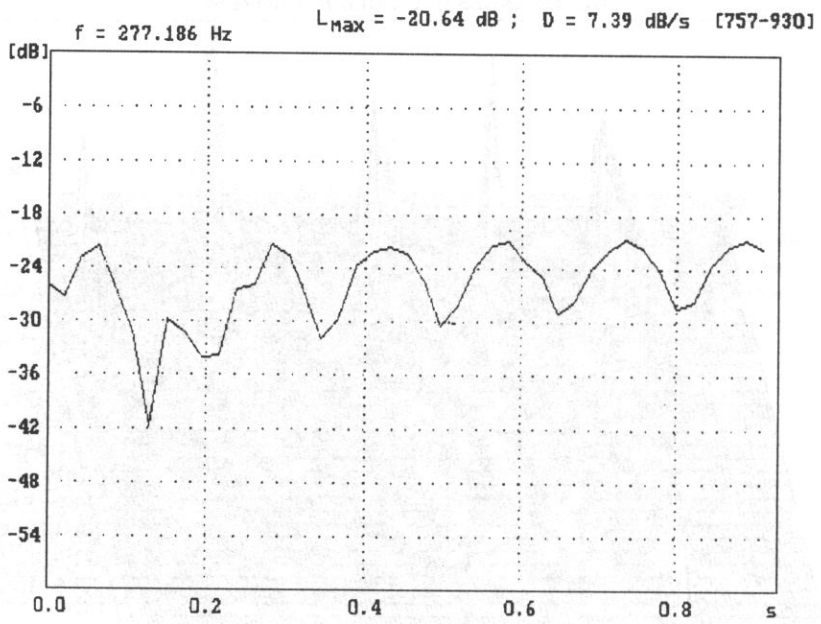

Fig. 11. Example of beats on the Prime partial of the sound cis′ (Note the paradox of a positive value of D – a partial growing in time; compare this result with the evolutive spectrum in Fig. 7, where an unusual pit on lower frequency partials is visible between about 300 to 600 ms).

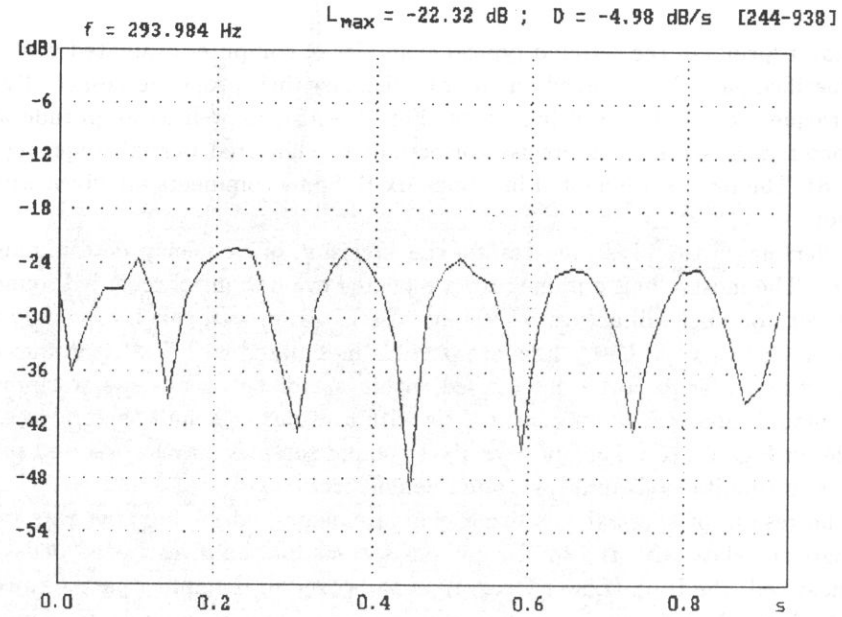

Fig. 12. Example of beats on the Prime partial of the sound d′ (The beats deeply modulate the partial and their waveform is regular; beat frequency is about 7 Hz; despite their depth these beats can not be perceived on the evolutive spectrum in Fig. 5).

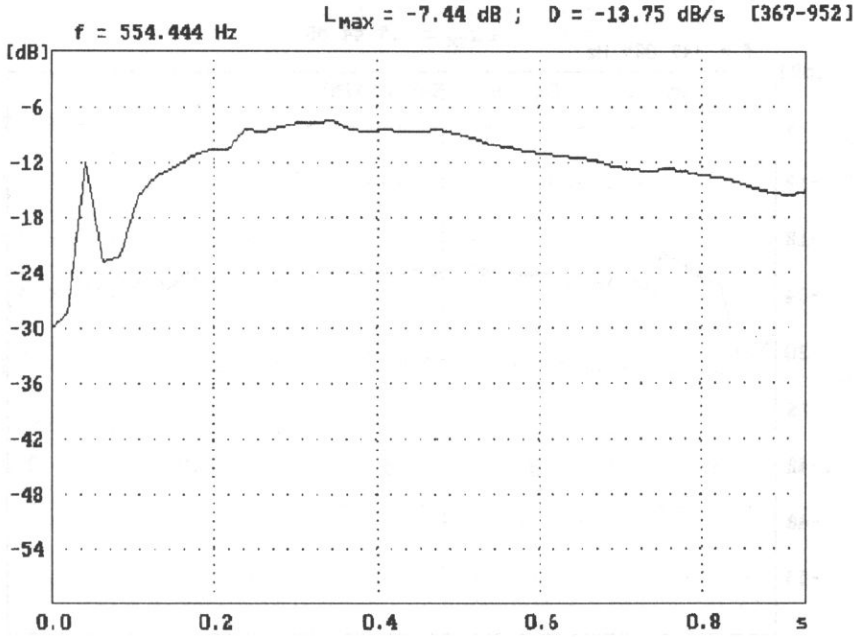

Fig. 13. Example of a strong partial – Octave of the sound cis′ (Strong partial have usually flat phase characteristics which permit correcting the value of the analyzed frequency automatically and evaluate it with six digital precision).

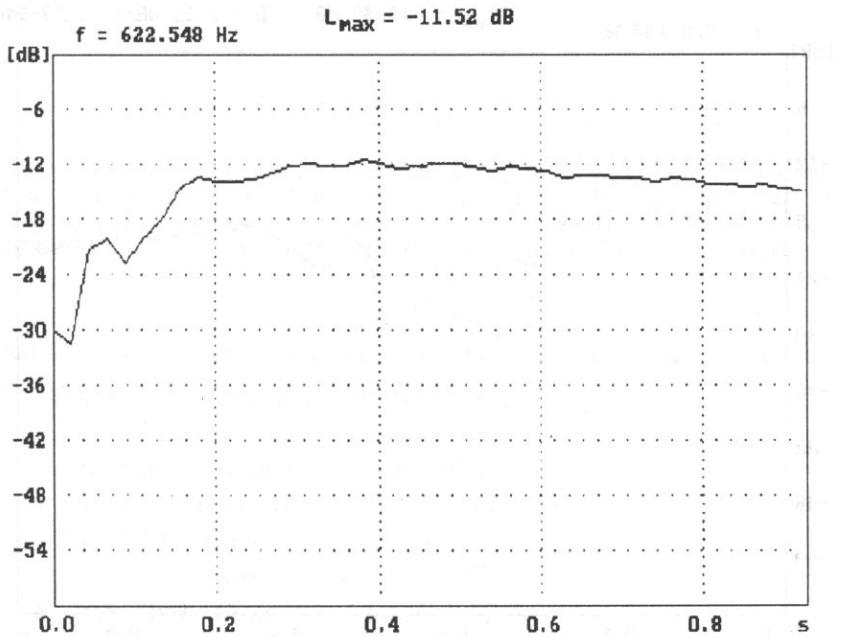

Fig. 14. Example of a strong partial – Minor Third of the sound c″ (The strongest partial, easily noticed in Fig. 10, having extremely low damping rate; such unique property of this bell, basically advantageous, disqualifies it rather as a component of bell chords).

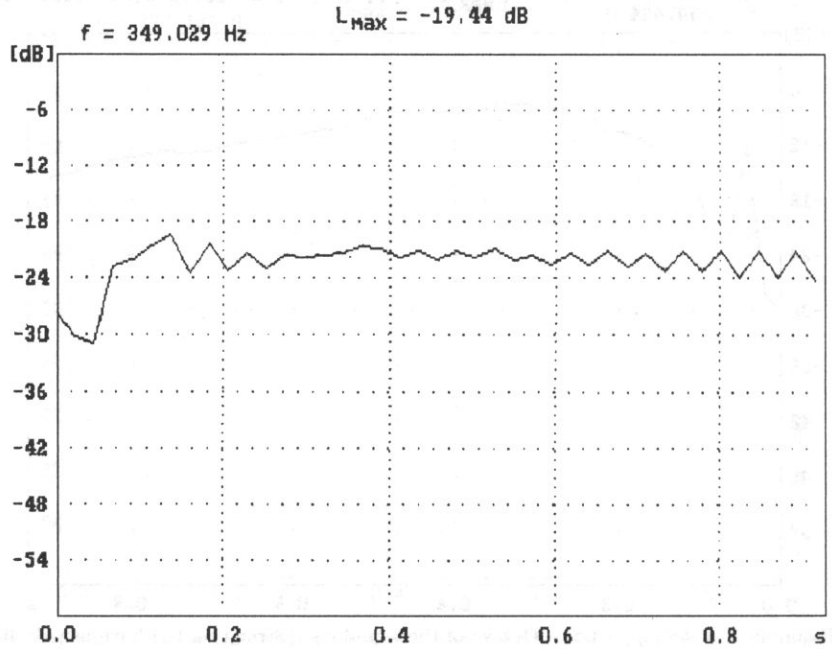

Fig. 15. Example of beats on the Prime partial of the sound f' (Beats with frequency of about 23 Hz shallowly modulating the partial).

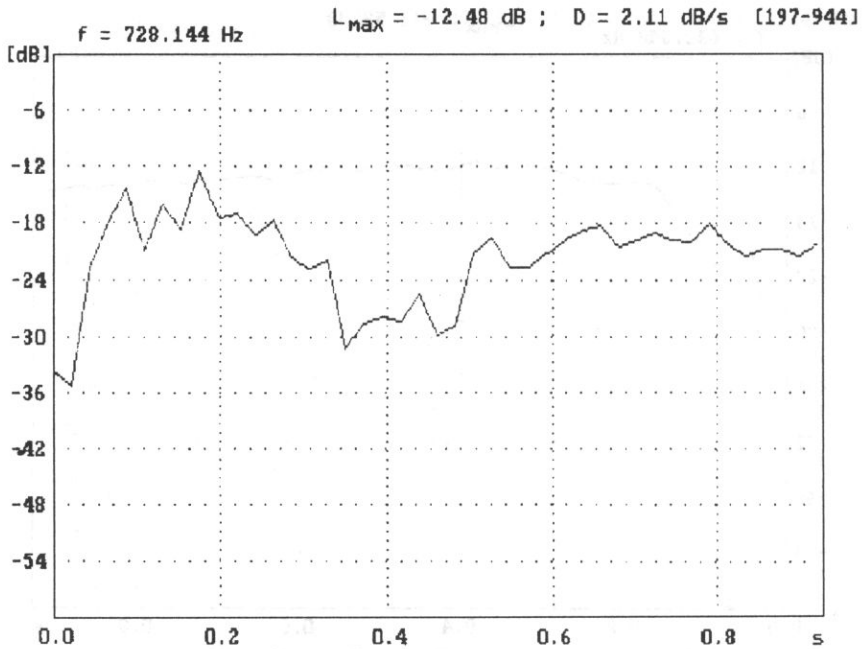

Fig. 16. Example of beats on the Fifth partial of the sound cis' (The pit mentioned in the comment to Fig. 11 is distinct here, as well as beats with frequency of about 8 Hz).

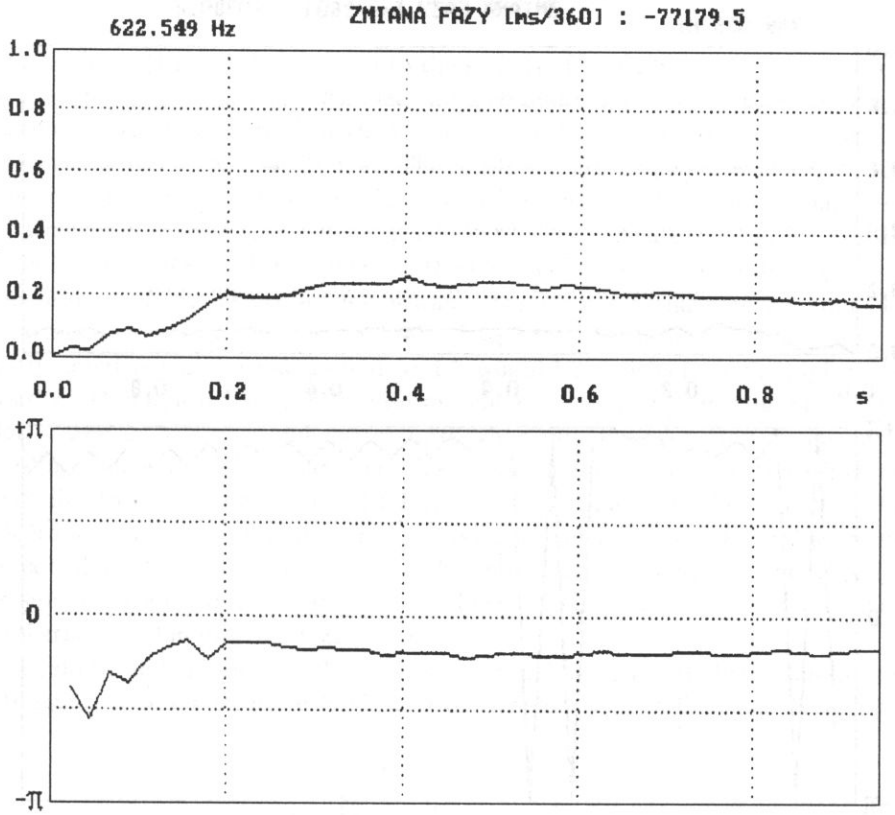

Fig. 17. Example of amplitude and phase versus time characteristics done during the analysis process with FFT-lab program on the Minor Third partial of the sound c″ (Strong amplitude and flat phase characteristics permit attaining a precise correction for frequency evaluation; here, one step before reaching the final value displayed at the completed evaluation, see Fig. 14, the frequency value differs only by 0.001 Hz).

The following chords were synthesized from the recorded sounds in seven categories:

I 10 Minor Thirds (from c′ – es′ to a′ – c″);
II 9 Major Thirds (from c′ – e′ to as″ – c″);
III 8 Pure Fourths (from c′ - f′ to g′ – c″);
IV 7 Augmented Fourths (from c′ – fis′ to fis′ – c″);
V 6 Pure Fifths (from c′ – g′ to f′ – c″);
VI 5 Minor Sixths (from c′ – as′ to e′ – c″);
VII 4 Major Sixths (from c′ – a′ to es′ – c″).

The remaining intervals as inherently dissonant were abandoned.

The sounds of all the mentioned chords were studied objectively and subjectively. Subjective assessments averaged were carried on by five experienced listeners (authors and their co-workers).

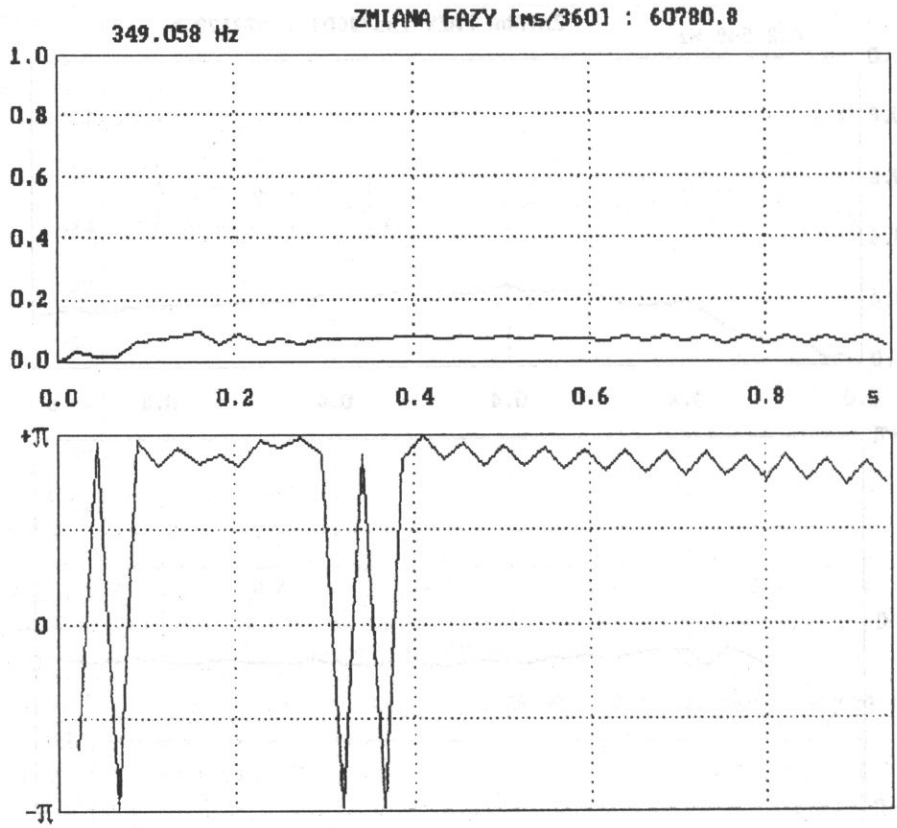

Fig. 18. Amplitude and phase versus time characteristics done during the analysis process with FFT-lab program on the Prime partial of the sound f′ (Same sound as in Fig. 15, however, before the final correction of evaluated frequency; phase fluctuations, with the exception of jumps by 2π, are synchronous with amplitude beats on about 23 Hz).

In each of the category about 50% of the well sounding chords were selected, while others were disqualified. As criteria served: lack of audible beats, good fusion of two sounds, uniform sound decay, long duration of both lowest frequency partials (hums) and a general sensation quality. Then, bells entering into those selected chords were qualified as well fusionable. The three bells, selected as good in that way among thirteen investigated, were: g′, a′, and e′. The fourth one, the c″, perhaps the best sounding otherwise, fell out of fusion due to its too loud Minor Third partial, which masked its other long sounding frequencies. The worst sounding among the bells of the middle octave was the cis′ bell.

The general result of study has showed that chords synthesized exclusively of well sounding bells sounded consonantly, while others less or more dissonantly. It means that the tuning precision as required in the specialized literature [11] does not determine a sufficient criterion of sound quality for contemporary carillons.

3. Sounds of a former carillon

Having devoted so much attention to the sounds of actually existing St. Catherine's carillon, authors cannot give up the idea of disseminate information on an old recording containing several notes played by the former St. Catherine carillon, in the years before the outbreak of the Second World War. The recording, existing as an analogue tape copy (or most probably multiple re-copy) of an acetate disc remained within the content of the sound archives of the Gdańsk Broadcasting Centre and was in the seventies transferred to the Sound Engineering Department of the Gdańsk University of Technology.

The recording contains two single-voice ancient melodies lasting together about 1 min. and played on six bells only: h′, c″, d″, e″, f″, and g″. The duration of particular notes is mostly about one and a half second, which would be sufficient for the high precision analysis, which might deliver precise information about tuning properties of the ancient carillon. However, the vow and flutter introduced into the recording during multiple rerecordings causes the phase characteristics to become instable to a degree, which makes it impossible to use the FFT-anl or FFT-lab programs efficiently. The sound quality of the recording and the tuning of sounds are poor. Nevertheless the general structure of those six bells evolutive spectra were studied by means of the Sound Designer II program. The results are shown in the Figs. 19 to 24. The comparisons to the spectra of the new St. Catherine carillon may be instructive.

It should be added here that the ancient carillon, having had 37 bells, had been built in 1910 by the bellfounder Franz Schilling from Apolda. The carillon was dismounted in

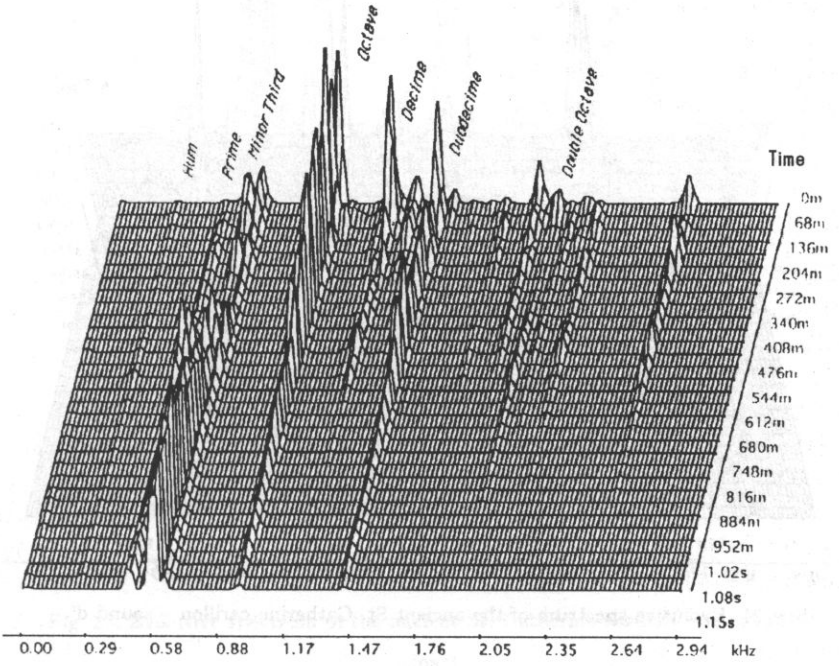

Fig. 19. Evolutive spectrum of the ancient St. Catherine carillon – sound h′.

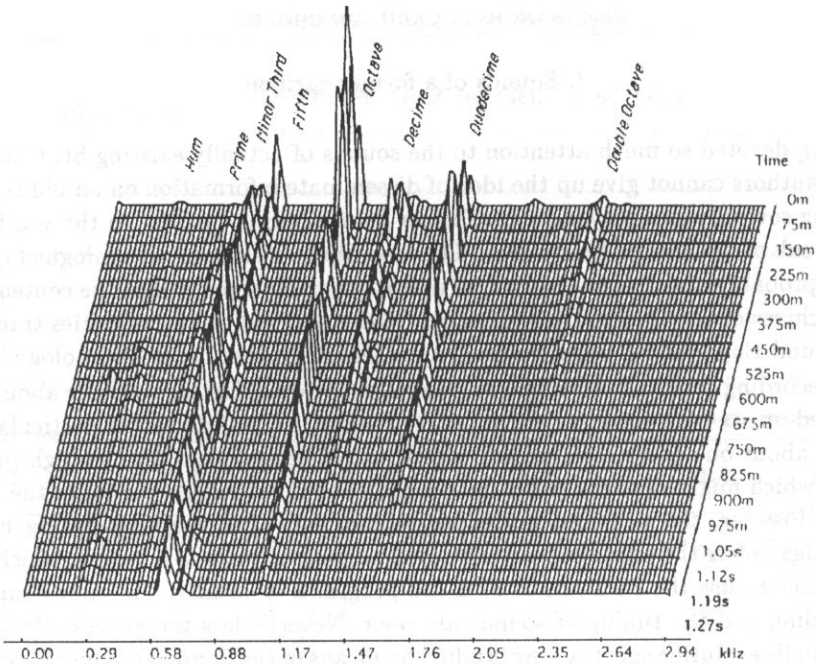

Fig. 20. Evolutive spectrum of the ancient St. Catherine carillon – sound c′.

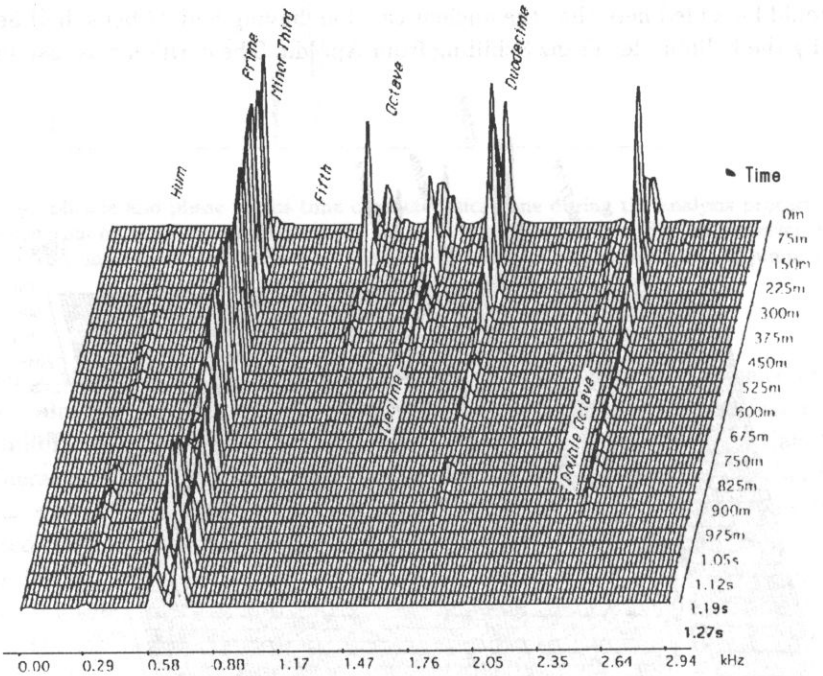

Fig. 21. Evolutive spectrum of the ancient St. Catherine carillon – sound d′.

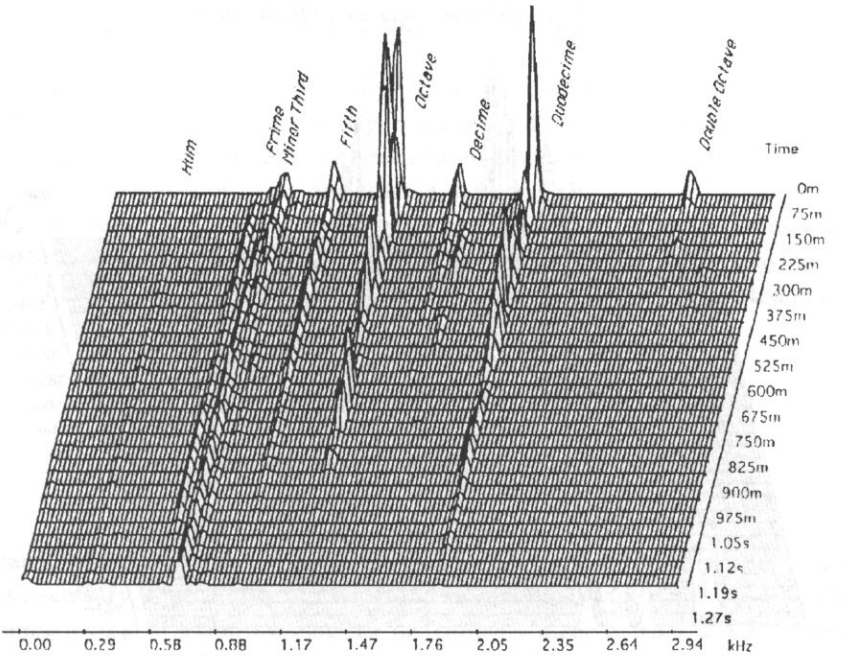

Fig. 22. Evolutive spectrum of the ancient St. Catherine carillon – sound e′.

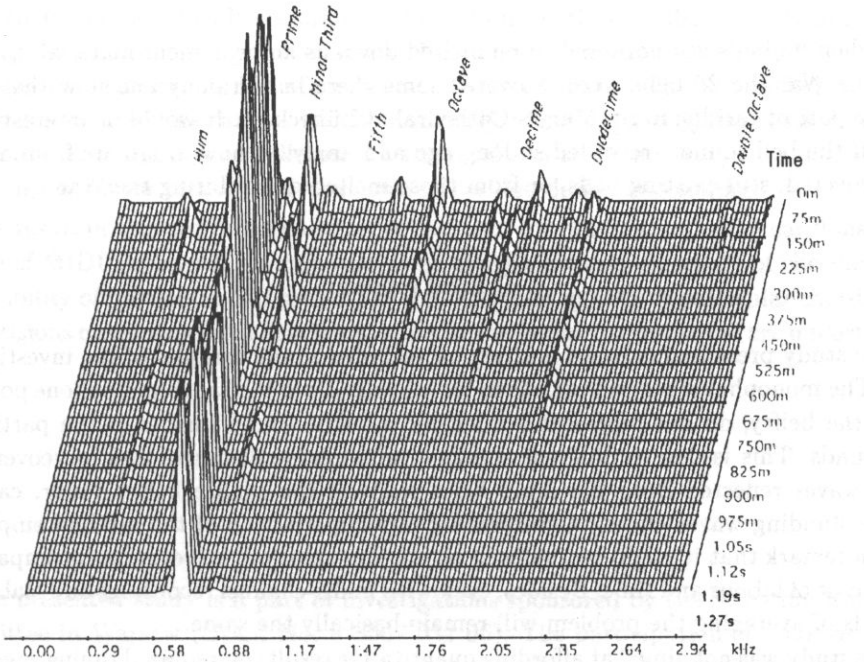

Fig. 23. Evolutive spectrum of the ancient St. Catherine carillon – sound f′.

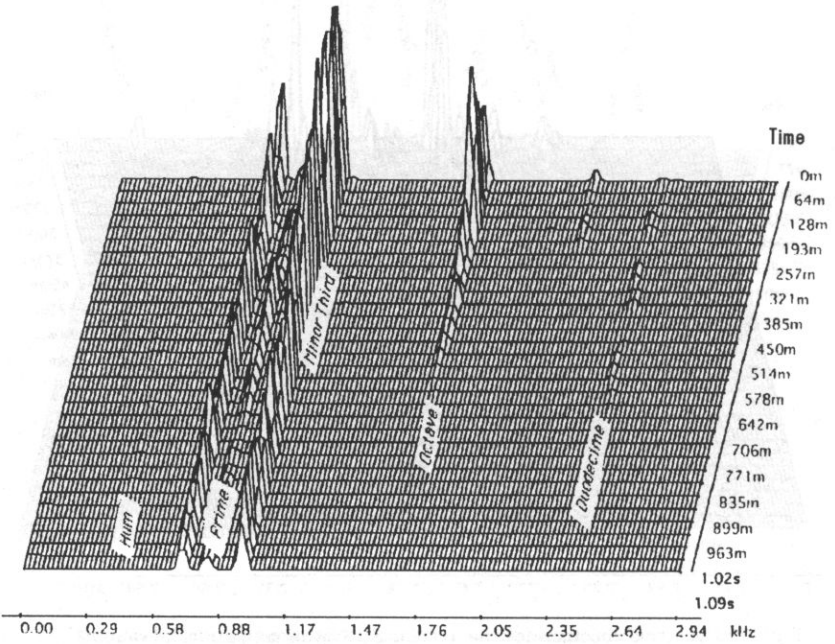

Fig. 24. Evolutive spectrum of the ancient St. Catherine carillon – sound g′.

1942 when its bells were ordered to be melted down as an armament material. Luckily, after the War the 28 bells were recovered somewhere in Germany and now they have become part of carillon in St. Mary's Cathedral at Lübeck [4]. It would be interesting to check if the bell sounds, recorded so long ago and analyzed now, originate from among the recovered, still existing bells, or from those melted down during the War.

4. Critical remarks

The study presented is based entirely on recorded sound samples of the investigated bells. The monophonic recordings, taken for all bells, from the same microphone position inside the belfry, do not represent accurately the true sound images of the particular bell sounds. This is due to different source – microphone distances and moreover – to sound waves reflected from the inner brick walls of the square belfry tower, causing intense standing waves effects. Commenting this imperfection of the method employed one can remark that it might be replaced by another solution, however, at incomparably higher cost of labour and time. Besides, even with multi-channel recordings and elaborate methods of averaging the problem will remain basically the same.

The study was not aimed at affording quantitative results on required tuning precision of consonant carillon sounds. The results presented are given rather as examples of imperfections of the timbre perceived by a common listener of carillon music, as an attempt to define their character, and as hints to their possible removal.

Authors think that the attention of acousticians, working on problems connected with carillon music, was, so far, mostly concentrated on improvement of the tuning methods of carillon bells. An amazing precision was achieved. However, not so much is known on the mechanism of beats and warble, affecting the perceived sound quality of bell sounds, in particular the quality of bell chords. Without suppression of warble or at least reduction of its level by about twenty dB, the use of chords for playing carillon music should be strictly limited, and applied only to cases of a few preselected harmonies of sounds.

5. Conlusions

The carillon music in the past was single-voiced. This was due to carillonists' difficulty and effort necessary to set in motion two or more keys simultaneously. The introduction of electromagnetical traction systems to instruments steered from a MIDI-keyboard, allowed for frequent use of chords in carillon music. This opens a new problem of higher requirements relative to the quality of carillon bell sounds.

The assessment of sound properties of the investigated bells presented ought to be evaluated in relation to all remaining information on those bells, in particular their sound spectra, their tuning precision etc. Part of the information is contained in the Appendices. The more detailed information is without doubt available at the belllfoundry which had produced this carillon i.e. the Koninklijke Klokkengieterij Eijsbouts in Asten. After a proper evaluation and discussion, the results of this study may turn out to be a useful suggestion for further improvements in carillon design and tuning.

The result of this study may also serve as a hint for musicians playing carillons with the use of MIDI keyboards. It may turn their attention to the necessity of checking the fusion-ability of particular bell sounds, as well as sound quality of particular chords, before decisions on arrangement and mode of performed music composition are undertaken.

6. Acknowledgements

The presented study is a part of investigations sponsored by the Scientific Research Committee in Warsaw (Grant No. 8 S507 031 06). The participation of Grzegorz Szychliński, DSc., and Marek Szczerba, MA, at the carillon sound recordings is gratefully acknowledged. The authors express their thanks to Roman Perucki, Director and Conductor of the Baltic Philharmonic Orchestra, for an inspiring discussion at the St. Catherine's carillon keyboard.

Appendix A. St. Catherine's carillon – list of the bells [5]

No.	Note	Diameter [m]	Mass [kg]
1	c′	1.564	2200
2	cis′	1.474	1840
3	d′	1.390	1535
4	dis′	1.310	1285
5	e′	1.235	1075
6	f′	1.166	905
7	fis′	1.100	760
8	g′	1.038	640
9	gis′	0.980	535
10	a′	0.925	450
11	ais′	0.873	375
12	h′	0.824	320
13	c″	0.774	263
14	cis″	0.727	220
15	d″	0.686	186
16	dis″	0.646	162
17	e″	0.611	141
18	f″	0.580	123
19	fis″	0.554	108
20	g″	0.532	95
21	gis″	0.510	84
22	a″	0.487	74
23	ais″	0.468	66
24	h″	0.448	59
25	c‴	0.431	53
26	cis‴	0.413	48
27	d‴	0.396	44
28	dis‴	0.382	40
29	e‴	0.366	35
30	f‴	0.352	32
31	fis‴	0.341	30
32	g‴	0.328	27
33	gis‴	0.317	25
34	a‴	0.306	23
35	ais‴	0.296	21
36	h‴	0.287	19
37	c⁗	0.270	18

Appendix B. The measurement results

BELL		Hum		Prime		Third		Fifth	
No.	Note	f [Hz]	Δf [ct]	f [Hz]	Δf [ct]	f [Hz]	Δf [ct]	f [Hz]	Δf [ct]
1	c′	130.814	0	261.505	−0.8	311.097	−0.1	399.313	31.2
2	cis′	138.554	−0.5	277.186	0	329.752	0.6	*	*
3	d′	146.517	−3.8	293.984	1.8	349.367	0.6	*	*
4	dis′	155.586	0.2	311.273	0.8	369.863	−0.7	*	*
5	e′	164.853	0.4	329.784	0.4	392.784	3.4	*	*
6	f′	174.431	−1.9	349.029	−0.9	414.817	−2.1	*	*
7	fis′	184.556	−4.2	369.756	−1.2	440.308	1.2	*	*
8	g′	195.856	−1.3	*	*	466.422	0.9	*	*
9	gis′	207.301	−2.9	415.006	−1.3	494.718	2.9	626.461	11.6
10	a′	219.987	−0.1	439.591	−1.7	523.191	−0.2	*	*
11	ais′	232.949	−0.9	466.328	0.6	554.973	1.9	703.457	12.3
12	h′	247.124	1.2	494.288	1.4	587.822	1.4	724.017	−37.8
13	c″	261.651	0.1	523.339	0.2	622.548	0.8	790.233	13.7

BELL		Octave		Decime		Duodecime		Double Oct.	
No.	Note	f [Hz]	Δf [ct]	f [Hz]	Δf [ct]	f [Hz]	Δf [ct]	f [Hz]	Δf [ct]
1	c′	523.031	−0.6	651.256	−21.2	786.254	4.9	1074.064	45.1
2	cis′	554.444	0.2	728.144	−28.3	833.965	6.9	1153.421	68.4
3	d′	587.161	−0.5	748.261	19.2	884.049	7.9	1224.119	71.4
4	dis′	621.685	−1.7	790.487	14.2	934.989	4.9	1293.464	66.8
5	e′	659.629	0.9	*	*	994.508	11.7	1377.721	75.9
6	f′	698.139	−0.8	906.558	51.4	1054.207	12.7	1461.087	77.7
7	fis′	739.086	−2.2	952.904	37.8	1112.509	5.8	1539.701	68.4
8	g′	784.011	0	985.706	−3.7	1183.991	13.7	1643.025	80.9
9	gis′	829.934	−1.5	1065.238	30.7	1227.781	−23.5	1727.311	67.5
10	a′	880.308	0.6	1143.772	53.8	1325.814	9.5	1837.195	74.8
11	ais′	932.059	−0.5	1204.972	44.1	1408.349	14.1	1954.346	−18.7
12	h′	988.183	0.7	1294.448	68.1	1489.629	11.2	2062.688	74.7
13	c″	1046.810	0.5	1351.806	43.1	1575.208	7.9	2177.602	68.6

* denotes uncertain result due to insufficient partial level or excessive beats.

References

[1] H. BAGOT, *Bells. Their design and tuning*, Acoustics Australia, **14**, 2, 35–41, 1986.

[2] E. DUNKER, *Psychologie des Hörens*, [in:] Gauer-Kramer-Jung, Psychologie des Menschen, Band 12, Urban and Schwarzenberg, München 1972.

[3] E.W. VAN HEUVEN, *Acoustical measurements on church bells and carillons*, De Gebr. van Cleef, The Hague 1949; [in:] Acoustics of Bells, T.D. ROSSING [Ed.], Van Nostrand, N. Y. 1984.

[4] A. JANUSZAJTIS, *St. Catherine's Church in Gdańsk* [in Polish], O.O. Karmelici, Gdańsk 1989.

[5] *Königliche Eijsbouts, Glockenliste für das spielbare Glockenspiel der St. Katharinenkirche in Danzig*, Gdańsk 1989.

[6] R. PERRIN, T. CHARNLEY, J. DEPONT, *Normal modes of the Modern English Church Bell*, J. Sound and Vibration, **90**, 1, 29–49, (1983); [in:] Acoustics of Bells, T.D. ROSSING [Ed.], Van Nostrand, New York 1984.

[7] A. RAKOWSKI, *Dissonance described by psychoacoustic investigations* [in Polish], Zeszyty Naukowe PWSM, Warszawa 1979.

[8] T. ROGALA, A. RAKOWSKI, *Sensory dissonance of two simultaneously sounding tones* [in Polish], Scientific Papers of the Institute of Telecommunication and Acoustics, No. 78, 407–410, Technical University of Wrocław, 1994.

[9] T.D. ROSSING, *Acoustics of Bells*, Part III, pp. 134–135, Van Nostrand, New York 1984.

[10] M. SANKIEWICZ, A. KACZMAREK, G. BUDZYŃSKI, *Acoustic investigation of the carillons in Poland*, Arch. Acoust., **19**, 3, 333–353 (1994).

[11] C.-R. SCHAD, *Form-Klang-Rechnungen an Glocken*, Acustica, **64**, 272–285 (1987).

[12] F.H. SLAYMAKER, W.F. MEEKER, *Measurements of the tonal characteristics of carillon bells*, Journal of the Acoustical Society of America, **26**, 515–522 (1954); [in:] Acoustics of Bells, T.D. ROSSING [Ed.], Van Nostrand, New York 1984.

[13] C. SLOANE, *Proportionality of beat rate and tempering of musical intervals*, J. Sound and Vibration, **112**, 198–199 (1987).

[14] C. SLOANE, *Effects of tempering on relative major and minor chords*, J. Sound and Vibration, **147**, 2, 359–360 (1991).

[15] C. SLOANE, *Corrections to "Effects of tempering..."*, J. Sound and Vibration, **155**, 2, 373–374 (1992).

[16] C. SLOANE, *A further note on tempered minor chords*, J. Sound and Vibration, **170**, 2, 261–262 (1994).

[17] J.W. STRUTT-RAYLEIGH, *The theory of sound*, Vol. 2, (Macmillan ed., 1896), 2nd ed., Dover Publ., New York 1945.

ARCHIVES OF ACOUSTICS
22, 3, 267–275 (1997)

AIR VOLUME RESONANCES AND THEIR INFLUENCE ON HALL ACOUSTICS

V. STAUSKIS

Vilnius Gediminas Technical University
(Saulėtekio al. 11, 2040 Vilnius, Lithuania)

V. KUNIGELIS

Vilnius University
(Saulėtekio al. 9, 2040 Vilnius, Lithuania)

The influence of resonances in a small rectangular music-hall on its reverberation characteristics was investigated. The length, width and height of the hall are $13.6 \times 10.7 \times 7$ m, respectively. The sound absorption coefficients of all the hall surfaces are very small and equal to $0.03 - 0.05$ through the whole frequency range.

It has been established experimentally that the attenuation of the sound field in the empty hall is close to an exponential one. When 120 and 170 semi-upholstered chairs are placed in the hall, the sound field is characterized by early and steep attenuation which is determined by an additional sound absorption and by the late and slow attenuation determined by the repetitive echoes and resonances between the rows of chairs. The late character of attenuation starts from about $700 - 800$ ms and depends on the distance between the microphone and the source.

When the number of semi-upholstered chairs arranged in rows is increased from 120 to 170, the reverberation time up to 160 Hz, approximated by the attenuation from 0 to -30 dB, is not reduced, as one would expect, but grows from $5 - 6$ s to $9 - 10$ s and is even longer than the reverberation time of the empty hall. The late reverberation time of approximately -25 to -30 dB at 160 Hz has a pronounced resonant character and equals 12 s. On increasing the number of chairs to 170, the reverberation time peaks at 100 Hz achieves as much as 20 s. The late reverberation time shows that there exist resonances in the hall, evoked by a repetitive echo. After eliminating the echo, the resonances disappear.

1. Introduction

Halls small in area and volume are usually designed for the performance of and listening to chamber music. Existing small halls are renovated and adapted for musical purposes. The layout of such renovated old halls is usually rectangular, while their volume is small. The floor plane is horizontal and upholstered or semi-upholstered chairs are arranged on it. The surfaces of such halls are made of materials that reflect the sound energy well. The average sound absorption coefficient of the hall planes is usually small.

Rectangular halls with parallel walls, well reflecting sound, are risky from the acoustic point of view. Repetitive echoes of low repetitive frequency as well as air volume resonances may occur in such halls. Both the echoes and the resonances may also be influenced by chairs, especially those arranged on the horizontal plane. It is therefore necessary to investigate the influence of such negative phenomena on the hall acoustics.

The purpose of this paper is to study the influence of different quantities of semi-upholstered chairs arranged in rows and the tapestries hung on all the walls of the hall on the acoustics of a small hall.

2. Methods

The experiment was carried out in a hall 13.6 m long, 10.7 m wide and 7.0 m high. The volume of the hall was a small one of 1018 m^3. The parquet floor was horizontal and without a stage. All the wall and ceiling planes were plastered, therefore their sound absorption coefficients were very small. The front, back and lateral walls of the hall were even. There were two beams, 60 cm high and 60 cm wide, all of them extending along the width of the hall. The hall has one window of 2 m^2. The layout and the longitudinal section of the hall are shown in Fig. 1.

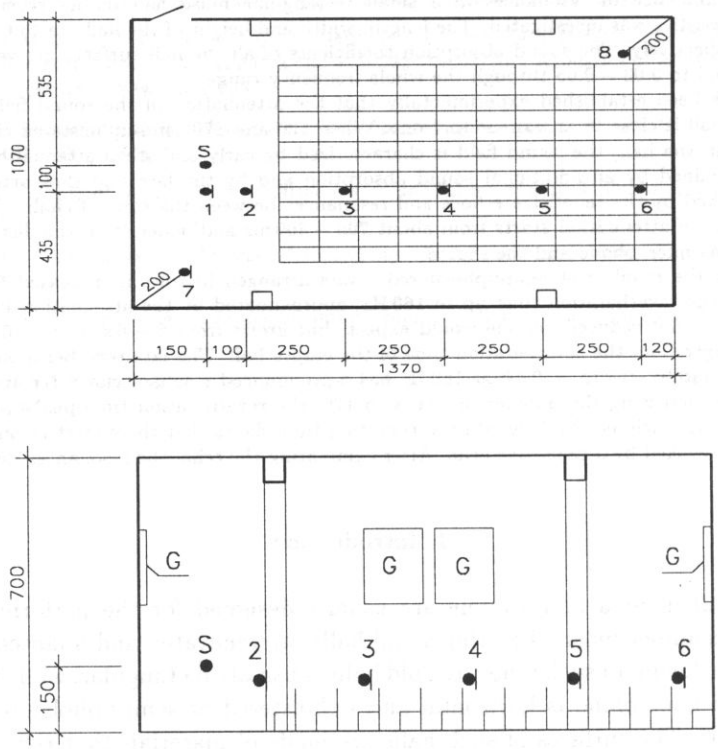

Fig. 1. The layout and section of the hall under investigation with the allocation of study points.

A 9 calibre sound pistol was used as sound source. In all cases, the sound source was situated on the longitudinal axis of the hall at a height of 1.5 m and a distance of 1.5 m from the front of the hall. It was stiffly fixed to a microphone stand.

The investigations were conducted at eight points in the hall. The selected longitudinal axis of the measurements was 1 m aside from the sound source axis. The microphones were placed at a height of 1.2 m.

The sound signal was transmitted from the microphone to the microphone amplifier, from the latter to a 2-channel, 16-bit analog-digital converter, and then to the computer memory. The acoustic analysis of signals was performed with the aid of a specially prepared program.

The main acoustic features were measured for five different cases of the hall settings: 1) empty hall; 2) hall with 120 semi-upholstered chairs; 3) hall with 170 semi-upholstered chairs; 4) hall with 170 semi-upholstered chairs and tapestries on the four walls; and 5) hall with 120 semi-upholstered chairs and 60 people.

The chair backs were upholstered with soft fabric. The edges of the chair backs were made of hard wood, while their external sides were covered with plywood covered with thin fabric. The chairs were arranged in the middle of the hall. The tapestries, whose overall area was about 11 m^2, were hung at a height of 3.3 m from the floor. The height of the tapestries was about 1.3 m. The width of the tapestries arranged on the lateral walls varied from 2.4 m to 2.8 m, while the width of those hung on the back and the front wall was 1.6 m.

In this paper the results of the investigations are represented by the measurements carried out at point 3. The distance from the point No. 3 to the sound source was 3.6 m and the distance to the right wall was 4.3 m.

3. Results

The time-dependence of the decay of the sound field energy in different hall settings is presented in Fig. 2.

When the hall is empty, the sound field decays along an exponential curve. The field decay on the logarithmic scale is almost a straight line. When there are 120 semi-upholstered chairs in the hall, the sound field attenuation has a different character. Here one may observe two markedly distinct regions: an early and a late one. The early decay is determined by the additional attenuation caused by the chair absorption, while the late decay is determined in our opinion by the resonant sound field caused by the repetitive echoes between the parallel walls and the chairs arranged in rows. The resonances occur between the rows of chairs, and the repetitive echo maintains the sounding of the excited resonances due to which the entire decay rate of the sound field is decreased considerably. When the number of chairs is increased to 170, the early sound field decay is identical to that observed in the hall with 120 chairs. Further, however, the sound field decays even slower than in the latter case. After the tapestries are hung on all the four walls of the hall, the repetitive echoes and the resonances disappear. This is evidenced by Fig. 2 which shows that both the early and the late sound

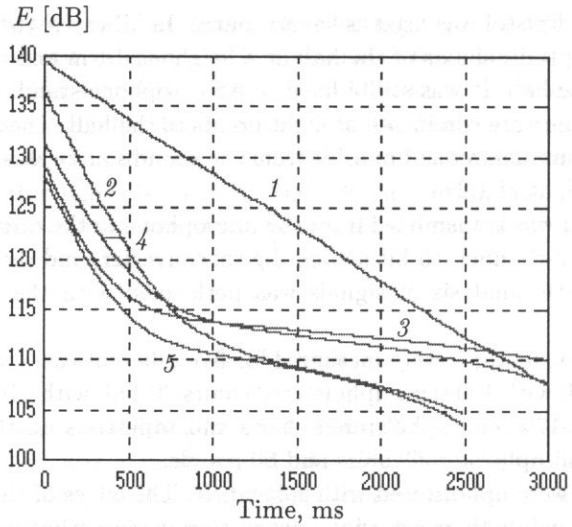

Fig. 2. Time-dependence of the sound field for different hall settings: *1* – empty hall; *2* – hall with 120 semi-upholstered chairs; *3* – hall with 170 semi-upholstered chairs; *4* – hall with 170 semi-upholstered chairs and tapestries on the walls; *5* – hall with 120 semi-upholstered chairs and 60 people.

field decay regions become steeper. This cannot be explained only by the slight increase in absorption caused by the tapestries. The change of the slopes of decay curves, occurring at around 700 – 800 ms, is clearly seen. The position of this change depends on the distance between the microphone and the sound source.

The occurrence of the resonances should be confirmed or denied by the frequency characteristics of the early and the late reverberation time. The results of the analysis in the early reverberation time are presented in Fig. 3.

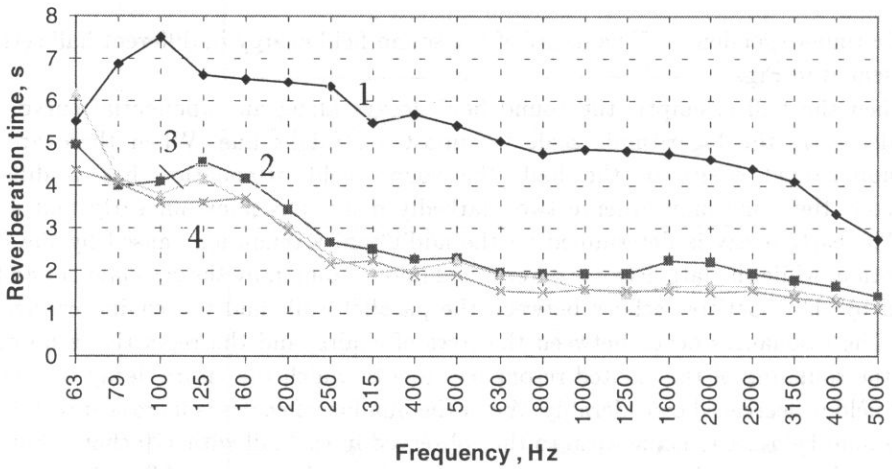

Fig. 3. Early reverberation time vs. frequency for different hall settings: *1* – empty hall; *2* – hall with 120 semi-upholstered chairs; *3* – hall with 170 semi-upholstered chairs; *4* – hall with 170 semi-upholstered chairs and tapestries.

In this case, as expected, the resonances are not observed. Filling of the hall with chairs greatly reduces the reverberation time almost equally throughout the whole frequency range. The increase in the number of chairs and additional tapestries on the walls have hardly any effect on the reverberation time.

Results of the analysis of the late reverberation time, approximated from −25 to −30 dB, are shown in Fig. 4.

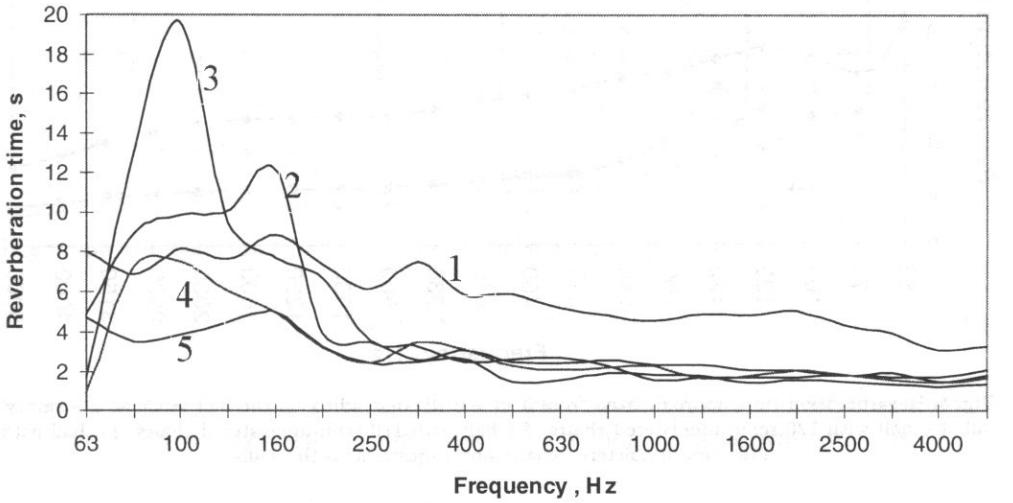

Fig. 4. Late reverberation time, approximated from −25 to −30 dB, depending on the hall settings: *1* – empty hall; *2* – hall with 120 semi-upholstered chairs; *3* – hall with 170 semi-upholstered chairs; *4* – hall with 170 semi-upholstered chairs and tapestries on the walls; *5* – hall with 120 semi-upholstered chairs and 60 people.

One can see that, after the increase in the number of chairs arranged in rows, the late reverberation time is also prolonged, but only at the resonant frequency. When there are 120 chairs, at the resonant frequency of 160 Hz, the late reverberation time is equal to 12 s. As the number of chairs is increased to 170, the reverberation time is prolonged still further and at 100 Hz it equals as much as 20 s. From this one may conclude that the resonance is evoked in the low-frequency range by the rows of chairs. The resonance is supported by the repetitive echoes after the elimination of which the resonance disappears. This is confirmed by the fact that both the repetitive echoes and the resonances almost disappear after the tapestries are hung, while the reverberation time equals about 4 s only. When there are 120 chairs and 60 people in the hall, the resonance is retained at low frequencies, but its character is different as compared with the resonance in the hall without listeners.

The time decay of the sound field of the filtered signal differs greatly from that of the non-filtered signal. At the resonant frequencies, the fast and slow parts of the decay curve can no longer be so clearly distinguished. Thus, in this case, the single reverberation time may by defined in the region 0 to −30 dB. The region chosen differs from the standard one of −5 to −35 dB because in the latter case the obtained dynamic range was too low.

Figure 5 depicts the frequency characteristics of the reverberation time approximated from 0 to −30 dB.

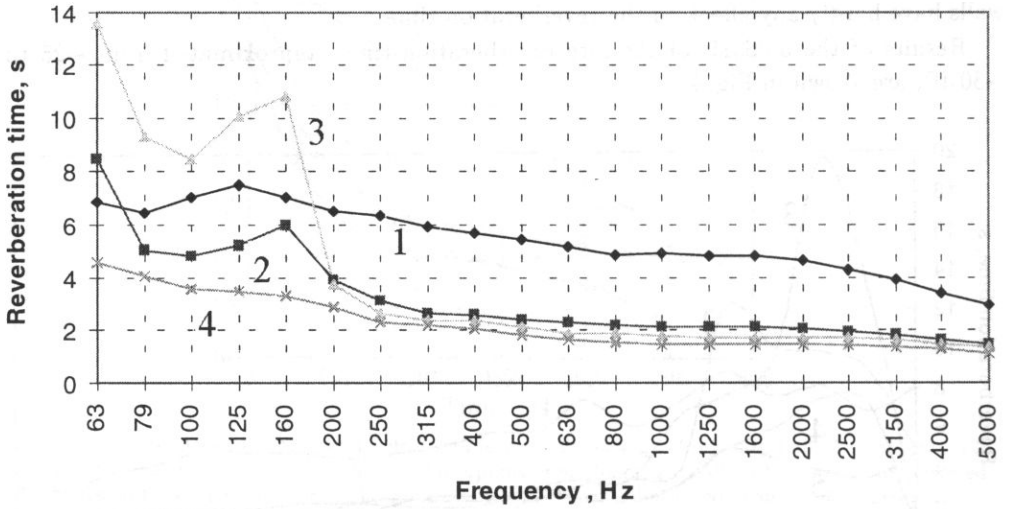

Fig. 5. Reverberation time approximated from 0 to −30 dB depending on the hall settings: *1* – empty hall; *2* – hall with 120 semi-upholstered chairs; *3* – hall with 170 semi-upholstered chairs; *4* – hall with 170 semi-upholstered chairs and tapestries on the walls.

When the hall is empty, the reverberation time appears to be only slightly different from the early reverberation time (EDT). With 120 chairs in the hall, the reverberation time is considerably longer than EDT for the same number of chairs. When the number of chairs is increased from 120 to 170, the reverberation time in the range up to 160 Hz becomes much longer, exceeding that of the empty hall. It is well known that the larger the number of chairs introduced the greater the sound absorption. This implies that the reverberation time should be decreased. The experiment, however, shows a contrary result: the time is increased. Such phenomenon may be explained by the repetitive echoes which evoke resonances between the chair rows. Therefore the sound field decay curve has two, though not significantly different, decay regions: an early and a late one. Upon eliminating the repetitive echo, the resonances must disappear. This is confirmed by curve 4. After the tapestries are hung on the walls of the hall with 170 chairs, the reverberation time is reduced to 4 – 8 s in the low-frequency range, i.e. up to 160 Hz.

The appearance of the resonance may be explained by the periodical allocation of the chairs along one coordinate and the existence of repeating echoes with respect to this coordinate. In this case, the chairs may be considered to be an infinite one-dimensional periodical structure. The geometry for the analysis of such a problem is shown in Fig. 6.

The space above the chairs is assumed to be free; this is valid when the period of the resonance, obtained in such a periodical structure, is considerably shorter than the time of sound transition between the chairs and the ceiling (we will see after the calculations that this is just the case). The acoustic field above the chairs, using notations shown in

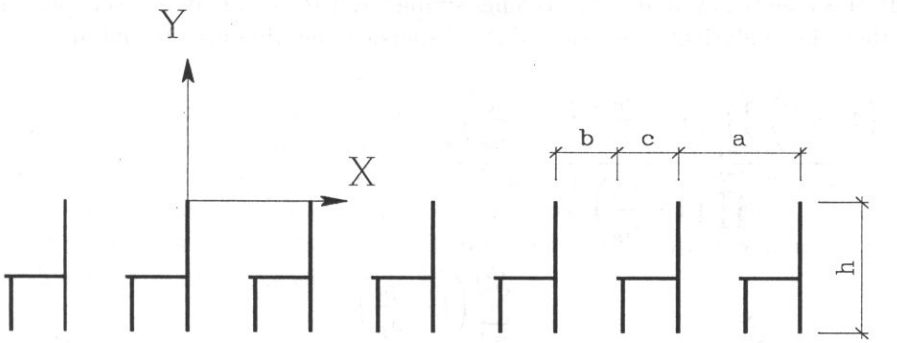

Fig. 6. The periodical infinite structure of the chairs. The height of the chair back is assumed to be equal to half of the chair height.

Fig. 6, may be described by means of the Floke waves [1]:

$$\psi_1 = \sum_{n=-\infty}^{\infty} B_n e^{i\beta_n x} e^{-\gamma_n y}, \tag{3.1}$$

where $\beta_n = \beta_0 + (2\pi n/a)$; $\gamma_n^2 = \beta_n^2 - k^2$, k is wave number and $y > 0$, whereas the field between the chairs, by means of the waves of a non-homogeneous waveguide, is

$$\psi_2 = \sum_{m=0}^{\infty} A_m ch\alpha_m(y+h)\cos k_m x\,, \tag{3.2}$$

where k_m is obtained from the equation

$$h \operatorname{tg} k_m b + \frac{h}{2} \operatorname{tg} k_m c = 0 \qquad \text{and} \qquad \alpha_m = k_m - k^2.$$

These solutions are related to the chair height level where the functions and their normal derivatives must be equal. At these boundary conditions, an infinite system of equations is obtained:

$$\sum_{n=-\infty}^{\infty} B_n \beta_n \frac{1}{\gamma_n - \alpha_p} = \frac{\varepsilon a \alpha_p A_p}{j[1-(-1)^p e^{j\beta_0 a}]} e^{-\alpha_p h}, \tag{3.3}$$

$$\sum_{n=-\infty}^{\infty} B_n \beta_n \frac{1}{\gamma_n + \alpha_p} = \frac{\varepsilon a \alpha_p A_p}{j[-1(-1)^p e^{j\beta_0 a}]} e^{-\alpha_p h}, \tag{3.4}$$

where $p = 0, 1, 2, ...$, $\varepsilon = 1$ or $1/2$, when $p = 0$, or $p \neq 0$ respectively.

Since the terms of this equation are of a special form, the system determinant may be expressed by means of an infinite product.

When solving these equations, one must first find the dispersion equation for γ_0. For this purpose, we shall accept a number of approximations:

Only the terms with $p = 0$ are left, thus $a_0 = i \times k$. This approximation will be suitable solely for wavelengths exceeding a and $h > a/p$.

In this case the system (3.1) becomes simpler and $B_n \times b_n$ may be expressed through A_0; then the analytical expression of the dispersion equation may be obtained:

$$\frac{\left(1-\frac{\alpha}{\gamma_0}\right)\prod_{m=1}^{N}\left(1-\frac{\alpha_0}{\gamma_m}\right)\left(1-\frac{\alpha_0}{\gamma_m}\right)}{\prod_{p=1}^{2N}\left(1-\frac{\alpha_0}{\alpha_p}\right)} \times \sum_{n=-N}^{N} \frac{\sum_{p=1}^{2N}\left(1-\frac{\gamma_n}{\alpha_p}\right)}{\left(1-\frac{\gamma_n}{\gamma_0}\right)\left(1-\frac{\alpha_0}{\gamma_n}\right)\prod_{m=1}^{N}\left(1-\frac{\gamma_n}{\gamma_m}\right)\left(1-\frac{\gamma_n}{\gamma_m}\right)} = -e^{2ikh}. \tag{3.5}$$

Furthermore, in the case of such approximations, only the terms with $n = 0$ must remain. Finally, the dispersion equation is as follows:

$$\frac{ika}{\pi}\ln 2 - i2\mathrm{arctg}\frac{k}{\gamma_0} - \frac{\gamma_0 a}{\pi}\ln 2 = 2ikh + i\pi. \tag{3.6}$$

It can be seen from this equation that β_0 (obtained from γ_0) has resonances, but in the case of the above approximations, only the frequency of the first resonance is correctly determined. Figure 7 shows the dependence of the resonance frequency f_{rez}, e.g. when $\beta_0 \to \infty$, on the distance between the chairs.

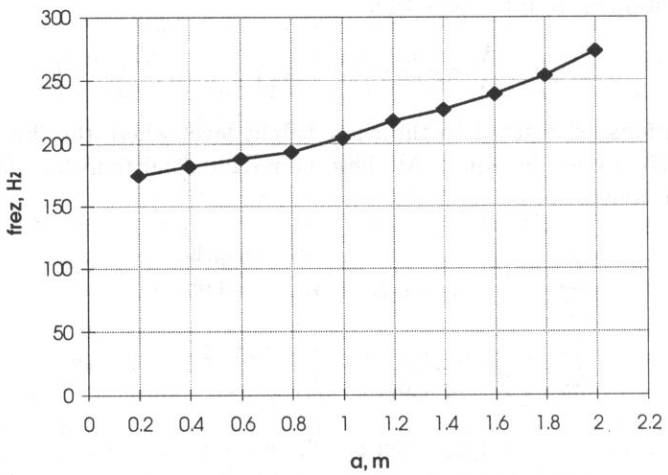

Fig. 7. Dependence of the resonance frequency on the distance between the chairs.

One can see from Fig. 7 that the arrangement of the chairs in the rows may cause a resonance in the low frequency region provided there is an echo. Eliminating the echo leads to the disappearance of the resonance.

4. Conclusions

1. In a small rectangular hall with semi-upholstered chairs arranged in rows, the sound field decay is characterized by pronounced early and late regions. The late decay is determined by the repetitive echoes and the resonances between the chair rows. The resonant frequency obtained from theoretical calculations is close to the measured one.

2. When the hall contains 170 chairs and tapestries on all the four walls, the repetitive echoes and resonances are practically eliminated. The reverberation time undergoes a considerable decrease at frequencies up to 160 Hz.

References

[1] R. MITRA, S.W. LEE, *Analytical techniques in the theory of guided waves*, The Macmillan Company, N.Y., London 1971.

ARCHIVES OF ACOUSTICS
22, 3, 277–295 (1997)

DETECTION AND SIGNAL PROCESSING IN THE ACOUSTIC ECHOLOCATION SYSTEM FOR THE BLIND

R. SALAMON, R. KOWALIK and I. POSTAWKA

Department of Acoustics, Department of Optoelectronics
Gdańsk University of Technology
(80-952 Gdańsk, ul. Narutowicza 11/12)

The paper presents a method of design, the general features and parameters of the acoustic, multibeam echolocation system for the blind which uses an electret microphone array and a digital beamformer with second order sampling. The system in question detects various obstacles that a blind person encounters on his or her way. It also determines the location of obstacles and the presumable shape and gives verbal messages about the situation observed. The paper includes a detailed description of signal processing in the beamformer and the conditions of detecting the observed obstacles. Theoretical and measured beam patterns of the system have been presented as well as the results of detecting and locating obstacles.

1. Introduction

In recent years, thanks to technological achievements, there has been a great deal of interest in designing aids for visually handicapped people. However, up till now only few of them have become commonly available as commercial products. The most significant progress has been made in the accessibility of printed materials, computers and telecommunications systems for the blind. There are several speech output systems for blind computer users which are available on the market in a great number of languages of the world. Current research on screen and print access technology – speech synthesis and text recognition is focused on naturalness, prosody, flexibility and improvement of optical character recognition techniques. Relatively more difficulties have been encountered in the area of travel and navigation aids for the blind. Visually disabled people who travel on their own have two kinds of problems: first "micro" navigation, e.g. walking along clear paths and avoiding obstacles around a known environment, and second – planning a journey to new places and keeping to the planned route. Although a number of navigation aids using optical, infrared and ultrasound sensors have been presented as prototypes, none of them have been commonly accepted, [2, 4, 6]. The main problem lies in the interaction between the system and the blind person, [3, 5]. Those devices use complicated audio signals which send out too much information to the user and obscure the external sounds from the environment. Technologically it is easy to obtain a digital

representation of the surrounding with a miniature camera, however, the extraction of useful information on a safe path or nearby obstacles and then transmission to the user needs implementation of complicated signal processing procedures. That process takes too much time and in spite of the recent progress in signal processing technology and artificial intelligence methods, it cannot be used in real time systems. Infrared information systems have been presented in several places such as the London Underground, Paris and Hamburg Underground. These methods, however, have not become popular as they require the installation of a set of transmitters which is a very costly undertaking [7]. In radar and acoustic systems the image of the scrutinized space is relatively simpler and that is why the obstacles can be detected and signalized in a satisfactory time by a laptop computer. However, radar systems use a harmful microwave radiation which additionally is difficult to process due to its high frequency. Taking into account the restrictions mentioned above, an acoustic echolocation method seems to be a more attractive way of solving the problem of navigation aids for the blind because of its:

- simplicity of emission and detection of acoustic waves,
- small size of the acoustic array,
- low operating frequency,
- harmlessness to the user and environment.

Basing on the data pointed out, a multibeam echolocation system for the blind has been designed [8]. The results of pilot experiments confirmed the correctness of the assumptions and the effectiveness of the design and signal processing methods.

2. General operating features of the device

In line with its purpose, the system should perform the following functions:

- detection of obstacles in front of the blind person, in the road surrounding that he is using,
- determination of the position of the obstacles detected,
- classification of the obstacles,
- analysis of the spatial situation and providing short, verbal messages to the blind user about the recommended direction to follow or to stop.

In echolocation systems the first three of the above functions are called detection, parameter estimation and target classification. The fourth function is not related to acoustics and constitutes a separate problem in the area of image recognition and analysis. That is why it will not be discussed in this paper.

The above functions are realized in a system whose block diagram is shown in Fig. 1. The computer generates periodically every 100 ms discrete sinusoidal pulses at a frequency of 18 kHz and of a rectangular envelope. These pulses are processed in a digital-analog converter into the analog form, amplified in the power amplifier and radiated through a high frequency loudspeaker in a beam of approximately 60° width. Pulse duration takes 1.1 ms which shows that the system's range resolution is about

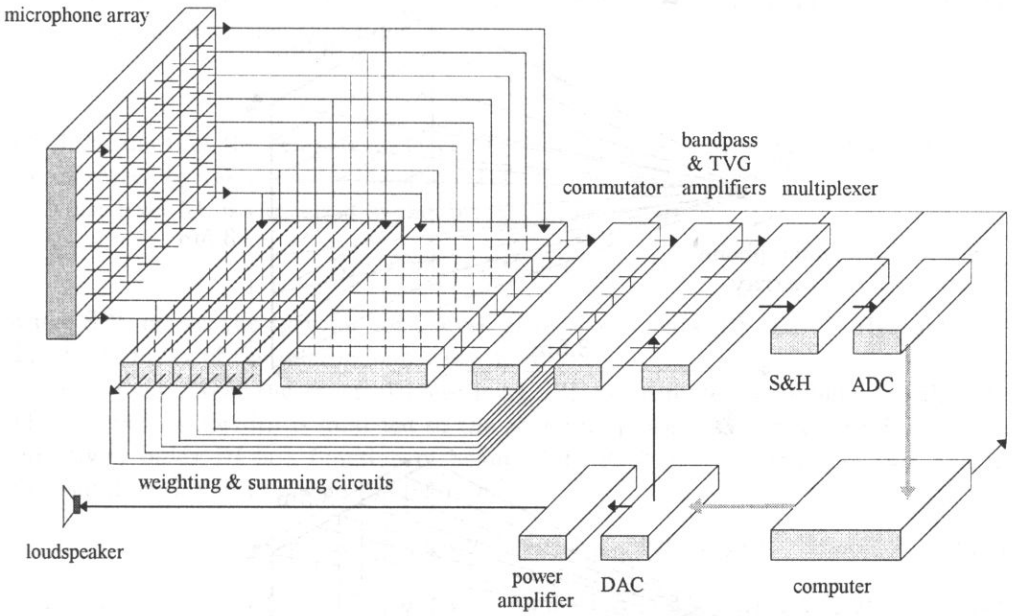

Fig. 1. Block diagram of the echolocation system for the blind.

20 cm([1]). After they are reflected from an obstacle, echo pulses are received by an array of 8×8 electret microphones, then weighted and summed up along eight rows and eight columns. The commutator in one transmission feeds to the eight channel receiver the signals from the eight rows and in the next transmission – the signals from the eight columns. They are amplified, filtered and normalized in the eight channel receiver. Analog echo signals are then successively sampled and fed into the memory of the signal processor. The processor realizes numerically the function of the beamformer which simultaneously produces 7 receiving beams at about 12° width mutually deflected by 9°. They cover the observation area at angular dimensions of about $60° \times 60°$. As a result of the beamformer and commutation set performance in one transmission we get 7 vertical beams and in the next transmission we get 7 horizontal beams located as shown in Fig. 2. The method of beams determining is described comprehensively in Sec. 4.

The digital signals from the 7 beams of the beamformer are transferred to a laptop computer which is used to determine the location and to classify the detected obstacles. The results of the calculations are then analyzed for their possible threat to the blind person. It is only in the case of a coming collision that the synthetizer produces verbal messages which warn the blind individual against a collision or indicate a safe direction of a further route. This method of giving information is preferred by the blind because they have to continuously use their hearing to communicate with the surrounding.

([1]) The range resolution ΔR is theoretically equal $\Delta R = c\tau/2$, where c is the velocity of acoustic wave in air and τ is the pulse duration. For $c = 340\,\mathrm{m/s}$ and $\tau = 1.1\,\mathrm{ms}$ value of the range resolution is 18.7 cm.

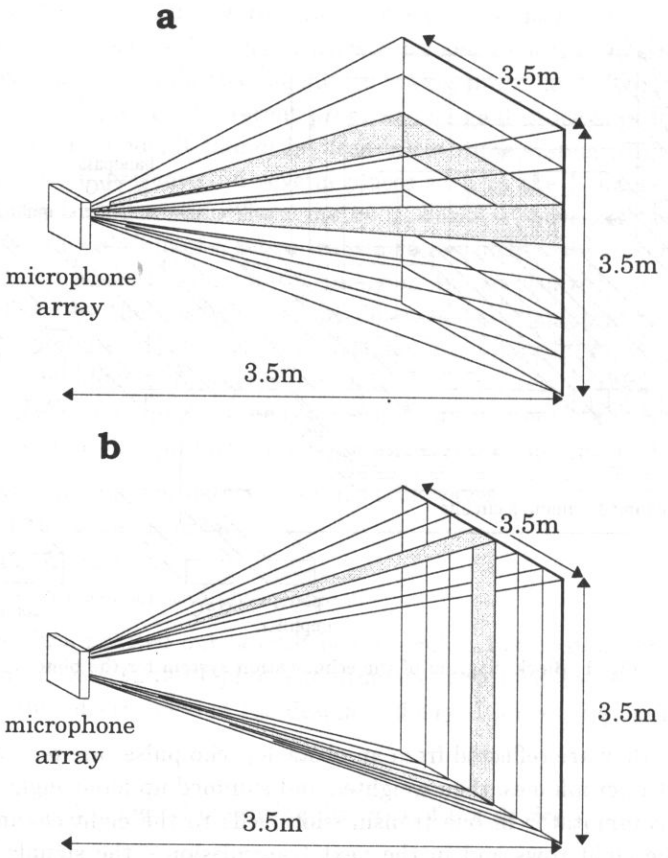

Fig. 2. Receiver beams configuration, a) horizontal configuration, generated by 8 columns of the microphone array, b) vertical configuration, generated by 8 rows of the microphone array.

3. Obstacle detection

The primary condition of an effective performance of the device is to detect the obstacle from a sufficient distance. For a normal speed of walking of a blind person, the distance must be long enough to accommodate the measurements, analyze the situation, give the message and stop or change the direction of movement. Based on the experience collected by the blind and having estimated the pace of the device's operations, it was assumed that the total time necessary to perform these activities is 3.5 s. Given the walking speed of 1 m/s, the necessary range is equal to 3.5 m. Calculations and experimental examinations showed that the target strength of the majority of dangerous obstacles (poles, trees, curbs, chains, people) is not less than TS $= -30$ dB([2]). That is why the system's parameters must be selected in a way that will enable detection of obstacles at target strength TS $= -30$ dB at a distance of 3.5 m. To determine these parameters, a design procedure was adapted, developed by R.J. URICK for underwater acoustics [11].

([2]) Target strength TS $= -30$ dB is exhibited by a perfectly reflected sphere at a diameter of 12 cm.

According to this procedure it is assumed that the following inequality must be fulfilled as the detection condition:

$$\mathrm{EL} \geq \mathrm{NL} + \mathrm{DT}, \tag{3.1}$$

which means that the echo signal level EL([3]) must be at least equal to the noise level NL increased by the detection threshold DT.

Noise level NL is expressed in the formula:

$$\mathrm{NL} = \mathrm{SPL} + 10 \log B/B_0 - \mathrm{DI}, \tag{3.2}$$

where SPL means the spectral noise level, B receiver bandwidth, $B_0 = 1\,\mathrm{Hz}$, and DI – directivity index of the microphone array used.

On a busy street the spectral noise level SPL is estimated at about – 85 dB [12]. The receiver bandwidth is matched to the sounding pulse and amounts to $B = 1\,\mathrm{kHz}$. Directivity index DI is a function of beam width θ, Ψ in the vertical section and in horizontal section in line with the relation:

$$DI \cong -10 \log \sin(\theta/2) - 10 \log \sin(\Psi/2) + 4\mathrm{dB}. \tag{3.3}$$

Substituting $\theta = 12°$ and $\Psi = 60°$ we obtain DI = 17 dB. Formula (3.2) shows that the expected level of acoustic noise in the system is $NL = -72\,\mathrm{dB}$.

Detection threshold DT expresses in decibels the signal to noise ratio at the system's input, necessary to perform detection of the useful signal. Due to the stochastic character of noise, detection is taking place at a certain PD probability. Sporadically we can observe so called false alarms where with no useful signal and a temporary high amplitude of noise it is assumed that a target is there. For the Gaussian noise, probability of detection and probability of a false alarm PFA explicitly define the necessary value of detection threshold DT. With respect to the blind person's safety, the designed system should assume a high value of the detection threshold. On the other hand, a low value of probability of a false alarm will ensure that a blind person will not be unnecessarily bothered by apparent obstacles. In line with this reasoning it was assumed that PD = 98% and PFA = 10^{-5}([4]). For known signal and the Gaussian noise, the assumed values PD and PFA are matched by the detection threshold DT = 15 dB, [9].

The calculations made so far enable the determination of the minimum echo signal level in the system. In line with formula (3.1) the level amounts to EL = −57 dB. Given the microphone sensitivity VR used in the acoustic antenna we can calculate the voltage level UL at the input of the receiver. It is:

$$\mathrm{UL} = \mathrm{EL} + \mathrm{VR}. \tag{3.4}$$

([3]) All dimensions that denote the level are defined as $20 \log(p/p_0)$, where p is the acoustic pressure of the respective signal and $p_0 = 1\,\mathrm{Pa}$.

([4]) Further increase in detection probability is not justified because it increases on its own when the blind person is nearing an obstacle. This is caused by an increase in the amplitudes of the echo and consequently by an increase in the signal to noise ratio. This effect is not observed in respect to false alarm probability. It is constant for a detection threshold set at a specific value. False alarm probability pertains to a time range that is equal to the sounding pulse duration. The value PFA = 10^{-5} in the system in question, means that on the average one false alarm comes up approximately every 8 minutes.

The sensitivity of the electret microphones is equal to 10 mV/Pa, that is VR = −40 dB([5]). The above formula shows that UL = −97 dB which means that the minimum voltage of a useful echo signal is equal to $u = 14\,\mu$V([6]).

The last step in designing the system from the standpoint of detection conditions is to determine the source level SL. This level can be determined by transforming the basic equation of echolocation:

$$\mathrm{EL} = \mathrm{SL} - 2\mathrm{TL} + \mathrm{TS} \tag{3.5}$$

to the following form:

$$\mathrm{SL} = \mathrm{EL} + 2\mathrm{TL} - \mathrm{TS}, \tag{3.6}$$

where the symbol 2TL means transmission loss.

Assuming a spherical model of propagation, transmission loss is calculated from the formula:

$$2\mathrm{TL} = 40 \log R/R_0 + 2\alpha R, \tag{3.7}$$

where range $R = 3.5$ m, $R_0 = 1$ m and α is the absorption coefficient. Given a frequency of 18 kHz, its value is $\alpha \cong 1$ dB/m, [10], and so 2TL ≅ 29 dB.

After substituting the parameters determined earlier of the range equation to formula (3.6) we obtain SL = 2 dB. This source level ensures a loudspeaker radiating an acoustic wave whose acoustic pressure at a 1 m distance from the membrane on the acoustic axis is equal to 1.2 Pa. Electric power of the power amplifier is experimentally set at a value where the acoustic pressure of the sounding signal is equal to the above conditions.

Formulas (3.5) and (3.7) show that when a blind person is nearing an obstacle at the same time echo signal level increases. The amplitude of the echo signal is not just a function of target strength (the size of the obstacle) which makes analysis of the situation difficult. In order to reduce this negative effect, the receiver uses time varied gain (TVG). The echo level at the output of the TVG is expressed in the general formula:

$$\mathrm{EL}_{\mathrm{TVG}} = \mathrm{SL} + \mathrm{TS} - 2\mathrm{TL} + K, \tag{3.8}$$

where K is the variable in time function of amplification, selected for the purpose of a complete or partial compensation of transmission loss and a possible change of target strength together with the distance. The system uses time varied gain which realizes the function:

$$\begin{aligned} K &= -\infty && \text{for} \quad R \leq R_1 \quad \text{and} \quad R > R_M\,, \\ K &= 20 \log R/R_1 + 2\alpha R + K_0 && \text{for} \quad R_1 < R \leq R_M\,, \end{aligned} \tag{3.9}$$

where $R_1 = 0.5$ m is the minimal distance of observation, $R_M = 3.5$ m is the system range, and K_0 is the constant receiver gain([7]). Given this gain function the echo level

([5]) Voltage response VR = $20 \log[(u/u_0)(p_0/p)]$, where $u_0 = 1$ V, $p_0 = 1$ Pa, u = voltage at the output of the microphone, p – acoustic wave pressure falling on the microphone. Voltage level UL = $20 \log u/u_0$.

([6]) It should be noted that rms voltage of acoustic noise at the output of the microphone is greater by DI − DT = 2 dB (amounts to about 18 μV) because the reduction of noise happens only at the output of the beamformer. This does not pertain to the electric noise because for this noise, an improvement of the noise ratio at the output of the beamformer amounts only to about $\sqrt{n}$-th times (n – effective number of microphones considering weighting factors). For $n = 16$ rms voltage of electric noise at the output of the microphone should not exceed 10 μV at detection threshold DT = 15 dB and absence of acoustic noise. To ensure acoustic noise dominance in the system, rms voltage of electric noise should be 2 to 3 times lower.

([7]) The TVG gain changes in the function of time according to the formula: $K(t) = k_0(t/t_1)10^{\alpha ct/20}$, where $k_0 = 10^K$ and $t_1 = 2R_1/c$.

in the range of distances $R_1 < R \leq R_M$ is described with the following formula:

$$\mathrm{EL_{TVG}} = \mathrm{SL} + \mathrm{TS} - 20\log R/R_1 + K_0 - 12\,\mathrm{dB}. \tag{3.10}$$

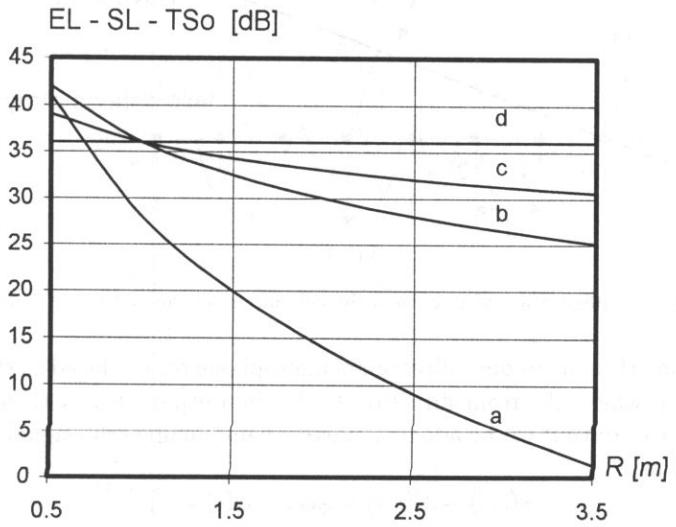

Fig. 3. Changes of the echo level EL in the function of the distance normalized in relation to the source level SL and the target strength coefficient $\mathrm{TS_0}$. a) $\mathrm{TS_0}$ = const, no TVG, b) $\mathrm{TS_0}$ = const, TVG on c) $\mathrm{TS} = \mathrm{TS_0} + 10\log R/R_0$, TVG on, d) $\mathrm{TS} = \mathrm{TS_0} + 20\log R/R_0$, TVG on.

Figure 3 shows the changes of echo level for a case of a constant target strength and target strengths described using the relations $\mathrm{TS} = \mathrm{TS_0} + 10\log R/R_0$ (poles, tress) and $\mathrm{TS} = \mathrm{TS_0} + 20\log R/R_0$ (large surfaces, walls). As the presented charts show for the most negative and practically rare case of an object of a constant target strength, the dynamics of echo signal decreased from 40 dB for the system without TVG (formula (3.7)) to 17 dB with the TVG system. The system in question used linear gain control in the receiver and absorption loss is compensated numerically in the computer.

4. The beamformer principle

The above principle of the device shows that in order to identify an obstacle it is necessary to generate seven mutually deflected receiver beams. These beams are generated in the beamformer that cooperates with the microphone array. The method of beam generation is identical for vertical deflection and horizontal deflection. For vertical deflection the signals are summed and weighted in each of the eight rows of the microphone array. As a result we obtain 8 independent signals from eight sources that form a linear column array. For vertical deflection as a result of the commutator's operations the situation is reverse: signals from each of the eight columns of the array are summed up and in the end effect we have at our disposal eight independent signals from a linear

row array. The position of the sources in both linear arrays is identical and the placement of the sources is shown in Fig. 4.

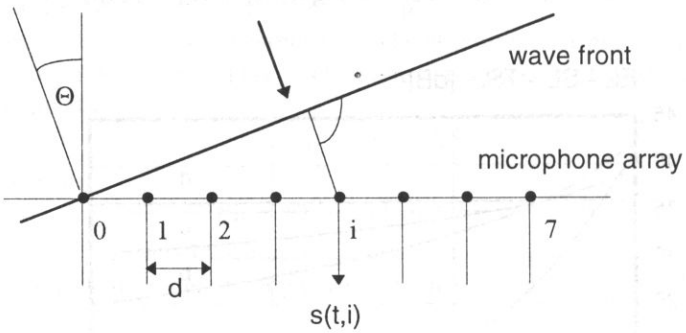

Fig. 4. Configuration of sources in the column or row array ($d = 11.5$ mm).

Let us assume that on an omnidirectional microphone array placed as shown in Fig. 4, a plane acoustic wave falls from direction θ. At the output of an i-th microphone (in practice at the i-th output of the adder) a narrow band analog echo signal appears which can be written as:

$$s(t,i) = S(t,i)\sin[\omega_0 t - \alpha(i) + \varphi], \tag{4.1}$$

where $S(t,i)$ is the slow changing envelope of echo signal, $\omega_0 = 2\pi f_0$ is the angular frequency of sounding signal ($f_0 = 18$ kHz), φ is the phase of carrier signal, and $\alpha(i)$ is phase shift resulting from the direction of the acoustic wave incidence. For an incidence angle of θ the phase shift is equal to:

$$\alpha(i) = \omega_0(id/c)\sin(\theta), \qquad i = 0, 1, ..., I-1, \tag{4.2}$$

where c is the velocity of the acoustic wave in the air, d is the distance between the neighboring microphones, and I – the number of microphones in a row or a column ($I = 8$).

In the device in question a delay-sum beamformer was used with second order sampling. The first stage of the signal processing in this beamformer was a special sampling which for discrete signals – as will be shown later – is the equivalent of quadrature detection. The idea of second order sampling is to cyclically collect two samples of each signal at a time interval equal to 1/4 of the period of carrier signal. The principle of sampling is illustrated in Fig. 5.

As the result of sampling we obtain two sequences of samples that consist of N segments with I samples in each segment. As is shown in Fig. 5, the values of the samples in both sequences can be written as:

$$\begin{aligned} s_s(i,n) &= S\left[\frac{T}{2}(nI+i)\right]\sin\left[\omega_0\frac{T}{2}(nI+i)+\alpha(i)+\varphi\right], \\ s_c(i,n) &= S\left[\frac{T}{2}(nI+i)+\frac{T}{4}\right]\sin\left\{\omega_0\left[\frac{T}{2}(nI+i)+\frac{T}{4}\right]+\alpha(i)+\varphi\right\}, \end{aligned} \tag{4.3}$$

where $T = 1/f_0$ is the period of the sounding signal.

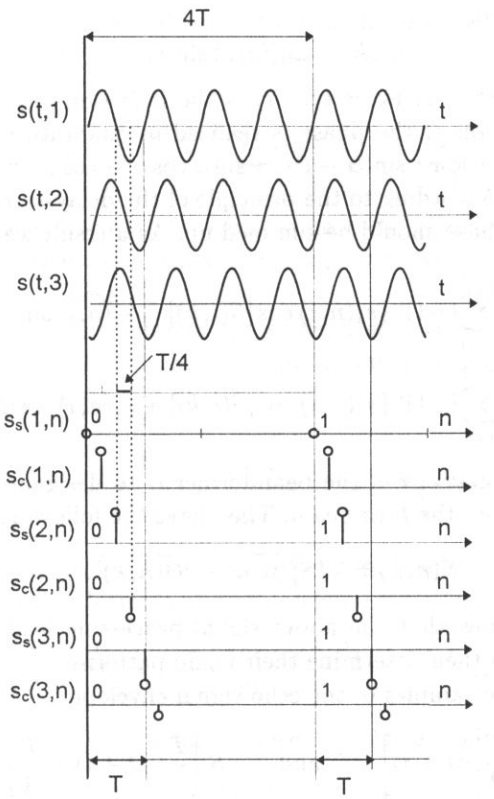

Fig. 5. Second order sampling of echo signals realizing quadrature detection ($T = 1/f_0 = 55.5\,\mu s$).

After applying simple trigonometric identities, the expressions (4.3) are transformed to the following form:

$$\begin{aligned} s_s(i,n) &= (-1)^i S\left[\frac{T}{2}(nI+i)\right]\sin[\alpha(i)+\varphi], \\ s_c(i,n) &= (-1)^i S\left[\frac{T}{2}(nI+i)+\frac{T}{4}\right]\cos[\alpha(i)+\varphi]. \end{aligned} \tag{4.4}$$

The above formulas show that as a result of second order sampling we obtain from each i-th microphone two sequences of samples of echo signal envelopes multiplied by sinus and cosine of the phase shift. That is why they are in fact samples of quadrature components of echo signal. The samples of the i-th sequence appear in time intervals $IT/2$ which must be smaller than the sampling period that results from Nyquist's theorem: $IT/2 < 1/2B$ so $I < f_0/B$. In the system in question this condition is met with a surplus because $I = 8$, and $f_0/B = 18$.

In order to generate a deflected beam, the phases of the received signals should be changed so that in each i-th channel the phase of the signal received from the direction of the beam axis is identical. This can be achieved by subtracting from phase $\alpha(i) + \varphi$

phase$\beta(i)$ that is equal to:

$$\beta(i,k) = \omega_0(id/c)\sin(\theta_k), \tag{4.5}$$

where $\theta_k = -27^\circ + \Delta\theta(k-1)$ $(k = 1,...,7)$ is the defection angle of the k-th axis of the beam. The subtraction of the phase is realized in quadrature detection using the known trigonometric relations: $\sin(\alpha-\beta) = \sin\alpha\cos\beta - \cos\alpha\sin\beta$ and $\cos(\alpha-\beta) = \cos\alpha\cos\beta + \sin\alpha\sin\beta$. According to the principle of the delay-sum beamformer signals that are shifted in the phase should be summed up. As a result we obtain:

$$\begin{aligned} S_s(n,k) &= \sum_{i=0}^{I-1}(-1)^i\{s_s(n,i)\cos[\beta(i,k)] - s_c(n,i)\sin[\beta(i,k)]\}, \\ S_c(n,k) &= \sum_{i=0}^{I-1}(-1)^i\{s_c(n,i)\cos[\beta(i,k)] + s_s(n,i)\sin[\beta(i,k)]\}. \end{aligned} \tag{4.6}$$

The last step of calculations in the beamformer is to designate the samples of the echo envelope coming from the k-th beam. They have the following form:

$$S(n,k) = \sqrt{S_s^2(n,k) + S_c^2(n,k)}\,. \tag{4.7}$$

Now we are going to show that the above signal processing leads to a generation of deflected beams. We will then determine their beam patterns.

Let us notice that the samples of the echo signal envelope

$$S\left[\frac{T}{2}(nI+i)\right] \qquad \text{and} \qquad S\left[\frac{T}{2}(nI+i)+\frac{T}{4}\right]$$

are practically equal because given the narrow envelope spectrum the changes of its temporary values cannot happen all too quickly. In line with this reasoning a significant error is avoided by assuming that

$$S\left[\frac{T}{2}(nI+i)\right] \cong S\left(\frac{T}{2}nI\right),$$

which means that within one cycle of sampling, the envelope assumes an almost constant value. Given these assumptions, the relations (4.6) are reduced to the form:

$$\begin{aligned} S_s(n,k) &= S\left(\frac{T}{2}nI\right)\sum_{i=0}^{I-1}\sin[\alpha(i,k) - \beta(i,k) + \varphi] \\ &= S\left(\frac{T}{2}nI\right)\sum_{i=0}^{I-1}\sin[\omega_0(id/c)(\sin\theta - \sin\theta_k) + \varphi], \\ S_c(n,k) &= S\left(\frac{T}{2}nI\right)\sum_{i=0}^{I-1}\cos[\alpha(i,k) - \beta(i,k) + \varphi] \\ &= S\left(\frac{T}{2}nI\right)\sum_{i=0}^{I-1}\cos[\omega_0(id/c)(\sin\theta - \sin\theta_k) + \varphi]. \end{aligned} \tag{4.8}$$

After substituting the above relations to formula (4.7) and after some elementary transformations, we obtain:

$$S(n,k) = S\left(\frac{T}{2}nI\right)\sqrt{\left[\sum_{i=0}^{I-1}\sin(ix)\right]^2 + \left[\sum_{i=0}^{I-1}\cos(ix)\right]^2}, \tag{4.9}$$

where $x = \omega_0(d/c)(\sin\theta - \sin\theta_k)$. As is visible now, the effect of the operations of data using formula (4.7) is that the results of the calculations become independent of the unknown and accidental phase φ.

In order to determine the sums of the series from formula (4.9) we substitute the trigonometric functions with complex exponential functions and after algebraic operations, we obtain:

$$S(n,k) = S\left(\frac{T}{2}nI\right)\sqrt{\sum_{i=0}^{I-1}\exp(jix)\sum_{i=0}^{I-1}\exp(-jix)}\,. \tag{4.10}$$

The sums in the above formula are the sums of geometric series. After they are computed using the known formula and after some reductions, we obtain:

$$S(n,k) = S\left(\frac{T}{2}nI\right)\frac{\exp(jIx/2) - \exp(-jIx/2)}{\exp(jx) - \exp(-jx)} = S\left(\frac{T}{2}nI\right)\frac{\sin(Ix/2)}{\sin(x/2)}\,. \tag{4.11}$$

After substituting $x = \omega_0(d/c)(\sin\theta - \sin\theta_k)$ we have finally:

$$S(n,k) = S\left(\frac{T}{2}nI\right)\frac{\sin[(\pi Id/\lambda)(\sin\theta - \sin\theta_k)]}{\sin[(\pi d/\lambda)(\sin\theta - \sin\theta_k)]} = S\left(\frac{T}{2}nI\right)b_k(\theta), \tag{4.12}$$

where $\lambda = c/f_0$ is the length of the acoustic wave in the air and $b_k(\theta)$ is the beam pattern.

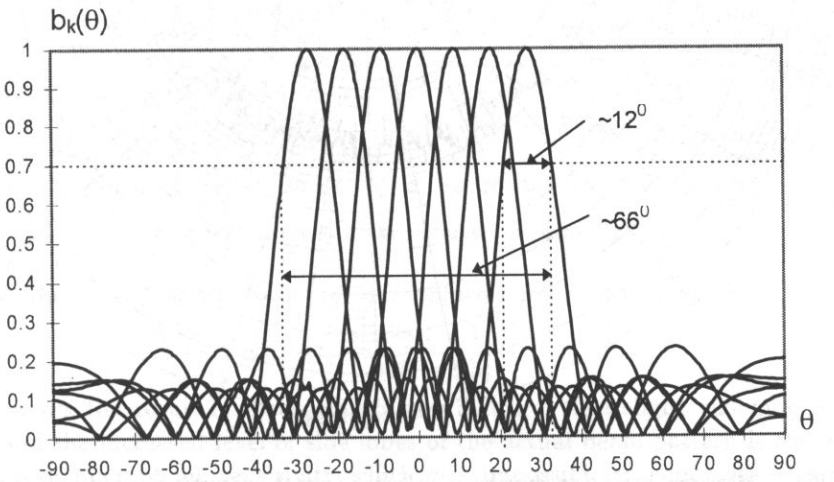

Fig. 6. Configuration of 7 narrow receiver beams.

As is known, the fraction expression seen in formula (4.12) describes beam pattern $b_k(\theta)$ of the linear array consisting of I omnidirectional microphones placed at a distance d from each other. The beam axis is deflected by the assumed angle θ_k which shows that the above described beamformer with second order sampling correctly performs its function. Figure 6 shows the calculated patterns of the microphone array used in the device. As a comparison, Fig. 7 illustrates a measured beam of the device deflected to the right by $\theta_6 = -27° + 5 \cdot 9° = 18°$. As the chart shows, the beam width is slightly greater than the width determined analytically which is due to the measurement errors and the technical imperfection of the beamformer's performance.

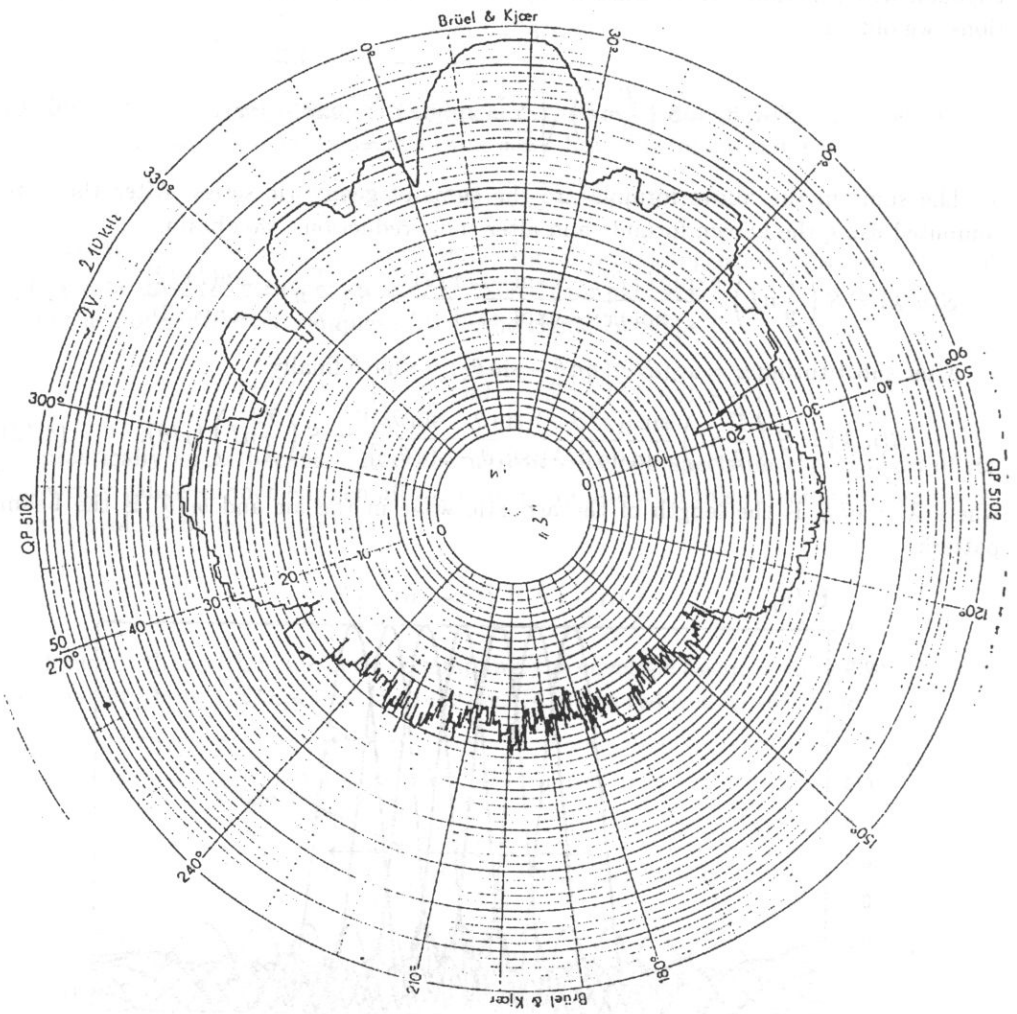

Fig. 7. Measured narrow receiver beam deflected from the acoustic axis of the microphone array by 18°.

5. Method of increasing the beam width

The majority of echolocation systems strive to reduce the level of side lobes the side effect of which is an increased beam width. In the device in question, the technique used to reduce the level of side lobes was applied in order to increase the beam width and to cause it to adopt the demanded shape. According to the adopted method of field searching, beam width in both sections must be significantly differentiated and amount to about $12° \times 60°$. Width of $12°$ is provided by a linear set of microphones cooperating with the beamformer. In order to obtain a width of $60°$ in the second section a strong amplitude of echo signals was used with reversing of the phase. A function of the type $\sin x/x$ was selected as the weighting distribution. This function ensures a significant increase in the beam width and caused it to assume a shape close to a rectangle. Beam patterns of a linear series of 8 microphones with amplitude weighting is described by the formula:

$$b(\theta) = \left[\sum_{i=0}^{7} w(i) e^{j\frac{\omega_0}{c} d(i-3.5)\sin\theta}\right] \Big/ \left[\sum_{i=0}^{7} w(i)\right], \tag{5.1}$$

where $w(i)$ is a weighting function.

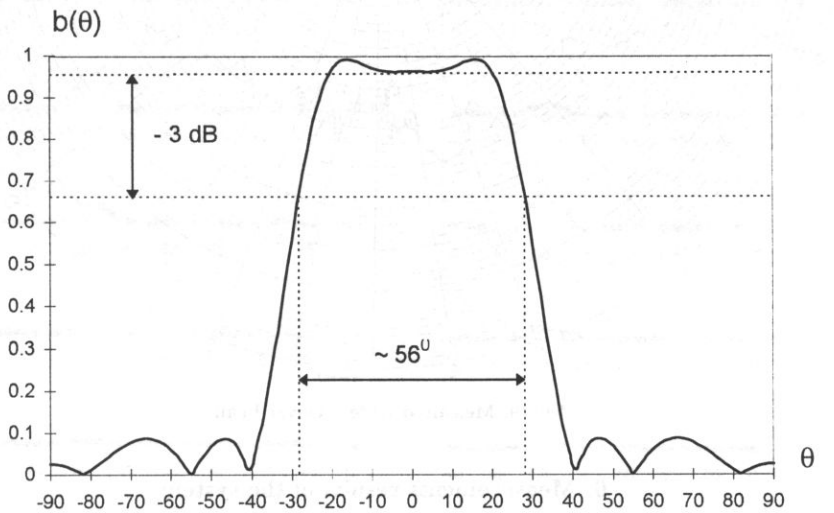

Fig. 8. Wide receiver beam calculated numerically.

Figure 8 illustrates beam pattern $b(q)$ determined numerically in which

$$w(i) = \frac{\sin[1.94(i-3.5)]}{1.94(i-3.5)}$$

and Fig. 9 shows the result of measuring of this pattern. The slight widening of the main lobe and the increased level of side lobes of the actual beam pattern is the effect of dispersion of microphone sensitivity which was impossible to compensate using a correction of the weighting factors.

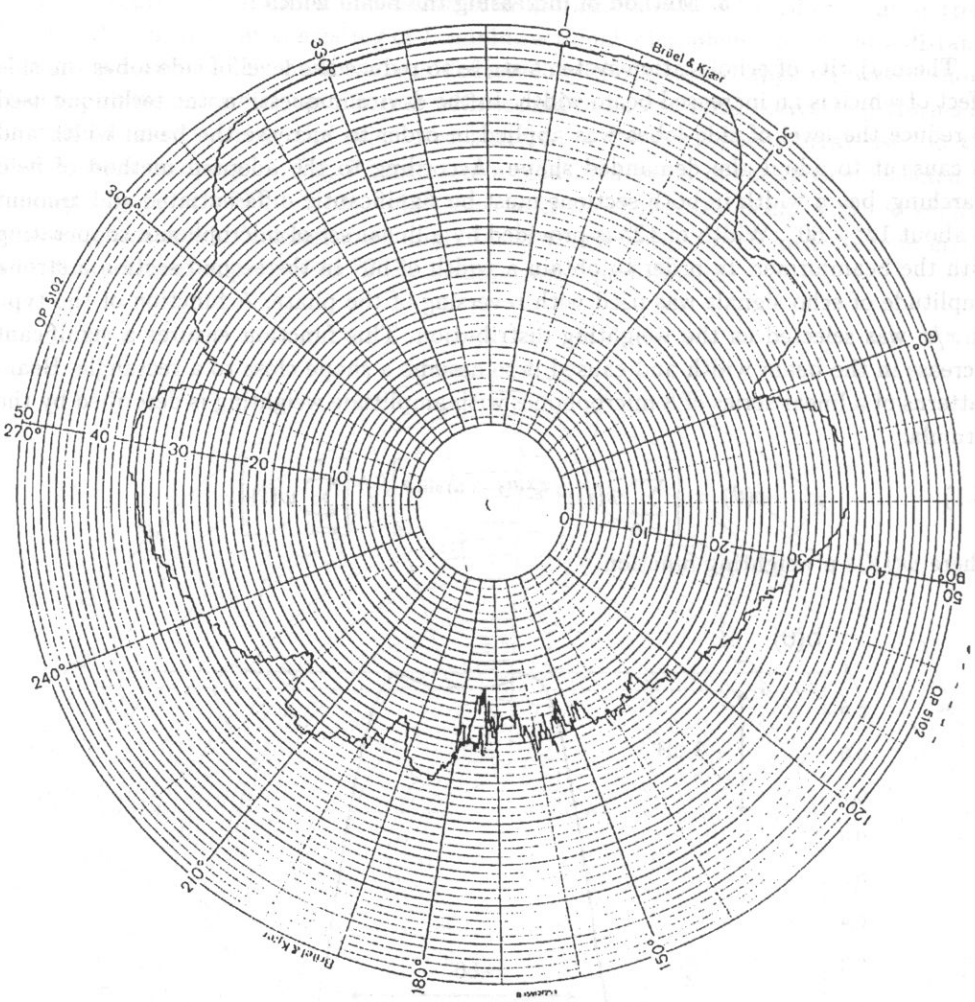

Fig. 9. Measured wide receiver beam.

6. Measurements results of the system

The constructed and launched system was then examined. The purpose of the examination was to verify the applied method of signal processing and the adopted design assumptions. All beam patterns of deflected narrow beams were measured as well as the patterns of non-deflected wide beams. It was found that the deflection angles are in line with the design assumptions, and the beam widths – despite a slight widening – fit into the permissible tolerances. Beam patterns of the loudspeaker covers with just a slight surplus the angular observation sector at a width of 60°. The electric power of the signal was selected in a way that caused the acoustic pressure at a distance of 1 m from the loudspeaker on its acoustic axis to be 1.2 Pa which matches the assumed value of the

source level SL = 2 dB. In order to determine the range of the system, an observation was made of the echo signals from a sphere at a diameter of 12 cm (TS = −30 dB). In a quiet, closed laboratory room, the echo from the sphere was clearly visible in the background of noises when the sphere was on the axis of each of the beams 3.5 m away from the microphone array. The assumed range of the system was accomplished even though the electric noise level adopted in design calculations was exceeded. This voltage, related to the output of the microphone, amounted to 30 μV and dominated the voltage of acoustic noises. The echo signal from the sphere was also masked with a noise, however, at the input to the system its amplitude exceeded at least twice the noise level. The result of the increase in noise level is therefore a reduction of the detection threshold DT from 15 dB to 6 dB. This defect will be removed in the system's prototype by a more careful separation of analog and digital systems (use of transoptors).

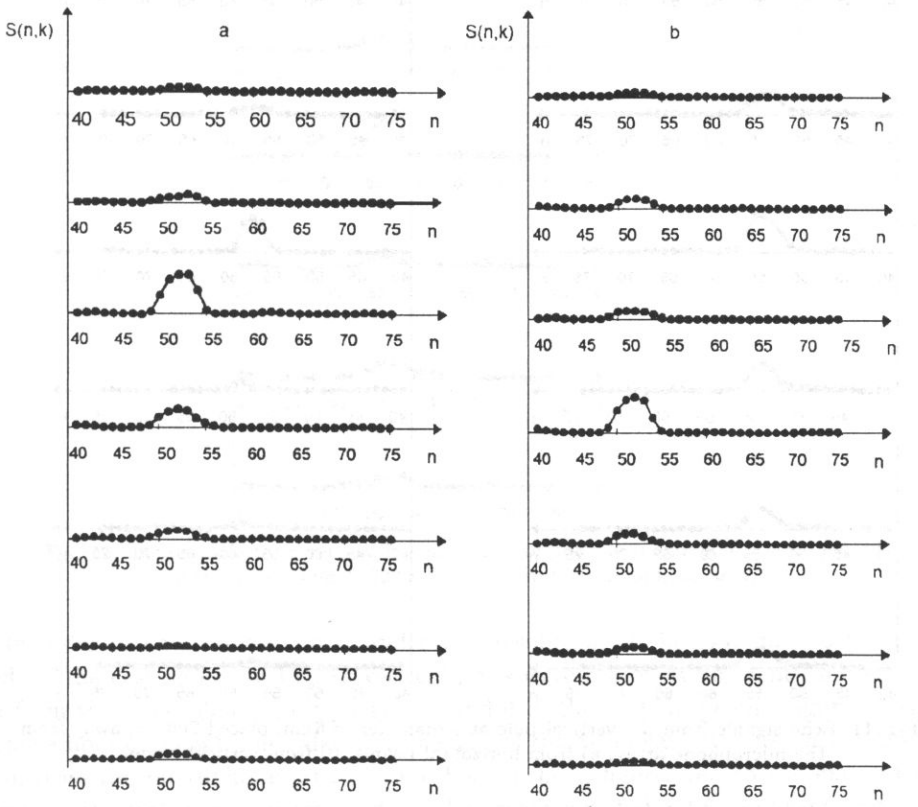

Fig. 10. Echo signals from a sphere at a diameter of 12 cm placed 200 cm away from the microphone array: a) from horizontal beams, b) from vertical beams.

Further measurements pertained to the system's ability to define the location and identify obstacles. Examples of measurement results are shown in the consecutive figures. Figure 10 shows the echo from a sphere at a diameter of 12 cm placed 2 m away from the microphone array. The sphere was hanged at the point where the vertical beam 3 and

horizontal beam 4 intersect. As was expected in the respective beams clear echo signals were observed, much bigger than the background interference and the small echoes in the other beams caused by the side lobes of beam patterns.

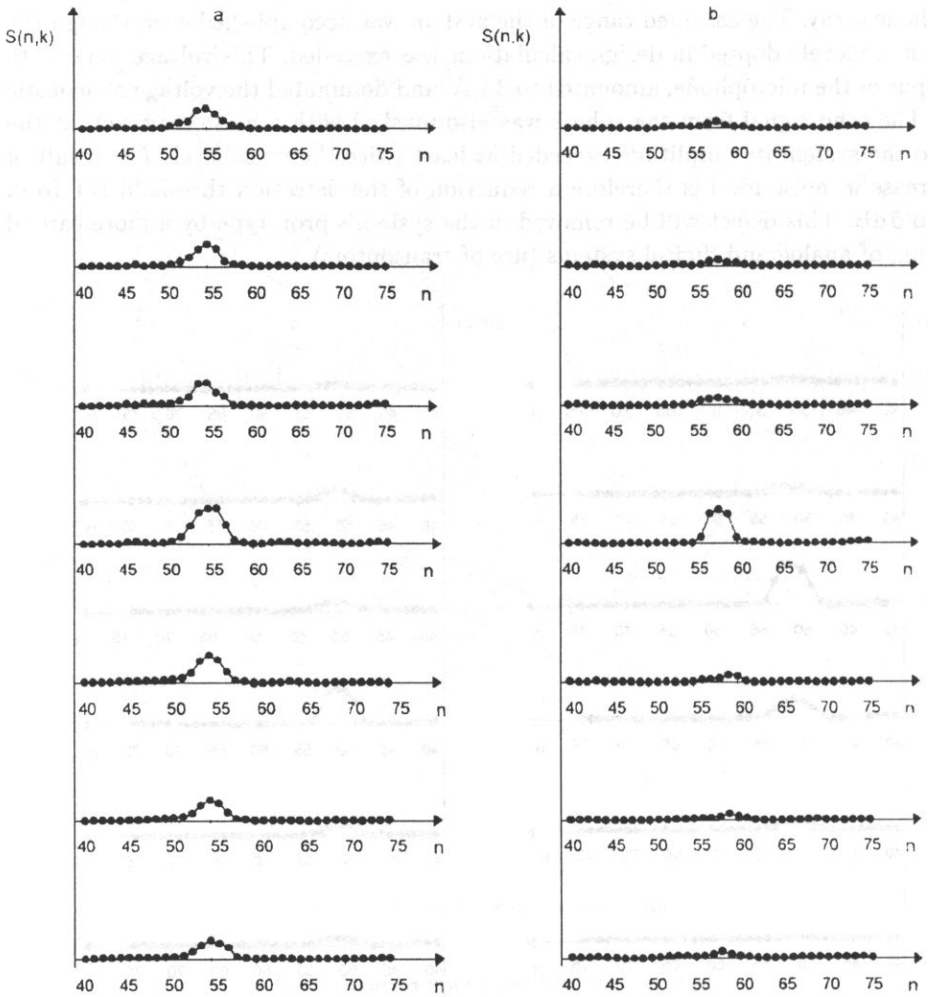

Fig. 11. Echo signals from the vertical pole at a diameter of 6 cm, placed 200 cm, away from the microphone array: a) from horizontal beams, b) from vertical beams.

The idea of the next experiment was to place a vertical or a horizontal pole of a 6 cm diameter in the observation field of the system. Figure 11 shows visible echo signals from the pole placed vertically in the axis 4 of the vertical beam. In line with the principle of the system's performance, a strong echo appeared in 4-th vertical beam and in all horizontal beams, [8]. The highest amplitude was exhibited by the echo in 4-th central horizontal beam because the direction of incidence of the acoustic wave on the pole is at that time perpendicular. The smallest echo amplitudes are observed in extreme end

beams (the first and seventh) because the wave in these beams falls on the pole at an angle of about 30°. Analysis of the distribution of the echoes in the particular beams allows both a determination of the object's location ($R \approx 2\,\mathrm{m}$, $\theta \approx -18°$), as well as its identification (vertical pole).

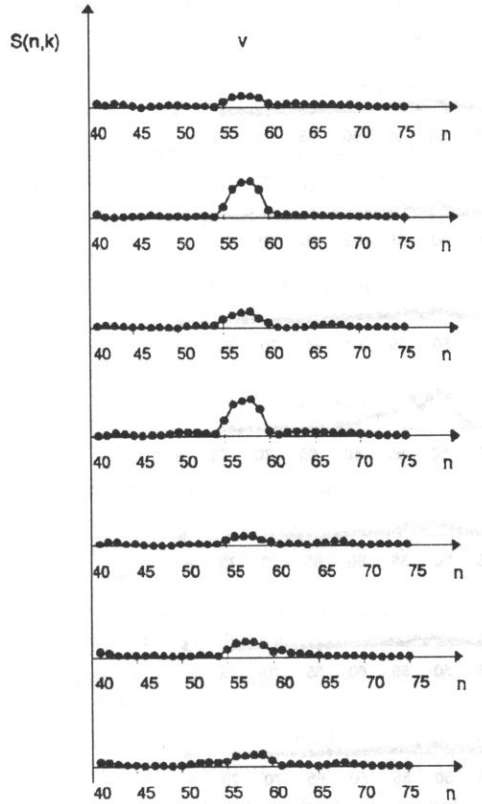

Fig. 12. Echo signals from vertical beams from two poles at a diameter of 6 cm placed on the axes 2 and 4, 220 cm away from the microphone array.

In order to determine angular and range resolution of the system, two poles were used. In the case shown in Fig. 12 vertical poles were placed at an identical distance of 2 m from the microphone array in axes 2 and 4 of the vertical beam. Figure 13 shows visible echoes from two poles placed in the axis of the 4-th beam at a distance of 2 m and 2.2 m from the microphone array. The echoes in both figures match the expectations. Therefore the system has an assumed angular resolution of about 9° and range resolution of about 20 cm([8]). Despite the fact that the design assumptions were met, the system is not fully explicit upon determining the number of observed objects and their location. As an example, when a single pole is placed at a point of the beams' intersection, the echo signals are equal in both beams. The same picture is formed when in the axes of the

([8]) The range resolution ΔR on the display is equal $\Delta R = c\Delta\tau/2$ (see footnote 1). Here $\Delta\tau$ signifies the time between well distinguishable maxima of adjacent received signals. Figure 13 shows that $\Delta\tau \cong 5T_s$, where $T_s = 4T$ is the sampling time in the system. For $T = 55.5\,\mu\mathrm{s}$ we obtain $\Delta R \cong 19\,\mathrm{cm}$.

neighboring beams two identical poles are placed. This lack of identical identifications is eliminated when the microphone array is moving (the blind person) because as we near the objects they appear in other beams. At the same time, for angular resolution, the spatial resolution of the system improves.

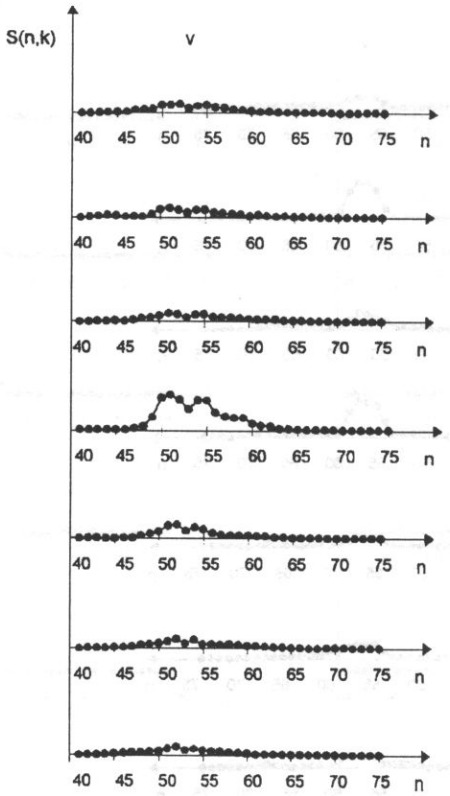

Fig. 13. Echo signals from vertical beams from two poles at a diameter of 6 cm placed at 20 cm gaps in the 4-th beam.

7. Conclusions

The acoustic echolocation system was built following the principles presented in the paper and has technical and operating parameters that enable detection, positioning and identification of obstacles that are a threat to the blind person. Currently it is being used for measurements in the field. The collected measurement data will be used to verify the algorithms that analyze the pictures observed and generate adequate verbal messages. The algorithms developed so far define the position of simple obstacles (poles, walls) that are placed in uncomplicated configurations. Verbal messages only tell the direction of the obstacles discovered. If the results of the studies are positive, further research should concentrate on reducing the size of the device and its full automation.

What is especially necessary is replacing the laptop with a specialized processor. It is estimated that given the current state of technology it is possible to fit the entire device (including the battery) to the size of a medium size book. Parallel research is being carried out on the use of a satellite navigation system which – by cooperating with an acoustic echolocation system – would facilitate walking in a vast, unknown area.

Acknowledgments

The authors wish to thank the design engineers of the system – Andrzej JEDEL, Zawisza OSTROWSKI, Waldemar LIS, Stanisław KWAŚNIEWSKI and other employees of the Department of Acoustics of the Gdańsk University of Technology who participated in the design, building and testing.

This work was supported by the grant no. 4 1078 91 01 of Polish State Committee for Scientific Research.

References

[1] P. BLENKHORN, D.G. EVENS, S. PETTITT, *An investigation of global positioning system (GPS) technology for disabled people*, Lecture Notes in Computer Science, **860**, 556–562 (1994).

[2] J. BORENSTEIN, Y. KOREN, *The Nave-Belt- A computerized Multi-sensor travel aid for active guidance of the blind*, CSUN's 5th Annual Conf. on Technology and Persons with Disabilities, pp. 125–132, Los Angeles 1990.

[3] E. DE BAETSELIER, G. DE MEY, *A thick film resistor circuit as prosthesis for blind persons*, Proc. of the 9th European Hybrid Microelectronic Conference, pp. 269–276, (1993).

[4] J.M. GILL, *An orientation and navigation system for blind pedestrian*, Royal National Institute for the Blind, London 1996.

[5] R. KOWALIK, I. POSTAWKA, *Some aspects of reduction of information in sodars for the blind*, Proc. of the XIth Symposium on Hydroacoustics, pp. 211–214, Gdynia 1994.

[6] S.P. LEVINE, D.A. BELL, Y. KOREN, *Nav-Chair: an example of a shared-control system for assistive technologies*, Lectures Notes in Computer Science, **860**, 136–143 (1994).

[7] P. MAYER, M. BUSBOOM, A. FLAMM, W.L. ZAGLER, *I.R.I.S – A Multilingual Infrared orientation System for the Visually Impaired*, Proc of the 3rd Int. Conf. Computers for Handicapped Persons, pp. 344–352, Vienna, 1992.

[8] R. SALAMON, J. MARSZAL, A. RAGANOWICZ, *Multibeam echolocation system for the blind*, Proc. of the XIth Symposium on Hydroacoustics, pp. 267–274, Gdynia (1994).

[9] W.S. BURDIC, *Underwater Acoustic System Analysis*, Prentice-Hall, Englewood Cliffs, NJ 1984, p. 398.

[10] H. KUTTRUFF, PHYSIK UND TEDCHNIK DES ULTRASCHALLS, S. Hirzel Verlag, Stuttgart, 1988, p. 199.

[11] R.J. URICK, *Principles of Underwater Sound for Engineers*, 2nd ed. McGraw-Hill Book Company, New York 1975.

[12] Z. ŻYSZKOWSKI, *Principles of Electroacoustics* [in Polish], WNT, Warszawa 1966, p. 332.

ARCHIVES OF ACOUSTICS
22, 3, 297–306 (1997)

TOTAL SCATTERING CROSS-SECTION OF A NONDEFORMABLE SPHERE PARTIALLY INSONIFIED AT A CIRCULAR ANNULAR SPOT

O. PIDDUBNIAK

Pidstrygach Institute of Applied Problems in Mechanics and Mathematics,
National Academy of Sciences of Ukraine
(L'viv, Naukova str., 3-B 290601 Ukraine)

The axisymmetric problem of scattering of a finite sound beam with an annular cross-section by an acoustically soft or immovable rigid sphere immersed in a fluid medium is considered. The pressure in the incident quasi-plane wave is represented in terms of the partial impact parameters by the superposition of the spherical harmonics with the Lorentz multipole resonance distribution. The analysis of the total scattering cross-section vs frequency and wave beam parameters is performed. It is shown that a high-resolution of the total scattering cross-section resonances corresponding to the Franz creeping waves is achieved when the base rays of the incident wave are grazed on the sphere and the beam is narrowing. The particularities of these resonances are considered for the case of soft and rigid spheres.

1. Introduction

The problem of interaction of the sound waves with spherical objects in a liquid has been considered by many investigators for a long time. Although the formal solution of the corresponding mathematical problem is relatively simple, its interpretation meets with some difficulties caused by the complexity of the physical phenomena of the acoustic scattering process (see, e.g. [3, 4]). It is known that the structure of the echo-signal from a deformable solid sphere is formed by the geometrical waves of the reflection and transmission as well as by the reradiated diffractive (surface and creeping) waves excited when the sound rays incident on the obstacle's surface at critical angles or grazely. The isolation from echoes or others contributions can be made using, for example, the resolution property of the angular spectra of the incident wave that is peculiar for finite wave beams [9, 15]. Thus, insonifying nondeformable spheres or circular cylinders by well collimated and centrally incidented bounded acoustic beams, the differential cross-sections vs circular frequency and the beam width were studied [6, 7, 13]. In particular, differences between the sonar cross-sections for the acoustically soft and rigid objects were found [13]. It was shown that the structure of those cross-sections are formed by a superposition of specularly reflected waves and of the waves reradiated by the edge points of the sound spot on the scattering surface as well as of the Franz

creeping waves. In order to investigate the spectral properties of the diffracted waves of the any type in a "clear" form, it is necessary to concentrate the incident sound beam in the neighbourhood of the critical point of wave excitation on the scatterer's surface. Then the contribution of this wave in the total echo will be most intensive. Hence, in several experiments an elective reradiation of the surface acoustic waves of Rayleigh and Lamb types was observed when a finite sound beam incidents on solid and hollow elastic circular cylinders [2, 9, 18], or of circumferential waves of the Franz and Stoneley type when a solid cylinder is insonified almost grazely by a narrow beam [9, 17]. Analogously, in optics rainbow and glory were observed by oblique illumination of a water droplet by a laser beam [5], however the explanation of these phenomena presented most extensively by H. NUSSENZWEIG [10, 11] was carried out utilizing the plane wave theory neglecting the finiteness of the wave beam dimensions.

In this paper we propose a method based on the selection of the Franz creeping wave by means of a sound beam with a ring cross-section. Note that using of an annular acoustic beam makes it possible to obtain a non-specular reflection from an elastic sphere [12, 14] that was first established experimentally by S. SASAKI [6] when an entire ultrasonic beam was directed on a plane water-metal interface. Note also that in [12, 14] the pressure distribution across the beam section was assumed step-wise that did not permit to describe the scattering of the sound beam incidented tangentially on the sphere. This demerit is removed by the introduction of an annular wave beam with modal Lorentz cross-section distribution of the acoustic pressure amplitudes.

2. Solution of the problem

Let us assume in an ideal (nonviscous and nonheat-conducting) compressible fluid an acoustically impenetrable (soft or immovable rigid) sphere of radius a, the centre of which is simultaneously the origin of the spherical coordinates r, θ, φ. Suppose that a harmonic sound wave (with time dependence of $e^{-i\omega t}$, where ω is the circular frequency and t is the time) excited by a keen-directive transducer into the direction $\theta = 0$ incidents on the sphere. Then the acoustic pressure in the incident wave beam may be described as follows:

$$p_{\mathrm{inc}}(R, \psi, \omega) = A(\psi, k) R^{-1} e^{ikR} + O\left[(\xi_0/R)^2\right] \qquad (R \gg \xi_0), \tag{1}$$

where $A(\psi, k)$ is the axisymmetric directivity with acoustic axis passing across the center of the target, $k = \omega/c$ is the wavenumber, c is the sound velocity in the fluid; R, ψ, φ are spherical coordinates with origin in the center of the transducer; the active surface characteristic linear dimension of the latter is ξ_0. Furthermore

$$\begin{aligned} R &= \sqrt{\xi^2 + x_3^2} = \sqrt{r^2 + 2 r x_3^0 \cos\theta + (x_3^0)^2}\,, \\ \xi &= |\boldsymbol{\xi}|, \qquad \boldsymbol{\xi} = (x_1, x_2), \qquad x_3 = R\cos\psi = x_3^0 + r\cos\theta, \end{aligned} \tag{2}$$

where x_3^0 is the distance between the centre of the transducer and that the scatterer, ξ and x_3 are the radial and axis coordinates of the beam cross-section, respectively.

If the sound beam is sufficiently narrow, then from Eq. (1) we get the following expressions for the quasi-plane wave [15]:

$$p_{\text{inc}}(r,\theta,\omega) = A(k)R(\xi/x_3^0,k)e^{ikr\cos\theta} + O\left[1/(kx_3^0)^2\right] \qquad (kx_3^0 \gg 1) \tag{3}$$

or

$$p_{\text{inc}}(r,\theta,\omega) = A(k)\sum_{l=0}^{\infty} i^l(2l+1)R_l(k)j_l(kr)P_l(\cos\theta). \tag{4}$$

Here the function $A(k)$ is defined from the condition:

$$\begin{gathered} A(\psi,k)(x_3^0)^{-1}\exp(ikx_3^0) = A(k)R(\xi/x_3^0,k) \\ (\psi \approx \operatorname{tg}\psi = \xi/x_3^0, \quad \psi \ll 1) \end{gathered} \tag{5}$$

and corresponds to the Fourier-spectrum of the incident pulse modulation, $R(\xi/x_3^0,k)$ is the directive pattern of the quasi-plane wave,

$$R_l(k) \equiv R_l(\varrho/x_3^0,k) \tag{6}$$

is the coefficient determining the directivity of the partial wave with the impact parameter $\varrho_l = \sqrt{l(l+1)}/k$ and the angular moment l, that satisfies the inequality $\varrho_l \ll x_3^0$; $j_l(kr)$ is the Bessel spherical function of order l, $P_l(\cos\theta)$ is the Legendre polynomial.

Thus, the acoustic scattering pressure is determined by the formula

$$p_{\text{sc}}(r,\theta,\omega) = f(\theta,k)r^{-1}e^{ikr} + O\left[(a/r)^2\right] \qquad (r \gg a) \tag{7}$$

as $r \to \infty$, where

$$f(\theta,k) = k^{-1}\sum_{l=0}^{\infty}(2l+1)f_l(k)R_l(k)P_l(\cos\theta) \tag{8}$$

is the scattering amplitude (or form function) and $f_l(k)$ is the partial scattering amplitude

$$f_l(k) = i\Omega j_l(x)/\Omega h_l^{(1)}(x) \qquad (x = ka, \quad l = 0,1,2,\ldots), \tag{9}$$

where $h_l^{(1)}(x)$ is the Hankel spherical function of order l of the first kind, $\Omega \equiv 1$ and $\Omega \equiv d/dx$ for the soft and rigid spheres, respectively.

In the experiments, the total (effective) scattering cross-section $\sigma_t(k)$ is an important characteristic [1] which, in the case of a sphere insonified by a finite wave beam, is written as follow [15]:

$$\sigma_t(k) = Z_0^{-1}\sum_{l=0}^{\infty}|R_l(k)|^2\sigma_l(k); \tag{10}$$

here $\sigma_l(k)$ is the partial cross-section corresponding to the plane wave scattering:

$$\sigma_l(k) = (4\pi/k^2)(2l+1)|f_l(k)|^2 \qquad (l = 0,1,2,\ldots) \tag{11}$$

and

$$Z_0 = \sigma_0^{-1}\int_{\sigma_0}|R(\xi/x_3^0,k)|^2\,d\boldsymbol{\xi}, \tag{12}$$

where σ_0 is a square of the beam cross-section over which the averaging of the incident Poynting vector is carried out.

Let suppose that the directivity pattern of the quasi-plane wave near the scatterer have the the Lorentz form

$$R(\xi/x_3^0, k) = \frac{i\nu/2}{(\xi_0 - \xi)/x_3^0 + i\nu/2}, \tag{13}$$

where $x_3^0\nu$ is an effective beam width.

Because

$$R_l(k) = \frac{i\nu/2}{(\xi_0 - \varrho_l)/x_3^0 + i\nu/2}, \tag{14}$$

in accoudance with Eq. (8), the essential contribution to the scattering amplitude $f(\theta, k)$ will be due to the partial waves with impact parameters satisfying the equality

$$\varrho_l = \xi_0 . \tag{15}$$

Equation (14) corresponds to a single-level representation of the angular spectra of the incident wave amplitude.

3. Analysis of the results

On the base of the Eqs. (10) – (15), the calculation of the effective cross-section $\sigma_t^0(k) = Z_0\sigma_t(k)/a^2$ were performed as a function of the nondimensional frequency x for the case of the acoustically soft sphere (Figs. 1, 2) and the acoustically rigid immovable sphere (Figs. 3, 4).

The plots show that when a solid cylindrical beam (nondimensional impact parameter $\widetilde{\varrho}_0 = \xi_0/a$ is equal to zero, $Z_0 = \ln 2$) or a ring cylindrical beam ($Z_0 = \pi/4$) with $\widetilde{\varrho}_0 < 0.5$ incidents on the spherical surface then the cross-sections for wide beams ($0.5 < \gamma_0 \leq 1$, $\gamma_0 = x_3^0\nu/a$) qualitative unimportant are distinguished from the corresponding cross-sections of the plane wave incidence case [1]. However with the increasing sound spot dimension the frequency dependence of $\sigma_t^0(k)$ is getting an oscillatory character with increasing an amplitude more and more because of the narrowing Fresnel zones of the different phases that are formed on the insonified sphere side [6, 7, 13]. Then also the minimal levels of $\sigma_t^0(k)$ approach the zero value. The increasing beam impact parameter ($\widetilde{\varrho}_0 \to 1$) and the decreasing effective width γ_0 yield amplitude fluctuations of $\sigma_t^0(k)$ displayed in the almost whole frequency range that is considerable. The values of $\sigma_t^0(k)$ for the soft and rigid spheres are clearly distinguished between earth by the phase modulation. Note that in the case of the plane wave scattering similar differences are not observed because the cross-section $\sigma_t^0(k)$ approaches the asymptote $2\pi a^2$ in both cases of the soft and rigid obstacles.

A specific scattering of the narrow sound beam occurs when base rays incident grazely on the spherical object ($\widetilde{\varrho}_0 = 1$). Then the general amplitude level of $\sigma_t^0(k)$ is unimportant because only one half of the whole energy transported by the beam is lost in the interaction process. Furthermore, with narrowing beam the role of the specular reflection sharply decreases. Then, the amplitude oscillations, which are observed leading off with $\widetilde{\varrho}_0 \geq 0.5$, become specially expressive and periodic and disappear slowly for

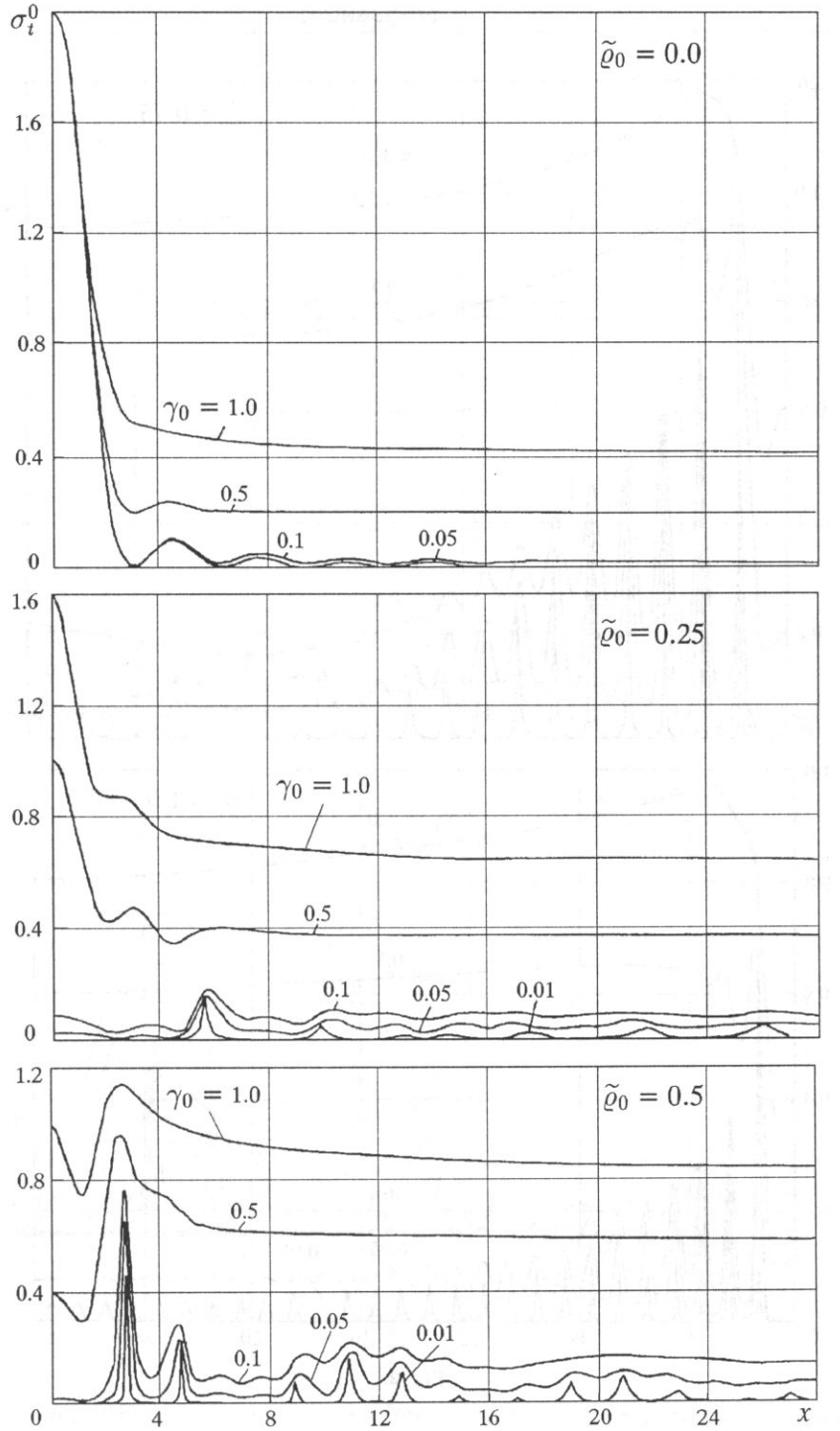
σ_t^0
$\tilde{\varrho}_0 = 0.0$
$\gamma_0 = 1.0$
0.5
0.1
0.05
$\tilde{\varrho}_0 = 0.25$
$\gamma_0 = 1.0$
0.5
0.1
0.05
0.01
$\tilde{\varrho}_0 = 0.5$
$\gamma_0 = 1.0$
0.5
0.05
0.01
0.1
0
0.4
0.8
1.2
1.6
4
8
12
16
20
24
x

Fig. 1.

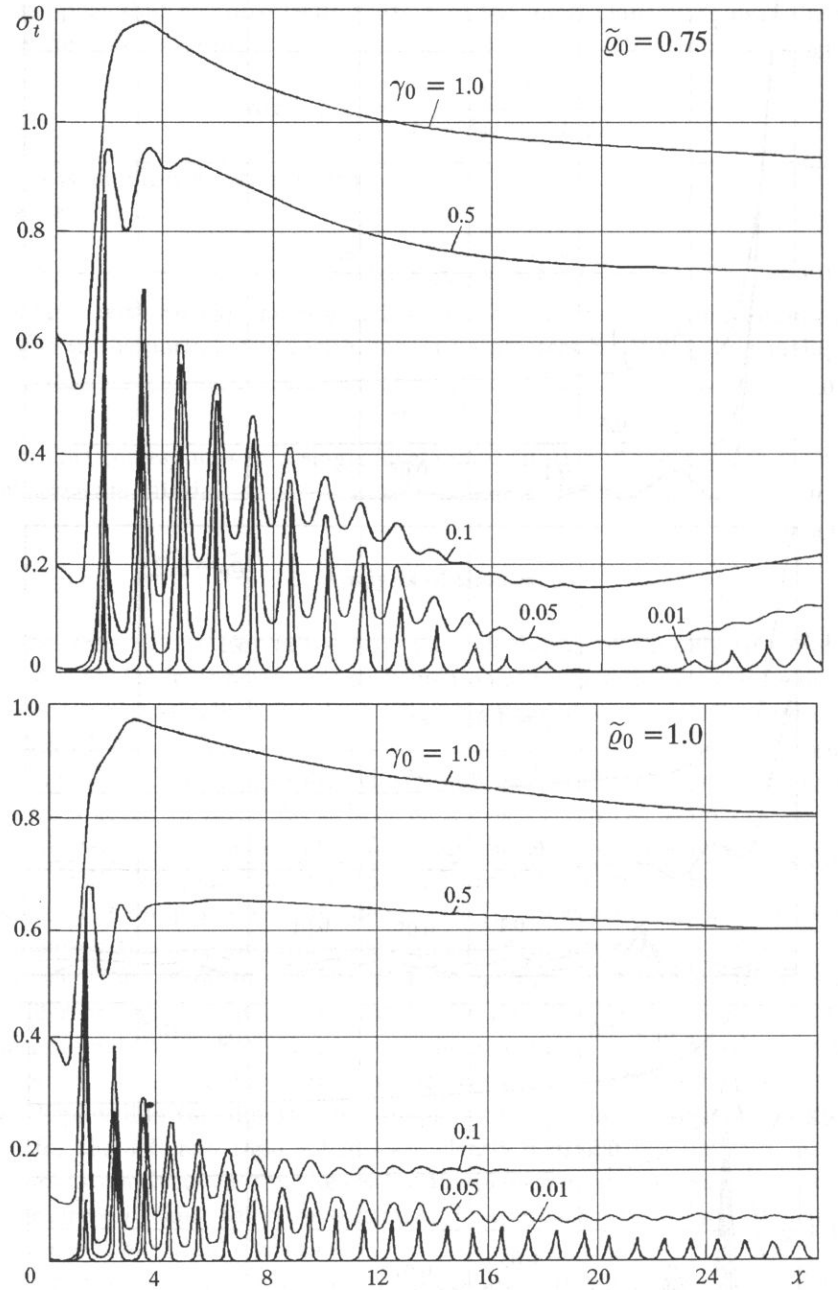

Fig. 2.

$\widetilde{\varrho} \approx 1$ (Figs. 2, 4). The resonance positions on the frequency scale with a step of $\Delta x \approx 1$ determining the phase and group circumferential wave velocities indicate resonances cor-

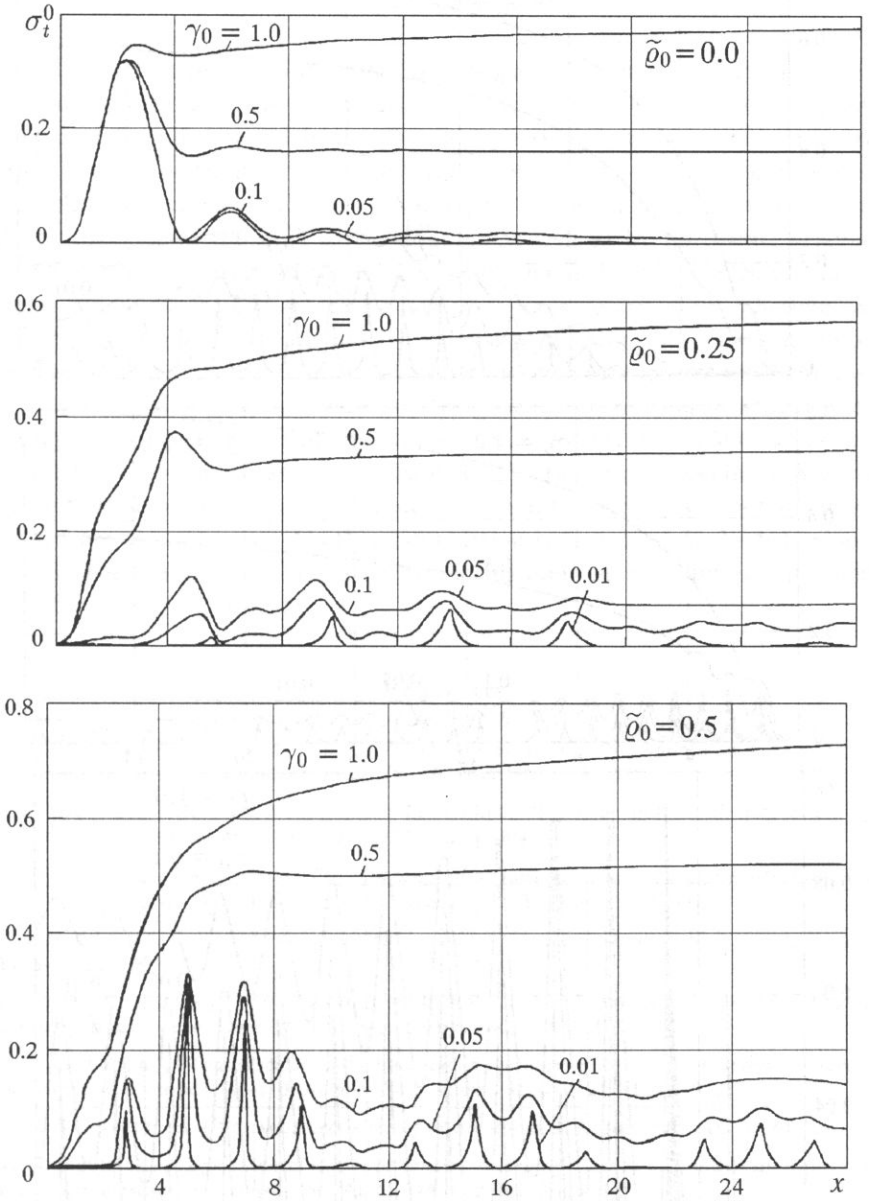

Fig. 3.

responding to the Franz creeping waves. Here these waves are separated very explicitly when $\widetilde{\varrho}_0 = 1$ and $\gamma_0 \ll 1$. It has also shown that within a considerable frequency range the resonance amplitude of $\sigma_t^0(k)$ for the soft sphere is almost twice as much than for the rigid one.

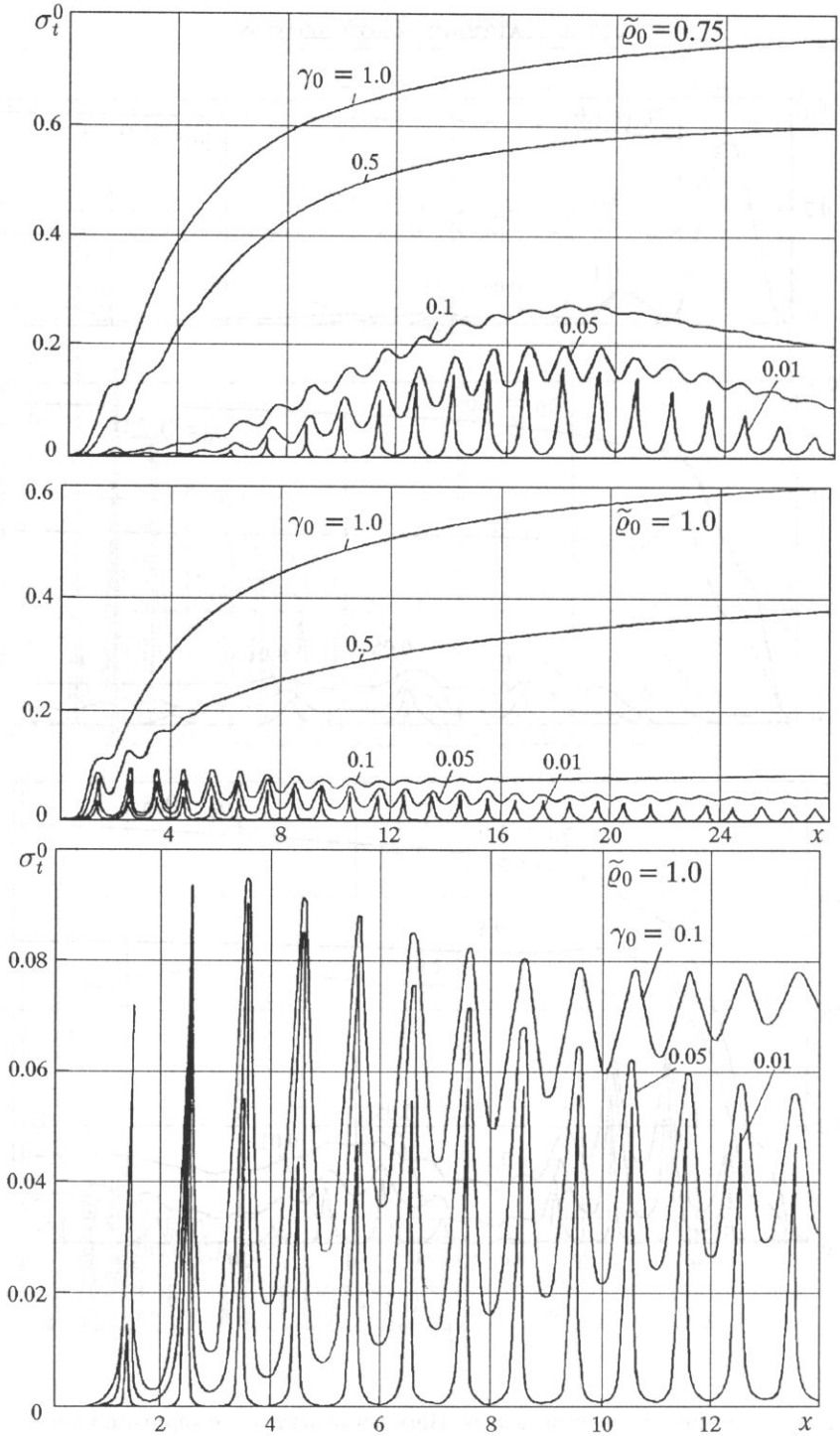
σ_t^0
$\tilde{\varrho}_0 = 0.75$
$\gamma_0 = 1.0$
0.5
0.1
0.05
0.01
0
0.2
0.4
0.6
$\gamma_0 = 1.0$
$\tilde{\varrho}_0 = 1.0$
0.5
0.1
0.05
0.01
4
8
12
16
20
24
x
σ_t^0
$\tilde{\varrho}_0 = 1.0$
$\gamma_0 = 0.1$
0.05
0.01
0.02
0.04
0.06
0.08
2
4
6
8
10
12
x

Fig. 4.

4. Conclusions

One of the effective methods of selection of the different contributions to the echo-signal from obstacles immersed in a fluid (gas) includes the control over the parameters of an incident bounded sound beam. For the spherical scatterer case by directing the acoustical axis of the transducer to the target center, this beam can be chosen axisymmetric with a ring cross-section. By scanning of the beam based rays on the obstacle spherical surface from the pole to the equator as well as by narrowing gradually the beam ring width an analysis of the generative mechanisms of the reflective and diffractive waves can be made. The acoustic beam pressure is described by spherical harmonic superpositions with the Lorentz partial amplitude distribution. The computations of the total scattering cross-section σ_t as a function of the frequency show the resonance character of this value under grazed insonifying (with succesive narrowing of the hollow beam ring) acoustically soft and immovable rigid spheres. The distances between the resonances indicate that these resonances belong to the Franz creeping waves. The resonance amplitude level of this waves scattered from the soft sphere is two times larger than that from the rigid one. Another information is contained in the behaviour of the envelope of these resonances. This is the oscillating function with different particularities for the soft and rigid scatterers.

References

[1] J.S. ASVESTAS, J.J. BOWMAN, P.L. CHRISTIANSEN *et al.*, *Electromagnetic and acoustic scattering by simple shapes*, North-Holland Publ. Co., Amsterdam, 728, 1969.

[2] R.E. BUNNEY, R.R. GOODMAN, S.W. MARSHALL, *Rayleigh and Lamb waves on cylinders*, J. Acoust. Soc. Amer., **46**, 5 (Part 2), 1223–1233 (1964).

[3] L. FILIPCZYŃSKI, T.KUJAWSKA, *The reflection of a Gaussian pulse of a plane ultrasonic wave from rigid and elastic spheres in water*, Arch. Acoust., **12**, 3, 113–128 (1987).

[4] L. FILIPCZYŃSKI, T. KUJAWSKA, *Acoustical shadow of a sphere immersed in water*, Arch. Acoust., **14**, 3-4, 181–190 (1989).

[5] P. GILLIS, C. DELEUZE, V.P. HENRI, J.M. LESCEUX, D.J. TRITTON, *Backscattering of light from a water droplet – the glory effect*, Amer. J. Phys., **50**, 5, 416–420 (1982).

[6] G.C. GAUNAURD, *Monostatic and bistatic cross-sections of the large (capped) sphere partially insonified at a circular spot*, J. Acoust. Soc. Amer., **61**, 5, 1121–1132 (1977).

[7] G.C. GAUNAURD, H. ÜBERALL, *Acoustics of finite beams*, J. Acoust. Soc. Amer., **63**, 1, 5–16 (1978).

[8] W.G. NEUBAUER, *Experimental measurement of "creeping" waves on solid aluminium cylinder in water using pulses*, J. Acoust. Soc. Amer., **44**, 1, 298-299 (1968).

[9] W.G. NEUBAUER, *Observation of acoustic radiation from plane and curved surfaces*, Phys. Acoust.: Principles and Methods, **10**, 61–126, Academic Press, New York, London 1973.

[10] H.M. NUSSENZVEIG, *High-frequency scattering by a transparent sphere. II. Theory of the rainbow and the glory*, J. Math. Phys., **10**, 1, 125–146 (1969).

[11] H.M. NUSSENZVEIG, *The theory of the rainbow*, Sci. Amer., **236**, 4, 116–127 (1977).

[12] A.P. PODDUBNYAK, *High-frequency asymptotics of an acoustic pressure in scattering of a bounded wave beam by elastic sphere* [in Russian], Prikladnaya Matematika i Mekhanika, **53**, 6, 931–938 (1989).

[13] A.P. PODDUBNYAK, V.V. POROKHOVSKII, *Scattering of a sound beam by a nondeformable sphere and cylinder*, Sov. Phys.-Acoust. (USA), **34**, 5, 529–532 (1988).

[14] A.P. PODDUBNYAK, V.V. POROKHOVSKII, *Nonspecular reflection of a bounded sound beam from an elastic sphere in a liquid*, Sov. Phys.-Acoust. (USA), **35**, 4, 423–425 (1989).

[15] JA.S. PODSTRIGACH, A.P. PODDUBNYAK, *Scattering of sound beams by elastic bodies of the spherical and cylindrical form* [in Russian], Naukova Dumka, Kiev, 262, 1986.

[16] S. SASAKI, *Back reflection of ultrasonic wave obliquely incident to solid surface in water*, Jap. J. Appl. Phys., **2**, 3, 198 (1963).

[17] A.J. STOYANOV, H. ÜBERALL, F. LUPPEÉ, G. QUENTIN, *Observation of surface waves on a solid cylinder in a fluid*, J. Acoust. Soc. Amer., **85**, 1, 137–140 (1989).

[18] M. TALMANT, G. QUENTIN, *Study of the pseudo-Lamb wave S_0 generated in thin cylindrical shells insonified by short ultrasonic pulses in water*, Progr. Underwater Acoust.: Proc. 12 Int. Congr. Acoust. Assoc. Symp. Underwater Acoust., Halifax, July 16-18, 1986, 134–144, New York, London (1987).

ARCHIVES OF ACOUSTICS
22, 3, 307–331 (1997)

MATCHED ALL-PASS FILTERING OF THE RECEIVED ECHOES FOR RANGE IMPROVEMENT IN MEDICAL ULTRASOUND IMAGING

A. NOWICKI, A. KUBERA, K. RENE

Department of Ultrasound,
Institute of Fundamental Technological Research,
Polish Academy of Sciences
(00-049 Warszawa, ul. Świętokrzyska 21)

P.A. LEWIN

Drexel University, Philadelphia, USA

T. PAŁKO

Warsaw University of Technology, Warsaw, Poland

The purpose of this work was to investigate a possibility of using chirp waveforms in very high frequency ultrasound medical imaging to increase range resolution and concurrently maximize penetration depth. It is shown that the improvement in range resolution can be achieved by using appropriately designed all pass matched filter at the receiver input. The paper describes in depth theoretical optimization process and computer simulation of the matched 96-th order all pass filter for chirp waveforms of 1 μs duration in the frequency range 30 MHz – 50 MHz. A prototype of 24-th order filter was constructed to verify the results of analytical and numerical methods. Excellent agreement was observed between the theoretical predictions and experimental data. Continuation of this work will include design and optimization of superwide bandwidth transducers.

1. Introduction

Ultrasound imaging systems are widely used in clinical practice. For imaging of internal organs of human body frequencies from 2 MHz to about 12 MHz are applied. The range or axial resolution in tissue is determined by the duration of the ultrasound waveform launched into the body. Typically, the waveform contains two and a half periods, which leads to axial resolution of approximately 2 mm at the frequency of 2 MHz. Although at 10 MHz the resolution improves to 0.4 mm with increasing frequency, tissue attenuation also increases which, in turn, limits the penetration depth. Thus, while at

2 MHz the penetration depth may be on the order of tens of centimeters it decreases to tens of millimeters at 10 MHz.

Recently, very high frequency ultrasound imaging gained attention in surface tissue imaging and intraluminal examination of vessel walls [1, 2, 7, 13]. YANO *et al.* [15] were among the first researchers to describe a system permitting skin imaging using a 40 MHz lithium niobate transducer. They reported a – 6 dB beamwidth of about 0.1 mm in the focal zone. The axial resolution, determined from measurements of the length of a pulse reflected from an ideal reflector, was equal to 0.25 mm.

Several research groups used imaging transducers made of piezoelectric polivinylidene (di)fluoride (PVDF). Although PVDF suffers from a relatively low pulse-echo sensitivity in comparison with the conventional PZT piezoelectric ceramics (PVDF's electroacoustic coupling coefficient k_t is approx. 0.15 versus 0.5 for a conventional PZT ceramic material) it allows extremely wide bandwidth to be achieved, thus permitting the use of excitation signals with varying frequency. HOSS, EMERT *et al.* [8] described an imaging system with a pulse-echo PVDF transducer working at the centre frequency of 40 MHz and having −6 dB bandwidth of about 50 MHz. They have overcome the issue of low PVDF transducer sensitivity by employing chirp modulation as an excitation waveform and reported a significant increase in the overall imaging sensitivity. Chirped PVDF transducers were also studied by LEWIS [12]. BERSON *et al.* [2] described an ultrasound scanner operating at the center frequency of 47 MHz with axial resolution of about 0.1 mm and lateral resolution of 0.3 mm. FEUILLARD *et al.* [5] improved Berson's system replacing a PZT ceramic transducer by a broadband 45 MHz co-polymer transducer made of P(VDF-TrFe).

It is well known that range resolution can be improved by using chirp waveforms in which instantaneous frequency content changes as a function of elapsed time. Such waveforms with linear frequency modulation are widely used in the radar technique. By appropriately selecting duration of the waveform and modulation band and applying (e.g. surface acoustic wave) delay filters, both the resolution and range of the radar system can be enhanced [4, 6, 9, 14].

In medical ultrasound imaging the range resolution and penetration depth depend on the type of the interrogating waveform and processing of the returning echoes. Penetration depth can be improved by increasing the signal-to-noise ratio at the receiver output. However, for a given receiver noise level, such improvement requires increased energy level of the interrogating waveform. In practice, this can be achieved only by extending the pulse duration of transmitted waveforms as their peak amplitude is usually limited either by transmitter electronics or safety regulations [10]. The range resolution increases with decreasing duration of the echoes. In traditional pulse-echo ultrasound imaging it is well known that two objects can be distinguished if their respective echoes are separated by a time longer than the length of the interrogated waveforms. Thus, in conventional medical ultrasound imaging systems there is a clear trade-off between the range resolution and penetration depth. For the purpose of the discussion which follows it may be useful to note that the minimum distinguishable distance ΔR between neighbouring structures is defined as $\Delta R(c/2\Delta F)$, where c is the ultrasonic wave propagation velocity in the medium (tissue) and ΔF is the frequency bandwidth of the transmitted

signal. Thus, the 20 MHz bandwidth would correspond to the resolution in soft tissue ($c = 1540\,\mathrm{m/s}$) on the order of 0.04 mm.

The primary purpose of the work presented here was to investigate the conditions for simultaneous optimization of range (axial) resolution and penetration depth in very high frequency ultrasound medical imaging. The approach proposed uses chirp waveforms. As mentioned above such waveforms involve signals in which instantaneous frequency content changes as a function of elapsed time and can be considered as frequency modulated signals. The optimal use of chirp signals involves a form of echo compression techniques. HOSS *et al.* [8] reported application of similar signals in diagnostic ultrasound applications. However, their study did not discuss the issues involved in designing special receiver filters which would ensure echo compression by filter matching.

This paper is organized in the following way: In section 2 the theoretical background of echo compression technique using all pass matching filtering is outlined. Section 3 describes computer simulations and numerical solutions which allow optimizing of 96-th order filter. Experimental results obtained by testing a prototype of 24-th order filter are presented in Sec. 4. The theoretical and experimental results are compared in Sec. 5 which also contains conclusions and indicate the future work needed to further improve the proposed approach.

2. Theory of echo compression with frequency modulation using all-pass matching filtering

In this section theoretical analysis of ultrasound echo compression for transmitted waveforms with linear frequency modulation (chirps) is presented. The frequency spectrum of the chirp signal $s(t)$ considered has an almost rectangular envelope in the band ΔF around the centre frequency f_0. Such a chirp of duration T in which the frequency $f(t)$ varies linearly as a function of time, can be analytically expressed as:

$$s(t) = A\cos[f(t)], \tag{2.1}$$

where

$$f(t) = \begin{cases} \left(f_0 - \dfrac{\Delta F}{2}\right) + \dfrac{\Delta F}{T}t & \text{for} \quad 0 < t < T, \\ 0 & \text{for} \quad |t| > T. \end{cases}$$

As already mentioned the main advantage of using a chirp signal is that it enhances penetration depth by increasing the energy of the transmitted ultrasound wave providing that the echoes returning from the organs under examination are time compressed. This can be conveniently achieved by applying all pass (AP) matched filter approach to obtain pulse compression [3]. This technique involves implementation of a time dependent delay of the frequency components of the returning echoes. The delay increases linearly with increasing frequency of the individual components of the echo. The amplitude response of the AP filters is constant over the frequency bandwidth, i.e. signals with different frequency components are transferred by a filter with identical attenuation. The AP filters are ideally suited to implement specific delays, e.g. a constant delay or one which varies

linearly, over a given frequency range. As implied above, the use of pulse compression technique requires a filter with a linear delay. Both compression and decompression can be performed using the same AP filters [3].

Transfer characteristics of all-pass filters. Any overall characteristic of AP filters can be implemented by cascade connection of AP filters of the first and second orders. This can easily be shown by considering the following transformations.

The transfer function of the nth-order AP filter can be represented as:

$$H(s) = \frac{s^n + \beta_1 s^{n-1} + ... + \beta_n}{s^n + \alpha_1 s^{n-1} + ... + \alpha_n}, \tag{2.2}$$

where $s = j\omega$ and the coefficients α_n and β_n at the successive powers are real.

If $H(s)$ polynomial represents an AP type filter the poles and zeros of this function must follow a specific pattern. For the first order filter a pole and zero are located at equal distances from the origin. The pattern of the second order filter is often referred to as having quadrantal symmetry; here the poles and zeroes have equal but opposite real and imaginary parts (complex conjugate pattern). The patterns of higher order filters can be composed by a superposition of first and second order patterns.

Assuming that all the poles and zeros of $H(s)$ are complex conjugate except for one real pole and one real zero, the function $H(s)$ can be represented in the following way:

$$H(s) = \frac{s - \alpha_1}{s + \alpha_1} \times \frac{(s - \alpha_2)^2 + \beta_2^2}{(s + \alpha_2)^2 + \beta_2^2} \times ... \times \frac{(s - \alpha_{(n+1)/2})^2 + \beta_{(n+1)/2}^2}{(s + \alpha_{(n+1)/2})^2 + \beta_{(n+1)/2}^2}, \tag{2.3}$$

i.e., in this representation, $H(s)$ is the product of first- and second-order functions only. Such representation of the transfer function can always be obtained for AP filters with real coefficients at the successive powers of s. As mentioned above, in practice, $H(s)$ can be implemented by a cascade connection of AP filters of the first and second orders. In such implementation the total delay corresponds to the sum of the delays associated with individual filter sections. The cascade connection can be implemented since the individual sections exhibit constant electrical resistance. More specifically, the value of the input impedance of the filters is constant irrespective of the frequency. Higher order sections are seldom implemented because the savings in terms of the number of individual sections or components are negligible in comparison with the increased complexity of the filter and difficulties involved in its tuning.

In this work it was assumed that a filter with the appropriate phase delay function can be implemented by a cascade connection of the second order filters. The corresponding transfer function $H(s)$ is given by equation (2.4).

$$H(s) = \frac{(s - \alpha_2)^2 + \beta_2^2}{(s + \alpha_2)^2 + \beta_2^2} \times ... \times \frac{(s - \alpha_{(n+1)/2})^2 + \beta_{(n+1)/2}^2}{(s + \alpha_{(n+1)/2})^2 + \beta_{(n+1)/2}^2}. \tag{2.4}$$

Second-order all-pass filters. The transfer function of a second-order AP filter has the following form:

$$H_2(s) = \frac{(s - \alpha)^2 + \beta^2}{(s + \alpha)^2 + \beta^2}, \qquad \alpha > 0. \tag{2.5}$$

The delay function or phase response of the filter as a function of frequency is given by:

$$\theta_2(\omega) = -2\tan^{-1}\frac{2\alpha\omega}{\alpha^2+\beta^2-\omega^2}. \tag{2.6}$$

Therefore, the group delay function can be expressed as:

$$D_2(\omega) = -\frac{d\theta_2}{d\omega} = \frac{4\alpha(\omega^2+\alpha^2-\beta^2)}{(\alpha^2+\beta^2-\omega^2)^2+4\alpha^2\omega^2}. \tag{2.7}$$

It is more convenient to compare the behaviour of the function $D_2(\omega)$ for different values of α and β by introducing new variables:

$$\begin{aligned} \overline{\omega}_0^2 &= \alpha^2+\beta^2, \\ k &= \frac{2\alpha}{\overline{\omega}_0}, \\ \mu &= \frac{\omega}{\overline{\omega}_0}, \\ \alpha &= \frac{k\overline{\omega}_0}{2}, \\ \beta &= \overline{\omega}_0\sqrt{1-\frac{k^2}{4}}. \end{aligned} \tag{2.8}$$

where $\overline{\omega}_0$ – the normalized frequency, μ – the relative frequency.

Now the phase response of the filter can be expressed as:

$$\theta_2(\mu) = -2\tan^{-1}\frac{k\mu}{1-\mu^2}. \tag{2.9}$$

For $\mu = 0$, $(\omega = 0)$, the phase displacement is one of zero degrees and reaches 360° for the "infinite" frequency. The phase is 180° for $m = 1$ $(\omega = \omega_0)$ for all values of k.

With the new variables the group delay function is given by:

$$\overline{\omega}_0 D_2(\mu) = \frac{2k(1+\mu^2)}{(1-\mu^2)^2+k^2\mu^2}. \tag{2.10}$$

This function is shown in Fig. 1. The low values of k result in a narrow delay function with relatively large peak values. With increasing values of k the corresponding peak values decrease. For $k = 1.73$ the peak vanishes and the function is maximally flat for the angular frequency $\omega = 0$.

The impulse response of the matched filter for to the input signal $s(t)$ has the form:

$$h(t) = \begin{cases} \dfrac{2\sqrt{D}}{T}\cos\left(\omega_0 t - \dfrac{\Delta\omega}{2T}t^2\right) & -\dfrac{T}{2} \le t \le \dfrac{T}{2}, \\ 0 & |t| > \dfrac{T}{2}, \end{cases} \tag{2.11}$$

where $\omega_0 = 2\pi f_0$, $\Delta\omega = 2\pi\Delta F$.

The response $h(t)$ is characteristic of the non-causal system as the impulse response exists for negative time. To some extent, this facilitates the analysis since the filter

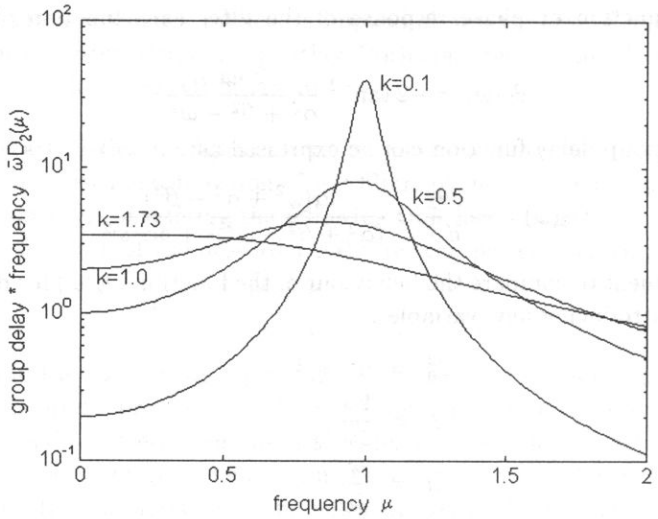

Fig. 1. The group delay function of the second-order filter.

response to the signal $s(t)$ is symmetrical with respect to $t = 0$. As evidenced later the filter implemented in practice shows an impulse response with an initial delay t_1.

The response of the matched filter to the signal $s(t)$ is given by the convolution integral:

$$y(t) = \frac{2\sqrt{D}}{T} \int_{-\infty}^{\infty} \cos\left(\omega_0 \tau + \frac{\Delta\omega \tau^2}{2T}\right) \cos\left[\omega_0(t-\tau) - \frac{\Delta\omega}{2T}(t-\tau)^2\right] d\tau. \tag{2.12}$$

The integration limits can be conveniently defined considering a graphic interpretation of the convolution integral and bearing in mind that the response $h(t)$ precedes the one at the input (at time t_0) by the time $T/2$. After a few transformations the following expression can be obtained:

$$y(t) = \begin{cases} \dfrac{\sqrt{D}}{T} \displaystyle\int_{-T/2}^{t+T/2} P_1(t,\tau)\, d\tau + \dfrac{\sqrt{D}}{T} \int_{-T/2}^{t+T/2} P_2(t,\tau)\, d\tau & t < 0, \\ \dfrac{\sqrt{D}}{T} \displaystyle\int_{t-T/2}^{T/2} P_1(t,\tau)\, d\tau + \dfrac{\sqrt{D}}{T} \int_{t-T/2}^{T/2} P_2(t,\tau)\, d\tau & t \geq 0, \end{cases} \tag{2.13}$$

where

$$P_1(t,\tau) = \cos\left[\omega_0 t - \frac{\Delta\omega}{2T} t^2 + \frac{\Delta\omega}{T} t\tau\right],$$

$$P_2(t,\tau) = \cos\left[\omega_0(2\tau - t) + \frac{\Delta\omega}{T}\tau(\tau - t) + \frac{\Delta\omega}{2T} t^2\right].$$

The first integral can be estimated in the following way:

$$\int_a^b \cos\left[\omega_0 t - \frac{\Delta\omega}{2T}t^2 + \frac{\Delta\omega}{T}t\tau\right] d\tau = \frac{\sin\left[\omega_c t - (\Delta\omega/2T)t^2 + (\Delta\omega/T)t\tau\right]}{(\Delta\omega/T)t}\Bigg|_{\tau=a}^{\tau=b}.$$

The second integral depends on higher frequencies and, in practice, its impact on the total response can be neglected.

For $t \geq 0$ the filter response can be determined from:

$$y(t) = \frac{\sqrt{D}}{\Delta\omega t}\left\{\sin\left[\omega_0 t - \frac{\Delta\omega}{2T}t^2 + \frac{\Delta\omega}{2}t\right] - \sin\left[\omega_0 t - \frac{\Delta\omega}{2T}t^2 + \frac{\Delta\omega t}{T}\left(t - \frac{T}{2}\right)\right]\right\}. \tag{2.14}$$

The estimation of the first integral for $t < 0$ leads to similar expression; as a result, the output of the matched filter can be adequately described by the following expression:

$$y(t) = \sqrt{D}\frac{\sin\pi D\frac{t}{T}\left(1 - \frac{|t|}{T}\right)}{\pi D\frac{t}{T}}\cos\omega_0 t \qquad \text{for} \quad -T \leq t \leq T. \tag{2.15}$$

This is the autocorrelation function of the input waveform $s(t)$.

Thus, an amplitude-modulated signal with the carrier frequency f_0 is obtained at the filter output. The width of the compressed pulse is measured over the amplitude interval from $(2/\pi)\sqrt{D}$ to $\sqrt{D}$ (about 4 dB below the peak value) for the times $t = \pm 1/(2\Delta F)$; hence the total width of pulse is:

$$\Delta t = t_1 + \frac{1}{2\Delta F} - \left(t_1 - \frac{1}{2\Delta F}\right) = \frac{1}{\Delta F}. \tag{2.16}$$

This width or pulse duration is the inverse of that of the rectangular pulse. The ratio between the duration of the input signal T and the duration of the output pulse is $T/(1/\Delta F) = \Delta FT = D$. Further examination shows that the maximum value of the output signal is $\sqrt{D}$ times higher than that of the input signal, and the maximum output power in the pulse is D times higher than the input power. However, the mean power remains the same. The above analysis indicates that the principle of matching filtering as applied to the linear FM signal combines the advantages of short and long pulses. In this way, relatively high power can be transmitted in a short pulse.

The linear group delay can now be examined in more detail. This delay can be expressed as:

$$D(\omega) = -\frac{d\theta(\omega)}{d\omega} = t_1 + T\left(\frac{\omega_c - \omega}{\Delta\omega}\right), \tag{2.17}$$

where $\Delta\omega = 2\pi\Delta F$.

Knowledge of instantaneous frequency and linear delay of the filter is sufficient to perform a qualitative analysis of the amplitude transfer function and determine voltage gain for $t = t_1$.

The input signal $s(t)$ can be considered to consist an infinite number of sinusoid components the frequencies of which are defined by $\omega(t)$ for each instant of time. For

instance, for $t = t_a$ one specific sinusoid has the frequency $\omega(t_a) = \omega_0 + (\Delta\omega/T)t_a$. At the receiver input this sinusoid component is delayed with the optimum filter by the value $D(\omega)$, where $\omega = \omega(t_a)$. This sinusoid reaches the filter output after the time $t_a + D(\omega)\Big|_{\omega=\omega(t_a)}$. For a given sinusoid component the time delay from the receiver input to its output can be determined from:

$$t+D(\omega)\Big|_{\omega=\omega(t)} = t+t_1+\frac{T}{\Delta\omega}(\omega_0-\omega)\Big|_{\omega=\omega(t)} = t+t_1+\frac{T}{\Delta\omega}\left[\omega_0-\left(\omega_0+\frac{\Delta\omega}{T}t\right)\right] = t_1. \quad (2.18)$$

Therefore, all the components of the spectrum of the input signal, irrespective of their frequencies, reach the filter output at the same time t_1. Since the phase of all components is identical, the amplitude of the output signal increases for $t = t_1$. This increase in the amplitude of the output signal by a factor of $\sqrt{D}$ can be explained in the following way. The FM impulse can be expressed as the composition of N pulses each having a unit amplitude. Therefore, the width or duration of each pulse is T/N. The carrier frequency of each component pulse is constant, and approximates the linear frequency function in the corresponding interval of this component pulse (see in Fig. 2).

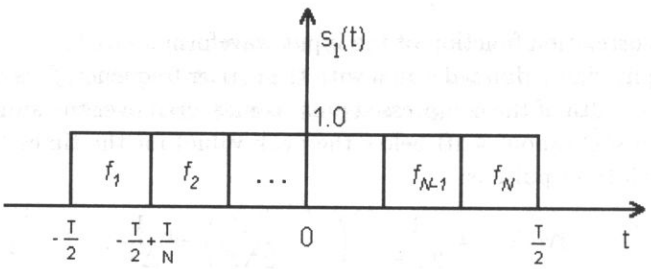

Fig. 2. The approximation of a pulse with linear FM modulation by N pulses with different carrier frequencies.

The frequency of the k-th pulse is given by:

$$f_k = f_0 - \frac{\Delta f}{2} + \frac{(2k-1)\Delta f}{2N} \qquad (k = 1, 2, ..., N), \quad (2.19)$$

which occurs for

$$t_k = -\frac{T}{2} + \frac{(2k-1)T}{2N}.$$

It is now necessary to determine the value of N to minimize the approximation error and ensure that $s'(t)$ would be the appropriate approximation of $s(t)$. The spectra of N individual component pulses can be added to obtain the overall transfer function of the chirp signal. For the frequency f_k the amplitude remains constant since the amplitude of the other components passes through zero at this frequency.

The condition for a partial superimposition of the neighbouring pulses spectra can be formulated in the following way:

$$f_{k+1} - f_k = \frac{N}{T}. \quad (2.20)$$

From the previous formulae (Eqs. (2.19) and (2.20))

$$f_{k+1} - f_k = f_0 - \frac{\Delta F}{2} + \frac{(2k+1)\Delta f}{2N} - \left[f_0 - \frac{\Delta F}{2} + \frac{(2k-1)\Delta F}{2N} \right] = \frac{\Delta F}{N} . \quad (2.21)$$

Combining (2.20) and (2.21) results in the following expression:

$$N = \sqrt{\Delta F T} = \sqrt{D} . \quad (2.22)$$

Equation (2.22) indicates that the first-order approximation of the chirp signal consists of individual components (pulses) each of duration $T/\sqrt{D}$. If $\sqrt{D}$ is not an integer $s'(t)$ cannot be implemented in practice, however, the mathematical model continues to hold.

In this study the development of the AP filter was undertaken over the frequency range from 30 MHz to 50 MHz. This is because, as mentioned in Introduction, the ultrasound imaging in this frequency range is gaining attention. Since the bandwidth available with conventional PZT ceramic transducers is not adequate the filter design described assumed that the wideband transducer characteristics could be met by using piezoelectric polymer transducers [11].

Careful analysis of the trade-off between the pulse-echo sensitivity of the superwideband PVDF transducer and the corresponding PZT transducer was carried out and it was determined that the PVDF transducer will exhibit approximately 20 dB lower sensitivity. This result was subsequently used to analyse the conditions appropriate for practical implementation of the all pass filter. The analysis resulted in selection of linear modulation range of 20 MHz and chirp signal duration of 1 μs.

As the gain of reflected echoes after compression is proportional to $\sqrt{D}$, these filter parameters will result in the $\sqrt{D} = \sqrt{1\,\mu s \cdot 20\,MHz} \cong 4.5$, close to the value of 13 dB which would greatly compensate for the 20 dB loss due to the use of PVDF transducer. It is appropriate to note that in the present analysis the influence of the tissue load was neglected. However, the practical implementation of the chirp technique would require frequency dependent attenuation effects to be taken into account. To simplify the analysis of the filter parameters, such as the compression coefficient and the duration of side lobes, it was assumed that the chirp signal amplitude was unity – this assumption does not affect the general nature of the analysis and the practical implementation of the delay line designed.

All pass filter design. The AP filter is a matched filter implementing the inverse time delay function with respect to the transmitted chirp signal. Since the chirp waveform used here has linear frequency modulation, the characteristic of the delay line needs to be linear, too. Such characteristic of the delay transfer function can be approximated using maximally flat, equiripple and least squares designs. The least-squares method was selected here as it offers an adequate compromise between the maximally flat and equiripple designs. Although the equiripple method provides a sharper roll-off characteristic than the least-squares method, it is achievable at the expense of maximally flat response. On the other hand, the maximally flat design does not provide satisfactory

results at cut-off frequencies and in the lower frequency range. The least-squares method is a compromise between these types of solutions.

Estimation and minimization of error. Optimization of the filter design requires minimization of the order of the filter and simultaneous minimization of the error between the ideal (theoretical) and achievable filter response. Another issue to be addressed in the optimization of the design is associated with the matching between the input signal and the filter. The optimum filter should be relatively insensitive to variations in the shape of the input signal.

A procedure of estimating the approximation error is presented below. The procedure allows the impact of variations in the values of the filter parameters on the linearity of the delay characteristic to be determined. In addition, the procedure makes it possible to analyse the effect of delay nonlinearity on the shape and compression of the output signal.

The total delay of a filter consisting of N cascade-connected second-order filters is given by:

$$D_a(\omega) = 4 \sum_{j=1}^{N} \frac{\alpha_j(\omega^2 + \alpha_j^2 + \beta_j^2)}{(\alpha_j^2 + \beta_j^2 - \omega^2)^2 + 4\alpha_j^2\omega^2} \,. \tag{2.23}$$

The value of error in the delay can be estimated as follows:

$$\varepsilon = \int_{\omega_1}^{\omega_2} [D_d(\omega) - D_a(\omega)]^2 \, d\omega \,, \tag{2.24}$$

where $D_d(\omega)$ is the required delay over the interval $\omega_1 \leq \omega \leq \omega_2$.

The error is minimized if the partial derivatives are zero for each variable, i.e., $d\varepsilon/d\alpha_j = 0$ and $d\varepsilon/d\beta_i = 0$. The solution of these equations yields the optimum parameters.

3. Numerical verification of the analytical results

Since analytical solution is impractical in design practice, numerical verification of the analytical results was carried out. Typically, the numerical solution will minimize the error with increasing number of approximations. The trade off here is between minimizing the error and ensuring a reasonable computation time.

There are many algorithms for numerical integration. If the integral is replaced by the equivalent rectangles the following expression is obtained:

$$\varepsilon = \Delta\omega \sum_{k=1}^{P} \left(D_{d_k} - D_{a_k}\right)^2 \,. \tag{3.1}$$

The function of Eq. (2.25) was calculated for P frequencies over the range $\omega_1 \leq \omega \leq \omega_2$, where $\Delta\omega$ is the integration interval. The first frequency to be calculated

was $\omega_1 + \Delta\omega/2$, the next one was $\omega_1 + 3\Delta\omega/2$, etc. The last frequency calculated was $\omega_2 - \Delta\omega/2$. This approach resulted in the following expression:

$$\Delta\omega = \frac{\omega_2 - \omega_1}{P}, \tag{3.2}$$

where the coefficient P is defined as $P = 4N + 5$ (N is the number of second orders filters used in the design). The higher P is the more accurately the value of the integral is determined. The initial values for the parameters α_j and β_j which usually yielded satisfactory results are given by [3]

$$\begin{aligned} \alpha_j &= \frac{\omega_2 - \omega_1}{N}, \\ \beta_j &= \omega_1 + \frac{(2j-1)(\omega_2 - \omega_1)}{2N}, \qquad j = 1, 2, ..., N. \end{aligned} \tag{3.3}$$

Prior to describing the results of numerical evaluations it may be useful to reiterate the requirements for the filter characteristics.

The purpose of the optimization procedure was to obtain a delay function with the following properties: 1) the delay function should be linear – this requirement results directly from the assumptions of the matching filtering model adopted here, 2) the total filter delay was chosen to be 1 μs over the frequency range from 30 MHz to 50 MHz and, moreover, the filter was assumed to consist of four cascade-connected sections, each with a delay of 250 ns, 3) the maxima in transfer functions of individual filters should fall between the frequency range from 30 MHz to 50 MHz.

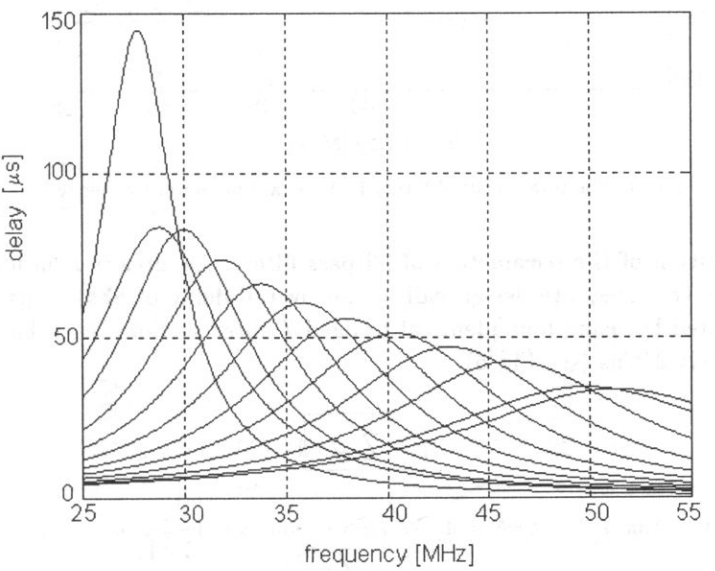

Fig. 3. The delays of filters 1 – 12 as a function of frequency.

The optimization process was performed on a Hewlett Packard 9000 series workstation using the Mathematica 2.0 software (Wolfram Research). The function Nonlinear

Curve Fitting (nonlinea.m from the Statistics package) was used. This program allows the nonlinear plot to be fitted to an arbitrary function. More specifically, Nonlinear Curve Fitting implements nonlinear approximation of a specific function using the least-squares method, such as the Levenberg-Marquardt method which minimizes chi2. The numerical analysis indicated that already for the 24-th order filter (12 second order filters), the value of the error was minimized. Further increase in the filter order did not show any significant improvement. The delays of the individual filters and the overall delay of the 24-th order filter are shown in Figs. 3 and 4. The initial and post-optimization parameter values of the filters are shown in Appendix.

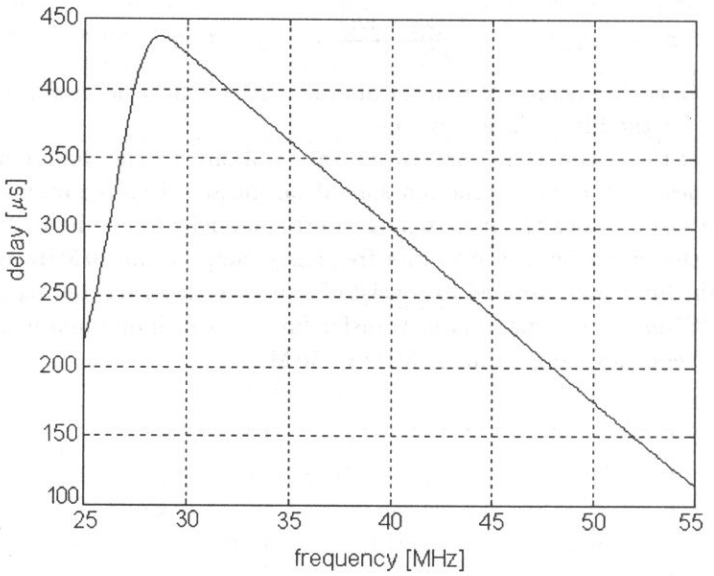

Fig. 4. The total delay of filters 1 – 12 as a function of frequency.

The calculation of the parameters of all pass filters. As already mentioned, the requirements for the adequate design call for an overall delay of about 1 μs. This delay was implemented by using four identical bridged T filter sections, each having a delay of approximately 270 ns (see Fig. 5).

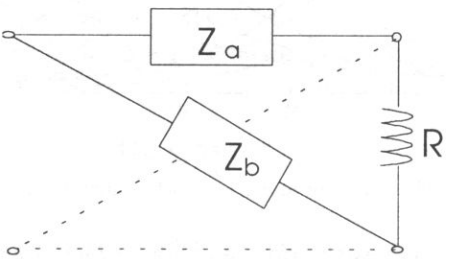

Fig. 5. Bridge-T filter with constant resistance.

For such filters the output resistance of one section of the filter R is the input resistance of its next section:

$$Z_a \, Z_b = R^2. \tag{3.4}$$

The transfer function of (3.4) has the following form:

$$H(\omega) = \frac{R - Z_a}{R + Z_a} \tag{3.5}$$

and providing that Z_a is represented by the reactance $jX(\omega)$, the filter is all-pass.

Second order Bridged T filters. For the second-order AP lattice the impedance of the anti-resonance circuit is:

$$Z_a = \frac{j\omega L}{1 - LC\omega^2} \tag{3.6}$$

and, hence, formula (3.5) becomes:

$$H(\omega) = \frac{-\omega^2 - j\omega(1/RC) + 1/LC}{-\omega^2 + j\omega(1/RC) + 1/LC}. \tag{3.7}$$

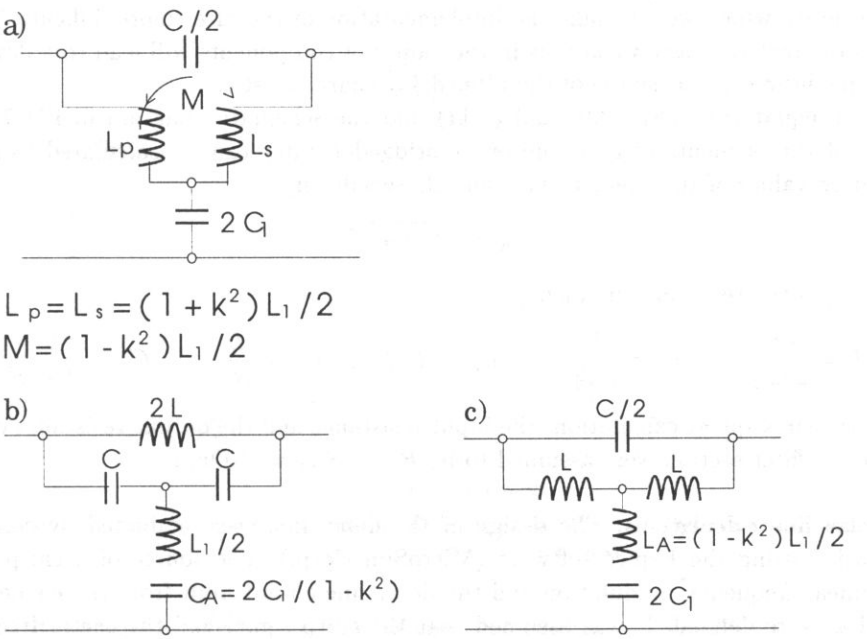

Fig. 6. The schematic diagrams of second-order bridge-T filters for $k > 1$ (a) and for $k < 1$ (b and c).

Comparison between $H(\omega)$ and $H_2(\omega)$ (Eq. (2.5)) shows that

$$\frac{1}{RC} = 2\alpha = k\overline{\omega}_0, \qquad \frac{1}{LC} = \alpha^2 + \beta^2 = \overline{\omega}^2 \tag{3.8}$$

and, hence the following expression is valid:

$$L = \frac{kR}{\overline{\omega}_0}, \qquad C = \frac{1}{k\overline{\omega}_0 R} = \frac{1}{L\overline{\omega}_0^2}. \tag{3.9}$$

The parallel resonance of L and C occur at the frequency ω_0, which with the use of (3.4) leads to:

$$Z_b = \frac{R^2\left(1 - LC\omega^2\right)}{j\omega L} = j\omega R^2 C + \frac{1}{j\omega(L/R^2)} = j\omega L_1 + \frac{1}{j\omega C_1}. \tag{3.10}$$

This is the impedance of a series circuit containing L_1 and C_1, where:

$$\begin{aligned} L_1 &= R^2 C, \\ C_1 &= L/R^2. \end{aligned} \tag{3.11}$$

The series resonance also occurs at ω_0.

The second-order bridged-T filter for the values $k > 1$ and $k < 1$ ($k = 2\alpha/\omega_0$) is shown in Fig. 6 a. When high-frequency signals are used a better choice is to use the capacitance circuit (Fig. 6 b) because higher values of inductances needed. It should be noted that the assembly and measurements of low inductances are more difficult and less accurate which would make the implementation of the filter more difficult. This is due to the fact that any variations in the values of components will lead to a deviation from the desired linear shape of the filter delay characteristic.

From equations (3.8), (3.9) and (3.11) and the schematic diagram in Fig. 7 b, the values of the elements of a second-order bridged-T filter can be calculated using the optimized values of the coefficients α and β. Specifically:

$$\omega_0 = \sqrt{\alpha^2 + \beta^2},$$

where ω_0 is the resonance frequency,

$$L = \frac{kR}{2\pi\omega_0}, \qquad C = \frac{1}{L\omega_0^2}, \qquad L_1 = R^2 C, \qquad C_1 = \frac{L}{R^2}, \qquad C_A = \frac{2C_1}{1 - k^2}.$$

In the subsequent calculations the input resistance and the output resistance of each bridged T filter section were assumed to be $R_{\text{in}} = R_{\text{out}} = 50\,\text{Ohms}$.

Delay line calculations. The design of the delay line was conducted by computer simulation using the Pspice software (MicroSim Corp.). The source of a chirp signal with linear frequency modulation and the delay line circuit built from the elements R, L and C were defined. It was assumed that the chirp signal had the centre frequency $f_0 = 40\,\text{MHz}$, $\Delta F = 20\,\text{MHz}$, the pulse duration $T = 1080\,\text{ns}$ (four filter section were assumed each having a $T = 270\,\text{ns}$).

As mentioned previously in the computer simulation a 24-th order filter section consisting of 12 second-order cascaded filters sections was investigated. The values of the discrete R, L, C elements were determined from the calculations outlined above. Figure 7 a, b shows the frequency responses of the filter obtained for different delays. As

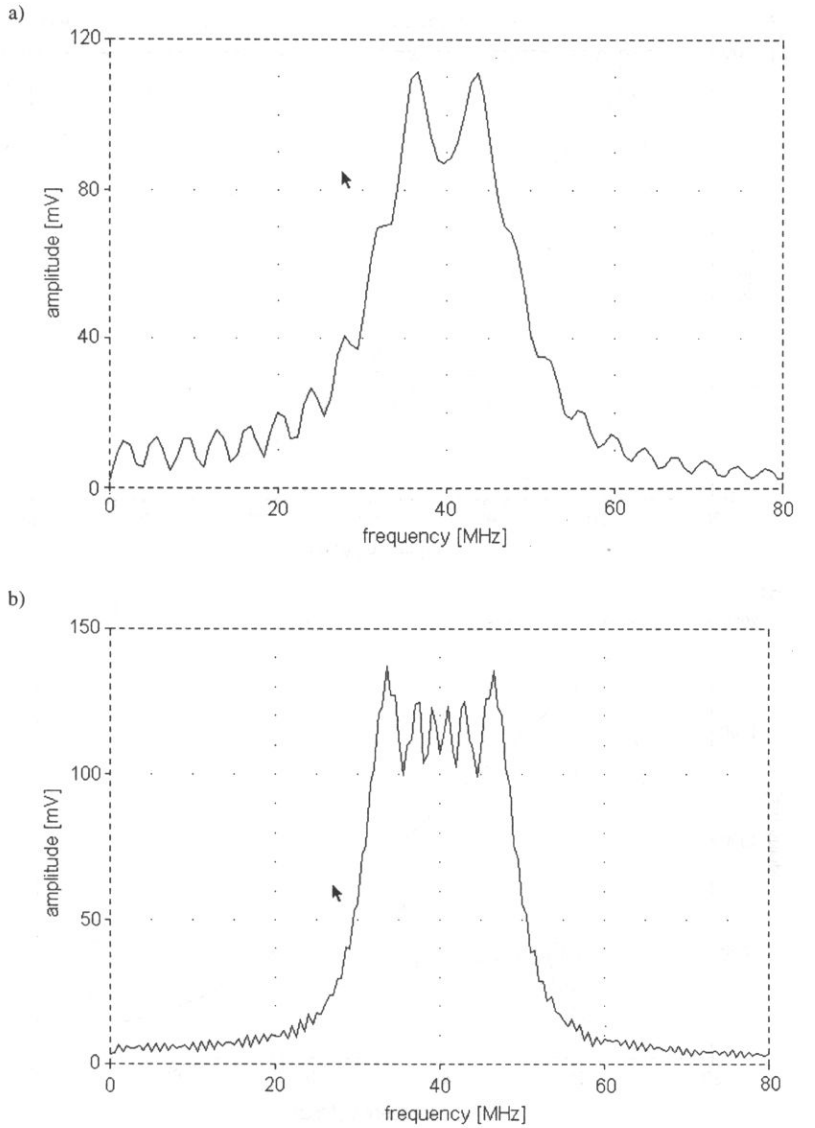

Fig. 7. Spectral amplitude of the rectangular chirp signal (a) $T = 270\,\text{ns}$ (for one filter section), (b) $T = 1080\,\text{ns}$ (for four filter sections).

expected the frequency responses show Fresnel inequalities which depend on the pulse length T (for the constant ΔF values). As the value of T increases these inequalities become smaller. A sinusoidal signal with a normalized amplitude over the frequency range between 25 and 55 MHz (this bandwidth was by $+/-5\,\text{MHz}$ wider than the modulation bandwidth) was used to determine the frequency response of the delay line model. The frequency response is the most important characteristic of the filter system, determining the quality of the matching of the model to the chirp signal.

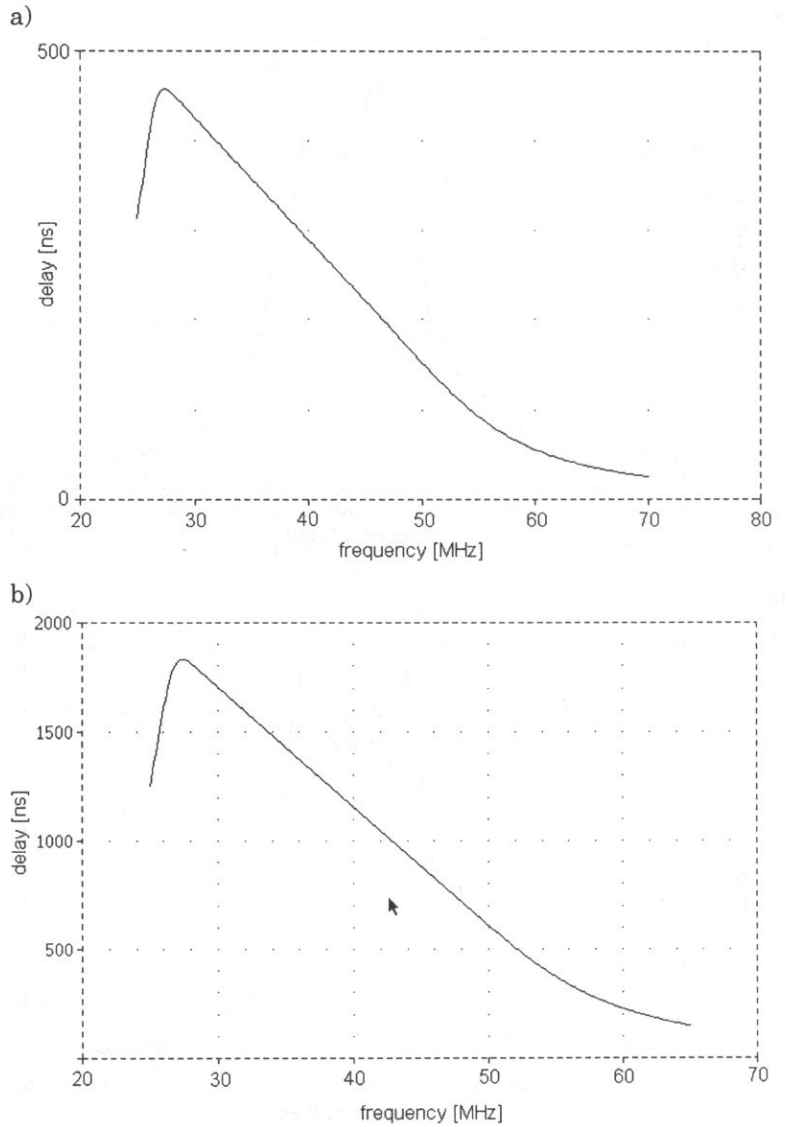

Fig. 8. The delay characteristic as a function of the frequency of the filter designed: (a) for one section of the filter, (b) for four sections of the filter.

The plots in Fig. 8 a, b show the delay characteristics of the chirp signal obtained for one filter section and four identical cascaded filter sections. The overall delay versus frequency, the achievable delay range for frequencies between 30 and 50 MHz and the initial and final chirp signal delays can be read from these plots. It can also be noted that the transfer function of an ideal, optimized filter consisting of one or more sections is linear in nature. This confirms that the filter design procedure presented here is adequately matched to the chirp signal.

Time response. As a next step in the numerical design the time response of the filter designed was investigated. Figure 9 a, b show pulses after compression for one and three series-connected filter sections.

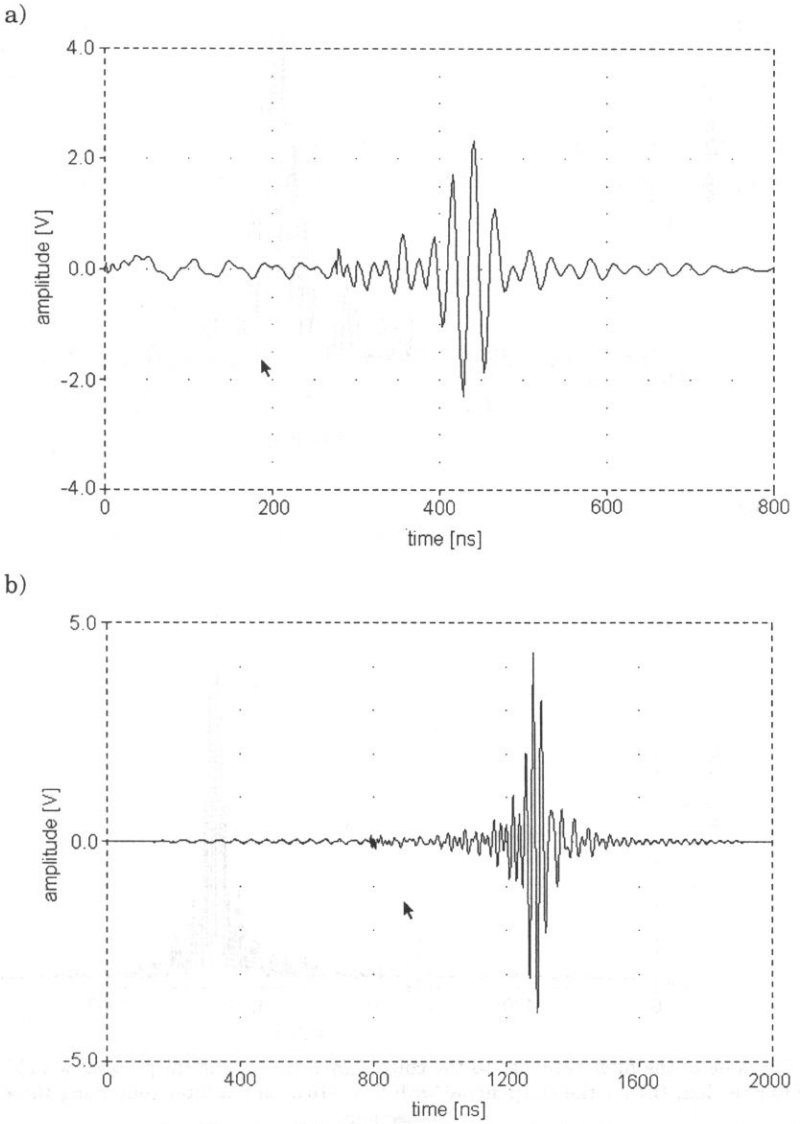

Fig. 9. Filter response to the chirp signal: (a) for the chirp signal with $T = 270$ ns and one filter section, (b) for the chirp signal with $T = 810$ ns and a filter containing three cascaded sections.

Given the very complex analysis of a system built from four sections, with the computer hardware configuration in hand the programme PSpice was able to perform a correct analysis of the transient response only for the filter consisting of up to three sections (72-nd order).

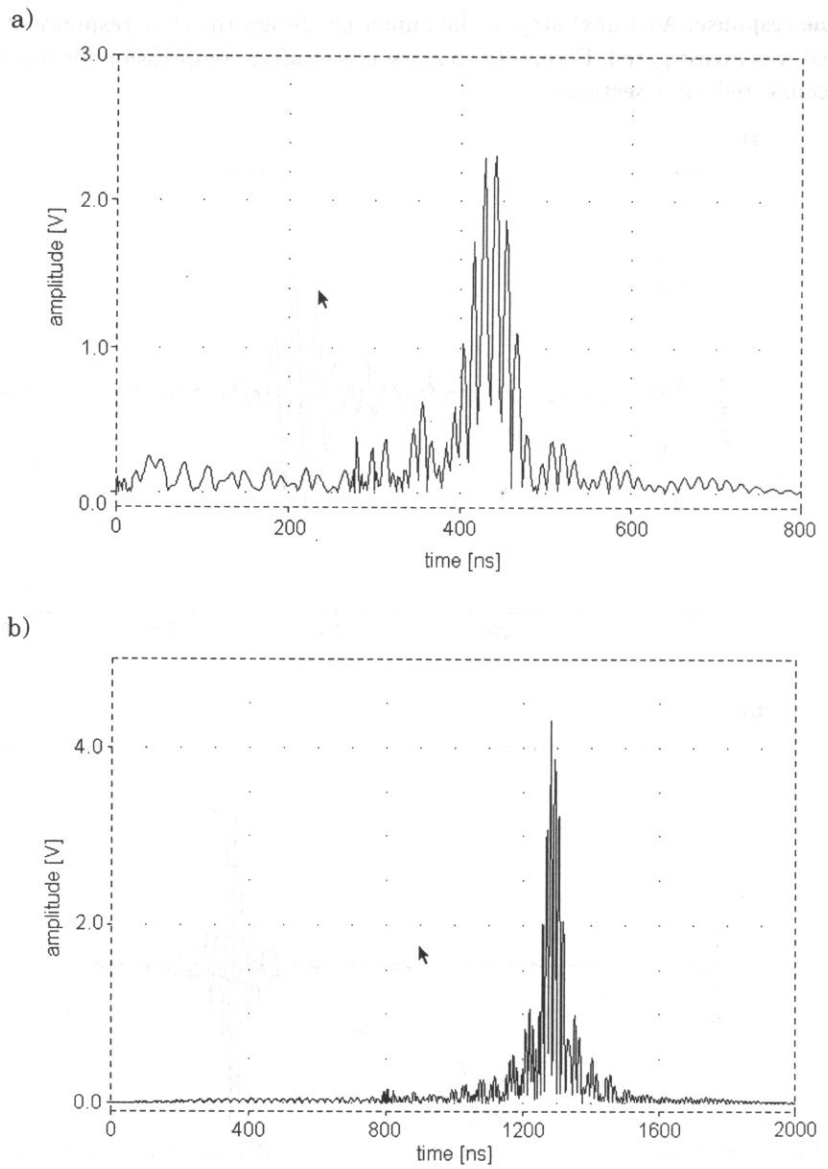

Fig. 10. Envelope of the filter response to the chirp signal: (a) for the chirp signal with $T = 270$ ns and one filter section, (b) for the chirp signal with $T = 810$ ns and a filter containing three cascaded sections.

Figure 10 a, b presents the transient response plots comparable to those presented in Fig. 9 a, b. The plots show the echo behaviour after compression. The calculated parameters of signal compression are listed in Table 1.

The results of the computer simulation presented above verify the analytical analysis and indicate the feasibility of the optimization of the matched filter.

Table 1.

	1 section ($T = 270$ ns)	2 sections ($T = 540$ ns)	3 sections ($T = 810$ ns)
Signal amplitude after compression $[A/A_0]$	2.35	2.90	4.20
Pulse width (main lobe) [ns]	~100	~110	~100

Sensitivity analysis. An analysis of the effect of the tolerance of the filter elements on the delay and transient response characteristics of the delay line was also performed.

a)

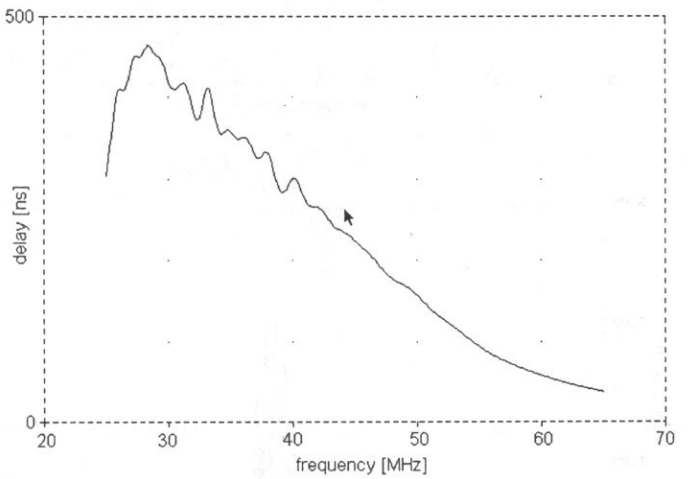

b)

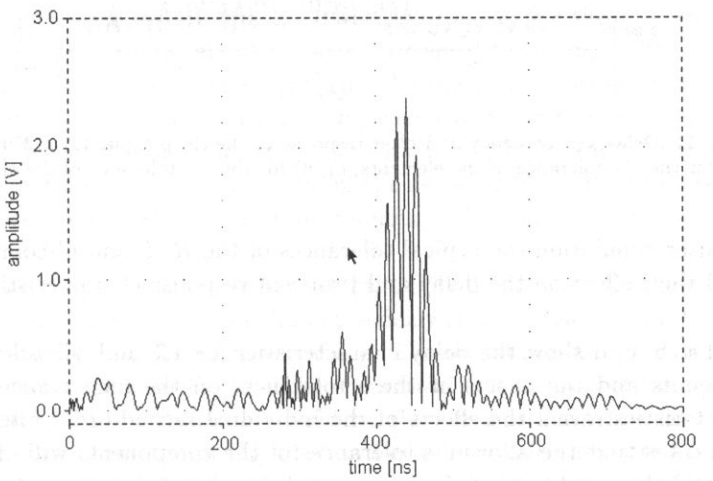

[Fig. 11 a, b]

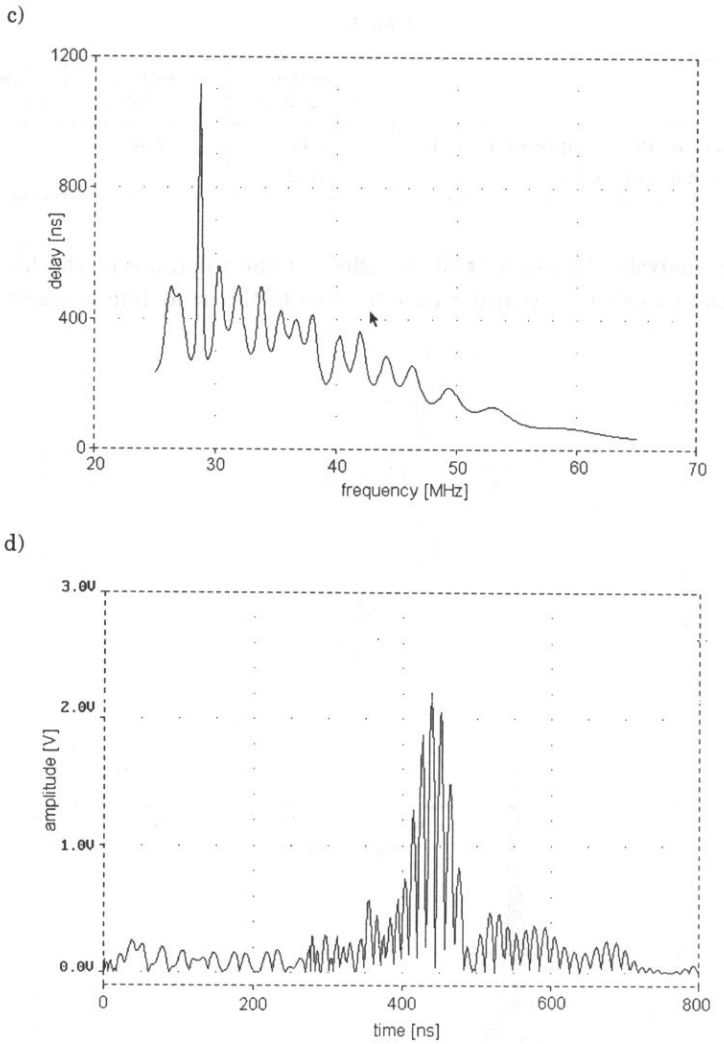

Fig. 11. Delay vs. frequency and filter response to the chirp signal ($T = 270$ ns): a), b) for the 1% tolerance of the elements, c), d) for the 5% tolerance of the elements.

In the computer simulation the typical tolerances of the R, L and C components were assumed and their effect on the delay and transient response characteristics was determined.

Figure 11 a, b, c, d show the delay characteristics for 1% and 5% tolerances of the filter components and the effects of these tolerances on the final transient response. Delay characteristics reveal the effects of the individual second-order filters. Transient response indicates that the allowable tolerances of the components will also affect (although slightly) the amplitude of the compressed signal and the range of the side lobes of the signal.

4. The implementation and experimental verification of the delay filter

One section of the 24-th order all pass filter was designed, constructed and characterized. The design was implemented using bridge-T type filter shown in Fig. 6 b. This implementation offered the most advantageous values of L and C components.

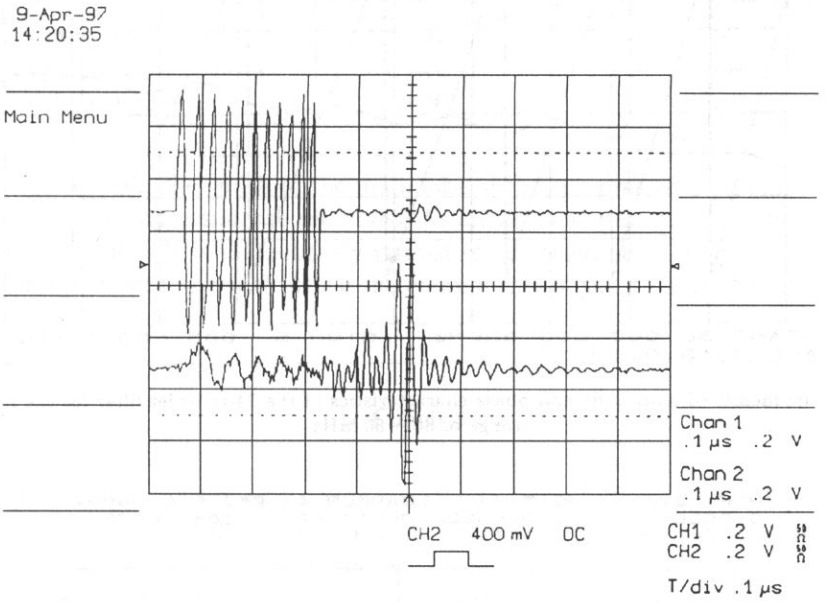

Fig. 12. The chirp signal at the input – (lower plot) and the filter response (upper plot).

The Arbitrary Function Generator LeCroy 9109 was used to generate the chirp signal. This chirp signal was fed to the input of the delay line (24-th order filter). Figure 12 presents the input chirp signal and the response of a single section of the delay line. The maximum output delay is about 250 ns with respect to the input (for a frequency of 40 MHz), which is in excellent agreement with the theoretical assumptions. The output signal from the single section is clearly compressed and has the maximum amplitude amplified by a factor of more than two than that of the input signal. Figure 13 shows the amplitude and phase transfer function of the designed filter. It can be seen that the amplitude varies slightly as a function of frequency; this amplitude variation is due to the losses in the design.

However, the properties of the filter are primarily determined by the delay transfer function or characteristic. Figure 14 shows the delay characteristic for one section of the filter versus frequency for the chirp waveform. The initial and final delays of the filter can also be determined from Fig. 14. The theoretical calculations of the delay transfer function indicate that the function should be that of a straight line (see Fig. 8 a, b), however, the results presented in Fig. 14 show behaviour which deviates somewhat from the expected straight line dependency. This is because the experimentally determined delay of the filter section was about 270 ns versus 250 ns used in computer simulations.

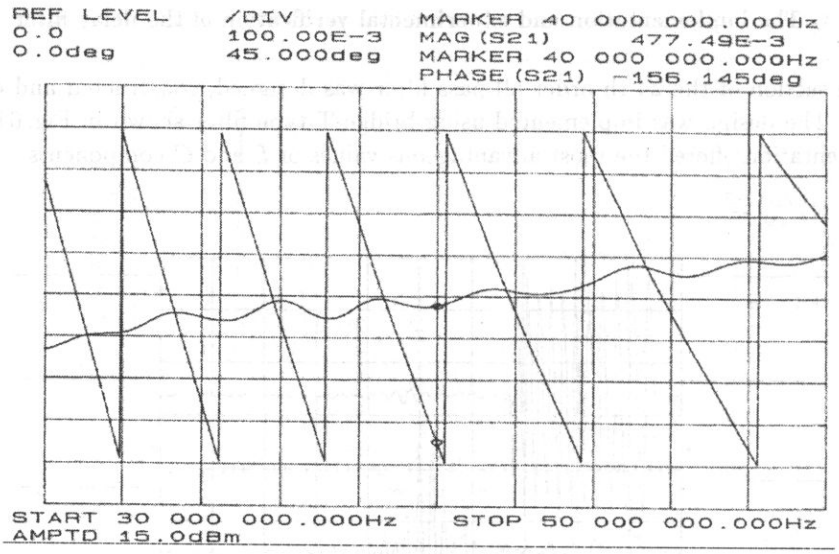

Fig. 13. The measured amplitude and phase characteristics of the 24-th order filter for the frequency range of 30 – 50 MHz.

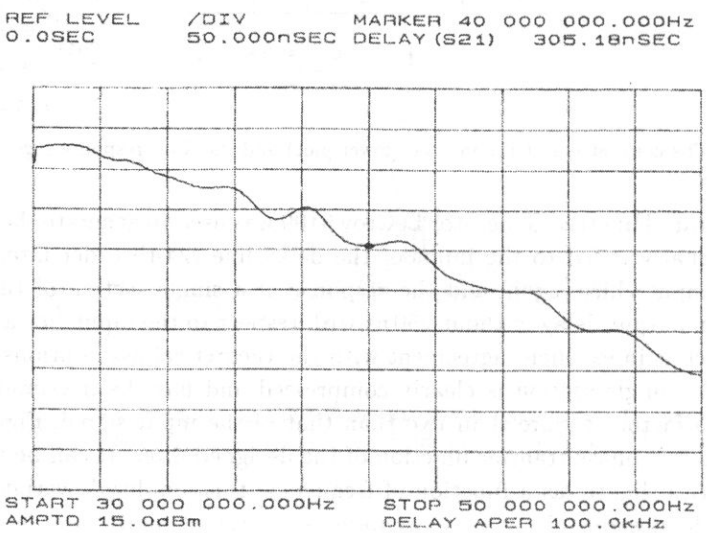

Fig. 14. The measured delay characteristic of the 24-th order filter.

Also, in the computer simulation of the filter section, the delay filter was implemented with ideal capacitance and inductance elements. Thus, the numerical model did not include the effects of parasitic or stray capacitances and assumed lossless L and C elements. Also, the existence of ripples in the characteristics can be traced to nonideal components and their tolerances and the achievable accuracy in filter tuning.

Table 2 compares key parameters of the all pass filter designed. The data of Table 2 indicate that the predicted and measured parameters are in very good agreement.

Table 2.

	Main lobe amplitude [$A/A0$]	Main lobe width [ns]
Mathematical model	2.32	100
Computer simulation	2.35	~100
Filter prototype	2.20	~100

In practice, both the width of the main lobe of the compressed signal and the signal amplitude after compression are preserved. As already mentioned, the slight drop in the value of the amplitude is undoubtedly related to the tolerancies of the filter prototype components and accuracy with which the components of the filter were tuned.

5. Conclusions

The primary goal of this work was to investigate a possibility of using chirp waveforms in very high frequency ultrasound medical imaging to increase range resolution and concurrently maximize penetration depth.

A mathematical analysis was conducted for the chirp waveform and the model of a matched all pass filter at the receiver input which appropriately delayed this signal. The analysis allowed the parameters of the filter to be optimized. The filter model calculated in this way was subsequently analysed by computer simulations which verified the results of the mathematical approach. The theoretical considerations were concerned with both a single filter section and the matched 96-th order all pass filter for chirp signal of 1 μs duration in the frequency range 30 MHz – 50 MHz. A prototype of 24-th order filter was constructed to verify the results of analytical and numerical methods. The filter was investigated in terms of the delay characteristics. Also, the parameters of the chirp signal after compression at the filter output were measured. Excellent agreement was observed between the theoretical predictions and experimental data.

Although the experimental results of this work indicate that the construction of the matched 96-th order all pass filter for chirp signal is feasible, the experimental evaluation of the 24-th order all pass filter was performed using electrical signal only, thus neglecting the effects associated with the electromechanical energy conversion. Continuation of this work will need to include design and optimization of superwide bandwidth transducers so the filter input will receive the echoes converted into the electrical waveforms by the ultrasound transducer. Accordingly, the next stage of this work will include determination of the transfer function of wideband PVDF transducers. The overall performance of the matched filter including degree of compression will most likely depend on the pulse-echo characteristics of those transducers.

Appendix

The delay of the 24-th order AP filtere is given by:

$$D_a(\omega) = 4\sum_{j=1}^{12} \frac{\alpha_j(\omega^2 + \alpha_j^2 + \beta_j^2}{(\alpha_j^2 + \beta_j^2 - \omega^2)^2 + 4\alpha_j^2\omega^2} .$$

Table 3. Starting values and the computed ones of the parameters α_j and β_j.

Starting values α and β for AP filter	Values of α and β after optimization
$\alpha_1 = \alpha_2 = ... = \alpha_{12} = 10.474e6$ [Hz]	$\alpha_1 = 24.211e6$ [Hz]; $\alpha_2 = 13.824e6$ [Hz]; $\alpha_3 = 24.024e6$ [Hz]; $\alpha_4 = 27.219e6$ [Hz]; $\alpha_5 = 30.273e6$ [Hz]; $\alpha_6 = 33.028e6$ [Hz]; $\alpha_7 = 36.169e6$ [Hz]; $\alpha_8 = 39.357e6$ [Hz]; $\alpha_9 = 43.012e6$ [Hz]; $\alpha_{10} = 47.600e6$ [Hz]; $\alpha_{11} = 59.969e6$ [Hz]; $\alpha_{12} = 58.758e6$ [Hz];
$\beta_1 = 193.729e6$ [Hz]; $\beta_2 = 204.204e6$ [Hz]; $\beta_3 = 214.678e6$ [Hz]; $\beta_4 = 225.145e6$ [Hz]; $\beta_5 = 235.619e6$ [Hz]; $\beta_6 = 246.093e6$ [Hz]; $\beta_7 = 256.561e6$ [Hz]; $\beta_8 = 267.035e6$ [Hz]; $\beta_9 = 277.503e6$ [Hz]; $\beta_{10} = 287.977e6$ [Hz]; $\beta_{11} = 298.451e6$ [Hz]; $\beta_{12} = 308.925e6$ [Hz];	$\beta_1 = 188.40e6$ [Hz]; $\beta_2 = 174.42e6$ [Hz]; $\beta_3 = 180.68e6$ [Hz]; $\beta_4 = 200.34e6$ [Hz]; $\beta_5 = 212.34e6$ [Hz]; $\beta_6 = 225.10e6$ [Hz]; $\beta_7 = 238.88e6$ [Hz]; $\beta_8 = 253.95e6$ [Hz]; $\beta_9 = 270.62e6$ [Hz]; $\beta_{10} = 289.64e6$ [Hz]; $\beta_{11} = 321.69e6$ [Hz]; $\beta_{12} = 312.93e6$ [Hz];

References

[1] P. ALTMEYER, S. EL-GAMMAL, K. HOFFMAN [Eds.], *Ultrasound in dermatology*, Springer-Verlag, Berlin 1992.

[2] M. BERSON, L. VAILLANT, F. PATAT, L. POURCELOT, *High resolution real time ultrasonic scanner*, Ultrasound Med. and Biol., **18**, 5, 471–478 (1992).

[3] H.J. BLINCHIKOFF, A.I. ZVEREW, *Filtering in the time and frequency domains*, J. Willey & Sons, New York 1976.

[4] J.L. EAVES and E.K. REEDY [Eds.], *Principles of modern radar*, Van Nostrand, Reihold, New York 1987.

[5] G. FEUILLARD, M. LETHIECQ, L. TESSIER, F. PATAT, M. BERSON, *High resolution B scan imaging of the skin using a 50 MHz P(VDF-TrFe)- based ultrasonic transducer*, European J. Ultrasound, **1**, 2, 183–189 (1994).

[6] J. FILIPIAK, *Zagadnienia syntezy podzespołów z akustyczną falą powierzchniową do obróbki sygnałów złożonych typu chirp* [in Polish], WAT, Warszawa 1993.

[7] H.S. FREW, R.A. GIBLIN, *The choice of ultrasound frequency for skin blood flow investigation*, Bioeng. Skin, **1**, 193–205 (1985).

[8] A. HOSS, H. ERMERT, S. EL-GAMMAL, P. ALTMEYER, *Signal processing in high-frequency broadband imaging systems for dermatologic application*, [in:] Acoustical Imaging, vol. 19, H. ERMERT and H.P. HARJES [Eds.], Plenum Press, New York, 243–249, 1992.

[9] J.R. KLAUDER, A.C. PRICE, S. DARLINGTON, W.J. ALBERSHEIM, *The theory and design of chirp radars*, The Bell System Technical Journal, **39**, 4 (1960).

[10] P.A. LEWIN, *New ultrasound safety indicators and their clinical implications*, Ultrasonografia Polska, **7**, 1, 7–14 (1997).

[11] P.A. LEWIN and M.E. SCHAFER, *Wideband piezoelectric polymer acoustic sources*, IEEE Trans. UFFC, **35**, 175–184 (1988).

[12] G.K. LEWIS, *Chirped PVDF Transducers for Medical Ultrasound Imaging*, Proceeding of Ultrasonic Symposium 1987.

[13] A. NOWICKI, J. LIWSKI, W. SECOMSKI, P. KARŁOWICZ, J. LITNIEWSKI and WYTRYKOWSKI, *Ultrasound system for tissue microsonography*, Proc. X Symp. on Hydroacoustics, 145–150, Gdynia 1993.

[14] M.I. SKOLNIK, *Introduction to Radar Systems*, McGrow-Hill Book Comp. New York 1962.

[15] T. YANO, H. FUKUITA, S. UENO, A. FUKUMOTO, 40 MHz *ultrasound diagnostic system for dermatologic examination*, IEEE 1987 Ultrasonic Symposium Proceeding, 857–878, 1987.

ARCHIVES OF ACOUSTICS
22, 3, 333–342 (1997)

THE CORRELATION BETWEEN THE FRACTURE INDUCED ACOUSTIC EMISSION AND THE COMPRESSIVE STATIC STRENGTH IN PLAIN AND HIGH STRENGTH CONCRETE

J. MIERZWA, K. POGAN

Institute of Building Materials and Structures,
Cracow University of Technology
(31-155 Cracow, 24 Warszawska Str.)

Z. RANACHOWSKI

Institute of Fundamental Technological Research,
Polish Academy of Sciences
(00-049 Warszawa, ul. Świętokrzyska 21)

In this article Acoustic Emission (AE) measurement results for six different concrete compositions, differing in compressive strength, are presented. The aim of the investigation was to find the dependence between the mechanical strength and the count sum of the registered Acoustic Emission. AE signals were measured by a quasi-axial compression test. Two acoustical parameters were examined and compared with the compressive strength and static strength of the compositions tested. The first one was the AE activity during the complete compression process and the second one was the AE activity measured to the point of the start of the instable crack growth propagation process.

1. Introduction

The load increase applied to a concrete structure causes a stress-vave generation process, reflecting the damages occuring in the structure. The Acoustic Emission measurements made in concrete elements under mechanical and thermal stress were described in [1–8]. The mentioned authors confirm the dependence between the parameters of the measuerd AE signal and the damage process in the loaded structure. This may lead to improvements of the concrete composition optimalisation, may help to recognize the destructed microstructures and to determine the mechanical strength of the investigated compositions.

The Acoustic Emission sensor attached to the tested structure converts the energy of the elastic waves mentioned above into electrical signals. The state-of-art in the AE instrumentation allows to detect very small signals, the power of which is of the order of

several picowatts. The sensivity of the AE processors allows them therefore to monitor the destruction processes within a wide range of load levels. This makes it possible to distinguish three separate regions with different AE records on the plot of the AE activity expressed as a function of the applied load:

a) Initial loading noise – the region is characterized by relatively high level of AE activity caused by the initial compaction of the concrete matrix and by the damages on the contact surface between a loading machine and a specimen.The effect described here is hardly detectable in high – strength concretes.

b) Region of the constant AE activity – with a lower level of AE activity caused by the stable growth of the internal microcracks.

c) Precursor to failure – the region of very rapidly increasing AE activity caused by the unstable growth of the microcracks leading to the failure of the structure.

The limit of the first one of the discussed regions corresponds to the limit of proportionality (LOP) that is to be determined from the stress-strain curve plotted during the compression test. This characteristic stress level is also called the initiation stress σ_{I} [1, 6, 7]. The limit of the second region has the notation σ_{II} and corresponds to the static strength [1, 2]. The determination of σ_{II} with the use of the AE measurement is not a complex task since at this stress level there is a significant increase of AE activity. The determination of σ_{I} is more difficult, however. The changes of AE activity preceding and following this stress level are less distinct and require a careful signal processing.

By now, however, there is no satisfactory quantitative relationship between the AE activity and the strength of tested compositions. This relationship, especially derived for high strength concretes, will be discussed in the following paper.

2. Experimental materials and methods

Six concrete compositions, labelled 1 to 6 and differing in their compressive strength were prepared as indicated in Table 1. Each of the prepared series of specimen consisted of 10 members. The compressive strength for these compositions was estimated in the range of 28 – 64 MPa. The cement of Grade "45" was used. The compositions labelled 1, 3 and 5 were based on crushed aggregates and the remaining compositions were based on river aggregates. Additionally, to make high strength compositions, a plasticizer was added to the compositions labelled 3, 4, 5, 6 and silica fume was added to the compositions labelled 5, 6. The specimens were 100 mm sided cubes. The hardening lasted for 28 days at the temperature 18° C and rel. air humidity 95%.

The compression tests were done using the instrumentation shown in Fig. 1. The hydraulical compression machine of type ZT 60 was used to load the specimen. The surfaces of the specimen were polished to uniform the stress distribution and improve the contact with the AE sensor. Additionally, the fibre plates were placed between the specimen and the test machine brackets to minimize the noises generated by the hydraulic drive.The loading was made with $5\,\mathrm{N/cm^2 \cdot s}$ of force increase as it is recommended in [6].

Table 1. Mix proportions of concretes used for the investigation.

Composition No.	Water to cement ratio	Components [kg/m^3]						Plasticity measured by slump test method [cm]
		Cement	Plasticizer	Silica fume	Water	Sand	Aggregates	
1	0.60	297	–	–	178	676	1248	6
2	0.60	349	–	–	210	532	1818	7
3	0.45	284	6	–	147	695	1281	7
4	0.45	359	7	–	162	433	1480	6
5	0.30	598	12	60	180	584	1078	1
6	0.30	645	13	64	194	359	1226	1

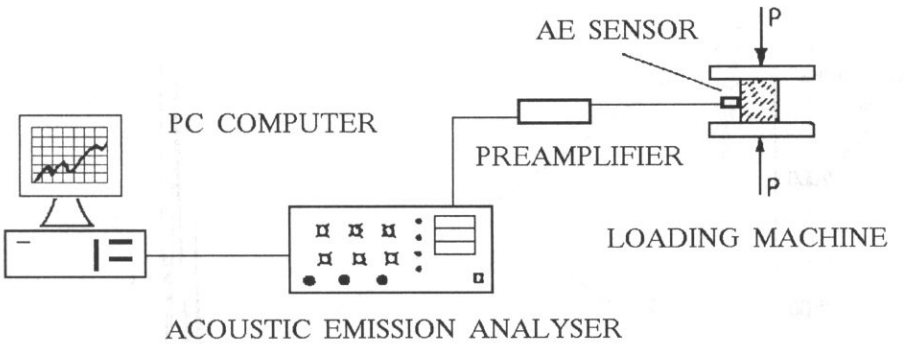

Fig. 1. The instrumentation used during the investigation.

The AE activity was measured by the 200 kHz AE resonance transducer connected to the 40 dB/6 μV RMS noise preamplifier and a 43 dB main amplifier. The AE processor registered the AE signals in the "count" mode, i.e. the internal counter registered each excess beyond the specified rejection level set to 1 V. The AE measurements and the current level of applied stress were transmitted to the PC compatible computer. The averaged results of the AE counts sum and the related compressive strength of the six sets of the examined specimen are shown in Table 2.

Table 2. Averaged AE counts sum measured for the investigated concretes.

Composition No.	Compressive strength [MPa]	AE counts sum registered:	
		until the end of the stable crack propagation region [pulses]	during the entire compression test [pulses]
1	25.9	128726	277073
2	24.4	156273	216203
3	34.8	84189	139024
4	35.9	91918	176468
5	63.6	516097	886318
6	52.1	254242	471905

3. Discussion of the results

The characteristic time plots of the registered AE counts rate during loading the specimens of type 1 and 5 are shown in Figs. 2 and 3, respectively. The AE activity shown in Fig. 2 is typical of the plain concrete. The linear stress increase and the related crack growth process makes the exponential AE counts rate increase. The exponential AE counts rate increase may be explained by the assumption that the number of the AE sources is proportional to the permanently increasing size of the cracks. The example of the AE activity registered in the high strength concrete present the different trend. After the initial counts rate increase a local region of quasi-stable AE generation is observed (as shown in Fig. 3). The crack growth in the mentioned quasi-stable region is blocked on the improved microstructure of the high strength concrete specimen.

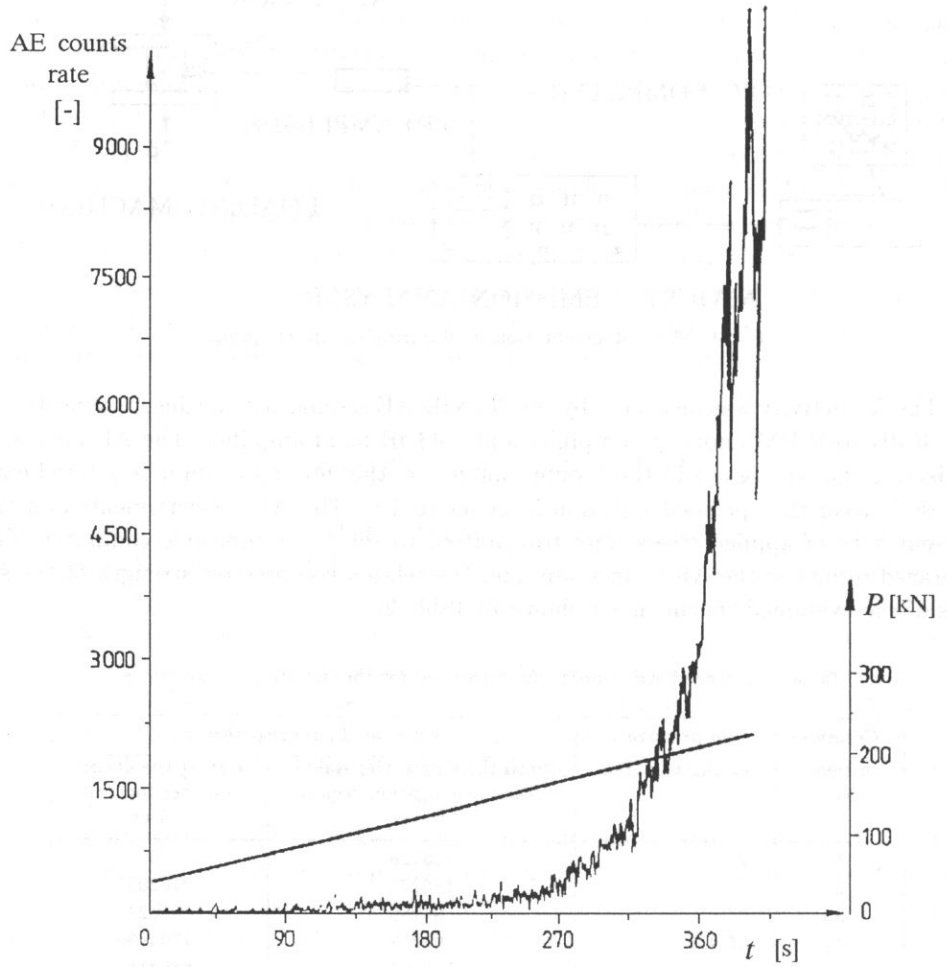

Fig. 2. Example of Acoustic Emission activity vs time plot, registered in compressed concrete composition No. 1.

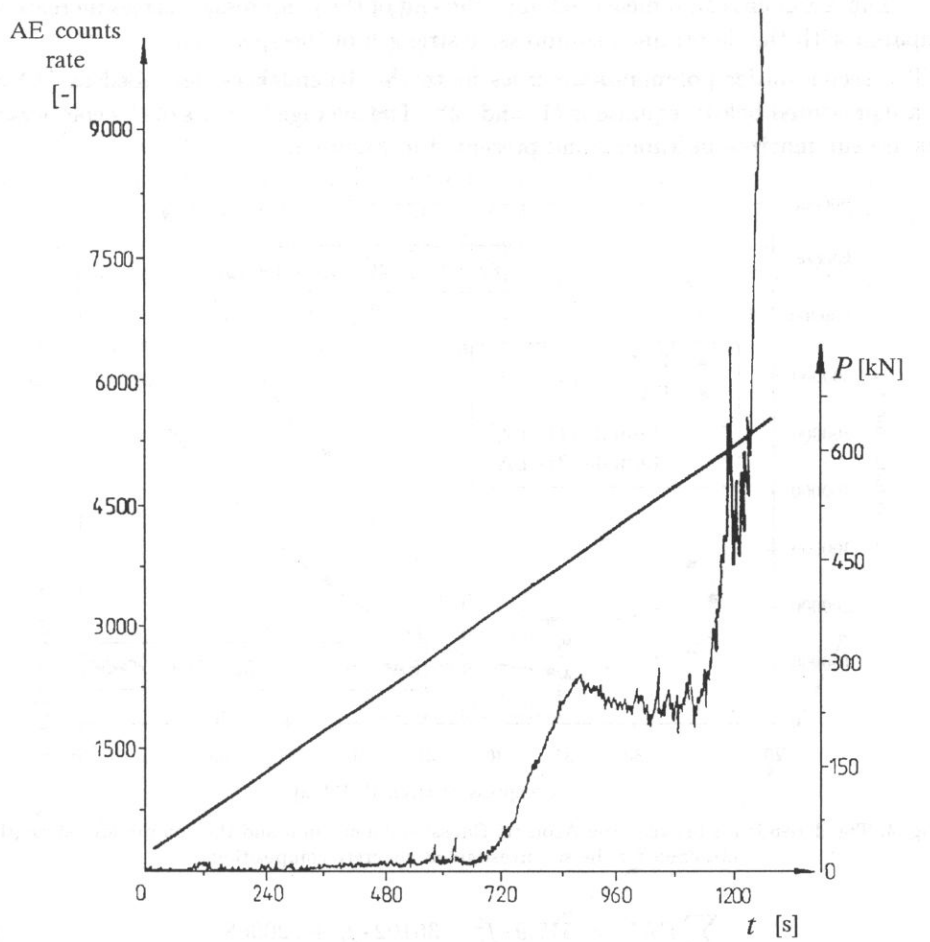

Fig. 3. Example of Acoustic Emission activity vs time plot, registered in compressed concrete composition No. 5.

The averaged records of the AE activity registered during the compression tests were used to determine the dependence upon the mentioned acoustical parameter and the averaged compressive strength which was evaluated for each concrete.

Two concurrent strategies were applied to determine the dependence mentioned above:

A. The AE counts sum measured until the end of the stable crack propagation region was compared with the determined compressive strength of the specimen. The recognition of the end of the stable crack propagation region, when the current couns rate exceeded the threshold value was performed by a software prepared to process the experimental data. The idea of the presented strategy of data processing led to the determination of the specimen parameters without the need of a final destruction of the tested structure.

B. The AE counts sum measured until the end of the compression stress increase was compared with the determined compressive strength of the specimen.

The second-order polynominal curves fit to the dependences described as (A) and (B) are presented below (equations (1) and (2)). The averaged results of the comperssion tests are summarized in Table 2 and presented in Figure 4.

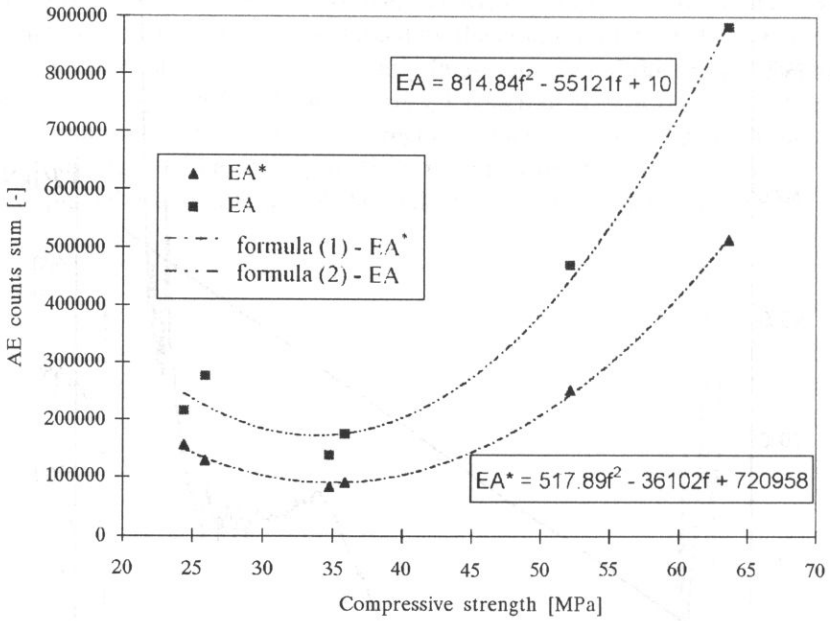

Fig. 4. The dependence between the Acoustic Emission counts sum and the compressive strength obtained for the six investigated concrete compositions.

$$\sum \mathrm{EA}^* = 517.9 \cdot f_c^2 - 36102 \cdot f_c + 720958, \tag{1}$$

$$\sum \mathrm{EA} = 814.8 \cdot f_c^2 - 55121 \cdot f_c + 10^6. \tag{2}$$

where $\sum \mathrm{EA}^*$ – AE counts sum registered until the end of the stable crack propagation region, $\sum \mathrm{EA}$ – AE counts sum registered during the entire compression test, f_c – compressive strength, [MPa].

The correlation coefficients related to the experimental results, presented in Table 2 and by the Eqs. (1) and (2) are equal 0.99 and 0.98, respectively. This confirms the usefullness of the testing strategy labelled A and discussed above. According to that strategy there is a possibility to cease the loading of the concrete elements when the first signs of the unstable crack propagation occurs. Some authors [3, 4] suggest the possibility of *e* self-curing of the fresh concrete after such a test. Using the experimental results listed in Table 2, it is also possible to derive an another regression curve presenting the dependence between the compression strength, $\sum \mathrm{EA}^*$ and $\sum \mathrm{EA}$.

$$\frac{\sum \mathrm{EA}^*}{\sum \mathrm{EA}} = 0.645 \cdot f_c \,. \tag{3}$$

The coefficient of proportionality (0.645) in Eq. (3) denotes the averaged stress level corresponding to the end of the stable crack propagation level for the tested compositions. In some papers [1, 3, 5, 6, 7] the end of stable propagation level in taken as approx. equal to the static strength σ_{II} of the tested structure. The analysis of the AE activity may be also used to determine the start of the stable crack propagation region σ_I. This characteristic material strength parameter is estimated as approx. equal to the LOP. The stress level σ_{II} is determined as the start of the final rapid noise increase region, respectively. The two characteristic stress levels, σ_I and σ_{II} can be recognized in the Fig. 5. and Fig. 6 constructed for all the six concrete compositions. The horizontal axis of the mentioned figures corresponds to the normalized stress understood as a fraction of the ultimate stress. The AE counts increase registered for the consecutive 10% of the normalized stress increase, is shown on the vertical axis.

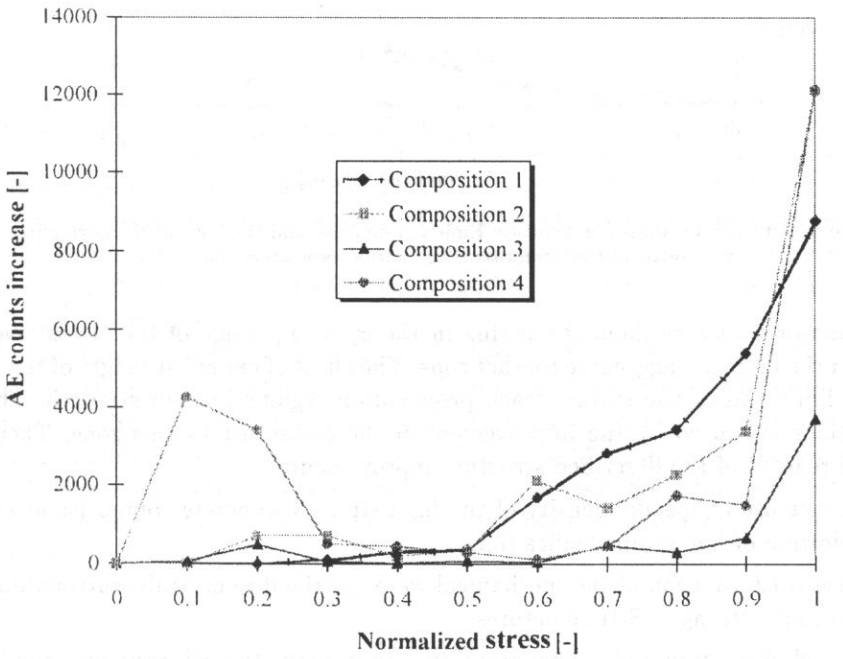

Fig. 5. The dependence between the Acoustic Emission increase and the level of the normalized strain registered in the compressed concrete compositions No. 1 – 4.

The determination of σ_I and σ_{II} with the use of Fig. 5 leads to the conclusion that for all plain concrete compositions the characteristic stress levels are nearly equal. The σ_I level corresponds to the $(0.3 \div 0.4)$ range of σ/f_c and the σ_{II} lone to the $(0.6 \div 0.7)$ range of σ/f_c. The characteristic stress levels presented for the high strength conctretes in Fig. 6 are radically different. There is an absence of the changes of the AE activity related to the σ_I level and the σ_{II} level is greather than 0.7 σ/f_c. The reason for the presented differences in the mechanical properties of plain and high strength concrete may be explained on the basis of microstructural investigations [3].

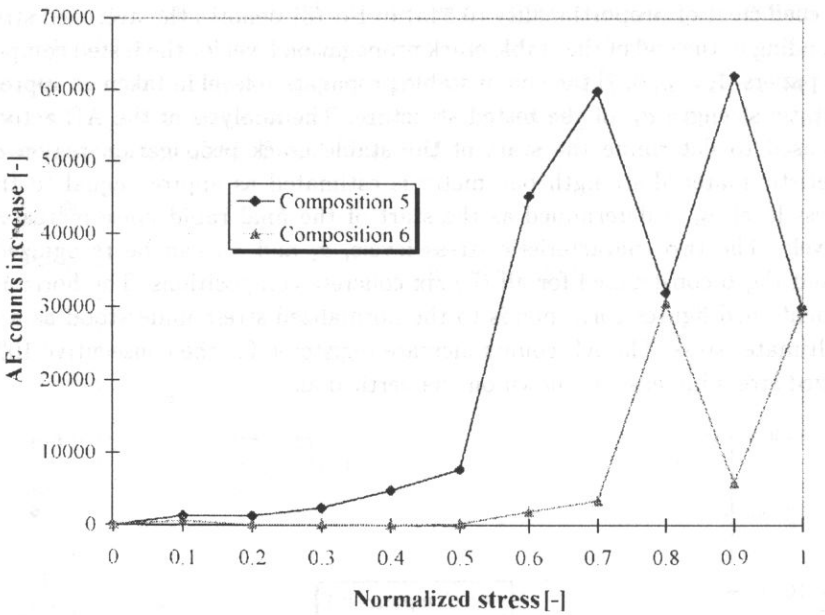

Fig. 6. The dependence between the Acoustic Emission increase and the level of the normalized strain registered in the compressed concrete compositions No. 5, 6.

The major structure damages arising in the σ_I to σ_{II} range of the stress level are located in the mortar – aggregate contact zone. The effect of extended ranges of the linear strength limit and of the stabile crack propagation regions in high strength concrete compositions is caused by the improvement of the endurance of this zone. There are following reasons of the described structure inprovements:

- the increase of specific density of the high strength concrete compositions caused by the addition of fine grained silica fume,
- phase trasformation of the mechanical weak portlandite crystals, surrounding the aggregates, into strong C-S-H structures.

The crack formation and propagation process in high strength concrete may be reconstructed with the use of the AE activity record shown in Fig. 6. in addition of the data presented in the Table 2. However the compressive strength of the high strength concretes is $2 \div 5$ times higher than that of the plain concrete, but the region of unstable crack propagation is relatively short in the high strength concretes. This results in increased brittleness of high strength concretes.

The influence of the kind of the aggregates used in the concrete compositions was discussed in [1], where the plain concrete compositions were prepared by using basalt, limestone and river aggregates. The results of measurements of the characteristic stresses σ_I and σ_{II} during these tests are shown in Table 3. The important conclusion is that the chemically active limestone aggregates form a durable contact zone in connection to the mortar despite its worst mechanical strength among the aggregates investigated.

Table 3. The dependence of characteristic stress levels σ_I and σ_{II} on aggregate type [1].

No.	Aggregate type used in concrete	Average stress levels	
		σ_I	σ_{II}
1	basalt	$0.45f_c$	$0.80f_c$
2	limestone	$0.51f_c$	$0.88f_c$
3	river aggregate	$0.44f_c$	$0.78f_c$

A similar mechanism seems to exist in the high strength concretes investigated by the authors of this paper. The major reason of increased durability of the investigated high strength concretes is the reduced number of structure deffects in the contact zone due to the additional fine grain components.

4. Conclusions

The Acoustic Emission measurements made during the compression tests of the concretes are a useful tool to provide information on the destruction processes in the investigated material. The changes of the AE activity, related to the crack growth and formation processes, enable the determination of the characteristic stages of destruction described by the σ_I and σ_{II} parameters. The parameters specified above are especially important for the understanding of the durability of different concrete compositions under long – term quasi-static loads.

The presented results of the Acoustic Emission measurements show the different destruction schemes in the plain and in the high strength concretes. The latter material is characterized by a relative small intensity of the crack formation process in the region of the initial and intermediate load and by a rapid progress of the instable crack propagation region. The acoustic method to determine the characteristic stress σ_I in the high strength concrete, similar to the procedure applied to the plain concrete will be the object of further investigations.

References

[1] K. Flaga, *The influence of characteristic stresses on the stress-evoked destruction and the strength parameters of concrete* [in Polish], Civil Engineering and Building, Warszawa, 6, pp. 315–322 (1995).

[2] J. Hoła, *Acoustic Emission in concretes* [in Polish], [in:] Acoustic Emission – Sources, Methods, Applications, Collected Papers ed. I. Malecki and J. Ranachowski, Pascal Publishers, Warszawa, 1994, pp. 221–240.

[3] J. Hoła, A. Moczko, *Analysis of destruction processes in chosen concrete structures with an application of ultrasound and AE methods*, D. Sc Thesis [in Polish], Institute of Civil Engineering, Wrocław Polytechnic School, 1984.

[4] J. Hoła, A. Moczko, J. Pyszniak, *The perspectives of the application of the AE method in concrete testing* [in Polish], Building Review, **11**, pp. 477–479 (1988).

[5] J. Hoła, Z. Ranachowski, *Acoustic Emission method in concrete testing* [in Polish], IFTR Reports, 26 (1991).

[6] Z. RANACHOWSKI, *Characteristic stresses determination in concrete with the application of the automatic AE measurements* [in Polish], Institute of Civil Engineering, Wrocław Polytechnic School, 1990.

[7] Z. RANACHOWSKI, *Application of Acoustic Emission method to determine the limit of proportionality and the static strength in concrete*, [in:] Brittle Matrix Composites 3., A.M. BRANDT and I.H. MARSHALL [Eds.], Elsevier Applied Science Publishers, London and New York 1991, pp. 234–239.

[8] H. RÜSCH, *Physicalische Fragen der Betonprüfung*, Zement – Kalk – Gips, **1** (1959).

ARCHIVES OF ACOUSTICS
22, 3, 343–349 (1997)

PHOTOACOUSTIC MEASUREMENTS OF THE THERMAL DIFFUSIVITY OF SOLIDS IN THE PRESENCE OF A DRUM EFFECT

Z. SUSZYŃSKI, M. MALIŃSKI and L. BYCHTO

Institute of Electronics
Technical University in Koszalin
(75-411 Koszalin, Partyzantów 17)

The photoacoustic measurements of the thermal diffusivity of the thick plates of metals are discussed when the drum effect is not quenched. The dominant machanism responsible for the photoacoustic signal was determined. Depending on the configuration arrangement, the ratio of the thermal signal to the thermoelastic bending one was determined. The thermal diffusivity was obtained from both the frequency dependence of the rear amplitude and rear phase characteristics. The influence of the thermoelastic bending on both rear and front frequency characteristics is discussed. The way of calculation of the thermal diffusivity in the case of the results showing strong thermoelastic bending effect is discussed.

1. Introduction

The thermal diffusivity α is defined as the ratio of the thermal conductivity λ, the density ϱ and the thermal capacity c as:

$$\alpha = \frac{\lambda}{\varrho c}. \tag{1.1}$$

It is the measure of the rate of diffusion of heat in a material [1]. There are several methods described in the literature concerning the measurement of this parameter [2–7]. The thermal diffusivity can be calculated from the slope of the I_F/I_R as a function of the frequency of modulation of the exciting beam of light, where I_F and I_R are the amplitudes of the photoacoustic front and rear signals. The same parameter can be drawn from the "phase-lag" method [2]. In this case the phase lag between the rear and front signals gives the information about $l \cdot a_s$ where l is the thickness of the measured sample and a_s is given by the formula:

$$a_s = \sqrt{\frac{\pi f}{\alpha}}. \tag{1.2}$$

For the given frequency of modulation f, the α parameter can be simply determined. This method is independent of the frequency of excitation but it is sensitive, just like the

former one, to the so-called "drum" effect. When this method is used for measurements, one must be sure that the "drum" effect is almost entirely quenched.

It is known that the photoacoustic signal measured at the rear side of the sample p_r is given by the formula [3]:

$$p_r \cong \frac{1}{\sigma \cdot \sigma_g} \cdot \frac{1}{\sinh(l \cdot \sigma)}, \tag{1.3}$$

p_r is the complex value of the periodical part of the overpressure in the photoacoustic cell (PA). The PA signal measured at the front of the sample is given by p_f which is given by:

$$p_f \cong \frac{1}{\sigma \cdot \sigma_g} \cdot \frac{\cosh(l \cdot \sigma)}{\sinh(l \cdot \sigma)}, \tag{1.4}$$

where l is the thickness of the sample, $\sigma = (1 + j) \cdot a_s$, where $a_s = 1/\mu_s$ (μ_s is the thermal diffusion length of the sample at a given frequency of modulation), σ_g is given by the relation $\sigma_g = (1 + j) \cdot a_g$ for air.

The presence of the temperature gradient causes additional contributions to the photoacoustic signal, caused by the expansion of the sample parallel to the beam direction and can create two effects: drum effect and piston effect. The piston effect can be neglected thanks to the construction of the PA cell. The value of the α parameter is important, among others, in the case of modelling of the thermal behaviour of electronic structures in the case of controlling the quality of production of electronic elements [8].

2. Experiment

All experiments were carried out using a photoacoustic cell that allowed to change the contribution of a drum effect in the total photoacoustic signal of the measured samples of different dimensions and shapes; the convenient fitting of the samples that allowed to exchange them quickly.

A schematic diagram of the photoacoustic cell is shown in Fig. 1.

A schematic diagram of the measuring arrangement is shown in Fig. 2.

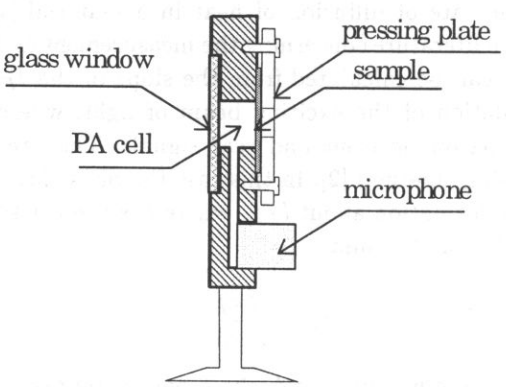

Fig. 1. Schematic diagram of the photoacoustic cell.

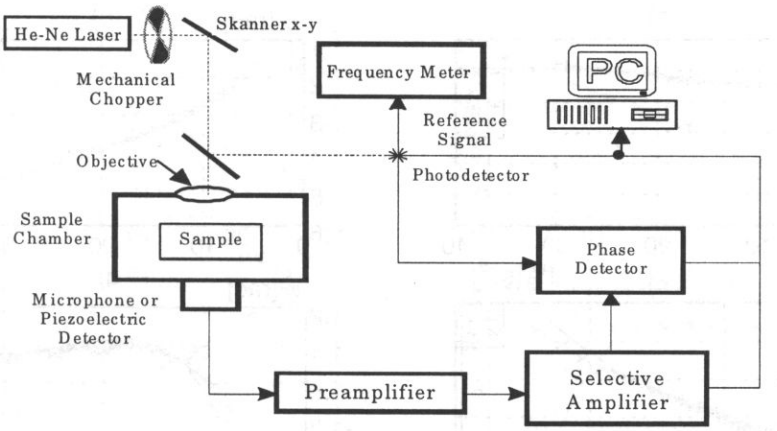

Fig. 2. Schematic diagram of the measuring arrangement.

For excitation of a temperature wave, the 640 nm laser beam of the HeNe laser LGM-222 of 50 mW output power was used. After chopping the beam is divided by the beam splitter. One beam is directed to the photodetector giving the reference signal to the phase detector that was a two channel Tektronix oscilloscope of the 2252 type. The main part of the laser beam is directed straight to the front side or the rear side of the sample. As a pressure detector, a condenser microphone of 10 mm diameter, mounted on one of the sides of the PA cell, was used. As indicated in the earlier articles, the samples needed a special shape, for example disks of 8 mm diameter were used. In our case the sample can be of any shape. It was obtained by a pressing plate with a whole for rear excitation. The samples studied were aluminium plates of the 500 μm thickness.

All the measured samples were optically opaque and the PA signal was strong enough, so that a special blacking of the surfaces was unnecessary.

3. Results and discussion

The results of the measurements for the Al plates are shown in Figs. 3 a, b, c, d.

The figures represent the results of measurements when the expected "drum" effect, caused by the thermoelastic bending of the samples, is maximum. Figure 4 a, b, c, d presents the measurements of the same samples when the pressing plate was used for quenching of the "drum" effect.

The ratio of R/R_c was 1, where R_c is the radius of the PA cell and R is the support radius of the sample. From the theoretical considerations in paper [3], one can state that the expected behaviour of the 4a curve should be as follows:

$$I_R = A \cdot \frac{1}{f} \cdot \exp\left(-c \cdot \sqrt{f}\right), \qquad \text{where} \quad c = l \cdot \sqrt{\frac{\pi}{\alpha}}. \tag{3.1}$$

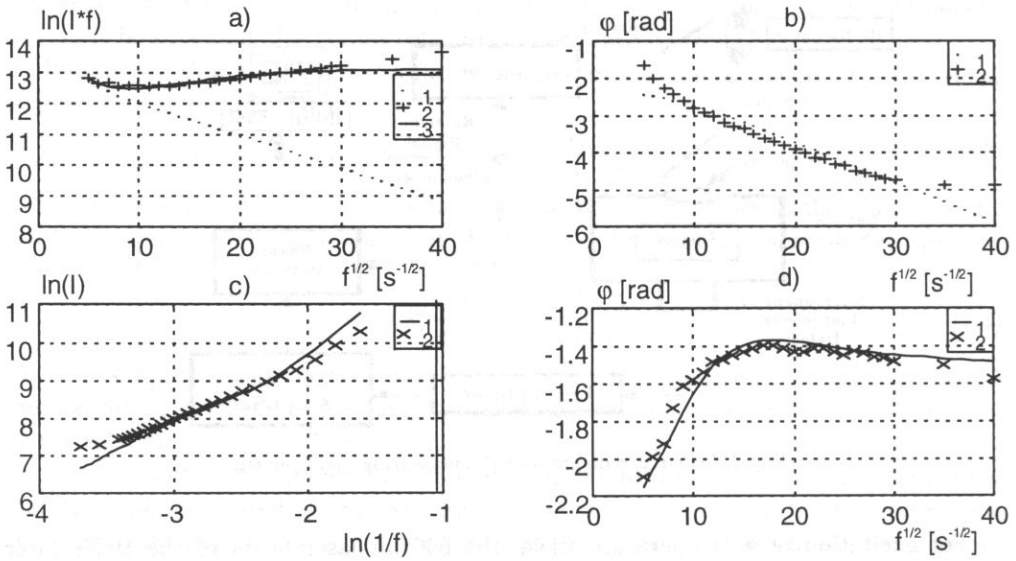

Fig. 3. Plots of the amplitudes and phases of the measured signals. Drum effect not quenched. a) $\ln(I \cdot f)$ versus $\sqrt{f}$ where I is the amplitude of the rear PA signal, the dotted line represents the results from Fig. 4 a (drumless case), b) phase shift of the signal in relation to the reference one versus $\sqrt{f}$, c) $\ln(I)$ versus $\ln(1/f)$ for the front signal, d) the phase shift signal in relation to the ref. signal versus $\sqrt{f}$.

Thus the slope of the curve, defined as

$$c = \frac{d(\ln(I_R \cdot f))}{d(\sqrt{f})}, \tag{3.2}$$

gives the thermal diffusivity of the sample in the measured case as

$$\alpha = \frac{\pi \cdot l^2}{c^2} = 0.67 \frac{\mathrm{cm}^2}{\mathrm{s}}. \tag{3.3}$$

This approximation is valid only for higher frequencies for which the phase of the front signal reaches the value of $\pi/2$. From Fig. 4 d it can be seen that $\sqrt{f} \geq 12.5\,[\mathrm{s}^{-1/2}]$. In such a case the measured object can be considerd to be thermally thick. In the light of the results, curve 4 d is important only at a proper choice of the range of frequencies for which this approximation is valid. For the same range of frequencies, the phase shift of the rear signal (Fig. 4 b) should be of the form $\varphi(\mathrm{rad}) = \mathrm{c} \cdot \sqrt{\mathrm{f}}$ with the same value of the c parameter.

$$c = \frac{d\varphi(\mathrm{rad})}{\mathrm{d}\sqrt{\mathrm{f}}} = \frac{d(\ln(I_R \cdot f))}{d(\sqrt{f})}. \tag{3.4}$$

From the slope of the curve 4 b we obtain the same value of c and consequently, the same value of $\alpha = 0.67\,\mathrm{cm}^2/\mathrm{s}$. From the above mentioned considerations, the equality of the slope coefficients obtained from the amplitude and phase dependences proves

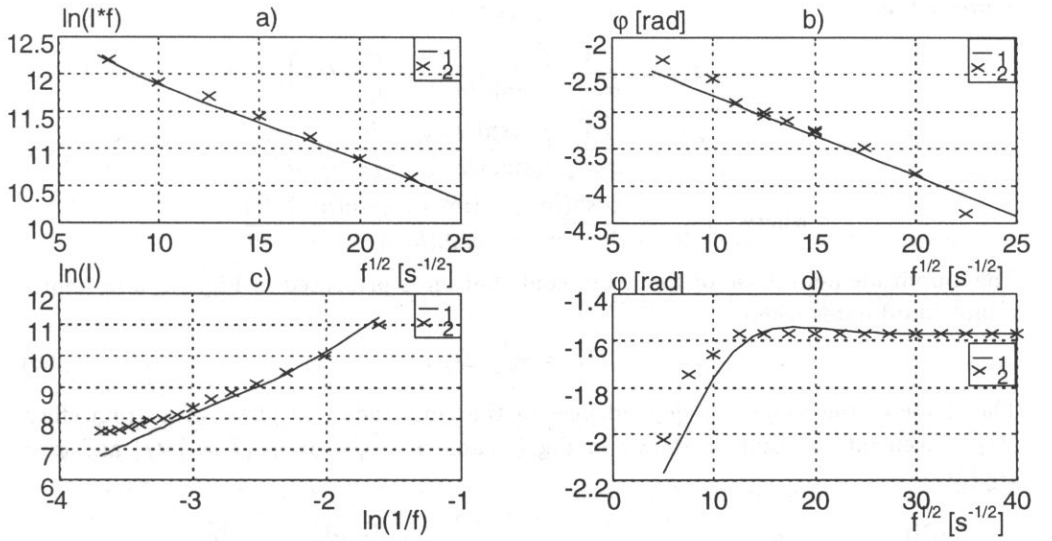

Fig. 4. Plots of the amplitudes and phases of the measured signals. Drum effect strongly quenched. a) $\ln(I \cdot f)$ versus $\sqrt{f}$ where I is the amplitude of the rear PA signal, b) phase shift of the signal in relation to the reference one versus $\sqrt{f}$, c) the phase shift signal in relation to the ref. signal versus $\sqrt{f}$.

that the "drum" effect can be neglected since it is almost entirely quenched by proper fastening in the PA cell.

The situation changes considerably in the case when the contribution of the drum effect can not be neglected as presented in Fig. 3.

The slope coefficients of the curves in Fig. 3 a and Fig. 3 b are considerably different. At the same time, these curves indicates that the sensivity of the parameters to the drum effect are considerably different. It was found that the amplitude characteristics are much more sensitive to it than the phase characteristics measured in the case of rear signal. Because the amplitude of the front signal is much greater than the rear signal but the contribution of the drum effect measured at the same level of excitation is the same in both cases, it follows that the front characteristrics presented in Fig. 4 c, d are much less sensitive to it.

Figure 3 a presents the three characteristics. Curve 1 shows the result for the drumless case for $\alpha = 0.67\,\mathrm{cm}^2/\mathrm{s}$, crosses represent the experimental values, and curve 2 shows the results of computations when the "drum effects" is taken into account. Taking into account the theoretical frequency dependence of the drum effect at some fitting parameters, good correlation between the experimental and calculated results were obtained. If the total PA signal can be presented in the form $\mathrm{PA} = A(\mathrm{PA}_T + B \cdot D_T)$, where PA_T is the thermal contribution to the measured signal and D_T is the drum contribution to the signal, then the B parameter is a measure of the ratio of drum to thermal contributions to the signal being measured. In this case the value $B = 2.5$ was determined. When the contribution of the drum effect can not be neglected then the total PA signal can be

expressed as:

$$P_r = \frac{A}{\sigma_S \sigma_g}\left(\frac{1}{\sinh(l\sigma_S)} + \frac{B}{\sigma_S}\cdot D'_T\right),$$
$$P_F = \frac{A}{\sigma_S \sigma_g}\left(\frac{\cosh(l\sigma_S)}{\sinh(l\sigma_S)} - \frac{B}{\sigma_S}\cdot D'_T\right), \tag{3.5}$$
$$\text{where} \quad D'_T = \frac{\cosh(l\sigma_S) - (l\sigma_S/2)\sinh(l\sigma_S) - 1}{\sinh(l\sigma_S)}.$$

The amplitude and phase of the drum contribution is presented in Fig. 5 a, b in appropriate coordinates where:

$$D_T = \frac{1}{\sigma_s^2 \sigma_g} D'_T. \tag{3.6}$$

The shape of the frequency dependences of the amplitude and phase of a drum effect (D_T) taken into account is shown in Fig. 5 a and b, respectively ($I = |D_T|$ and $\varphi = \arg(D_T)$).

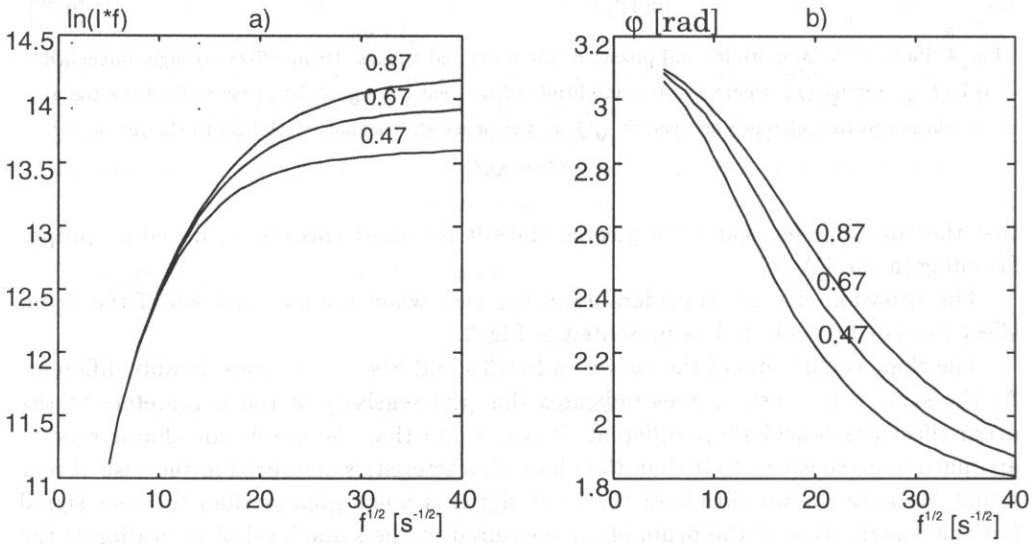

Fig.6. a) Amplitude and b) phase dependences of the drum effect versus $\sqrt{f}$ for diffusivities in cm^2/s for the aluminium sample of a diffusivity of 0.67 and thickness of 500 μm according to Eq. (3.6).

4. Conclusions

The results of the measurements of the thermal diffusivity of thick opaque objects are presented. The influence of the "drum effect" on different thermal wave characteristics was shown and discussed. It was shown that it is possible to calculate the proper value of α even from the results of experiments made on objects with strong drum effects. It was proved that the very simple method of reducing the drum effect applied in the PA cell is sufficient for almost entire quenching of the thermoelastic bending.

References

[1] S. WIŚNIEWSKI, *Thermal diffusivity* [in Polish], WNT, Warszawa, p. 129–138.

[2] O. PESSOA, IR.C.L CESAR, N.A. PATEL, H. VARGAS, *Two beam photoacoustic phase measurement of the thermal diffusivity of solids*, J. Appl. Phys., **60**, 4, 1316–1318 (1986).

[3] N.F. LEITE, N. CELLA, H. VARGAS, *Photoacoustic measurement of thermal diffusivity of polimer foils*, J. Appl. Phys., **61**, 8, 3025–3027 (1987).

[4] C.E. YEACK, R.L. MELCHER, D.S. IHA, *Measurement of thermal diffusivity using a pyroelectric detector*, J. Appl. Phys., **53**, 6, 3947–3949 (1982).

[5] H.J. LEE, R.E. TAYLOR, *Thermal diffusivity of dispersed composites*, J. Appl. Phys., **47**, 1, 148–151 (1976).

[6] A. LACHAINE, *Thermal analysis by photoacoustic phase measurements. Effect of sample thickness*, J. Appl. Phys., **57**, 11, 5075–5077 (1985).

[7] P. CHARPENTIER, F. LEPOUTRE, *Photoacoustic measurements of thermal diffusivity description of the drum effect*, J. Appl. Phys., **53**, 1, 608–614 (1982).

[8] Z. SUSZYŃSKI, M. MALIŃSKI, L. BYCHTO, Proceedings of the XVIII National Conference of the Circuit Theory and Electronic Circuits, Łódź 1995, vol. 1, pp. 329–333.

ARCHIVES OF ACOUSTICS
22, 3, 351–357 (1997)

OBSERVATION OF HYPERSONIC ACOUSTIC WAVES IN A $LiTaO_3$ CRYSTAL

T. BŁACHOWICZ and Z. KLESZCZEWSKI

Institute of Physics
Silesian Technical University
(44-100 Gliwice, ul. Krzywoustego 2)

In this paper, we would like to present theoretical considerations and results of the observation of acoustic quasi-longitudinal and quasi-transverse waves in a sample of known crystalographic orientation. The Brillouin light scattering method is suitable for investigations of the acoustic properties of materials in the hypersonic range. Results of the calculation based on ultrasonic data are not in agreement with experimental hypersonic measurements. We have observed a dispersion in the velocity of the acoustic waves.

1. Introduction

The Brillouin light scattering experiment has been well known for many years as a very sensitive method for studying phonons from acoustic branch in the hypersonic range, both in transparent (bulk phonons) [1, 2, 3, 4] and nontransparent media (surface phonons) [5, 6].

From the clasical point of view, the effect of scattering is connected with the Doppler shift in frequency caused by interaction between the electromagnetic and the driving acoustic waves. The elementary source of scattered light is a radiating dipole induced by the light wave. However, the most important feature are the space-time changes in the dielectric constant tensor of the investigated material. From the quantum point of view, the creation and annihilation processes of phonons by photons are responsible for a typical picture in that Brillouin lines appear.

The main problem for the experimental work is to meaure Brillouin signals in the presence of the elastically scattered light. In our case a single photon counting method was used. We would like to present results of measurements of velocity and frequency of the acoustic wave in piezoelectric $LiTaO_3$ crystal. Theoretical predictions were based on ultrasonic data.

2. Theoretical calculations

There are two main principles for performing the calculations. The first one is the second Newton's law describing the propagation of an acoustic wave in any direction

of the crystal. The second one is the momentum conservation law which connects the momentum wave vector of the incident light $\mathbf{k}$ with the wave vector of the scattered light $\mathbf{k}'$ and with the wave vector of the acoustic wave $\mathbf{q}$

$$\mathbf{q} = \mathbf{k}' - \mathbf{k}. \tag{2.1}$$

For the geometry of scattering presented in Fig. 1 we have

$$\begin{aligned} q_x &= k'_x - k_x\,, \qquad q_y = k'y - k_y\,, \qquad k'_x = k'\cos\alpha\,, \\ k'_y &= k'\sin\alpha, \qquad k_x = -k\sin\alpha, \qquad k_y = k\cos\alpha, \\ q_x &= k'\cos\alpha + k\sin\alpha \cong k(\sin\alpha + \cos\alpha), \\ q_y &= k'\sin\alpha - k\cos\alpha \cong k(\sin\alpha - \cos\alpha), \end{aligned} \tag{2.2}$$

where α is the angle between the [100] crystalographic axis and the direction of scattering. We can define the unit wave vector of the acoustic wave as

$$\boldsymbol{\chi} = \frac{\mathbf{q}}{q}; \tag{2.3}$$

from this point we can change the letter notation to the number one. Thus we have

$$\chi_1 = \chi_x = \frac{\sqrt{2}}{2}(\sin\alpha + \cos\alpha) \qquad \chi_2 = \chi_y = \frac{\sqrt{2}}{2}(\sin\alpha - \cos\alpha), \qquad \chi_3 = \chi_z = 0. \tag{2.4}$$

with the obvious condition for those vectors $\chi_1^2 + \chi_2^2 = 1$.

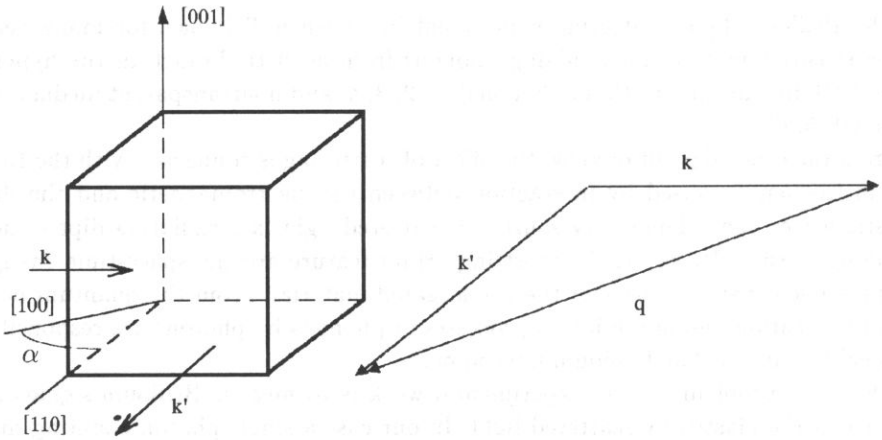

Fig. 1. Geometry of the scattering; α is the angle between the [100] crystalographic axis and the direction of scattering.

Detailed calculations of the expected values of frequencies, velocities and the kind of polarization of the acoustic wave can be find in [7] and in our earlier work [8]. Let us show the basic elements of the algorithm of calculations. By solving the equation of motion

$$\varrho\frac{\partial^2 u_i}{\partial t^2} = \frac{\partial}{\partial x_j}T_{ij} \tag{2.5}$$

(where ϱ is the material density, u_i is the vector of displacement caused by the acoustic wave and T_{ij} is the stress tensor connected by the Hook's law with strains represented by the strain tensor and the stress induced electric field

$$T_{ij} = c^{ef}_{ijkl} S_{kl} - e_{nij} E_n \tag{2.6}$$

in that the piezoelectric tensor e_{nij} appears) and modifying by the piezoelectric effect, the effective elastic constants are [9]

$$c^{ef}_{ijkl} = c_{ijkl} + \frac{e_{pij} e_{qkl} \chi_p \chi_q}{\varepsilon^S_{mn} \chi_m \chi_n} . \tag{2.7}$$

In the above formula the elements of the unit wave vector of the acoustic wave $\boldsymbol{\chi}$ become visible (see Eq. (2.4)). By substitution (2.7) to (2.6) and both those equations to (2.5), the following condition is obtained:

$$\det [Q_{ik} - X_i \delta_{ik}] = 0, \tag{2.8}$$

where the tensor $Q_{ik} = c^{ef}_{ijkl} \chi_j \chi_l$ is called the characteristic matrix the eigenvectors of which describe the kind of polarization, while the eigenvalues $X_i = \varrho v_i^2$ inform about the velocities of the acoustic waves. For our configuration of scattering the effective elastic constants are as follows [10]:

$$\begin{aligned}
c^{ef}_{11} &= c_{11} + \frac{e_{21} e_{21} (\sin\alpha - \cos\alpha)^2}{2\varepsilon_{11}}, & c^{ef}_{24} &= -c_{14} + \frac{e_{22} e_{24} (\sin\alpha - \cos\alpha)^2}{2\varepsilon_{11}}, \\
c^{ef}_{22} &= c_{11} + \frac{e_{22} e_{22} (\sin\alpha - \cos\alpha)^2}{2\varepsilon_{11}}, & c^{ef}_{56} &= c_{14} + \frac{e_{15} e_{16} (\sin\alpha + \cos\alpha)^2}{2\varepsilon_{11}}, \\
c^{ef}_{12} &= c_{12} + \frac{e_{21} e_{22} (\sin\alpha - \cos\alpha)^2}{2\varepsilon_{11}}, & c^{ef}_{21} &= c_{12} + \frac{e_{22} e_{21} (\sin\alpha - \cos\alpha)^2}{2\varepsilon_{11}}, \\
c^{ef}_{44} &= c_{44} + \frac{e_{24} e_{24} (\sin\alpha - \cos\alpha)^2}{2\varepsilon_{11}}, & c^{ef}_{55} &= c_{44} + \frac{e_{15} e_{15} (\sin\alpha + \cos\alpha)^2}{2\varepsilon_{11}}, \\
c^{ef}_{14} &= c_{14} + \frac{e_{21} e_{24} (\sin\alpha - \cos\alpha)^2}{2\varepsilon_{11}}, & c^{ef}_{41} &= c_{14} + \frac{e_{24} e_{21} (\sin\alpha - \cos\alpha)^2}{2\varepsilon_{11}}, \\
c^{ef}_{65} &= c_{14} + \frac{e_{16} e_{15} (\sin\alpha + \cos\alpha)^2}{2\varepsilon_{11}}, & c^{ef}_{66} &= \frac{c_{11} - c_{12}}{2} + \frac{e_{16} e_{16} (\sin\alpha + \cos\alpha)^2}{2\varepsilon_{11}}.
\end{aligned}$$

The other elastic constants are not modified by the stress induced internal electric field due to the piezoelectric effect. The elements of the characteristic matrix are as follows:

$$\begin{aligned}
Q_{11} = &\left[c_{11} + \frac{e_{21} e_{21}}{2\varepsilon_{11}} (sin\alpha - \cos\alpha)^2 \right] \frac{1}{2} (\sin\alpha + \cos\alpha)^2 \\
&+ \left[c_{66} + \frac{e_{16} e_{16}}{2\varepsilon_{11}} (\sin\alpha + \cos\alpha)^2 \right] \frac{1}{2} (\sin\alpha - \cos\alpha)^2, \\
Q_{22} = &\left[c_{66} + \frac{e_{16} e_{16}}{2\varepsilon_{11}} (\sin\alpha + \cos\alpha)^2 \right] \frac{1}{2} (\sin\alpha + \cos\alpha)^2 \\
&+ \left[c_{22} + \frac{e_{22} e_{22}}{2\varepsilon_{11}} (\sin\alpha - \cos\alpha)^2 \right] \frac{1}{2} (\sin\alpha - \cos\alpha)^2,
\end{aligned}$$

$$Q_{33} = \left[c_{55} + \frac{e_{15}e_{15}}{2\varepsilon_{11}}(\sin\alpha + \cos\alpha)^2\right]\frac{1}{2}(\sin\alpha + \cos\alpha)^2 + \left[c_{44} + \frac{e_{24}e_{24}}{2\varepsilon_{11}}(\sin\alpha - \cos\alpha)^2\right]\frac{1}{2}(\sin\alpha - \cos\alpha)^2,$$

$$Q_{23} = \left[c_{56} + \frac{e_{15}e_{16}}{2\varepsilon_{11}}(\sin\alpha + \cos\alpha)^2\right]\frac{1}{2}(\sin\alpha + \cos\alpha)^2 + \left[c_{24} + \frac{e_{22}e_{24}}{2\varepsilon_{11}}(\sin\alpha - \cos\alpha)^2\right]\frac{1}{2}(\sin\alpha - \cos\alpha)^2,$$

$$Q_{31} = \left[c_{14} + \frac{e_{21}e_{24}}{2\varepsilon_{11}}(\sin\alpha - \cos\alpha)^2 + c_{56} + \frac{e_{15}e_{16}}{2\varepsilon_{11}}(\sin\alpha + \cos\alpha)^2\right] \cdot \frac{1}{2}(\sin\alpha + \cos\alpha)(\sin\alpha - \cos\alpha),$$

$$Q_{12} = \left[c_{12} + \frac{e_{21}e_{24}}{2\varepsilon_{11}}(\sin\alpha - \cos\alpha)^2 + c_{66} + \frac{e_{16}e_{16}}{2\varepsilon_{11}}(\sin\alpha + \cos\alpha)^2\right] \cdot \frac{1}{2}(\sin\alpha + \cos\alpha)(\sin\alpha - \cos\alpha).$$

3. Numerical calculations

In our calculations and measurements the angle α is equal to 60°. The data for the calculations were taken from [11]. The results are collected in Table 1 and 2. The values of the Q_{ik} characteristic matrix elements are (in $\mathrm{N/m^2}$ units)

$$Q_{ij} = \begin{bmatrix} 2.23624 \cdot 10^{11} & 3.499963 \cdot 10^{10} & -5.499941 \cdot 10^{9} \\ 3.499963 \cdot 10^{10} & 1.02376 \cdot 10^{11} & -9.52662 \cdot 10^{9} \\ -5.499941 \cdot 10^{9} & -9.52662 \cdot 10^{9} & 9.4 \cdot 10^{10} \end{bmatrix}. \tag{3.1}$$

Table 1. Eigenvectors of the Q_{ik} matrix.

γ_1	γ_2	γ_3	polarization
−0.951566	−0.288025	0.107533	quasi-longitudinal
−0.253025	0.534991	−0.806079	quasi-transverse
−0.174642	0.794246	0.581957	quasi-transverse

($\boldsymbol{\gamma} = [\gamma_1, \gamma_2, \gamma_3]$ is a unit vector of the acoustic wave polarization).

Table 2. Velocities and frequencies of the acoustic waves.

quasi-longitudinal	quasi-transverse T_2	quasi-transverse T_1	
$2.36507 \cdot 10^{11}$	$1.20608 \cdot 10^{11}$	$8.62634 \cdot 10^{10}$	eigenvalues ($X = \varrho v^2$)
5634.3505	4023.5548	3402.7900	velocities [m/s]
36.3423	25.9525	21.9484	frequencies [GHz]

4. Experimental investigations

The measurements were performed with the set described in detail in the articles [8, 12]. The main elements are a single mode argon laser operating at the 514.5 nm line and a pressure scanned Fabry - Perot interferometer [13]. For the detection of very weak signals the single photon counting method was applied. The measurement results were stored in the computer at one second intervals. The Brillouin spectra were performed for 75 GHz and 21.43 GHz within the full spectral range (FSR). In the first case, all kinds of acoustic waves are observed (Fig. 2), but for the second one only a quasi-longitudinal wave (Fig. 3) is seen.

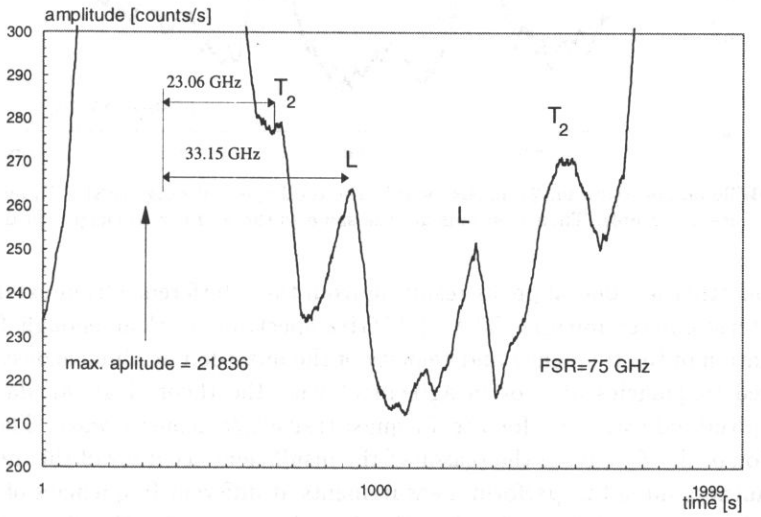

Fig. 2. Brillouin spectrum for 75 GHz within the total spectral range. The registered values of frequencies are as follows: $L = 3.15$ GHz (quasi-longitudinal wave), $T_2 = 23.06$ GHz (quasi-transverse wave). At $T_1 = 20.26$ GHz the quasi-transverse wave is not visible.

The frequency values, averaged over 8 measurements in the case of the quasi-longitudinal wave and over 4 measurements in the case of the T_2 quasi-transverse wave, are presented in Table 3.

Table 3. Measured velocities and frequencies of the acoustic waves.

quasi-longitudinal L	quasi-transverse T_2	quasi-transverse T_1	
5532 ± 73	3848 ± 153		velocities [m/s]
33.15 ± 0.44	23.06 ± 0.92	not found	frequencies [GHz]
1.3	2.2		relative uncertainty [%]

If we compare the Brillouin spectrum for 21.43 GHz and 75 GHz FSR, we can see that the first one is a more suitable for the longitudinal wave observation and it improves the accuracy of the measurements. In the 75 GHz FSR there are stored evanescent laser

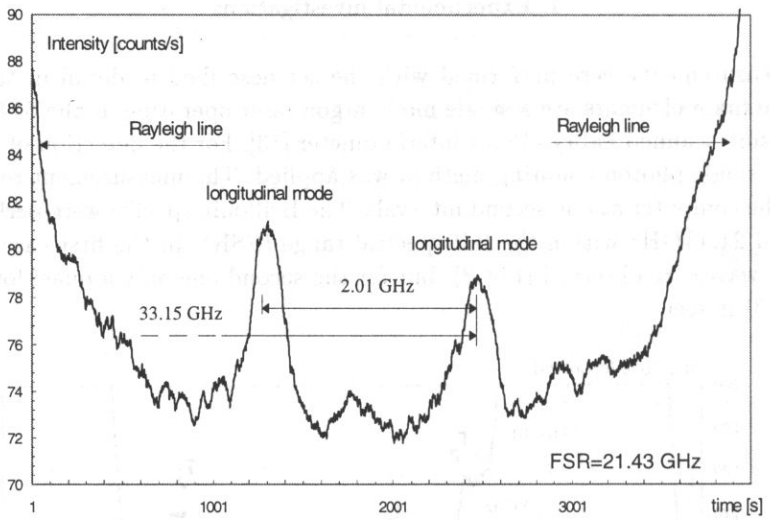

Fig. 3. Brillouin spectrum for 21.43 GHz within the total spectral range (FSR). Transverse waves are not visible. Their positions are the same as those of the Rayleigh's peaks.

modes and other accidental peaks resulting from the interference from external surfaces of the interferometer mirrors. The 21.43 GHz spectrum is clear enough for a precise determination of the frequency and velocity of the quasi-longitudinal acoustic wave. The determined frequencies are not in agreement with the theoretical calculations for the quasi-longitudinal wave and for the T_2 quasi-transverse acoustic wave. The lack of the observation of the T_1 wave is the reason of the insufficient accuracy of the measurements.

The authors intend to perform measurements at different frequencies of the acoustic waves in the same crystalographic direction in order to examine the dispersion relations.

References

[1] GEN LI, X.K. CHEN, N.J. TAO, H.Z. CUMMINS, R.M. PICK, G. HAURET, *Brillouin scattering studies of the transverse acoustic modes of incommensurate* K_2SeO_4, Phys. Rev., **B 44**, 13, 6621–6629 (1991).

[2] L.E. MCNEIL, M. GRIMSDITCH, *Elastic constants of* As_2S_3, Phys. Rev., **B 44**, 9, 4174–4177 (1991).

[3] J.J. VANDERWAL, P. ZHAO, D. WALTON, *Brillouin scattering from the icosahedral quasi-crystal* $Al_{63.5}Cu_{24.5}Fe_{12}$, Phys. Rev., **B 46**, 1, 501–502 (1992).

[4] U. SCHÄRER, P. WACHTER, *Negative elastic constants in intermediate valent* $Sm_xLa_{1-x}S$, Solid St. Comm., **96**, 497–501 (1995).

[5] R. DANNER, R.P. HUEBENER, C.L. CHUN, M. GRIMSDITCH, I.K. SCHULLER, *Surface acoustic waves in* Ni/V *superlattices*, Phys. Rev., **B 33**, 6, 3696–3701 (1986).

[6] M. HUES, R. BHADRA, M. GRIMSDITCH, E. FULLERTON, I.K. SCHULLER, *Effect of high-energy ion irradiation on the elastic moduli of* Ag/Co *superlattices*, Phys. Rev., **B 39**, 17, 12966–12968 (1989).

[7] J.L. FABIELINSKIJ, *Molekularnoje rassiejanie sveta*, Nauka, Moskva 1965.

[8] T. BŁACHOWICZ, Z. KLESZCZEWSKI, *Experimental studies of Brillouin scattering in the* $LiTaO_3$ *crystal* [in Polish], Molecular and Quantum Acoustics, **16**, *23–33 (1995)*.

[9] R.J. O'BRIEN, G.J. ROSACO, A. WEBER, *Brillouin scattering in Lithium Niobate*, [in:] Light scattering spectra of solids, Proceedings of the International Conference on Light Scattering Spectra of Solids, G.B. WRIGHT [Ed.], New York, September 1968, Springer Verlag, New York 1969, pp. 623–630.

[10] T. BŁACHOWICZ, Z. KLESZCZEWSKI, *Observation of the hypersonic waves in the* $LiTaO_3$ *crystal*, Molecular and Quantum Acoustics, **17**, 37–43 (1996).

[11] J. XU, R. STROUD, *Acousto-optic devices: principles, design and applications*, John Wiley and Sons Inc., New York 1992.

[12] T. BŁACHOWICZ, R. BUKOWSKI, Z. KLESZCZEWSKI, *Układ pomiarowy do badania rozpraszania Brillouina w cieczach i ciałach stałych* [in Polish], Zeszyty Naukowe Politechniki Śląskiej, **73**, 7–17 (1996).

[13] T. BŁACHOWICZ, R. BUKOWSKI, Z. KLESZCZEWSKI, *Fabry-Perot intrferometer in Brillouin scattering experiments*, Rev. Sci. Instrum., **67**, 12, 4057–4060 (1996).

ARCHIVES OF ACOUSTICS
22, 3, 367–372 (1997)

C H R O N I C L E

International Symposium on Hydroacoustics and Ultrasonics, 12–16 May 1997, Jurata

The International Symposium on Hydroacoustics and Ultrasonics was organized by the Underwater Acoustics Department of the Naval Academy in Gdynia and the Acoustics Department of the Technical University of Gdańsk as an EAA Symposium (formerly 13th FASE Symposium). It was held under the scheme of celebrating the Millennium of the City of Gdańsk (997–1997). The Symposium has evolved from domestic Symposia on Hydroacoustics that have been held annually since 1984.

The following well known scientists have accepted an invitation to be a member of the Scientific Committee of the Symposium:

Chairman: Prof. IGNACY MALECKI – Poland

Prof. Leif Bjorno – Denmark, Prof. Mack A. Breazeale – USA, Prof. Giovanni Bosco Cannelli – Italy, Dr Robert Chivers – U.K., Prof. Bengt Enflo – Sweden, Prof. Leszek Filipczyński – Poland, Prof. Juan Antonio Gallego–Juarez – Spain, Prof. Halvor Hobaek – Norway, Prof. Zenon Jagodziński – Poland, Prof. Hugh Jones – Canada, Prof. Eugeniusz Kozaczka – Poland, Prof. Werner Lauterborn – Germany, Prof. John S. Papadakis – Greece, Prof. Jerzy Ranachowski – Poland, Prof. Roman Salamon – Poland, Dr. Jean-Pierre Sessarego – France, Prof. Andrzej Stepnowski – Poland, Prof. Alexander Sutin – Russia, Prof. Antoni Śliwiński – Poland, Prof. Jan Thoen – Belgium.

All participants were accommodated in the same holiday centre in Jurata where the symposium took place. This gave the opportunity for further discussion of scientific problems. The programme consisted of 8 invited papers and 54 contributed ones. The invited papers were as follows:

C. BJERRUM-NIESE – Denmark — Simulated performance of an acoustic modem in a multipath channel,

Prof. M.A. BREAZEALE – USA — Overview of the development of nonlinear acoustics,

Dr. P.A. JOHNSON – USA — Earth solids and dynamic nonlinear elasticity,

Prof. E. KOZACZKA – Poland — Fifty years of Polish Hydroaocustics,

Dr. K. KREMER – Germany — Advanced underwater technology with emphasis on acoustic modeling and systems,

Prof. L.M. LYAMSHEV – Russia — Fractals in underwater acoustics,

Prof. A. STEPNOWSKI – Poland — Analysis of fish target strength estimation methods,

Prof. B. WOODWARD – UK — Progress in developing sonar systems for sea bed surveys.

The presented papers covered the following topics: nonlinear acoustics, scattering, sea bed surveying, ship noise and cavitation, signal processing and imaging, fisheries acoustics, sonar systems, sound propagation and modelling, underwater communication, ultrasonics and biomedical diagnostics. Apart from oral presentations a poster session on Ultrasonics was organized. The symposium was attended by 80 participants from 12 countries. The working language for the symposium was English.

The Opening Ceremony included both an introduction by the Chairman of the Board of the EAA Prof. JENS BLAUERT and a letter from the President of FASE Dr ROBERT CHIVERS which marked the continuity between these two organisations.

Apart from the technical programme the social events were organized every day. They started with an ice breaking party. An excursion to Gdańsk was organized on the second day of the symposium. After the cruise to Gdańsk by a sailing ship the participants saw the Old City of Gdańsk, were welcomed by the President of the Programming Council of the Gdańsk Millennium Committee at the Town Hall in Gdańsk and listened to the organ concert in the cathedral in Oliwa. A bonfire and a banquet were included in the social programme too.

The next Symposium on Hydroacoustics will take place in Jurata in May 1998.

XLIV Open Seminar on Acoustics,

Jastrzębia Góra, 15–18.09.1997

XLIV Open Seminar on Acoustics was organized under the sponsorship of the Gdańsk Division of the Polish Acoustical Society. The Seminar was organized by the scientists from the following institutions: Naval Academy (Akademia Marynarki Wojennej), University of Gdańsk (Uniwersytet Gdański), Technical University of Gdańsk (Politechnika Gdańska) and Musical Academy in Gdańsk (Akademia Muzyczna w Gdańsku). 183 participants took part in the event, including 4 guests from abroad. Two volumes of the proceedings contain 110 papers: 7 invited and 103 contributed. During the Seminar 106 papers were presented in 3 parallel sessions. The invited papers were as follows:

Prof. JENS BLAUERT (Germany, Ruhr-Universitaet Bochum): Product-Sound Quality: A New Aspect of Machinery Noise,

Prof. LEIF BJŘRNŘ (Denmark, Technical University of Denmark): Sources of ambient noise in shallow waters,

Prof. ANDRZEJ DOBRUCKI (Politechnika Wrocławska – Technical University of Wrocław): Technological progress and electroacoustic transducers,

Dr GRAŻYNA GRELOWSKA (Akademia Marynarki Wojennej – Naval Academy): Nearfield of high intensity wave sources,

Prof. ADAM LIPOWCZAN (Główny Instytut Górnictwa – Main Institute of Mining): Advisory system to assist localization decisions of road investments regarding sustainable development of the region,

Prof. ANDRZEJ RAKOWSKI (Akademia Muzyczna w Warszawie – Musical Academy in Warsaw): Pitch and pitch scale in music,

Prof. ROMAN SALAMON (Politechnika Gdańska – Technical University of Gdańsk): Detection and positioning of targets in passive sonars.

Other papers were divided into the following sections: Architectural Acoustics (2), Physical Acoustics (9), Medical Acoustics (7), Molecular Acoustics (4), Technical Acoustics (7), Electroacoustics (12), Photoacoustics (4), Noise Control (13), Hydroacoustics (11), Psychoacoustics (10) and Vibroacoustics (5).

The Scientific Committee of the Seminar was composed of the following well known Polish acousticians:

Prof. ANTONI ŚLIWIŃSKI – chairman

Doc. Danuta Augustyńska, Doc. Gustaw Budzyński, Prof. Zbigniew Engel, Prof. Stefan Ernst, Prof. Leszek Filipczyński, Prof. Edward Hojan, Prof. Zenon Jagodziński, Prof. Zbigniew Kaczkowski, Prof. Adam Lipowczan, Prof. Mikołaj Łabowski, Prof. Wojciech Majewski, Prof. Ignacy Malecki, Prof. Andrzej Milewski, Prof. Andrzej Nowicki,

Prof. Aleksander Opilski, Prof. Andrzej Rakowski, Prof. Jerzy Ranachowski, Doc. Jerzy Regent, Prof. Witold Rdzanek, Prof. Jerzy Sadowski, Doc. Marianna Sankiewicz, Prof. Roman Salamon, Prof. Andrzej Stepnowski, Prof. Zbigniew Wesołowski.

A few social events such as a bonfire, a banquet or an excursion were added to the interesting technical programme to enrich the programme of the conference.

The next Open Seminar on Acoustics will be organized by the Poznań Division of the Polish Acoustical Society in Kiekrz in September 1998.

Calendar of Meetings and Congresses

Compiled for the International Commission on Acoustics – May 1997

1997

03–05 June, Gothenburg, Sweden. **8th International Meeting on Low Frequency Noise and Vibration.**

04–06 June, Terni (Umbria), Italy. **International Conference on Computational Acoustics and its Environmental Applications.**

05–07 June, Bath, United Kingdom. **Conference on ICP and Inner Ear Pressure.**

15–17 June, State College, PA, USA. **NOISE-CON 97.**

15–20 June, Boulder, CO, USA. **8th International Symposium on Nondestructive Characterization of Materials.**

16–20 June, State College, PA, USA. **133rd Meeting of the Acoustical Society of America.**

18–20 June, Marseille, France. **Larynx 97.**

18–21 June, Prague, Czech Republic. **3rd European Conference on Audiology.**

24–27 June, Prague, Czech Republic. **1st European Conference on Signal Analysis and Prediction.**

25–27 June, Rotterdam, The Netherlands. **12th Symposium on Echocardiology and 9th Meeting of the International Cardiac Doppler Society.**

25–27 June, Porto, Portugal. **5th International Congress of the International Society of Applied Psycholinguistics.**

25–27 June, Kraków, Poland. **7th Symposium on Sound Engineering.**

02–04 July, Delft, The Netherlands. **Ultrasonics International '97.**

14–17 July, Southampton, United Kingdom. **6th International Conference on Recent Advances in Structural Dynamics.**

20–23 July, Toronto, Canada. **Conference on Transportation Related Noise and Vibration.**

21–25 July, Chilworth Manor, Hampshire, United Kingdom. **4th International Conference on Natural Physical Processes Related to Sea Surface Sound.**

01–05 August, Nottingham, UK. **11th International Symposium on Hearing.**

14–18 August, Newark, NJ, USA. **3rd International Conference on Theoretical and Computational Acoustics.**

16–19 August, Poznań, Poland. **Fechner Day'97**: 13th Meeting of the International Society for Psychophysics (ISP).

18–22 August, Stockholm, Sweden. **3rd EUROMECH Solid Mechanics Conference.**

19–22 August, Edinburgh, Scotland. **International Symposium on Musical Acoustics.**

21–23 August, Budapest, Hungary. **International Symposium on Active Control of Sound and Vibration (Active 97).**

24–27 August, Yokohama, Japan. **World Congress on Ultrasonics.**

25–27 August, Budapest, Hungary. **Inter-Noise 97.**

29–31 August, Regensburg, Germany. **Pan-European Voice Conference.**

01–04 September, Tokyo, Japan. **Modal Analysis Conference – IMAC-XV Japan.**

09–12 September, High Tatra, Slovakia. **31st International Acoustical Conference "Acoustics 97".**

10–12 September, Christchurch, New Zealand. **New Zealand Acoustical Society Biennial Conference.**

10–12 September, Stuttgart, Germany. **Biomechanics of Hearing.**

10–12 September, Cardiff, UK. **British Society of Audiology Annual Conference.**

12–13 September, Chicago, IL, USA. **Symposium on Sonoluminescence.**

15–18 September, Göttingen, Germany. **3rd Fluid Mechanics Conference.**

16–19 September, Jastrzębia Góra, Poland. **44th Open Seminar on Acoustics.**

17–19 September, Hokkaido, Japan. **Autumn Meeting of the Acoustical Society of Japan.**

18–19 September, Guanajuato, Mexico. **4th Mexican Congress on Acoustics.**

18–20 September, Athens, Greece. **Intonation: Theory, Models and Applications.**

21–23 September, Cape Cod, MA, USA. **Product Sound Quality 1997.**

22–24 September, Bethesda, MD, USA. **2nd Biennial Hearing Aid Research and Development Conference.**

22–25 September, Patras, Greece. **5th European Conference on Speech Communication and Technology (Eurospech'97).**

23–26 September, Delft, The Netherlands. **Fluid-structure interaction in acoustics.**

27–28 September, Rhodes, Greece. **Audio-Visual Speech Processing.**

07–10 October, Toronto, Canada. **1997 IEEE Ultrasonics Symposium.**

08–10 October, Windsor, Ont. Canada. **Acoustics Week in Canada 1997.**

23–26 October, Windermere, United Kingdom. **Reoproduced Sound 13.**

30–31 October, Bern, Switzerland. **Swiss Acoustical Society Meeting.**

19–21 November, Hong Kong. **WESTPRAC '97.**

27–30 November, Windermere, United Kingdom, **Autum Conference: Environmental Noise.**

01–05 December, San Diego, CA, USA. 134th Meeting of the Acoustical Society of America.

15–18 December, Adelaide, Australia. **5th International Congress on Sound and Vibration.**

1998

02–06 February, Moscow, Russia. **Ultrasonic Technological Processes - 98.**
(Secretariat UsTP-98, 64 Leningradski prosp., MADI-TU, Moscow, Russia.
Fax: + 7 095 151 7911; e-mail: utp@madi.msk.su)

23–27 March, Zurich, Switzerland. **DAGA 98.**

05–09 April, Ypsilanti, MI, USA. **NOISE-CON 98.**
(INCE, P.O. Box 3206, Arlington Branch, Poughkeepsie, NY 12603, USA;
Fax: +1 914 462 4006; e-mail: inceusa@aol.com)

12–15 May, Seattle, WA, USA. **1998 IEEE International Conference on Acoustics, Speech and Signal Processing.**

18–22 May, Gdańsk, Poland. **7th Spring School on Acoustooptics and Applications.**
(B. Linde, Institute of Experimental Physics, University of Gdańsk,
ul. Wita Stwosza 57, 80-952 Gdańsk, Poland;
Fax: + 48 58 41 31 75; e-mail: school@univ.gda.pl)

20–27 May, Naples, Italy. **Noise and Planning 98.**

08–10 June, Tallin, Estonia. **EAA/EEAA Symposium Transport Noise and Vibration.**

09–12 June, Umeå, Sweden. **8th Internatioinal Conference on Hand-Arm Vibration.**
(National Institute for Working Life, Conference Secretariat HAV98,
P.O.Box 7654. 90713 Umeå, Sweeden;
Fax: + 46 90 16 50 27; e-mail: hav98@niwl.se)

20–28 June, Seattle, WA, USA. **Joint Meeting: 16th International Congress on Acoustics (ICA) and 135th Meeting of the Acoustical Society of America.**

21–26 June, Gainesville, FL, USA. **13th U.S. National Congress of Theoretical & Applied Mechanics.**

16–18 September, Leuven, Belgium. **International Conference on Noise and Vibration Engineering.**
(Ms. L. Notré, K.U. Leuven, Division PMA,
Celestijnenlaan 300B, 3001 Leuven. Belgium;
Fax: + 32 16 32 29 87; e-mail: lieve.notre@mech.kuleuven,ac.be;
Web: http://www.mech.kuleuven.ac.be/pma/events/isma/isma.html)

12–16 October, Norfolk, VA, USA. **136th Meeting of the Acoustical Society of America.**

16–18 November, Christchurch, New Zeland. **Inter-Noise 98.**

22–26 November, Sydney, Australia. **Biological Effects of Noise (ICBEN 98.)**

30 November – 04 December, Sydney, Australia. **5th International Conference on Spoken Language Processing.**
(Tour Hosts, GPO Box 128, Sydney NSW 2001, Australia;
Fax: + 61 2 9262 3135; e-mail: tourhosts@tourhosts.com.au;
Web: http://cslab.anu.edu.au/icslp98)

1999

5–9 March, Berlin, Germany. **Forum Acusticum and 137th Meeting of the Acoustical Society of America.**

01–05 November, Columbus, OH, USA. **138th Meeting of the Acoustical Society of America.**

OSA 97

Lectures presented during the Seminar divided into section:

Invited lectures

L. Bjorno, Sources of ambient noise in shallow waters,

J. Blauert, Product-Sound Quality: A New Aspect of Machinery Noise,

A. Dobrucki, Technological progress and electro-acoustic transducers,

G. Grelowska, Nearfield of high intensity wave sources,

J. Kompala, I. Kubik, A. Lipowczan, Advisory system to assist localization decisions of road investments regarding sustainable development of the region,

A. Rakowski, Pitch and pitch scale in music,

R. Salamon, Detection and positioning of targets in passive sonars.

Acoustics of architecture

R. Bolejko, H. Idczak, Numerical model of acoustic plane wave scattering from surface irregularities and irregularities in surface acoustic admittance,

A. Flaga, G. Kubinyi, Acoustic analysis of a church with a crystal ceiling using a ray tacing technique,

Physical acoustics

A. Baranowska, Finite amplitude wave shape for different pressure distributions on an axial-symmetric source,

A. Brański, The different degrees multi-elements models of the acoustical source,

H. Czyż, Spatial distribution of the aerosol particles around the equilibrium points in the standing wave field,

J. Etienne, L. Filipczyński, T. Kujawska, B. Zienkiewicz, Measurements of shock waves by means of the electromagnetic hydrophone,

Z. Kaczkowski, Piezomagnetic parameters,

Z. Kaczkowski, E. Milewska, M. Muller, Ultrasound velocities in $Fe_{86}Zr_7B_6Cu_1$ metallic glass,

K. Opieliński, The influence of measurement errors on the ultrasound tomographic imaging,

J. Rzeszotarska, F. Rejmund, Acoustic emission of the Briggs-Rauscher oscillatory reaction: Effect of stirring,

T. Zamorski, Propagation of sound waves of finite amplitude in a horn at frequencies below the cut-off frequency,

Medical acoustics

J. Cieniawa, H. Gawda, In vitro comparison of acoustic and mechanical characteristics of gallstones,

A. Czyżewski, A. Kaczmarek, Investigation of fluency disorders based on vocal tract parameter analysis,

A. Dobrucki, K. Pres, P. Pruchnicki, The influence of the mechanical vibration on isolated skull bones,

H. Gawda, Hydrocortisone induced changes of acoustical parameters of long bones – the animal model,

K. Kycia, G. Łypacewicz, A. Nowicki, Ultrasonic composite probes for medical diagnostics,

W. Lis, J. Zienkiewicz, The wavelet transform analisys of the temporomandibular joint acoustic emission,

A. Lorens, A. Czyżewski, H. Skarżyński, A. Szady, B. Kostek, R. Królikowski, Multimedia catalog of hearing impairments,

W. Michalski, L. Pośpiech, W. Dziewiszek, M. Bochnia, Amplitude-phase distribution pattern of cochlear microphonics at guinea pigs,

T. Powałowski, L. Hilgertner, Z. Trawiński, Noninvasive ultrasonic examination of the input vascular impedance in the common carotid artery for persons with the atherosclerotic changes in the internal carotid artery,

K. Wojtowicz, H. Gawda, W.I. Gruszecki, Ultrasound absorption study on organization of amphotericin B in lecithin membranes.

Acoustics of speach

Cz. Basztura, P. Staroniewicz, The diphones statistics of English and Polish speech with relationships to ASR,

K. Baściuk, Speech enhancement by the spectral subtraction method – theoretical model,

K. Baściuk, Speech enhancement by the spectral subtraction method – practical implementation,

S. Brachmański, K. Baściuk, W. Majewski, W. Myślecki, A relation between the logatom intelligibility measured by means of classical and forced choice method in delta CVSD telecommunication channels,

S. Brachmański, J. Żuk, Application of RASTI system for quality evaluation of Polish speech transmission in analog communication system,

A. Olaczek, S. Brachmański, An objective measure for quality evaluation of speech coding,

R. Pazuchin, Floating formants and invariance in speech signal,

T. Przeorek, E. Łukasik, Sound signals coding using wavelet transform,

P. Staroniewicz, P. Lisiak, The structure of hybrid ANN/HMM system of short utterances recognition for Polish language,

Musical acoustics

J. Fyk, A. Rakowski, I. Kiuila, Intonation zones of melodic intervals played on the violin with piano accompaniment and without it,

M. Kaczmarek, C. Szmal, R. Tomczyk, Application of samplers and processors for sound spectrum shaping,

B. Kostek, Analysis of subjective testing results by means of intelligent decision algorithms,

J. Regent, Influence of the environment on the human voice intonation,

M. Szczerba, Fundamental frequency tracking methods applicable for wind instrument sounds,

G. Szwoch, S.K. Zieliński, The influence of the upper lip offset on the spectrum of the sound in the digital waveguide model of the organ flue pipe,

A. Wieczorkowska, Evaluation of usefulness of musical instrument sound parameters for the need of automatic classification,

Molecular acoustics

B. Linde, E. Rosenfeld, A. Christ, Acoustical investigation of mixtures water and 1,3-dioxane,

S. Pogorzelski, A. Śliwiński, J. Szurkowski, An evaluation of the PAS signal in a water – oil layered system,

D. Samatowicz, Influence of organic covering on elastic properties of metals,

A. Sikorska, M. Grus, Photoacoustic investigation of the absorption edge in the CdS:Cu polycrystalline powder.

Technical acoustics

T. Gudra, K. Opieliński, Sources of the measurement errors in the ultrasonic flowmeters applied to measurement of gas flow velocity,

A. Jaroch, M. Rabiega, Input sound power in determination of pseudo transmission loss in acoustical ducts,

A. Jaroch, M. Rabiega, Pseudo transmission loss in acoustical ducts – laboratory investigations,

R.A. Makowski, A method of seismic signal analysis,

A. Pawełek, A. Piątkowski, Z. Jasieński, A. Litwora, H. Paul, Dislocation mechanisms of acoustic emission in metal monocrystals subjected to channel-die compression,

S. Weyna, The new measurement techniques applied 'in-situ' in research of acoustics insulation properties of partitions,

E. Zielewicz-Madej, The influence of ultrasonic field on fatyty acides production and phosphours discharge in hydrolysis of sewage sludge,

Electroacoustics

M. Baszun, L. Książek, J. Narkiewicz-Jodko, W. Roguski, Ultrasonic transducers array for application at industrial robots,

D. Czekaj, Z. Surowiak, A.A. Bakirov, Properties of the piezoelectric thin PZT film sensors,

J. Dudek, Z. Surowiak, A.E. Punich, The creation of piezoelectric executive-command devices for automatically regulated systems,

M. Głowacki, I. Czarnecki, A multitone method of the transient intermodulation distortion measurement in power amplifiers,

A. Gołas, W. Ciesiełka, Adaptive system for active noise attenuation in an enclosed room,

T. Hanzlik, A full-bridge power audio amplifier of class BD having low distortion,

A. Lisińska-Czekaj, J. Dudek, Z. Surowiak, M.G. Aminodov, V.K. Dolia, Influence of the polarization process on stability of parameters of piezoelectric ceramics,

M. Niewiarowicz, H. Łopacz, Impulse characteristics of loudspeakers system,

P. Pruchnicki, The use of NARMAX method for dynamic loudspeaker modelling,

J. Stanclik, OpAmp macromodel for audio power amplifiers,

Z. Surowiak, R. Skulski, J. Dudek, The properties of the elektrome-chanical transducers on the basis of electrostrictive ceramic,

B. Żółtogórski, Optimizing of loudspeaker magnetic circuit dimensions,

Photoacoustics

M. Maliński, L. Bychto, Low frequency photoacoustic amplitude method of determination of the thermal para-meters of solids and liquids,

Z. Suszyński, Photoacoustic diagnostic of the power transistors encapsulation,

Z. Suszyński, The optymisation of the fluid's thermal effusivity changes registration,

Z. Suszyński, Thermal wave visualisation of the semiconductor chip quality adhesion to the lead frame,

Noise

D. Augustyńska, Assessment of occupational risk resulting from exposure to noise,

B. Bogusz, The influence of the arrangement of the pressure equalization on the phase characteristic of pressure microphone,

A. Chyła, T. Wszołek, W. Wszołek, Proposal of choice criteria for airport noise monitoring systems by example of airport Kraków Balice,

Z. Engel, J. Piechowicz, The propositions of indices of the acoustic assessment of industrial halls,

Z. Engel, T. Wszołek, Discussion of the project of the standard Pr PN-N-01339 Noise. Method for the measurement and evaluation of audible noise from over-head transmission lines,

J. Figwer, Z. Ogonowski, The choice of disturbance transfer function in pole/zero placement for active noise control,

H. Idczak, A. Snakowska, Sound power of the sum of a random number of independent acoustical events,

W. Mikulski, Method to calculate SPL of noise emitted by industrial buildings taking into consideration the uneven distribution of SPL on the shop floor,

M. Mirowska, Subjective and objective methods of noise assessment in dwellings,

D. Pleban, Indicatory acoustic assessment of machines,

J. Rak, M. Macko, G. Domek, Influence of geometrical shape on noise of toothed belt drives,

B. Rudno-Rudzińska, K. Rudno-Rudziński, Traffic noise level – measurements and calculations for different heights,

J. Żera, E. Kotarbińska, Danger signals for workplaces,

Hydroacoustics

P. Bittner, Determination of the acoustics field of a vibrating ship's hull by means of the superposition method,

Z. Dolny, Synchronous detection methods for the measurement of small signals,

J. Gawrysiak, Analisis of active hydroacoustic systems range versus conditions of sound propagation,

I. Gloza, E. Kozaczka, Determination of transmition losses of low frequency waves in shallow water,

E. Kozaczka, A. Makar, Determination of the delay between underwater acoustic signals,

Z. Łubniewski, A. Stepnowski, Fractal dimension as a significant parameter in sea bottom typing,

J. Maciołowska, A. Stepnowski, Fuzzy expert system for pelagic fish schools identification,

M. Moszyński, A. Stepnowski, Determining of transducer beam pattern PDF's,

A. Partyka, M. Moszyński, A. Stepnowski, Portable System for Bottom Typing and Mapping in Geographical Information System (GIS),

W. Pogribny, Z. Drzycimski, A. Milewski, I. Rozankiwski, The processing of short time series for location opportunity,

A. Stepnowski, M. Moszyński, Newly developed indirect methods of solving inverse problem in fish target-strength estimation,

Psychoacoustics

E. Aranowska, T. Rogala, The utility of Cluster Analysis in psychoacoustics,

A. Czyżewski, H. Skarżyński, B. Kostek, Z. Furman, A. Lorens, R. Królikowski, Preprocessing of audio signals in cochlear implants,

A. Jaroszewski, T. Fidecki, P. Rogowski, Hearing loss and its effects on pitch and loudness perception,

A. Jaroszewski, T. Fidecki, P. Rogowski, Exposures and thresholds in music students due to training sessions,

U. Jorasz, Modeling of auditory perception,

M.J. Kin, Perception of mixed modulation in harmonic complex for low modulating frequencies,

M. J. Kin, J. Renowski, Pitch perception of frequency-modulated tones,

R. Królikowski, Application of intelligent decision systems to the method of perceptual noise reduction,

A. Sęk, E. Skrodzka, Masking in the modulation domain. Modulation tuning curves,

A. Wicher, E. Ozimek, Pitch perception for beating sinusoids,

Vibroacoustics

J. Cieślik, Distribution of surface structure intensity along the beam with notch,

A. Gołas, P. Malcharek, R. Olszewski, Application FEM for analysis acoustical field inlimited space,

A. Kobyłecki, Classification of vehicles based on ground vibration emited during their motion,

L. Leniowska, Active attenuation of circular plate vibration by using LQR controller,

J. Wiciak, M. Iwaniec, R. Panuszka, Vibrational flow distribution of the parts of the car muffler.

Organizing Committee:

Prof. dr hab. eng. Eugeniusz Kozaczka – president,

Prof. dr hab. eng. Roman Salamon & dr Bogumił Linde – vice-chairmen,

Dr eng. Grażyna Grelowska – scientific secretary,

Dr eng. Jerzy Dobrzeniecki – organizing secretary,

Dr eng. Wiesław Kiciński – in charge of M. Kwiek competition,

Members – prof. dr hab. Andrzej Kulowski, Prof. dr hab. ing. Andrzej Stepnowski, Doc. dr Jerzy Regent, Dr eng. Lech Kilian, Dr Danuta Lewandowska, Mgr Anna Baranowska, Mgr eng. Paulina Bittner, Mgr eng. Andrzej Partyka.